MACQUARIE University
SYDNEY·AUSTRALIA

SILK-BASED FIBRES vs COLLAGEN GEL: MAJOR ORGANIC COMPONENTS OF BIVALVE SHELLS

A DISSERTATION SUBMITTED IN PARTIAL FULFILLMENT OF THE REQUIREMENTS

FOR THE DEGREE OF DOCTOR OF PHILOSOPHY

IN BIOMINERALISATION

BY

OLUWATOOSIN BUNMI ADEBAYO AGBAJE

DEPARTMENT OF EARTH AND PLANETARY SCIENCES

FACULTY OF SCIENCE AND ENGINEERING

MACQUARIE UNIVERSITY

SYDNEY, AUSTRALIA

SUPERVISOR: PROFESSOR DORRIT E. JACOB

OCTOBER, 2017

Declaration

I certify that the work in this thesis entitled “silk-based fibres vs collagen gel: major organic components of bivalve shells” has not been submitted for a degree nor has it been submitted as part of requirement for a degree to any other institution or university other than Macquarie University.

I also certify that the dissertation is an original piece of research and it has been written by me. All help and assistance that I have received in my research work and the preparation of the thesis itself have been appropriately acknowledged.

In addition, I certify that all information sources and literature used are acknowledged appropriately.

(Student #: 43536034)

Dedication

To God Almighty. I am that I am. The creator of all things. This work is also dedicated to the brightest future that has been declared by Him (God) for me.

Blessed be the name of God forever and ever, for wisdom and might are His.

Daniel 2:20

With the ancient is wisdom and in length of days understanding. With Him is wisdom and strength, He hath counsel and Understanding.

Job 12:12-13

TABLE OF CONTENTS

Acknowledgements

I am greatly indebted to you Oh Lord—the God of my fathers, for you are the glory of my strength, and in your favour my horn is exalted (Psalm 89:17). Thank you for your mercy, provisions and infinite grace over my life.

I would like to express my profound gratitude to my supervisor, Professor Dorrit E. Jacob. It has been a great privilege to be her PhD candidate. I'm indeed grateful for her effort starting from the moment I sent my application to this point and time; Thank you for your gentle push, constructive critiques and for challenging me not only to think and not only to experience but most of all to enjoy my PhD lifestyle. I would also like to express my gratitude to my supervisor's hubby, Professor Steve Foley, your big hug at the Sydney airport is still keeping me warm and welcoming, thanks for your love and kindness. Many thanks to the staffs and students of Department of Earth and Planetary Sciences, most especially Profs Simon George, Suzanne Y. O'Reilly and Bill Griffin; Drs Jinxiang Huang, Montgarri Castillo Oliver, Bruno Colas, Olivier Alard; Ms Sally-Ann Hodgekiss, Summer Luo, Anna Wan, Magdalene Wong-Borgefjord, Rosa Didonna, Nora Liptai, Mr Sarath Kumara and Henry Hadrien. Each of these individuals contributed directly or indirectly to this success.

My success as a graduate student would not have been possible without the support of people that gave freely of their time and experience. Most especially I am grateful to the facility staffs at Macquarie University Microscopy Unit: Ms Sue Lindsay, Nicole Vella, and Drs Timothy Murphy, Nadia Suarez-Bosche, who have spent countless hours teaching me the beauty of microscopy and how to find art in unexpected places. Thank you to Mark Tran, Drs Christopher McRae, Mehdi Mirzaei and Alfonso E. Garcia-Bennett of Chemistry and Biomolecular Sciences, Macquarie University for their incessant technical supports.

I thank my group members, Benedikt Demmert, Laura Otter and Dilmi Herath, for helping each other, and the camaraderie we shared. To Higher Degree Research (HDR) Mentors family, you are well-appreciated. May we always keep in contact and extend friendships forged here to

span across the globe! To Anusha Cheruku and Dr Jen Rowland, knowing you are divine and thank you for being there always. My sincere thank you also go to the Faculty of Science and Engineering HDR committee for allowing me to stand on the shoulders of giants. I gratefully acknowledge the financial funding received towards my PhD from the Higher Degree Research, it has significantly aided the study and helped me to become who I am today.

To the Cornerstone Church, Eastwood Chapter, New South Wales, the family of Irawan, King, Lingat, Liem, Tang and Bolarinwa thank you very much for your love, friendship and support and for making me feel welcome in your family. To the family of Dr and Mrs Tevi, your love and contribution toward this success is valuable. You will be thought of very fondly.

It was because of my teachers, people who did see my potential that I am more than just what my past might suggest. I am truly blessed, and for this, I am grateful to my primary and secondary school teachers; Mr David Oluwole Adesina (Big daddy); Profs Oluwadayo Olatunde Sonibare, Aderoju Amoke Osowole (late) of University of Ibadan, Nigeria; Profs John Adekunle Oyedele Oyekunle, Festus Mayowa Adebiyi and Olumuyiwa Sunday Falade of Obafemi Awolowo University Ile-Ife, Nigeria.

Warm thank you go to my parents, Elder and Lady Evangelist A. A. Agbaje, and my siblings. You have all influenced the essential elements of my life/destiny. Thank you so much. **I LOVE YOU**.

My first teacher and brother, Adedapo Gabriel AGBAJE (Late)

……. pray as if you will pray no more, read as if you will read no more

Professor Aderoju Amoke OSOWOLE (Late)

……..nothing is new but God will keep some things for you to discover

List of Publications during my PhD

The following is a list of publications in this thesis

- **Agbaje O.B.A.,** Thomas D.E., Mclnerney B.E., Molloy M.P., Jacob, D.E. (2017) Organic macromolecules in shells of Arctica islandica: comparison with nacroprismatic bivalve shells. Marine Biology (2017) 164:208. doi.org/10.1007/s00227-017-3238-2.
- **Agbaje O.B.A.,** Wirth R., Morales L.F.G., Shirai K., Kosnik M.A., Watanabe T., Jacob D.E. (2017) Architecture of crossed-lamellar bivalve shells: The Southern Giant Clam (*Tridacna derasa*, Röding, 1798). *Open Science*. 4(9):170622. http://dx.doi.org/10.1098/rsos.170622.
- Jacob D. E., Wirth R., **Agbaje O. B. A.,** Branson O., Eggins S. M. (2017). Planktic foraminifera form their shells via metastable carbonate phases. *Nature communications.* doi:10.1038/s41467-017-00955-0.
- **Agbaje O.B.A.,** Shir I.B., Zax D.B., Schmidt A., Jacob D.E. Silk-based Fibres not Chitin: Major Organic Component of Bivalve Shells Revealed by Solid-State NMR. *To be submitted*
- **Agbaje O.B.A.,** Thomas D.E., Dominguez J.G., Mclnerney B.E., Kosnik M.A., Jacob D.E. Inorganic-organic relationships in the crossed lamellar shells. *To be submitted*.
- **Agbaje O.B.A.,** Dominguez J.G., Jacob D.E. Bioorganic-inorganic fibre network in the crossed lamellar bivalve shells: Architecture of shells of *Callista* spp. *To be submitted*.

CONFERENCE/TALK AND POSTER PRESENTATIONS

- The organic matrix in mollusc shells with structural analogues to spider silk
  ComBio Conference - Adelaide - October 2017

- Molecular recognition in mollusc shells using solid-state NMR spectrometry
  EPS Department, Macquarie University - HDR Presentation Day - June 2017

- Faculty of Science and Engineering Commencement Program
  Student Representative's Experience - **Macquarie University Semester 2 – July 2017**

- Faculty of Science and Engineering Commencement Program
  Student Representative's Experience - **Macquarie University Semester 1 – February 2017**

- Insights into the diversity of organic matrices in bivalve shells with different microstructure - **Gordon Research Seminar on Biomineralisation Girona, Spain – August 2016**

- Insights into the diversity of organic matrices in bivalve shells with different microstructure - **Gordon Research Conference on Biomineralisation 2016 Girona, Spain – August 2016**

- Organic macromolecules mineralization
  Israel Institute of Technology, Technion City, Israel - September 2016

- Insight into the formation of crossed lamellar bivalve shells
  EPS Department, Macquarie University - HDR Presentation Day - June 2016

- Comparative analysis of organic moieties in bivalve shells
  EPS Department, Macquarie University - HDR Presentation Day – Nov. 2015

- The secret of shells: composition of the organic matrix
  EPS Department, Macquarie University - HDR Presentation Day - June 2015

AWARDS AND GRANT

- International Macquarie University Research Excellence Scholarship (iMQRES)
  (October 2014 - October 2017)

- Best Oral Presentation Award 2016 - Staff Vote
  2016 Higher Degree Research Presentation Day, Department of Earth and Planetary Sciences

- Macquarie University Postgraduate Research Fund 2016 – Round 2

VISIT TO RESEARCH LABORATORIES DURING MY PhD

- **Laboratory 1**
  Mawson Laboratories, School of Physical Sciences, University of Adelaide.
  Host: Dr Tony Hall
  Instrument: MSSV-Pyrolysis-Gas Chromatography-Mass Spectrometry
  Date: March 2016

- **Laboratory 2**
  Schulich Faculty of Chemistry and Russell Berrie Nanotechnology Institute, Technion − Israel Institute of Technology, Technion City, Haifa, Israel.
  Host: Professor Asher Schmidt
  Instrument: Solid State Nuclear Magnetic Resonance
  Date: August – September 2016

VOLUNTEERING SERVICE AND APPRECIATION

- Faculty of Science and Engineering Committee Member, Macquarie University (Higher Degree Research Student Representative) – 2016-2017

- Higher Degree Research Mentoring Program (Macquarie University, NSW) – 2016 - 2017

- HDR Presentation Day – Department of Earth and Planetary Sciences, Macquarie University. Member of the Organizing Committee and Chair of the session - 2016

- HDR Mentoring Program Macquarie University Presentation Day. Member of the Organising Committee and Chair of the session - 2016

- Inter-university School Postgraduate Research Excellence (InSPiRE) - 2016 (University of Technology Sydney, Sydney)

- Macquarie Minds Showcase (Macquarie University, NSW) - 2016

LIST OF FIGURES

LIST OF TABLES

ABSTRACT

Biominerals are biogenic hierarchical nanocomposite materials consisting of mineral phases, such as calcite, aragonite or vaterite, and intimately intergrown with the organic macromolecules, including proteins, polysaccharides and lipids. There is a large diversity among biominerals, each with its structural motifs, inorganic crystal formation ─ shape, and micro- or macroscopic properties. For instance, shells of mollusc are formed with different ratios of inorganic-organic materials and different structural motifs resulting in a large variety of calcareous biocomposites with material properties outperforming those of their synthetic counterparts. Amongst all different shell microstructures, nacre is the most studied to date, while comparable knowledge is lacking for non-nacre shell structures such as homogeneous and crossed-lamellar structures. In this work both, nacre and non-nacre structures are investigated and compared for commonalities and differences. The aims are to characterise inorganic-associated macromolecules in shells of different bivalve species with different microstructures and to study the interface and the interactions between mineral and biomolecules. To achieve these aims, shells of 12 species from 7 molluscan families are studied. The calcareous shells are grouped into nacroprismatic (*Hyriopsis cumingii, Cucumerunio novaehollandiae, Alathyria jacksoni, Pinctada maxima, Pinctada fucata martensii*, *Diplodon chilensis patagonicus*), homogeneous (*Arctica islandica*) and crossed-lamellar (*Tridacna gigas*, *Tridacna derasa, Fulvia tenuicostata, Callista disrupta, Callista kingii*) based on their shell microstructures. Except for *Pinctada* shells that consist both calcitic and aragonitic layers, all shells are entirely aragonitic.

A common phenomenon exists between the compositions of organics present in the nacreous layer of the studied nacroprismatic shells. Thermogravimetric analysis exhibits a total amount of organics in the range of 3.14 - 4.13 wt%. The amino acid composition reveals a high amount of glycine and alanine (ca 54% in total) and consists of moderate polar amino acids – aspartate and glutamate (~ 16% in total). Solid-State Nuclear Magnetic Resonance (NMR) spectroscopy using Cross-Polarization Magic-Angle Spinning (CP-MAS) was employed and revealed silk-based fibres as the primary organic framework in nacre. As shown by electron microscopy, extensive hydrogen-bonded β-sheet nanocrystals are well-organised along and within a semi-amorphous protein (in analogy to the spider dragline silk and *Bombyx mori* (cocoon) silk). While it may certainly be beneficial to explore available sugar moieties in the organic macromolecules, these appear to be present in concentrations not necessarily significantly higher than, for instance, phosphates post-translationally intercalated into the silk fibroins as discovered in this thesis. Moreover, the sugar moiety is probably *N*-glycosylated and is significantly different from that found in non-nacre microstructures.

The composition of shells with homogeneous and crossed lamellar structures are significantly distinct from that of nacre. Though the calcareous microstructures of non-nacre shells are divergent, the amounts of organics are comparable (1.6 wt% by TGA compared to 3-4 wt% for nacreous shells). Glycine, aspartate and proline (~40% in total) are the prominent residues. Different to nacreous and homogeneous shells, the decalcification method failed to extract and concentrate the insoluble organic moiety in crossed lamellar shells. The macromolecular content of homogeneous shells is not suggestive of a silk-like composition as in nacreous shells, instead, consists mainly of collagen gel. A remarkable structural feature of the biopolymer is a three-dimensional polygonal meshwork of type IV collagen gel aggregates, which, in turn, probably constitutes an *O*-glycosylated sugar moiety.

The ultrastructure of crossed lamellar shells was characterised with high-resolution electron microscopy. The imaging displays the fine structure of nanogranular particles that are composites of inorganic and organic matrices, arranged either in nanometer-sized laths or a polycrystalline fibre-like fabric. In the freshwater and marine bivalve shells studied in this project, the major biological scaffolding in nacre consist of silk-based fibres, while homogeneous (and probably crossed lamellar) shows proteinaceous content that is different from a silk-like biopolymer, instead, consists primarily of collagen gel. These findings are new and contrast with the long-standing view that chitin is the most important ingredient of the organic matrix in mollusc shells. Here, glucosamine (the monomer which upon acetylation is the basis of chitin) was found to represent only a very minor part of the organic moiety. Furthermore, the distinctly different biopolymers in nacre versus non-nacre shells found in this work suggests that the composition of the insoluble organic matrix differs depending on species, similarly to that of the soluble organic matrix, which is well-known in the literature.

As the chemical palette available to form a silk-based fibre and collagen gel include many building blocks, namely the 20 naturally occurring amino acids, this work presumes that it is worth reconsidering the relative importance of the available biopolymers that assist in providing templating for inorganic minerals. While the insoluble organic moiety in nacre (*Hyriopsis cumingii*, *Cucumerunio novaehollandiae*, *Alathyria jacksoni*, *Pinctada maxima*) consists primarily of silk-based fibres, and thus serve as structural proteins, that of homogeneous (and probably crossed lamellar) shells constitute mainly of collagen IV gel. Moreover, the presence and the structures of sugar moieties glucosamine and mannose for nacre; glucosamine, galactosamine and galactose for non-nacre shells support the importance of saccharides in composite biominerals, however, make an interesting contrast to the abundance of insoluble saccharides proposed in the literature.

1.0 INTRODUCTION

1.1 AN OVERVIEW OF THE THESIS

Herein structural mechanism and composition of a three-dimensional organic matrix from calcareous biominerals are examined. The three-dimensional assembly of shell biopolymers contains variable ratios of polyamino acids (proteins) and polysaccharides depending on the nanocomposite biomineral and microstructure. These components are actively involved in shell formation and proteins have been shown to control virtually all levels of mineralisation, including mineral polymorphs (calcite, aragonite or vaterite), sizes and shapes of the grains, and the overall microstructure of the biominerals [1-3].

For over one century [4], researchers across a number of fields, including materials science, biology, chemistry and biochemistry have made remarkable progress in characterising the organic matter of mollusc shells. Amongst all different shell materials and microstructures, nacre (mother-of-pearl) is the most studied to date due to its exceptional toughness [5, 6] and its biocompatibility [7], whereas comparable knowledge is lacking for non-nacreous (homogeneous and crossed lamellar) structures. Superficially, the identification and the characterisation of shell macromolecules were based on histochemical and biochemical analyses. The integration of these methods alongside with the multi-methods imaging such as cryogenic-scanning electron microscopy have condensed today that the major constituent of shell macromolecules is the polysaccharide β-chitin, a relatively hydrophobic silk protein, and a complicated assemblage of acidic macromolecules [1-3, 8]. To characterise in detail the composition of the shell biopolymers in the shells of bivalve from different taxonomic families and with different microstructures, the shells of 12 species from 7 molluscan families have been studied (Table 1.1). The shell samples are grouped into nacroprismatic, crossed lamellar and homogeneous shell microstructures [9].

The aims of this thesis are:

i) To determine whether different bivalve shells with different microstructures contain a similar population of matrix proteins, or not;

ii) To compare and to contrast the characteristics of the organic matrix between different microstructures and;

iii) To study the interface and the interactions between mineral and biomolecules.

Table 1.1

Taxonomic allocations and shell microstructures of the 12 species studied. CL: crossed lamellar layer, CCP: crossed composite prismatic, C: complex layer, N: nacreous layer and P: prismatic layer

Taxonomy	Shell microstructure
Tridacnidae *Tridacna derasa* Röding *Tridacna gigas* Linnaeus	CL
Cardiidae *Fulvia tenuicostata* Lamarck	CL
Veneridae *Callista disrupta* Sowerby *Callista kingii* Gray in King	CCP, CL, C
Arcticidae *Arctica islandica* Linnaeus	Homogeneous
Unionidae *Hyriopsis cumingii* Lea	N, P
Hyriidae *Diplodon chilensis patagonicus* d'Orbigny *Cucumerunio novaehollandiae* Gray *Alathyria jacksoni* Iredale	N, P
Pteriidae *Pinctada fucata martensii* Dunker *Pinctada maxima* Jameson	N, P

1.2 Structure of the thesis

The thesis is organised as thesis by publication consisting of six chapters excluding the introduction and general conclusions (Chapter 8).

Chapter 2 – characterises shell-associated macromolecules in homogeneous *Arctica islandica* shell. The comparison was made with the nacro-prismatic shells. This section aimed to explore overall commonalities and differences in the organic content in bivalve shells from the perspective of their shell microstructure. To achieve this goal, I designed new staining and fixing methods, as well as the decalcification methods. This chapter represents the article: **Organic macromolecules in shells of *Arctica islandica*: comparison with nacroprismatic bivalve shells (2017)** and published at Marine Biology. doi.org/10.1007/s00227-017-3238-2.

Chapter 3 – Silk-based Fibres vs Collagenous Gel: Major Organic Components of Bivalve Shells Revealed by Solid-State NMR explores the three-dimensional assembly of shell biopolymers. Nacreous layer of nacroprismatic shells and non-nacre (homogeneous and crossed-lamellar) shells were characterised with solid-state nuclear magnetic resonance as well as other spectroscopic techniques. This chapter revealed that, contrary to current belief, silk-based material featured β-sheet nanocrystals and not chitin is the major organic component in the nacreous shells microstructure. In homogeneous (and probably in crossed lamellar), however, the mesh networks formed by type IV collagen heparin sulfates and keratanasulfates is the primary organic scaffold rather than the more typical fibrillar form.

Chapter 4 – Architecture of crossed-lamellar bivalve shells: The Southern Giant Clam (*Tridacna derasa,* Röding, 1798) considered the crystallographic orientation of crossed lamellar shells and shell-associated macromolecules. The decalcification method that was failed to extract and concentrate the insoluble organic moiety in crossed lamellar shells in chapter 3 was modified. This section revealed how inorganic matrix of *Tridacna* species is intimately intergrown with biopolymers, namely polysaccharides, glycosylated and unglycosylated

proteins and lipids. This chapter of the thesis is published at Royal Society Open Science. http://dx.doi.org/10.1098/rsos.170622.

Chapter 5 – **Inorganic-organic relationships in the crossed lamellar shells** elucidated organic matter that occluded in the calcareous biominerals of crossed-lamellar shells structure. The models used are the bivalves *Tridacna* and *Fulvia tenuicostata* shells. Newly developed staining techniques alongside with the adapted decalcification methods depict for the first-time the presence of amino polysaccharide, as well as many prominent protein bands, glycoproteins and/or glycosaminoglycans of unknown size from crossed lamellar bivalve shells. This aspect of the thesis revealed that chitin-protein-complex and lipid-lipoproteins may be essential for shells with different microstructures.

Chapter 6 – **Bioorganic-inorganic fibre network in the crossed lamellar bivalve shells: Architecture of shells of *Callista* spp.** showed that *Callista* bivalve shells have complex microstructures consisting of fibrous aragonitic calcium carbonate. These are in turn interlayered at a constant angle and reminiscent of plywood. In-depth study of the inorganic matrix and the organic composition thus enabling to exhibit and characterise inorganic-associated biopolymers, including polysaccharides, proteins and glycoproteins. This aspect of the thesis revealed that organics are indeed, embedded and/or occluded within and along the inorganic fibrous to form a polycrystalline fibre-like fabric.

Over the years, it is well-known that planktic foraminifera is preserved in marine sediments as calcite, the stable polymorph of calcium carbonate. **Chapter 7** – **Planktic foraminifera form their shells via metastable carbonate phases** showed that shells of living planktic foraminifers *Orbulina universa* and *Neogloboquadrina dutertrei* originally form from the unstable calcium carbonate polymorph vaterite, implying a non-classical crystallisation pathway involving metastable phases that transform ultimately to calcite. This chapter of the thesis was published at Nature Communications. doi: 10.1038/s41467-017-00955-0.

1.3 Matrix Mineralisation in Calcareous Biominerals

1.3.1 Biomineralisation – An Overview

The term biomineralisation refers to the processes by which living organisms synthesise minerals. The formation of biominerals consists two basic classes: organic matter and inorganic matrix [2, 3, 10]. The biologically-formed minerals combined a significant level of intricacy and possess intriguing characteristics as required naturally complex nanostructures [2, 11].

Biomineralised structures are fashioned in a much wider number of diverse species, and in a wider variety of shapes and forms [1, 3, 11]. A few typical examples comprise diatoms and sponge spicules (silica), magnetotatic bacteria (iron oxide), teeth and bone (calcium phosphate) and shells of mollusc (calcium carbonate) [3, 11]. In general biogenic materials of every animal has an individual organisation, one can say that calcified storage structure has a layered structure and that the layers may alternate between the bioorganic matrix and inorganic minerals. These are fundamental for the excellent mechanical strength and toughness of the natural carbonates materials [5, 11, 12].

According to the previous authors [2], carbonated nanocomposite materials dominate in biomineralisation. They even occur in plants and fungi [13]. The calcium carbonate or calcium phosphate biominerals, respectively intimately intergrown with biopolymers (the organic matrix) such as polyamino acids (proteins) and polysaccharides, have such a high lattice energy and low solubility. Calcareous biocomposites are thermodynamically stable in biological and natural environments, and hence depict a number of polymorphs (see Table 1.2). The calcium carbonate biominerals of invertebrates, such as molluscs and sea urchin spines, have tremendously been studied due to their high degree of crystallographic control that is achieved in these biogenically formed minerals [2, 3, 13, 14]. Understanding the primary components that stabilised the polymorphism in invertebrate organisms can provide essential insights into main aims of synthesising inorganic (calcium) carbonate materials in the laboratory.

Table 1.2 Calcium carbonate composite materials and their function, modified after Mann 2001

Mineral	Formula	Organism	Location	Function
Amorphous	$CaCO_3.nH_2O$	Crustaceans	Crab cuticle	Mechanical strength
		Plants	Leaves	Calcium store
		Bivalve	Shell	Exoskeleton[a]
		Crustaceans	Pillbug	Exoskeleton/Reproduction[b]
Vaterite	$CaCO_3$	Gastropods	Shell	Exoskeleton
		Ascidians	Spicules	Protection
		Foraminifera	Shell	Exoskeleton[c]
Aragonite	$CaCO_3$	Molluscs	Shell	Exoskeleton
		Gastropods	Love dart	Reproduction
		Cephalopods	Shell	Buoyancy device
		Scleractinian corals	Cell wall	Exoskeleton
		Fish	Head	Gravity receptor
Mg-calcite	$(Mg, Ca)CO_3$	Octocorals	Spicules	Mechanical strength
		Echinoderms	Shell/spines	Protection
Calcite	$CaCO_3$	Molluscs	Shell	Exoskeleton
		Foraminifera	Shell	Exoskeleton
		Coccolithophores	Cell wall scales	Exoskeleton
		Crustaceans	Crab cuticle	Mechanical strength
		Birds	Eggshells	Protection
		Trilobites	Eye lens	Optical imaging
		Mammals	Inner ear	Gravity receptor

NB: a = Wolf et al. [15]; b = Tao et al. [16]; c = Jacob et al. [17].

1.3.2 Biomineralisation Mechanisms: classical and nonclassical nucleation theories

Calcium carbonate exists in six different polymorphs: an amorphous phase (amorphous calcium carbonate, ACC), anhydrous phases (vaterite, aragonite and calcite), and hydrated crystalline forms (calcium carbonate monohydrate (*monohydrocalcite*) and calcium carbonate hexahydrate (*ikaite*)) [18]. These inorganic minerals have the same principal composition, but their atomic structures, Ca^{2+} ions (and CO_3^{2-}, respectively), are stacked in different configurations thus possess different crystallographic orientations in the crystal lattices [19, 20]. Among these polymorphs, hydrated crystalline forms are sporadic [18].

From literature, it has been argued that biominiralising organisms fabricate calcareous biominerals by using two major pathways: the classical nucleation pathway and non-classical nucleation pathway [21, 22]. The former is based on the primary building blocks like atoms, ions or molecules, and thus involve the monomer-by-monomer addition to forming an isolated

cluster (Figure 1.1) [21-23]. This cluster may increase in size or shrink depending on the relative magnitude of surface and bulk energies available. As the favourable interfacial energy is dominant for small particle size, the cluster will reach critical nucleus, and thus proceeds to grow into larger single crystals via building blocks (e.g. ions) adsorption [22, 24].

In some studies, it was declared hypothetically that this process could be controlled/modified by adding additives, such as polyamino acids, polymeric biomolecules, ions [21, 24-26]. The additives will lower the energy barrier for nucleation to commence, and thus generate the aptly structured cluster that would then grow into a specific polymorph through basic monomers addition. In biomimetic mineralisation, however, these claims did not provide the answer to the question of how invertebrate organisms can shape crystalline units into the often-observed non-equilibrium morphologies [11, 26].

In contrast to classical monomer-by-monomer precipitation and aggregation of the particle motion, non-classical crystallisation pathway is facilitated by the aggregation of more complex particles, ranging from multi-ion complexes to nano-discrete particles [21, 24]. The assembly of structured nanocrystalline materials has been shown to exist via both oriented and non-oriented attachment (also known as ‘‘aggregation’’) as well as the amorphous addition [27-29]. Though recent evidence suggests coexistence of two pathways in a single system—including classical and non-classical mechanisms [30], invertebrate organisms, such as mollusc shells, primarily utilise non-classical crystallisation pathway to fabricate their calcareous biominerals [15, 22, 31, 32].

The organisms first produce an amorphous calcium carbonate (ACC) [21, 22, 33]. The self-assembly ionic Ca^{2+} (and CO_3^{2-}, respectively) clusters, and subsequently crystallises via metastable carbonate phases to form the resulting shell mineral. On the other hand, biologically-formed amorphous phase before it transforms into a given crystalline calcium carbonate, either aragonite and/or calcite, plays a significant role in the initiation of the biomineralisation process [34-36]; it can be used as temporary storage for shell mineral [37].

While nature is disordered, many biologically precipitated inorganic carbonates are known to form through complex mineralisation pathways involving metastable intermediate phases that transform stepwise into the final calcareous biomineral [17].

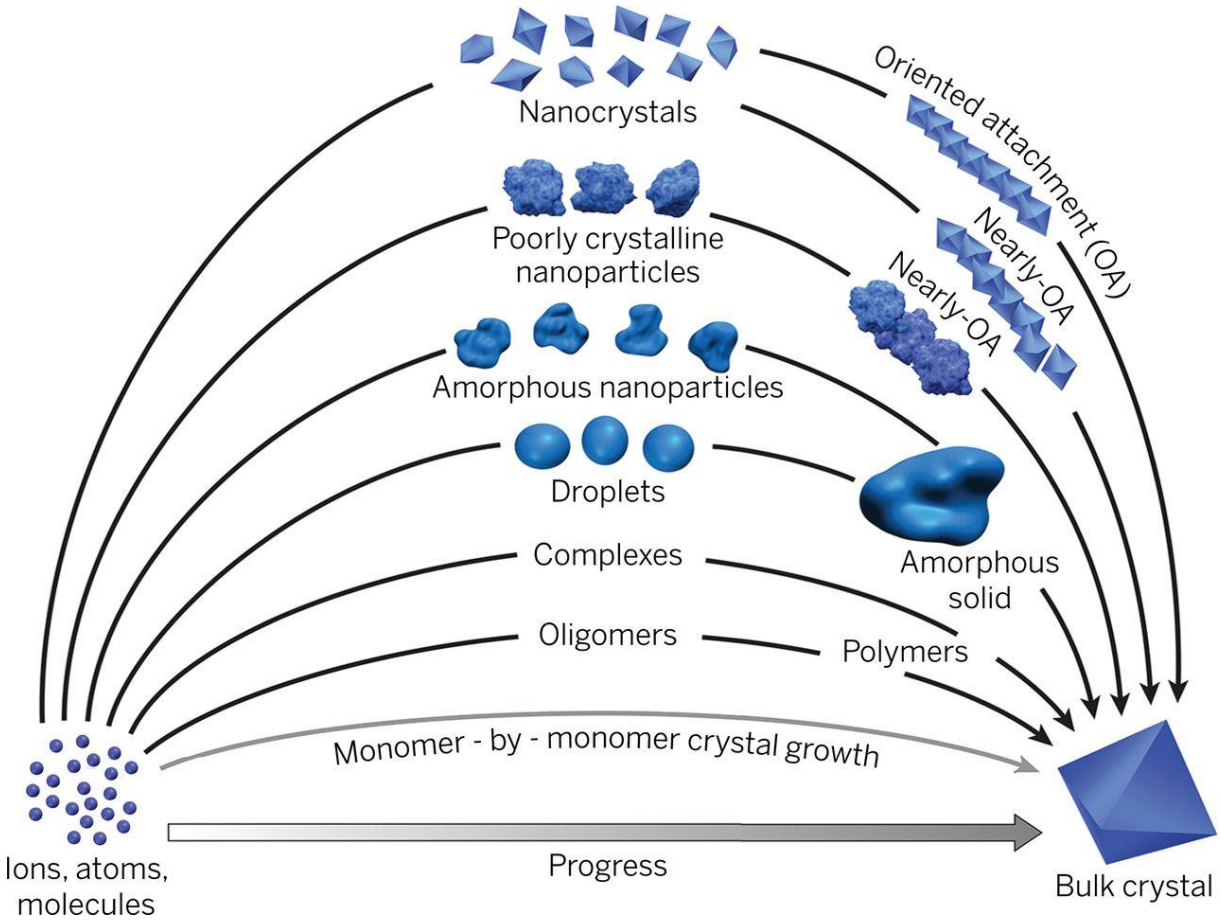

Figure 1.1: Cartoon of the proposed model for the pathways to crystallization by particle attachment (CPA). In contrast to classical nucleation theory (monomer-by-monomer crystal growth; grey curve), the formation of non-classical nucleation involves addition of higher-order species that first assemble into amorphous clusters. The amorphous clusters particle can be stabilised indefinitely by additives (such as polyamino acids, ions etc.), or can transform to fully formed nanocrystals. From [21].

The selection of early stage for calcareous biominerals either ACC [15, 21] or metastable vaterite [17] has been proved beyond doubt. One could think it should in principle be possible/easier to give a 'blueprint' of shell mineral in the laboratory. Layer-by-layer growth of calcareous biominerals is challenging. Moreover, *in vitro* ACC is unstable in the laboratory, it transforms to crystalline phase via dissolution and re-precipitation [38, 39], whereas most *in vivo* studies of skeletal structures demonstrate a solid-state phenomenon comprising

dehydration and structural rearrangement [34, 35]. In some of the biologically controlled materials, however, ACC occurs either as a final biomineralised structure or as a solid precursor phases of crystals [40-42] and intimately intergrown with the three-dimensional macromolecules [43, 44]. As recently reviewed [45], the organic matrix and/or minor metal elements in the shell could probably stabilise the amorphous phase or metastable vaterite phase [17].

Organic macromolecules, including proteins, polysaccharides, lipoproteins and low-molecular weights molecules such as citrate are a minor albeit vital component in biological materials: they regulate the prenucleation of inorganic mineral and select/control the polymorphs of calcium carbonate. It is believed organic components determine the structural patterns of calcareous biocomposites [2, 3, 43]. In nature mineralisation mechanism is under strict control, and include a great measure of organic-inorganic nanocomposites [2]. While our knowledge is increasing daily concerning the inorganic matrix of biominerals, the molecular mechanism of three-dimensional biopolymers is still vague.

1.4 Mollusc Shells – Overview

Shell-bearing molluscs first appeared about 543Mya in the earliest Cambrian time and contain circa 118,000 extant species [46, 47]. Calcareous shells differ significantly in size, ranging from a few millimetres to many centimetres forming biominerals composite patterns that are widespread globally [9]. As reviewed by Barthelat et al., the earlier calcareous shells were small, circa 0.2-0.5 cm, with shell assemblies very comparable to the modern shapes [48].

The molluscs might be considered the ultimate examples of "morphing," both in regard to details of their architectural pattern and details of the shell, itself. Nonetheless, the basic architectural pattern is one of front-to-back bilateral symmetry, with distinct nerve ganglia, gills, a blood circulatory system, as well as digestive, reproductive, and excretory organs [49].

The organ that responsible for the formation of shell is the mantle, a membranous tissue that covers the soft-body from the dorsal area [50, 51] and it consists of two epithelia (inner and outer) separated by tissues such as connective tissue. Typical to the mollusc shells, the mantle is divided into four main areas: mantle edge, mantle isthmus, mantle centre and mantle pallium [45]; among these four, mantle edge is the most active calcification and the length growth of the shells occur at the ventral margin to induce the growing animal. Although, there may be some discrepancies from group to group, nevertheless, the main principles that govern the physiology of shell-bearing molluscs' formation are somewhat common. Moreover, by conducting an *in vitro* regeneration research for the formation of shell [52-54], it was demonstrated that shell-associated macromolecules were secreted from the epithelial cells of mantle of Akoya pearl oyster (*Pinctada fucata*, Gould, 1850). While the formation of calcareous biominerals is still unclear, the observations showed that the mantle tissue has a key role in synthesizing shell mineral [45].

1.5 Matrix mineralisation

In the biologically controlled processes, the living organisms exert a significant degree of metabolic control on the formation of well-tailored minerals, for instance, shell-bearing molluscs [2]. Matrix mineralisation was described as a series of extracellular events occurring within compartments [9, 54]. Typically, shell formation/mineralisation involves the two-step sequence - nucleation and then crystal growth. The organics play a crucial role in the formation of shell mineral, whereas how and to what extent the shell macromolecules participate in one or both of these steps is not well understood [1].

Nonetheless, biomineralising organisms have used the two-step sequence to synthesise intricate calcareous structures for a significant amount of biominerals from Bivalvia, Gastropoda, and beyond. The bio-constructional framework (hard exoskeletal) relies on the expansion of an external bio-calcified rigid architectural pattern, the shell. The shells of mollusc (gastropods and bivalves) provide a reliable means of protection to their soft body against

predators, and used for precluding desiccation [9]. Mollusc shells are one of the most studied composite biomaterials and probably the fascinating species in the world of the living. They consist of non-calcified outer layer – periostracum, highly oriented calcium carbonate crystals that interspersed with thin sheets of organic macromolecules (the organic matrix). While total organic content that intercalated within the calcareous biominerals can be measured by thermal gravimetric analysis (TGA) and typically finds a total organic content that never exceeds 5%wt, these organics are organised in two different shell layers: The innermost layer is aragonitic and an outer layer, usually prismatic (Figure 1.2), depicts either aragonite or calcite, whereas metastable polymorph – vaterite is usually associated with shell repair [9, 55].

Regarding microstructure, molluscs used seven main types to fabricate their shells and these include nacre (columnar and sheet), prismatic, crossed lamellar (simple and complex), homogeneous and foliated (Figure 1.3) [56]. Among these microstructures, crossed lamellar is the most common followed by nacre and prismatic microstructures, respectively and perhaps, followed by homogeneous [9, 57].

1.5.1 Prismatic microstructure

The prismatic layers in calcareous biominerals show considerable diversity in structure, for example, individual prisms may be either single crystals or polycrystalline [58]. Carter [9] showed that the prism morphology is not uniform in all calcareous shells; they are found with different length/width ratios; regular or irregular cross-sections or may consist of fibrous, and or composite structure.

The prismatic layer from bivalve shells such as *Pinctada fucata*, has regular, which is called simple prismatic microstructure. The shell layers are mutually parallel with adjacent units that do not actively interdigitate along mutual boundaries [9]. However, other shells consist irregularly or regularly shaped first order prisms which are in turn comprise parallel or fan-like

(or feathery) shaped aggregates of fibrils or second order prisms or radial laths in vertical sections [9, 59, 60].

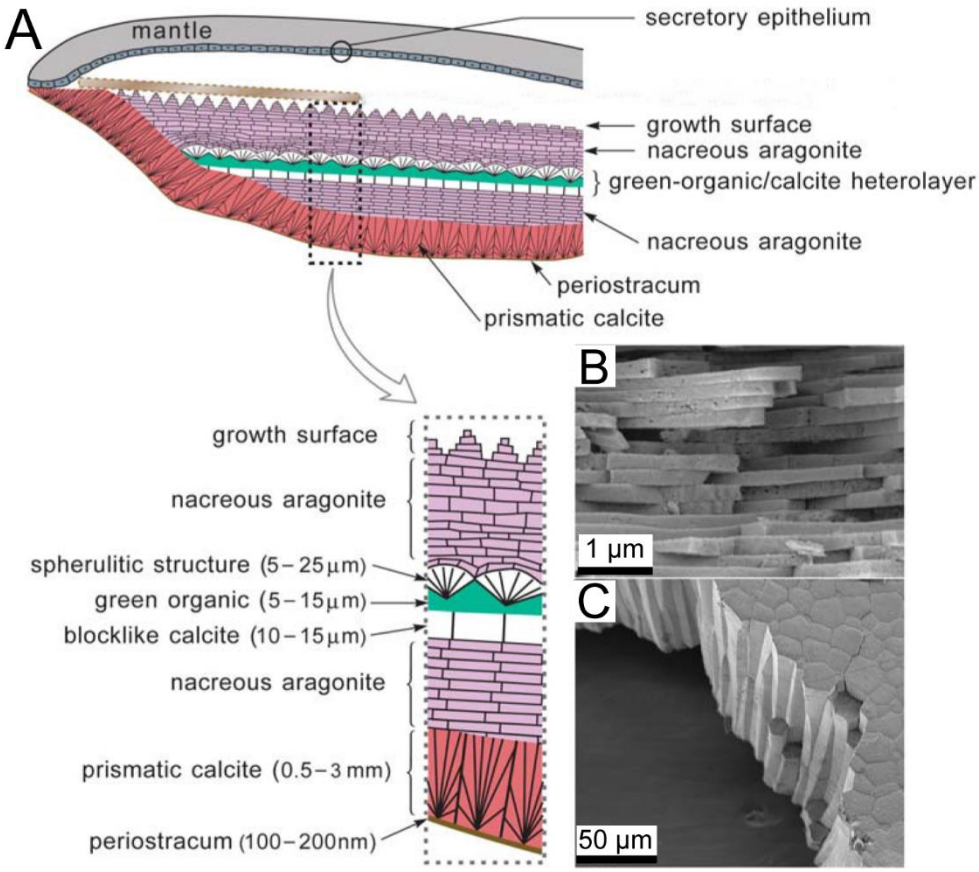

Figure 1.2: (a) Cartoon of biologically-formed shell materials. The image shows the interlayering of the inorganic matrix with bioorganic macromolecules. The bioorganic matrix appears as thin layers and provides substrate to lead the onset of newly formed layers; (b) demonstrates SEM image of interlocking aragonite tablets that constitute the nacreous layer; (c) depicts SEM image of prismatic calcitic outer layer of calcareous shell. [Adapted from [61]].

1.5.2 Nacreous microstructure

Nacreous structure, exclusive to molluscan families, found in gastropods, bivalves and in the septal chamber of cephalopod *Nautilus* composed of continuous lamellae built of polygonal tablets [9]. The diameter of a tablet is in the range 5-15 µm, the thickness of the tablets in the gastropod is about 0.5 µm, and it is around 0.3 µm for bivalve nacre shells. The lamellae are

separated by sheets of interlamellar organic matrices, and each tablet is surrounded by intertabular organic matrices [6, 62, 63].

Depending on the mode of polygonal tablets, there are two types of nacreous structures (Figure 1.3) when comparing the calcareous shells. In gastropods and to some extent in cephalopods, nacreous layer is stacked in columns [64, 65]. This microtexture is covered with a surface membrane thus protects the growing biogenic structural (nacre) surface from damage and desiccation when the soft-body of the animal withdraws into itself, shell. In bivalvia shells, however, the individual tablet-like crystals have a staggered 'bricks and mortars wall' appearance [66]. This latter one is known as sheet nacreous structure.

1.5.3 Homogeneous microstructure

Homogeneous microstructure refers to calcareous shell structures which do not present a superficial organisation of crystallites when observed with optical and scanning electron microscopies [9]. According to Boggild (1930), who described homogeneous structure from thin-sections imaging, this layer lack discernible substructure but has an arrangement of the crystallographic axes. Moreover, Kobayashi defined it as the aggregation of granule particles with more or less equidimensional [67], haphazardly shaped crystallites lacking clear-cut first-order architectural hierarchy except for possible accretion banding [68, 69]. While nature has found a way to insert organic macromolecules within shell mineral, the composition of the organic scaffold in homogeneous shell structure has not been characterised.

1.5.4 Crossed lamellar microstructure

The primary characteristic of crossed lamellar microarchitecture consists two sets of elongated crystals, each of which is tilted at some angle to the surface of the calcareous biomineral. Twinning of the aragonite crystals is ever-present in this microstructure [70, 71], and some structural models have described the architectural pattern (e.g. Figure 1.3b). Accordingly, fourth-order lamellae are stacked together in a particular direction and form thin

lamellar prisms called third-order lamellae. It was reported in 'the literature' [9, 57, 72-74] that third-order lamellae aligned in parallel and create second-order lamellae (broad tablet), which, in turn, arranged alternately changing the direction of the *c*-axis and hence piled up to form a series of undulating aragonite thick blocks, which may be hundreds of micrometres long – first order lamellae.

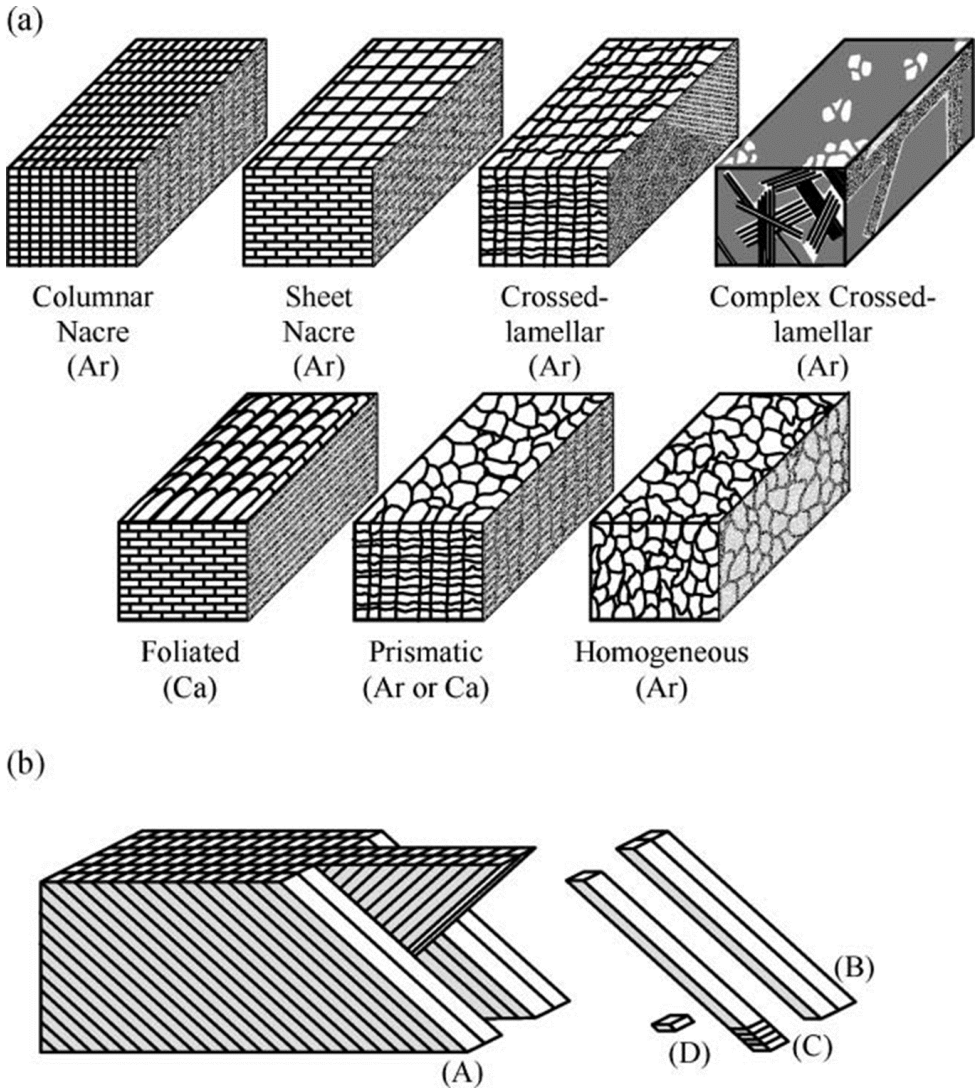

Figure 1.3: Schematic diagrams for shell microstructures: (a) the most common microstructures. Note: Ar = Aragonite and Ca = Calcite; (b) the hierarchical order of the crossed lamellar microstructure showing (A) first order, (B) second order, (C) third order and (D) fourth order lamellae. Figure adapted from Eichhorn et al. [56].

Crossed lamellar shell is highly mineralised, circa 99 wt% with a low amount of organic macromolecules, circa 1 wt%, and possess unusual mechanical performance [75, 76]. The effort

to characterise the organic macromolecules from nacre has an extensive history, whereas comparable effort is lacking for the most widespread microstructure – crossed lamellar. Herein, shell macromolecules are characterised from crossed lamellar bivalve shells, including proteins, polysaccharides and lipids.

1.6 Shell macromolecules (the organic matrix) in calcareous biominerals

The characterisation of 'modern' shell model started in 1969 with the work of Bevelander and Nakahara [77]. These authors studied some nacreous shells via electron microscope and proposed a 'compartment model'. Preformed interlamellar sheets existed for inorganic tablets to mineralise, however, Bevelander and Nakahara did not characterise the composition of the organic matrix. Due to the exceptionally architectural pattern in nacre, researchers from several fields including materials science, biochemistry and chemistry, and beyond have devoted to studying the composition of organic matrix and the inorganic minerals of the innermost layer of shell-bearing mollusc – nacreous.

The organic matrix within the nacreous layer (interlamellar, intertabular and intracrystalline) includes three main components: 1) acidic glycoproteins [63], some of which serve as nucleating centres for aragonite [78, 79]. 2) alanine- and glycine-rich silk-like fibril proteins [63, 80], present in a hydrated gel-like state [8]. 3) Polysaccharide β-chitin, positioned in the inter-lamellar matrix, serves as a scaffold [8, 81].

Regardless of phylum and shell microstructures, the concept of an organic matrix can be categorised into two fractions based on the demineralisation methods: i) the soluble organic fraction; ii) the insoluble organic fraction. Soluble organic moieties (including acidic glycoproteins/polysaccharides and/or proteoglycans) can further be classified into acid, water and EDTA; also, insoluble fraction can be grouped into acid insoluble – detergent-soluble components and acid-insoluble – detergent-insoluble organic fractions [45].

The soluble organic constituents such as nacrein [82], mucoperlin [83], N14 [84], Asp-rich hydrophilic [85] and Gly-rich peptides [86] are perhaps intracrystalline biomolecules regulating morphology and crystal growth. Tens to hundreds of different proteins [87-89] as well as silk-like fibroin gel [90, 91] are incorporated in bivalve shells. Not all of these components participate in shell mineralisation and fully characterising the organic moiety in shells is challenging. Nevertheless, numerous shell-associated matrix proteins have been characterized up to now, and show that the 'shellome' (i.e. the shell protein content active in matrix mineralisation; [89, 92] is apparently species-specific with very few similarities between different calcareous biominerals [84, 90, 93]. Moreover, the composition of the organic matrix changes between biominerals from related species with the same microstructure, this was evidenced within the matrix proteins of *Pinctada margaritifera* using SDS-PAGE and mass spectroscopy analysis [94].

Investigations of demineralised mollusc shells have shown that intercrystalline organic matrix is usually composed of highly oriented insoluble polysaccharide – β-chitin [8, 95]. β-chitin, a crystalline biopolymer (1 → 4)-linked 2-acetamide-2-deoxy β-D-glucan [96], sandwiched between layers of silk fibroin-like proteins is known to be coated by macromolecules rich with acidic sidechains (Figure 1.4) [85, 89, 97].

In mollusc, chitin was first identified in the shells of *Nautilus* species by using the chitinases histochemical treatment [98] and subsequently by many other authors (e.g. [63, 80, 99]. Weiner et al. used bioanalytical techniques to reveal three-dimensional biomatrix in shells and concluded that chitin is present in some molluscs and absent in others. Whereas other authors hypothetically declared that no significant differences in the abundance of polysaccharide β-chitin between nacreous layers of nacroprismatic shells [8]. Recently, Osuna et al. showed minor chitin component that forms a complex with the protein coat in the nacreous layer of bivalve *Pteria hirundo* shells [100], and thus contradict long-standing opinion concerning chitin as a major organic scaffold in nacre. While the hypotheses regarding the distribution of chitin

in nacre differ, very little is known to date about the organic scaffold in non-nacre, such as crossed lamellar and homogeneous shells.

1.6.1 Hydrophobic proteins - Silk fibroin gel

As described above, the effort to characterise shell-associated macromolecules has an extensive history. Much of that effort has focussed macromolecules rich with acidic sidechains (e.g. [85, 89, 97]) and chitin (e.g. [101-103]), whereas less attention has been devoted to the (typically) hydrophobic proteins - silk-like gel. The composition of organics in nacre constitutes the high amount of glycine, alanine and serine (ca 60%) characteristic of silk fibroin-like proteins [88, 91]. Although, the percentage of these residues are not always high, varied from shell to shell and within the same species [104]. Nonetheless, silk fibroin-like protein was proposed to be a space-filling agent, and thus provide and maintain the appropriate microenvironment for shell mineral [8, 95, 105]. *In vitro* study demonstrated that fibroin-like gel is a mild inhibitor of mineralisation, it could inhibit the precipitation of a critical nucleus from growing [8]. Gel-like organic matrix can also act as a site directing agent by either suppressing calcium carbonate crystallisation or modulate the growth of inorganic grains until stepwise transformation of inorganic mineral is in contact with the nucleating site or with the already formed shell mineral [2, 8]. *In vivo* studies revealed that silk-like hydrogel proteins do not occur alone, it attached with the chitin-containing carbohydrates. That such constructs are reasonable is supported by the observation of chitin fibres as a minor protein-associated component in the silk ducts of both the spider *Nephila* genus and the *Bombyx mori* silkworm cocoons [100].

The ability of arthropods to produce structural silk fibroin fibres is ancient [106, 107]. Two types of silk fibroins: *Bombyx mori* silkworm cocoons and dragline spider silk have been studied extensively (e.g. [108-110]). As is typical to silk fibres, they consist crystalline domains [108] and adopt an antiparallel β-pleated sheet conformation [109]. These domains have a

highly ordered and hydrophobic surface upon which hydrophilic sidechains adsorbed from solution, and thus enabled the strength and resiliency of silk fibres [111]. Up to date, no evidence of crystalline domains in the silk-like fibroin of mollusc shells. This work has demonstrated that the organic matrix in nacre is strikingly comparable to the spider dragline silk and *Bombyx mori* silk cocoon.

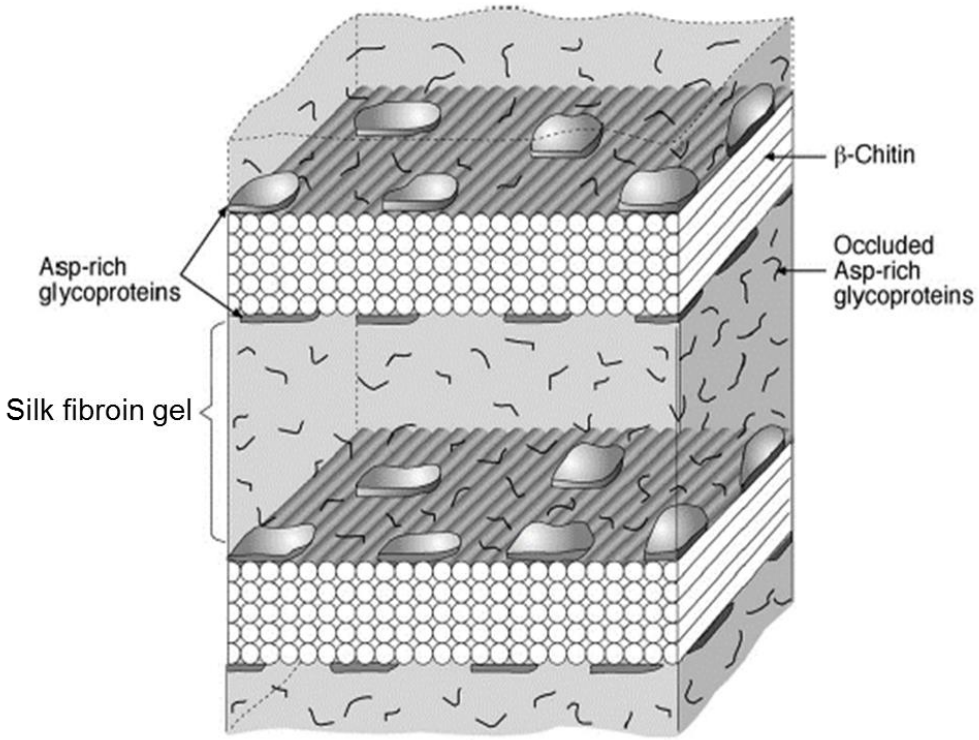

Figure 1.4: Cartoon of the organic matrix in the nacreous layer of *Atrina* according to Levi-Kalisman et al. [95]. Polysaccharide *β*-chitin is interspersed in a highly hydrated silk fibroin gel. The gel includes soluble acidic glycoproteins rich in aspartic acid, and thus bound to the *β*-chitin surface by means of hydrophobic or electrostatic interactions.

1.6.2 Soluble acidic polysaccharides in calcareous biominerals

Amino, neutral and acidic sugars constitute a part of the polysaccharide fraction [112, 113] and bound covalently to the protein core (Figure 1.5) [113]. Polysaccharides could be negatively charged containing sulfates, (poly)carboxylates or phosphates as functional groups, and bind to Ca^{2+} ions. Polysaccharide components lowering the interfacial energy between the solution and the macromolecular substrate, and therefore guide crystal nucleation and growth [114, 115].

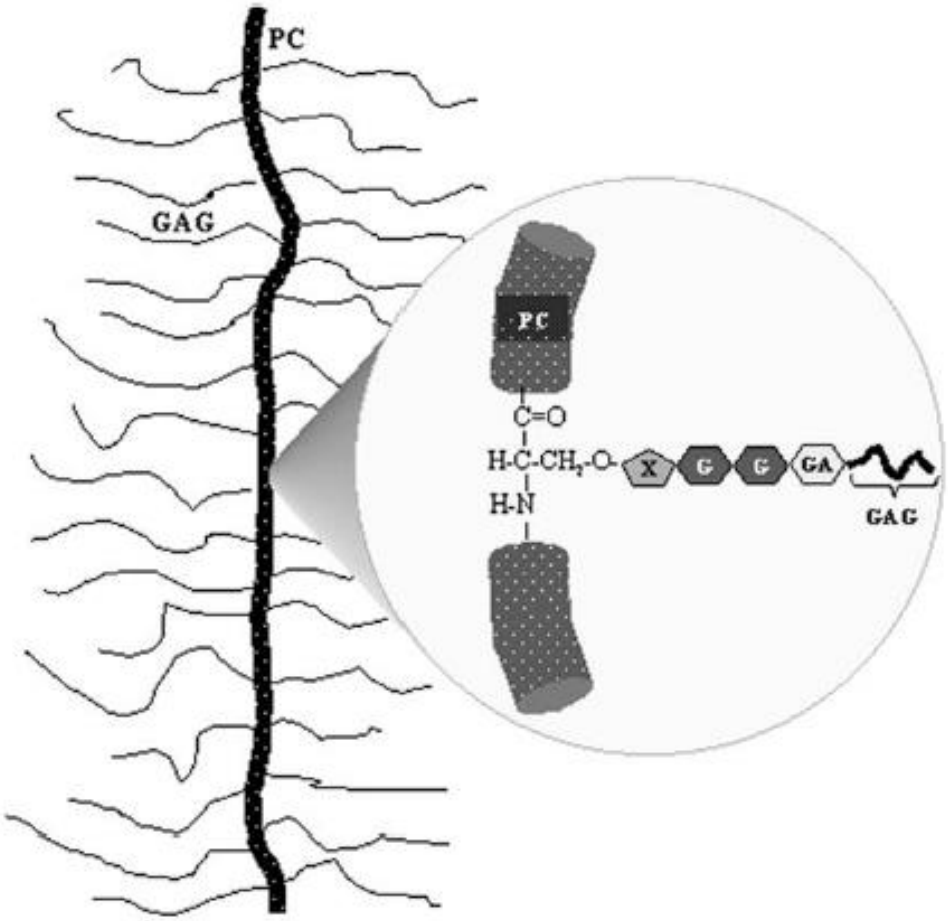

Figure 1.5: Cartoon of a proteoglycan showing chain of glycosaminoglycan (GAGs) that covalently linked to a protein core (PC). The GAG chain is attached to amino acid (serine) of the protein core via a linkage region comprised of a D-glucuronic acid (GA), one xylosyl group (X) and two D-galactose residues. From Arias et al. [113].

Post-translational modifications of proteins including, glycosylation, phosphorylation or sulfatation have been detected in shell-bearing molluscs by specific staining, such as Alcian Blue or by using bioanalytical techniques such as Fourier Transform Infrared (FTIR) (e.g. [112, 116, 117]). Based on histochemical protocols, Crenshaw and Ristedt [118] provided first evidence concerning the structure and composition of crystal nucleation sites. These authors decalcified nacreous layer of *Nautilus pompilius* shells, and therefore stained the interlamellar matrix to reveal the locations of sulfates, carboxylates and calcium binding sites. Crenshaw and Ristedt showed the acidic polysaccharides alongside with calcium binding properties in a specific regions within the sheets of shell macromolecules (the interlamellar matrix).

Following the work of Crenshaw and Ristedt [118], Nudelman et al. [119] further demonstrated that the acidic glycoproteins that present in *Nautilus pompilius* shells are chemically functionalised with sulfates and carboxylates. Similar findings are reported for gastropod *Haliotis rufescens* shells [120]. Bezares et al. showed in *H. rufescens* a carboxylates rich region at the centre of an interlamellar layer; surrounding the centre of an interlamellar layer there is a ring-shaped region rich in acidic sulfates [120]. The cephalopod *Nautilus pompilius* shell and gastropod *Haliotis rufescens* shell showed similarities in the structural mechanisms of an interlamellar matrix [119, 120]. Whereas in one of the well-studied bivalve shells – *Atrina rigida*, the location of sulfates and carboxylates could not be identified within the interlamellar matrix [119]. These findings assumed differences in the overall composition and structural mechanisms of an interlamellar matrix in shell-bearing molluscs.

1.6.3 Organic matrix of the shell of foraminifera

The occurrence and structure of the organic matrix, especially acidic polysaccharides, are essential for several calcium carbonate-based biominerals, such as foraminifera. Foraminifera is found in most marine environments, including the deep sea (benthic) and the upper water column (planktonic) [121]. These boring organisms that sometimes attached to the mollusc shells secrete special cementing membranes for firm attachment [122]. Cementing membranes include shell macromolecules and a certain amount of inorganic matrix [123]. These membranes comprised almost entirely of over-sulfated glycosaminoglycans [124, 125]. Unlike in the mollusc shells, the role of glycosaminoglycans (GAGs) is well-defined in the formation of foraminifera. GAGs form organic linings in foraminifera [126] and also play important role in biological morphogenetic processes [126, 127]. GAGs determined viscoelastic performances and used as attachment devices in a variability of epiphytic foraminifera [126]; and also serve as organic templates or stages for mineral deposition [128]. While the total organic macromolecules in foraminifera are minor [125] compared with the shells of mollusc [2] albeit

important in the calcareous formation, these components can be detected either by specific histochemical studies, such as Alcain Blue, periodic acid Schiff [122] or FTIR analysis [125, 129].

1.7 References

1. Addadi, L. and S. Weiner, *Biomineralization: mineral formation by organisms.* Physica Scripta, 2014. **89**(9): p. 098003.
2. Lowenstam, H.A. and S. Weiner, *On biomineralization*. 1989: Oxford University Press.
3. Mann, S., *Biomineralization: principles and concepts in bioinorganic materials chemistry*. Vol. 5. 2001: Oxford University Press.
4. Frémy, M., *Recherches chimiques sur les os.* Ann Chim Phys, 1855. **43**: p. 47-107.
5. Jackson, A., J. Vincent, and R. Turner, *The mechanical design of nacre.* Proceedings of the Royal Society of London. Series B. Biological Sciences, 1988. **234**(1277): p. 415-440.
6. Watabe, N., *Studies on shell formation: XI. Crystal—matrix relationships in the inner layers of mollusk shells.* Journal of ultrastructure research, 1965. **12**(3): p. 351-370.
7. Westbroek, P. and F. Marin, *A marriage of bone and nacre.* Nature, 1998. **392**(6679): p. 861-862.
8. Addadi, L., et al., *Mollusk shell formation: a source of new concepts for understanding biomineralization processes.* Chemistry-A European Journal, 2006. **12**(4): p. 980-987.
9. Carter, J.G., *Skeletal biomineralization: patterns, processes and evolutionary trends*. Vol. 1. 1990: Wiley Online Library.
10. Dorozhkin, S.V., *Nanodimensional and nanocrystalline apatites and other calcium orthophosphates in biomedical engineering, biology and medicine.* Materials, 2009. **2**(4): p. 1975-2045.
11. Gower, L.B., *Biomimetic model systems for investigating the amorphous precursor pathway and its role in biomineralization.* Chemical Reviews, 2008. **108**(11): p. 4551-4627.
12. Currey, J., *Mechanical properties of mother of pearl in tension.* Proceedings of the Royal Society of London. Series B. Biological Sciences, 1977. **196**(1125): p. 443-463.
13. Simkiss, K. and K.M. Wilbur, *Biomineralization*. 2012: Elsevier.
14. Berman, A., et al., *Intercalation of sea urchin proteins in calcite: study of a crystalline composite material.* Science, 1990. **250**(4981): p. 664-667.
15. Wolf, S.E., et al., *Nonclassical crystallization in vivo et in vitro (I): process-structure-property relationships of nanogranular biominerals.* Journal of Structural Biology, 2016. **196**(2): p. 244-259.
16. Tao, J., et al., *Magnesium-aspartate-based crystallization switch inspired from shell molt of crustacean.* Proceedings of the National Academy of Sciences, 2009. **106**(52): p. 22096-22101.
17. Jacob, D.E., et al., *Planktic foraminifera form their shells via metastable carbonate phases.* Nature Communications, 2017.
18. Weiner, S., *Microarchaeology: beyond the visible archaeological record*. 2010: Cambridge University Press.
19. Lippmann, F., *The Polymorphism Calcite-Aragonite*, in *Sedimentary Carbonate Minerals*. 1973, Springer. p. 97-147.
20. Meldrum, F., *Calcium carbonate in biomineralisation and biomimetic chemistry.* International Materials Reviews, 2003. **48**(3): p. 187-224.
21. De Yoreo, J.J., et al., *Crystallization by particle attachment in synthetic, biogenic, and geologic environments.* Science, 2015. **349**(6247): p. aaa6760.
22. Evans, J.S., *Polymorphs, Proteins, and Nucleation Theory: A Critical Analysis.* Minerals, 2017. **7**(4): p. 62.
23. Wallace, A.F., et al., *Microscopic evidence for liquid-liquid separation in supersaturated CaCO3 solutions.* Science, 2013. **341**(6148): p. 885-889.

24. Cölfen, H. and S. Mann, *Higher-order organization by mesoscale self-assembly and transformation of hybrid nanostructures.* Angewandte Chemie International Edition, 2003. **42**(21): p. 2350-2365.
25. Kalikmanov, V., *Classical nucleation theory*, in *Nucleation theory*. 2013, Springer. p. 17-41.
26. Sommerdijk, N.A. and H. Cölfen, *Lessons from nature—biomimetic approaches to minerals with complex structures.* MRS Bulletin, 2010. **35**(2): p. 116-121.
27. Penn, R.L. and J.F. Banfield, *Imperfect oriented attachment: dislocation generation in defect-free nanocrystals.* Science, 1998. **281**(5379): p. 969-971.
28. Banfield, J.F., et al., *Aggregation-based crystal growth and microstructure development in natural iron oxyhydroxide biomineralization products.* Science, 2000. **289**(5480): p. 751-754.
29. Zhang, H., J.J. De Yoreo, and J.F. Banfield, *A unified description of attachment-based crystal growth.* ACS nano, 2014. **8**(7): p. 6526-6530.
30. Nielsen, M.H., S. Aloni, and J.J. De Yoreo, *In situ TEM imaging of CaCO3 nucleation reveals coexistence of direct and indirect pathways.* Science, 2014. **345**(6201): p. 1158-1162.
31. Rodríguez-Navarro, C., et al., *Nonclassical crystallization in vivo et in vitro (II): nanogranular features in biomimetic minerals disclose a general colloid-mediated crystal growth mechanism.* Journal of Structural Biology, 2016. **196**(2): p. 260-287.
32. Walker, J.M., B. Marzec, and F. Nudelman, *Solid-state transformation of amorphous calcium carbonate to aragonite captured by cryoTEM.* Angewandte Chemie International Edition, 2017.
33. Gebauer, D. and H. Cölfen, *Prenucleation clusters and non-classical nucleation.* Nano Today, 2011. **6**(6): p. 564-584.
34. Politi, Y., et al., *Transformation mechanism of amorphous calcium carbonate into calcite in the sea urchin larval spicule.* Proceedings of the National Academy of Sciences, 2008. **105**(45): p. 17362-17366.
35. Weiner, S. and L. Addadi, *Crystallization pathways in biomineralization.* Annual Review of Materials Research, 2011. **41**: p. 21-40.
36. Tester, C.C., et al., *Time-Resolved Evolution of Short-and Long-Range Order During the Transformation of Amorphous Calcium Carbonate to Calcite in the Sea Urchin Embryo.* Advanced Functional Materials, 2013. **23**(34): p. 4185-4194.
37. Raz, S., et al., *Stable amorphous calcium carbonate is the main component of the calcium storage structures of the crustacean Orchestia cavimana.* The Biological Bulletin, 2002. **203**(3): p. 269-274.
38. Giuffre, A.J., et al., *Isotopic tracer evidence for the amorphous calcium carbonate to calcite transformation by dissolution–reprecipitation.* Geochimica et Cosmochimica Acta, 2015. **165**: p. 407-417.
39. Wolf, S.E., et al., *Early homogenous amorphous precursor stages of calcium carbonate and subsequent crystal growth in levitated droplets.* Journal of the American Chemical Society, 2008. **130**(37): p. 12342-12347.
40. Becker, A., et al., *Structural characterisation of X-ray amorphous calcium carbonate (ACC) in sternal deposits of the crustacea Porcellio scaber.* Dalton Transactions, 2003(4): p. 551-555.
41. Jäger, C. and H. Cölfen, *Fine structure of nacre revealed by solid state 13 C and 1H NMR.* CrystEngComm, 2007. **9**(12): p. 1237-1244.
42. Jacob, D., et al., *Nanostructure, composition and mechanisms of bivalve shell growth.* Geochimica et Cosmochimica Acta, 2008. **72**(22): p. 5401-5415.
43. Aizenberg, J., et al., *Factors involved in the formation of amorphous and crystalline calcium carbonate: a study of an ascidian skeleton.* Journal of the American Chemical Society, 2002. **124**(1): p. 32-39.
44. Addadi, L., S. Raz, and S. Weiner, *Taking advantage of disorder: amorphous calcium carbonate and its roles in biomineralization.* Advanced Materials, 2003. **15**(12): p. 959-970.
45. Suzuki, M. and H. Nagasawa, *Mollusk shell structures and their formation mechanism 1.* Canadian Journal of Zoology, 2013. **91**(6): p. 349-366.
46. Lydeard, C., et al., *The global decline of nonmarine mollusks.* BioScience, 2004. **54**(4): p. 321-330.

47. Lecointre, G., H. Le Guyader, and D. Visset, *Classification phylogénétique du vivant*. Vol. 2. 2001: Belin Paris.
48. Barthelat, F., J.E. Rim, and H.D. Espinosa, *A review on the structure and mechanical properties of mollusk shells–perspectives on synthetic biomimetic materials.* Applied Scanning Probe Methods XIII, 2009: p. 17-44.
49. Ruppert, E.E. and R.D. Barnes, *Invertebrate zoology*. 1994: Saunders College Publishing Fort Worth.
50. Beedham, G., *Observations on the mantle of the Lamellibranchia.* Journal of Cell Science, 1958. **3**(46): p. 181-197.
51. Zylstra, U., H. Boer, and T. Sminia, *Ultrastructure, histology, and innervation of the mantle edge of the freshwater pulmonate snailsLymnaea stagnalis andBiomphalaria pfeifferi.* Calcified Tissue International, 1978. **26**(1): p. 271-282.
52. Wada, K., *Initiation of mineralization in bivalve molluscs.* The mechanisms of biomineralization in animals and plants, 1980: p. 79-92.
53. Istin, M. and A. Masoni, *Absorption et redistribution du calcium dans le manteau des lamellibranches en relation avec la structure.* Calcified Tissue International, 1973. **11**(2): p. 151-162.
54. Wilbur, K.M., *Shell formation and regeneration*, in *Physiology of mollusca*. 1964, Academic Press. p. 243-282.
55. Carney, C.K., et al., *Biomineralization I: crystallization and self-organization process*. Vol. 270. 2006: Springer.
56. Eichhorn, S.J., et al., *The role of residual stress in the fracture properties of a natural ceramic.* Journal of Materials Chemistry, 2005. **15**(9): p. 947-952.
57. Boggild, O.B., *The shell structure of the mollusks.* Det Kongelige Danske Videnskabernes Selskabs Skrifter, Natruvidenskabelig og Mathematisk, Afdeling, Ser. 9, 1930. **2**: p. 231-326.
58. Kobayashi, I. and J. Akai, *Electron Microscopic Observations of Microtextures in Molluscan Biocrystals.* Skeletal Biomineralization: Patterns, Processes and Evolutionary Trends, 1989: p. 333-333.
59. Popov, S., *Formation of bivalve shells and their microstructure.* Paleontological Journal, 2014. **48**(14): p. 1519-1531.
60. Shimamoto, M., *Shell microstructure of the Veneridae (Bivalvia) and its phylogenetic implications.* 1986.
61. Dove, P.M., *The rise of skeletal biominerals.* Elements, 2010. **6**(1): p. 37-42.
62. Grégoire, C., *Structure of the conchiolin cases of the prisms in Mytilus edulis Linne.* The Journal of Biophysical and Biochemical Cytology, 1961. **9**(2): p. 395.
63. Weiner, S. and W. Traub, *X-ray diffraction study of the insoluble organic matrix of mollusk shells.* FEBS letters, 1980. **111**(2): p. 311-316.
64. Taylor, J.D., *The shell structure and mineralogy of the Bivalvia. Introduction. Nuculacea-Trigonacea.* Bull. Br. Mus. Nat. Hist.(Zool.), 1969. **3**: p. 1-125.
65. Kobayashi, I. and T. Samata, *Bivalve shell structure and organic matrix.* Materials Science and Engineering: C, 2006. **26**(4): p. 692-698.
66. Feng, Q., et al., *Crystal orientation, toughening mechanisms and a mimic of nacre.* Materials Science and Engineering: C, 2000. **11**(1): p. 19-25.
67. Kobayashi, I., *Internal shell micro-structure of Recent bivalvian molluscs.* Sci. Re., Niigata Univ.,(E), 1971. **2**: p. 27-50.
68. Carter, J.G. and G.R. Clark, *Classification and phylogenetic significance of molluscan shell microstructure. In: Bottjer, D.J., Hickman, C.S., Ward, P.D., Broadhead, T.W. (Eds.), Molluscs, Notes for a Short Course. University of Tenessee, Department of Geological Sciences Studies in Geology.* 1985: p. pp. 50-71.
69. Taylor, J.D., W.J. Kennedy, and A. Hall, *The shell structure and mineralogy of the bivalvia II. Lucinacea-Clavagellacea conclusions.* Bulletin of the British Museum, Zoology 1977. **22**(1971-1973): p. 256-294.

70. Kobayashi, I. and J. Akai, *Twinned aragonite crystals found in the bivalvian crossed lamellar shell structure.* The Journal of the Geological Society of Japan, 1994. **100**(2): p. 177-180.
71. Almagro, I., et al., *New crystallographic relationships in biogenic aragonite: the crossed-lamellar microstructures of mollusks.* Crystal Growth & Design, 2016. **16**(4): p. 2083-2093.
72. MacClintock, C., *Shell structure of patelloid and bellerophontoid gastropods (Mollusca).* Yale Univ. Peabody Mus. Nat. Hist, Bull., 1967. **22**: p. pls. 1-32.
73. Uozumi, S., K. Iwata, and Y. Togo, *The ultrastructure of the mineral in and the construction of the crossed-lamellar layer in molluscan shell.* Journal of the Faculty of Science, Hokkaido University. Series 4, Geology and mineralogy = Hokkaido University Faculty of Science, 1972. **15**(3-4): p. 447-477.
74. Wilmot, N., et al., *Electron microscopy of molluscan crossed-lamellar microstructure.* Philosophical Transactions of the Royal Society B: Biological Sciences, 1992. **337**(1279): p. 21-35.
75. Kamat, S., et al., *Structural basis for the fracture toughness of the shell of the conch Strombus gigas.* Nature, 2000. **405**(6790): p. 1036-1040.
76. Currey, J. and A. Kohn, *Fracture in the crossed-lamellar structure ofConus shells.* Journal of Materials Science, 1976. **11**(9): p. 1615-1623.
77. Bevelander, G. and H. Nakahara, *An electron microscope study of the formation of the nacreous layer in the shell of certain bivalve molluscs.* Calcified Tissue Research, 1969. **3**(1): p. 84-92.
78. Belcher, A.M., et al., *Control of crystal phase switching and orientation by soluble mollusc-shell proteins.* Nature, 1996. **381**(6577): p. 56.
79. Falini, G., et al., *Control of aragonite or calcite polymorphism by mollusk shell macromolecules.* Science, 1996. **271**(5245): p. 67-69.
80. Weiner, S., Y. Talmon, and W. Traub, *Electron diffraction of mollusc shell organic matrices and their relationship to the mineral phase.* International Journal of Biological Macromolecules, 1983. **5**(6): p. 325-328.
81. Falini, G., S. Weiner, and L. Addadi, *Chitin-silk fibroin interactions: relevance to calcium carbonate formation in invertebrates.* Calcified Tissue International, 2003. **72**(5): p. 548-554.
82. Miyamoto, H., et al., *A carbonic anhydrase from the nacreous layer in oyster pearls.* Proceedings of the National Academy of Sciences, 1996. **93**(18): p. 9657-9660.
83. Marin, F., et al., *Mucins and molluscan calcification Molecular characterization of mucoperlin, a novel mucin-like protein from the nacreous shell layer of the fan mussel Pinna nobilis (Bivalvia, Pteriomorphia).* Journal of Biological Chemistry, 2000. **275**(27): p. 20667-20675.
84. Kono, M., N. Hayashi, and T. Samata, *Molecular mechanism of the nacreous layer formation in Pinctada maxima.* Biochemical and Biophysical Research Communications, 2000. **269**(1): p. 213-218.
85. Gotliv, B.A., et al., *Asprich: A novel aspartic acid-rich protein family from the prismatic shell matrix of the bivalve Atrina rigida.* ChemBioChem, 2005. **6**(2): p. 304-314.
86. Bédouet, L., et al., *Identification of low molecular weight molecules as new components of the nacre organic matrix.* Comparative Biochemistry and Physiology Part B: Biochemistry and Molecular Biology, 2006. **144**(4): p. 532-543.
87. Gotliv, B.A., L. Addadi, and S. Weiner, *Mollusk shell acidic proteins: in search of individual functions.* ChemBioChem, 2003. **4**(6): p. 522-529.
88. Keith, J., et al., *Comparative analysis of macromolecules in mollusc shells.* Comparative Biochemistry and Physiology Part B: Comparative Biochemistry, 1993. **105**(3): p. 487-496.
89. Marin, F., et al., *Organic matrices in metazoan calcium carbonate skeletons: Composition, functions, evolution.* Journal of Structural Biology, 2016. **196**(2): p. 98-106.
90. Sudo, S., et al., *Structures of mollusc shell framework proteins.* Nature, 1997. **387**: p. 563-564.
91. Pereira-Mouriès, L., et al., *Soluble silk-like organic matrix in the nacreous layer of the bivalve Pinctada maxima.* European Journal of Biochemistry, 2002. **269**(20): p. 4994-5003.
92. Marin, F., et al., *Shellome': Proteins involved in mollusk shell biomineralization-diversity, functions.* Recent Advances in Pearl Research, 2013: p. 149-66.

93. Miyashita, T., et al., *Complementary DNA cloning and characterization of pearlin, a new class of matrix protein in the nacreous layer of oyster pearls.* Marine Biotechnology, 2000. **2**(5): p. 409-418.
94. Marie, B., et al., *Different secretory repertoires control the biomineralization processes of prism and nacre deposition of the pearl oyster shell.* Proceedings of the National Academy of Sciences, 2012. **109**(51): p. 20986-20991.
95. Levi-Kalisman, Y., et al., *Structure of the nacreous organic matrix of a bivalve mollusk shell examined in the hydrated state using cryo-TEM.* Journal of Structural Biology, 2001. **135**(1): p. 8-17.
96. Wan, A.C. and B.C. Tai, *Chitin—A promising biomaterial for tissue engineering and stem cell technologies.* Biotechnology Advances, 2013. **31**(8): p. 1776-1785.
97. Tsukamoto, D., I. Sarashina, and K. Endo, *Structure and expression of an unusually acidic matrix protein of pearl oyster shells.* Biochemical and Biophysical Research Communications, 2004. **320**(4): p. 1175-1180.
98. Goffinet, G., *Etude au microscope electronique de structures organisees des constituants de la conchioline de nacre du Nautilus macromphalus sowerby.* Comparative Biochemistry and Physiology, 1969. **29**(2): p. 835-839.
99. Peters, W., *Occurrence of chitin in Mollusca.* Comparative Biochemistry and Physiology Part B: Comparative Biochemistry, 1972. **41**(3): p. 541-550.
100. Osuna-Mascaró, A.J., et al., *Ultrastructure of the Interlamellar Membranes of the Nacre of the Bivalve Pteria hirundo, Determined by Immunolabelling.* PLoS One, 2015. **10**(4): p. e0122934.
101. Goffinet, G. and C. Jeuniaux, *Distribution et importance quantitative de la chitine dans les coquilles de mollusques.* Cahiers de Biologie Marine, 1979. **20**: p. 341-349.
102. Weiss, I.M., et al., *A simple and reliable method for the determination and localization of chitin in abalone nacre.* Chemistry of Materials, 2002. **14**(8): p. 3252-3259.
103. Cartwright, J.H. and A.G. Checa, *The dynamics of nacre self-assembly.* Journal of the Royal Society Interface, 2007. **4**(14): p. 491-504.
104. Furuhashi, T., et al., *Molluscan shell evolution with review of shell calcification hypothesis.* Comparative Biochemistry and Physiology Part B: Biochemistry and Molecular Biology, 2009. **154**(3): p. 351-371.
105. Nudelman, F., et al., *Forming nacreous layer of the shells of the bivalves Atrina rigida and Pinctada margaritifera: an environmental-and cryo-scanning electron microscopy study.* Journal of Structural Biology, 2008. **162**(2): p. 290-300.
106. Scott, H., *A new East African Species of Urodon (Coleoptera) bred from Gladiolus, with Notes on the Biology of the Genus.* Entomologist's Monthly Magazine, 1930.
107. Trogus, C. and K. Hess, *Studies on Natural Silk and Its Behavior with Acids and Alkalies.* Biochem. Z, 1933. **260**: p. 376.
108. Trancik, J., et al., *Nanostructural features of a spider dragline silk as revealed by electron and X-ray diffraction studies.* Polymer, 2006. **47**(15): p. 5633-5642.
109. Simmons, A.H., C.A. Michal, and L.W. Jelinski, *Molecular orientation and two-component nature of the crystalline fraction of spider dragline silk.* Science, 1996: p. 84-87.
110. Rousseau, M.-E., et al., *Study of protein conformation and orientation in silkworm and spider silk fibers using Raman microspectroscopy.* Biomacromolecules, 2004. **5**(6): p. 2247-2257.
111. Vepari, C. and D.L. Kaplan, *Silk as a biomaterial.* Progress in Polymer Science, 2007. **32**(8): p. 991-1007.
112. Marie, B., et al., *The shell matrix of the freshwater mussel Unio pictorum (Paleoheterodonta, Unionoida).* FEBS Journal, 2007. **274**(11): p. 2933-2945.
113. Arias, J.L., et al., *Sulfated polymers in biological mineralization: a plausible source for bio-inspired engineering.* Journal of Materials Chemistry, 2004. **14**(14): p. 2154-2160.
114. Giuffre, A.J., et al., *Polysaccharide chemistry regulates kinetics of calcite nucleation through competition of interfacial energies.* Proceedings of the National Academy of Sciences, 2013. **110**(23): p. 9261-9266.

115. Hamm, L.M., et al., *Reconciling disparate views of template-directed nucleation through measurement of calcite nucleation kinetics and binding energies.* Proceedings of the National Academy of Sciences, 2014. **111**(4): p. 1304-1309.
116. Dauphin, Y., *Soluble organic matrices of the calcitic prismatic shell layers of two pteriomorphid bivalves Pinna nobilis and Pinctada margaritifera.* Journal of Biological Chemistry, 2003. **278**(17): p. 15168-15177.
117. Marxen, J.C., et al., *Carbohydrates of the organic shell matrix and the shell-forming tissue of the snail Biomphalaria glabrata (Say).* The Biological Bulletin, 1998. **194**(2): p. 231-240.
118. Crenshaw, M.A. and H. Ristedt, *The histochemical localization of reactive groups in septal nacre from Nautilus pompilius L.* The mechanisms of mineralization in the invertebrates and plants, 1976: p. 355-367.
119. Nudelman, F., et al., *Mollusk shell formation: mapping the distribution of organic matrix components underlying a single aragonitic tablet in nacre.* Journal of Structural Biology, 2006. **153**(2): p. 176-187.
120. Bezares, J., R.J. Asaro, and M. Hawley, *Macromolecular structure of the organic framework of nacre in Haliotis rufescens: implications for growth and mechanical behavior.* Journal of Structural Biology, 2008. **163**(1): p. 61-75.
121. Huang, G., *Eukaryotic microbes, edited by Moselio Schaechter: Amsterdam, Academic Press, 2012, 496 pp., US $99.95 (hardback), ISBN: 978-0-12-383876-6*. 2012, Taylor & Francis.
122. DeLaca, T.E., *The morphology and ecology of Astrammina rara.* Journal of Foraminiferal Research, 1986. **16**(3): p. 216-223.
123. Hedley, R., *Cement and iron in the arenaceous foraminifera.* Micropaleontology, 1963: p. 433-441.
124. Delaca, T.E. and J.H. Lipps, *The mechanism and adaptive significance of attachment and substrate pitting in the foraminiferan Rosalina globularis d9Orbigny.* Journal of Foraminiferal Research, 1972. **2**(2): p. 68-72.
125. Weiner, S. and J. Erez, *Organic matrix of the shell of the foraminifer, Heterostegina depressa.* Journal of Foraminiferal Research, 1984. **14**(3): p. 206-212.
126. Langer, M.R., *Epiphytic foraminifera.* Marine Micropaleontology, 1993. **20**(3-4): p. 235-265.
127. Goldstein, S.T., *Foraminifera: a biological overview.* Modern foraminifera, 1999: p. 37-55.
128. Hemleben, C., et al., *Calcification and chamber formation in Foraminifera-a brief overview*. 1986. p. 237-249.
129. Allen, K., S. Roberts, and J. Murray, *Analysis of organic components in the test wall of agglutinated foraminifera by Fourier transform infrared and pyrolysis gas chromatography/mass spectrometry.* 2000: p. 1-13.

Organic macromolecules in shells of *Arctica islandica*: comparison with nacroprismatic bivalve shells

Oluwatoosin B. A. Agbaje[1], Denise E.Thomas[2], Bernie V. Mclnerney[2], Mark P. Molloy[2], Dorrit E. Jacob[1]

[1]Department of Earth and Planetary Sciences, Macquarie University, NSW, 2109 Australia

[2]Australian Proteome Analysis Facility (APAF), Macquarie University, NSW, 2109 Australia

Abstract A detailed characterisation of the organic composition of *Arctica islandica* (Linnaeus, 1767) shells with homogenous microstructure is compared with nacroprismatic shells of *Pinctada fucata martensii* (Dunker, 1872), *Hyriopsis cumingii* (Lea, 1852) *and Diplodon chilensis patagonicus* (d'Orbigny, 1835). Thermogravimetric analysis shows lowest total organic contents of 1.65 wt% for *Arctica islandica* shells, while all nacroprismatic shells are higher (3.14 - 4.13 wt%). Macromolecules extracted from the nacroprismatic shells are dominated by hydrophobic amino acids (~54%) in the acid extracts, while EDTA-extracts are moderately rich in aspartate and glutamate (16% in total) and in glycine-alanine (42%). In comparison, *Arctica islandica* shells have higher concentrations of proline, glycine and aspartate (ca 40%). Infrared spectroscopy shows some acidic protein bands in *Arctica islandica*, which cannot be found in the nacroprismatic shells. Alcian Blue and/or modified silver staining methods reveal many prominent bands. Protein bands at around 10, 14, 17, 21, 26, 31, 40 and 55 kDa are detected in *Arctica islandica* shells for the first time, thus may constitute a new set of proteins in mollusc shells. SDS-PAGE exhibits apparent molecular weights from 5 to 63 kDa in nacroprismatic shells. Distinct protein bands at around 17 and 26 kDa in *Arctica islandica* shells may correspond to a post-translational modification of proteins; these prominent bands, however, are absent in the nacroprismatic samples. Contrarily, SDS-PAGE of both, homogeneous and nacroprismatic shell microstructures show nonacidic-matrix-proteins.

Keywords *Arctica islandica*; *Pinctada martensii*; nonacidic-matrix-protein; glycosaminoglycans; proline; carbohydrate-protein-linkage

2.1 Introduction

2.1.1 Mollusc shell biomineralisation

Mollusc shells are natural biocomposites of calcium carbonate phases, such as calcite or aragonite, intimately intergrown with organic macromolecules [1]. The organic moiety in bivalve shells contains a mixture of lipids, glycoproteins, proteins and polysaccharides-chitin [2-4], with variable ratios of proteins and polysaccharides depending on the species. The organic macromolecules are actively involved in shell formation and have been shown to control virtually all levels of mineralization, including which mineral polymorph is formed (e.g. calcite, aragonite, vaterite), sizes and shapes of the grains, and the overall microstructure of the skeletal hard parts [5].

Due to this crucial role in shell formation, the organic matrix in bivalve shells has received increased attention, resulting a number of proteins potentially involved in the control of bio-carbonate formation having been described to date [6, 7]. These proteins contain carboxylates, sulfates, or phosphates as functional groups, which may bind to Ca^{2+} ions, thus lowering the interfacial energy between the solution and the macromolecular substrate and, in this way, being able to guide crystal nucleation and growth [8, 9].

Much of our knowledge about the composition and function of the organic matrix in mollusc shells is restricted to bivalves with nacroprismatic shells, whereas very little is known about the organic components in calcareous biominerals with different shell microstructures, such as crossed-lamellar or homogeneous structures [10-12]. *Arctica islandica* (Linnaeus, 1767) (Bivalvia: Veneroida), an extremely long-lived bivalve (>400 years) [13] has a distinct and complex shell structure, referred to as ‘homogeneous’ [14]. The biogenic material has gained considerable importance for climate reconstruction in the northern hemisphere [15]. Despite its importance, very little is known to date about the organic moieties in the calcareous biominerals of this species. In this study, we present the first detailed characterization of the shell organic

matrix of *Arctica islandica* and compare it to different bivalve shells with nacre-prism microstructure from marine and freshwater environments.

2.1.2 Shell microstructures

The homogeneous microstructure is widely distributed in the mollusc phylum. However, mollusc shell families consisting entirely of homogeneous layers are relatively rare in comparison to families with other shell microstructures such as the nacroprismatic structure [16]. *Arctica islandica* shells are completely aragonitic and have a two-layered structure that consists of granular and irregularly arranged micrometer-sized aragonite prisms but lacks any readily visible architecture [17]. According to Taylor [16], some of the mollusc shell families with almost entirely homogeneous layers descended from a nacroprismatic evolutionary ancestor.

The nacroprismatic structure is similarly widespread in the mollusc class [11] and consists of an outer layer of prism-shaped aragonite or calcite grains in individual organic envelopes and an inner layer of aragonite tablets arranged in a ‘brickwall’-like way and individually separated by peripheral thin layers of organic matrix [18]. In marine bivalve shells as *Pinctada fucata martensii*, the outer prismatic layer is typically calcitic, whereas freshwater shells with this microstructure (*Hyriopsis cumingii*, *Diplodon chilensis patagonicus*) are entirely aragonitic.

A major question in understanding the parameters governing the formation of different types of shell microstructure is whether shells with different microstructures contain a similar population of matrix proteins, or not. A first step is to characterize and compare the bulk composition of soluble organic molecules in shells with different microstructures, which is what we are attempting here.

2.1.3 Organic macromolecules in bivalve shells

Generally, organic macromolecules in bivalve shells amount to less than 5 wt% and can be extracted by decalcification using water- [4, 19, 20], EDTA- [4, 21, 22] or acid-based methods [20, 23, 24]. A large part of these macromolecules are composed of hydrophobic components such as chitin or silk-fibroin. These insoluble molecules are often intimately associated with acidic proteins, forming an extensive three-dimensional architecture [3]. In contrast, the soluble moiety is relatively low in content (< 2 wt%), and is composed of acidic proteins, glycoproteins, polysaccharides and polypeptides. Both, insoluble and soluble organic moieties are involved in carbonate crystal formation and particularly the silk-like protein component of the shell macromolecules is thought to have an important function in the biomineralization processes [5].

Depending on the extraction method, the organic shell component shows somewhat differing composition: water-based extracts after decalcification tend to have higher percentages of silk-like gel (glycine and alanine), whereas EDTA extracts generally show higher of acidic amino acid concentrations [4]. Pereira-Mouriès et al. (2002) suggested that the water-based methods mobilizes apolar proteins that are covalently attached to sugars, whereas these components are insoluble when using EDTA [4, 25]. Furthermore decalcification using water-based methods is less aggressive compared to extraction methods using acid or EDTA, which can be partially destructive for the organic molecules [19]. In this study, we present complementary results using both methods and aim at improving recovery.

2.2 Materials and methods

2.2.1 Materials

Arctica islandica (Arcticidae; Linnaeus, 1767), *Hyriopsis cumingii* (Unionidae; Lea, 1852), *Diplodon chilensis patagonicus* (Hyriidae; d'Orbigny, 1835) and *Pinctada fucata martensii*

(Pteriidae; Dunker, 1872) shells were used in this study. Samples are grouped by structure into nacre-prism structure (*H. cumingii*, *D. chilensis patagonicus* and *P. fucata martensii*) and homogeneous structure (*A. islandica*). All samples are entirely aragonitic except for *P. fucata*, which has a calcitic prism layer. *H. cumingii* and *D. chilensis patagonicus* are freshwater species, while *P. fucata* and *A. islandica* are marine bivalves.

2.2.2 Sample preparation and characterization

All shells are covered by an organic periostracum [26], which was mechanically removed with a DREMEL drill (Wisconsin, USA). Only ca. 2 mm of the outer shell containing the periostracum was removed. Mechanical removal of the periostracum also partially removed the prismatic layer, while complete removal of the prismatic layer is unlikely. The outer prismatic layer in the shells of all nacroprismatic bivalves studied here is of variable thickness, but is generally between 3 and 4 mm thick, while the nacreous layer is much thicker and generally makes up over 90% of the mineralized shell. Though small differences in compositions of the prismatic and nacreous layers in bivalves have been reported in the literature [27]; all our analyses are dominated by the composition of the nacreous shell layer. For homogeneous *A. islandica* shells and unlike for nacroprismatic shell, no significantly texturally different shell layers are known [28].

After mechanical cleaning, the fragments were immersed in 30% H_2O_2 (Merck KGaA, 64271 Darmstadt; Germany) for 1 h at room temperature combined with ultrasonic treatment to remove any organic contaminants, washed extensively with Milli-Q water and rinsed with acetone to facilitate drying. After drying in air, the samples were powdered in a cleaned rock mill before Thermogravimetric Analysis (TGA) was conducted using a TGA 2050 Thermogravimetric Analyzer (TA Instruments, USA). About 30mg of powdered sample was measured in a temperature interval from room temperature (21^{o}C) up to 1000^{o}C at 10^{o}C/min steps under nitrogen atmosphere.

2.2.3 Extraction of organic macromolecules

Powdered samples were decalcified for about 2 days either with a 10% ethylenediaminetetracetic acid disodium salt dihydrate (EDTA; Sigma-Aldrich) adjusted with KOH to pH ~8.0 or in 1 mM of HCl (pH > 5). After the addition of HCl solution to the shell material, pH of the shell solution was raised with Milli-Q water to the ~ 7. The extracts were centrifuged at 10,500 rpm (4ºC) for 20 min to separate the soluble and insoluble fractions. This

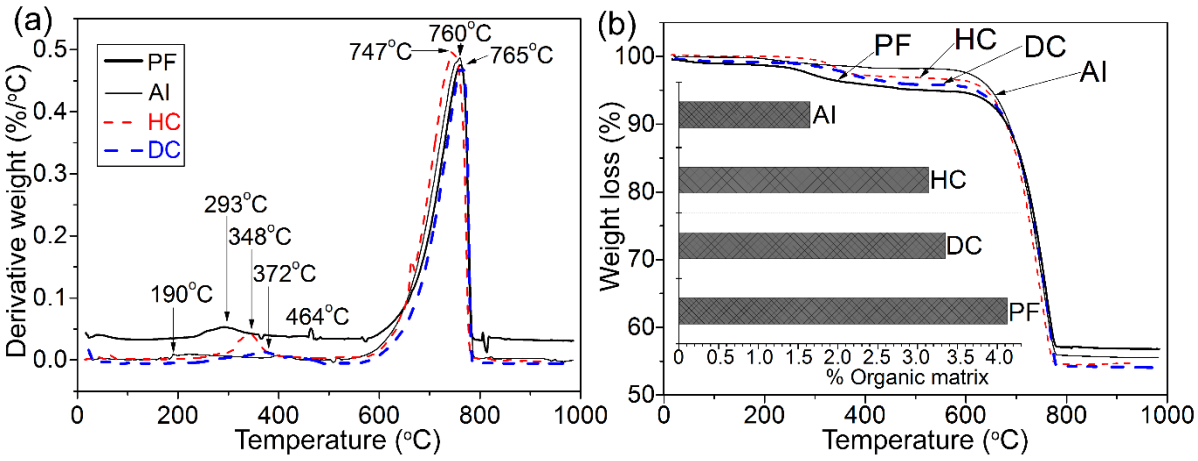

Figure 2.1. Differential thermal analysis (a) and Thermogravimetric analysis (b) show thermal stability and total organic matrix of homogeneous (AI: *Arctica islandica*) and nacroprismatic (HC: *Hyriopsis cumingii*, DC: *Diplodon chilensis patagonicus* and PF: *Pinctada fucata martensii*) shell structures. The bar chart insert in (b) represents the calculated total organic matrix for the range 150–500ºC.

procedure resulted in four different samples for *A. islandica* and *H. cumingii* shells, namely soluble fractions in EDTA ('EDTA-Soluble Moiety': ESM) and in dilute HCl ('Acid-Soluble Organic Moiety': ASM) as well as insoluble fractions ('EDTA-Insoluble Moiety' EIM and 'Acid-Insoluble Organic Moiety' AIM, Table 2.1). *D. chilensis patagonicus* and *P. fucata martensii* samples were decalcified only in 1mM HCl (pH > 5) not in EDTA, resulting in ASM and AIM fractions from these shells (Table 2.2).

In order to remove EDTA and HCl prior to lyophilisation, all insoluble fractions were washed thoroughly with Milli-Q water. Since EDTA can be removed by leaching from the

matrices when soaked or flooded with water [29], the soluble fractions (EDTA and HCl based) were mixed with equal volumes of water and stored at 4^{o}C for about one month prior to concentration and lyophilization. Fractionation followed the method described by Rahman et al. [30] using Sep-Pak C18-2g (Waters Corporation Milford, MA, USA).

Additional organic matrix extracts were obtained without prior decalcification to study potential variations in ratios of charged to hydrophobic organic molecules and variations for Ca^{2+} binding polypeptides. For this purpose, coarsely fragmented samples (~500 mg each) were partly decalcified in 20% HCl for ca. 10 min at room temperature. The extracts were centrifuged and the soluble extracts were dried using SpeedVac dryer.

2.2.4 Fourier Transform Infrared Spectroscopy and Amino Acid Analysis

Fourier Transform Infrared (FTIR) spectra were measured from lyophilized samples of the soluble fractions (ESM, ASM) with a Thermo Nicolet iS10 ATR-FTIR spectrometer (Nicolet, MA, USA) equipped with a smart performer accessory in air. Spectra were acquired between 4000 and 500 cm^{-1} with 64 accumulations and a resolution of 4 cm^{-1}. Backgrounds were recorded at the start of the analytical session and approximately after every half hour.

For the analysis of amino acids, samples were acid hydrolysed with 6 M HCl for 24 h at 110^{o}C under nitrogen. Subsequently, hydrolysed samples were dissolved in Milli-Q water and an aliquot was derivatized with AQC reagent [31] using AccQTag Ultra derivatisation kit (Waters Corporation, Milford, MA, USA). The separation and quantitation of the 16 acid hydrolysate amino acids was performed using a ACQUITY ultraperformance liquid chromatography (UPLC) system and BEH RP C18 1.7µm column (Waters Corporation, Milford, MA). A detailed protocol is described in Truong et al. [32]. The amino acid compositions expressed as mole percent represent the average of duplicate results (Table 2.1 and 2.2). Due to the deamidation of glutamine to glutamic acid and asparagine to aspartic acid under acidic conditions the amounts reported for Glx and Asx are the sum of those respective

components. Cysteine and tryptophan are partially destroyed by the acidic conditions and were not quantified.

2.2.5 Polyacrylamide gel electrophoresis of proteins

The separation of matrix components was performed under denaturing conditions by mono-dimensional SDS-PAGE using Laemmli sample buffer. Soluble organic matrix fractions were used for electrophoresis analysis at 200V. Proteins were separated on a pre-cast NuPAGE 4–12% Bis-Tris gel in MES running buffer according to protocols supplied by the manufacturer (Invitrogen; Carlsbad, CA, USA). After electrophoresis, the gels were stained with Coomassie Brilliant Blue G-250 and/or silver nitrate, Alcian Blue and/or modified silver nitrate. The Coomassie Brilliant Blue G-250 staining was followed by fixation in ammonium sulphate solution overnight. After recording the bands on the gel, it was destained in 10% glacial acetic acid overnight and stained with silver nitrate. For this step, a modified method was developed based on [33]. The modification entailed omission of the prefixed step, soaking of the gel in Milli-Q water for 3 h and use of 10 µg dithiothreitol for 20 mins. The molecular weights were estimated using the pre-stained (Invitrogen) Novex Sharp standard MW-SDS marker kit for electrophoresis.

Gels were also studied for potential glycosylation in the ASM and ESM fractions. Saccharides were studied using Alcian Blue 8GX [34] at pH 1 for the very specific acidic sulfated sugars, and subsequently stained with modified silver nitrate. The gel was washed with 50% ethanol twice to ensure clear backgrounds. The modification to the staining comprised fixation of the gel in 10 vol% methanol and glacial acetic acid, respectively and sensitisation in 10 vol% glutaraldehyde for 30 mins, prior to staining. After staining, the gel was soaked in 10 µg/mL dithiothreitol for 20 mins and the impregnation step was performed by treatment with a solution containing 6 mM silver nitrate and formaldehyde for 30 mins. Subsequently, the gel was developed in a solution containing 3 wt% sodium carbonate and formaldehyde. Staining

was terminated by adding citric acid (44 wt% in milli-Q water) and rinsing in Milli-Q water before scanning.

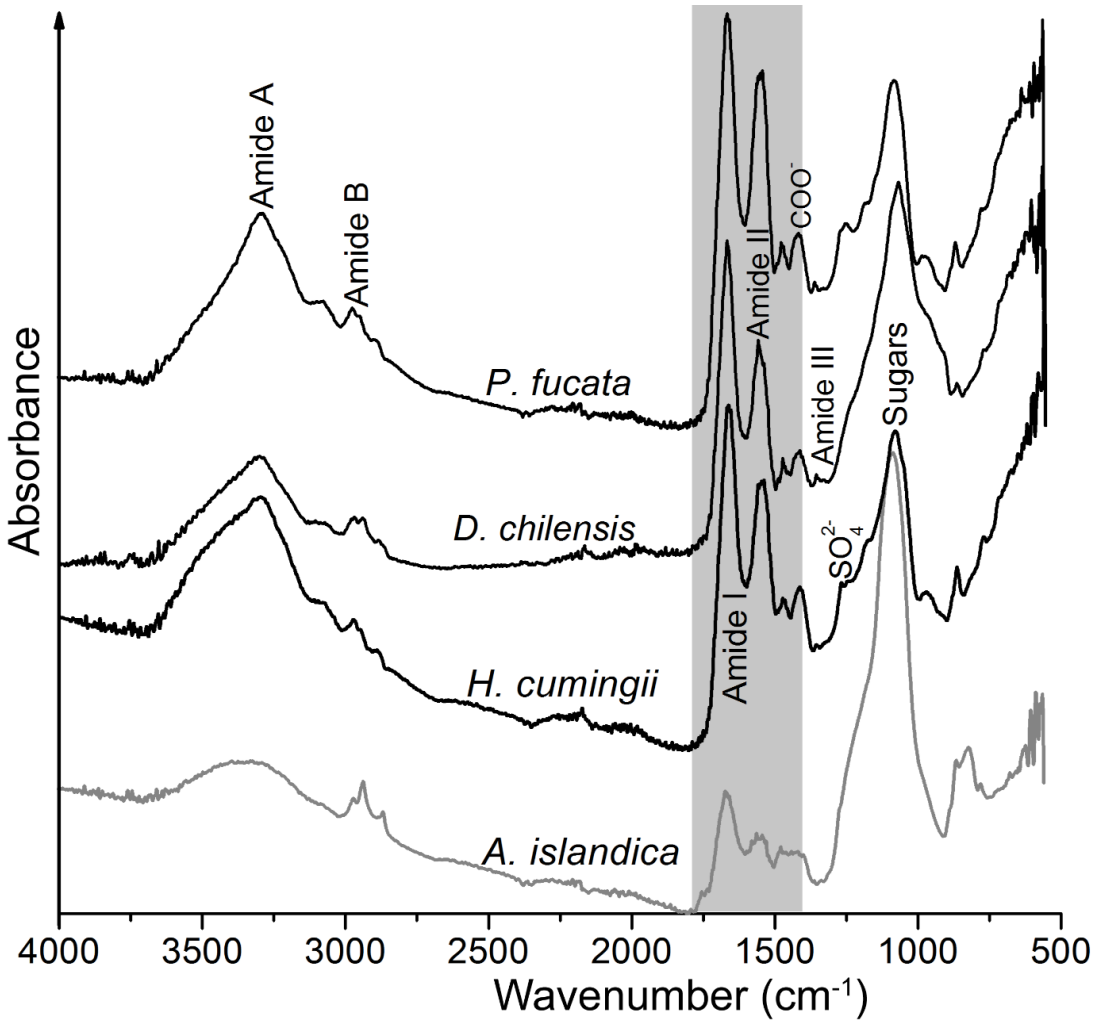

Figure 2.2a. FTIR spectra of Acid-Soluble Organic Moiety (ASM) of *A. islandica, P. fucata, D. chilensis* and *H. cumingii*. The grey bar indicates the wavenumber region between 1800 and 1400 cm^{-1}, which contains bands for amide I, II and the secondary structure of proteins. The shaded area is depicted in more detail in Figure 2.2b.

2.3 Results

2.3.1 Total organic content

Thermogravimetric Analysis coupled with Differential Thermal Analysis (TGA/DTA) were used to investigate thermal stability and total organic contents of the shells. Peaks in the range 190-464^{o}C (Figure 2.1a) are due to combustion of the complex mixture of proteins, glycoproteins and polysaccharides occluded in the shells and to transformation of aragonite to

calcite. At 747-765°C breakdown of calcium carbonate to calcium oxide and CO_2 is recorded. The weight loss of 41-42% (Figure 2.1b) at this temperature corresponds to the theoretical value of CO_2 released (44%) from the calcium carbonate. As determined from these analyses, *A. islandica* shells have the lowest organic content of 1.65 wt % (Insert; Figure 2.1b), while *H. cumingii* contains 3.14 wt%, similar to the *D. chilensis* shell 3.35 wt%. *P. fucata* yielded the highest content in this sample suite of 4.13 wt%. Thus, the nacroprismatic samples generally contain higher organic contents than *A. islandica* with homogeneous shell structure.

2.3.2 Bulk composition of the organic matrix

2.3.2.1 Acid soluble organic matrix (ASM)

FTIR spectra of the lyophilized ASM extracts from all shell samples are presented in Figure 2.2a. The organic moiety shows bands mainly in wavenumber areas characteristic for amide A (wavenumber area 3500-3000 cm^{-1}), amide B (2990-2800 cm^{-1}), amide I (1700-1600 cm^{-1}), amide II (1590-1300 cm^{-1}) and amide III (1290-1190 cm^{-1}).

Fig. 2b details the wavenumber region between 1400 and 1800 cm^{-1}, which contains bands for amide I, II and for the secondary structure of proteins. In this region, differences for the ASM between *A. islandica* and other samples are visible. Peaks at 1716 cm^{-1} (identified as aspartic acid, [23], 1578 cm^{-1} for aspartate, 1559 cm^{-1} for glutamic acid, 1508 cm^{-1} for tyrosine, 1736 cm^{-1} for carbonyl of ester and the symmetric carboxylate absorption peak at 1419.4 cm^{-1} are present in the shells of *A. islandica* (Figure 2.2b), while they are generally absent for the organic matrix in the nacroprismatic shells. *D. chilensis* presents an exception with shoulder bands at 1714.5 cm^{-1} for glutamic acid (Figure 2.2b) and 1418 cm^{-1} for symmetric carboxylate, respectively. Here again, the amide II peak near 1542 cm^{-1} is more distinct for *A. islandica* compared with the other samples. However, amide I peak at 1653 cm^{-1} for *A. islandica* is also prominent at 1652.5 cm^{-1} (α-helix conformation) for *D. chilensis* and 1646 cm^{-1} (random coil structure) for *H. cumingii* and *P. fucata* (Figure 2.2a). The band at 1638 cm^{-1}, present in all

samples (however as a shoulder in *D. chilensis*), could be assigned to the secondary protein (*β*-sheet) structure, which may originate from *N*-acetyl groups located on the polysaccharide. Similarly, lysine and C-H of aliphatic group peaks are present near 1522 cm^{-1} and 1456 cm^{-1} in all samples. Amide A and B regions are also present in all samples, but are not characteristic for secondary structures (Figure 2.2a).

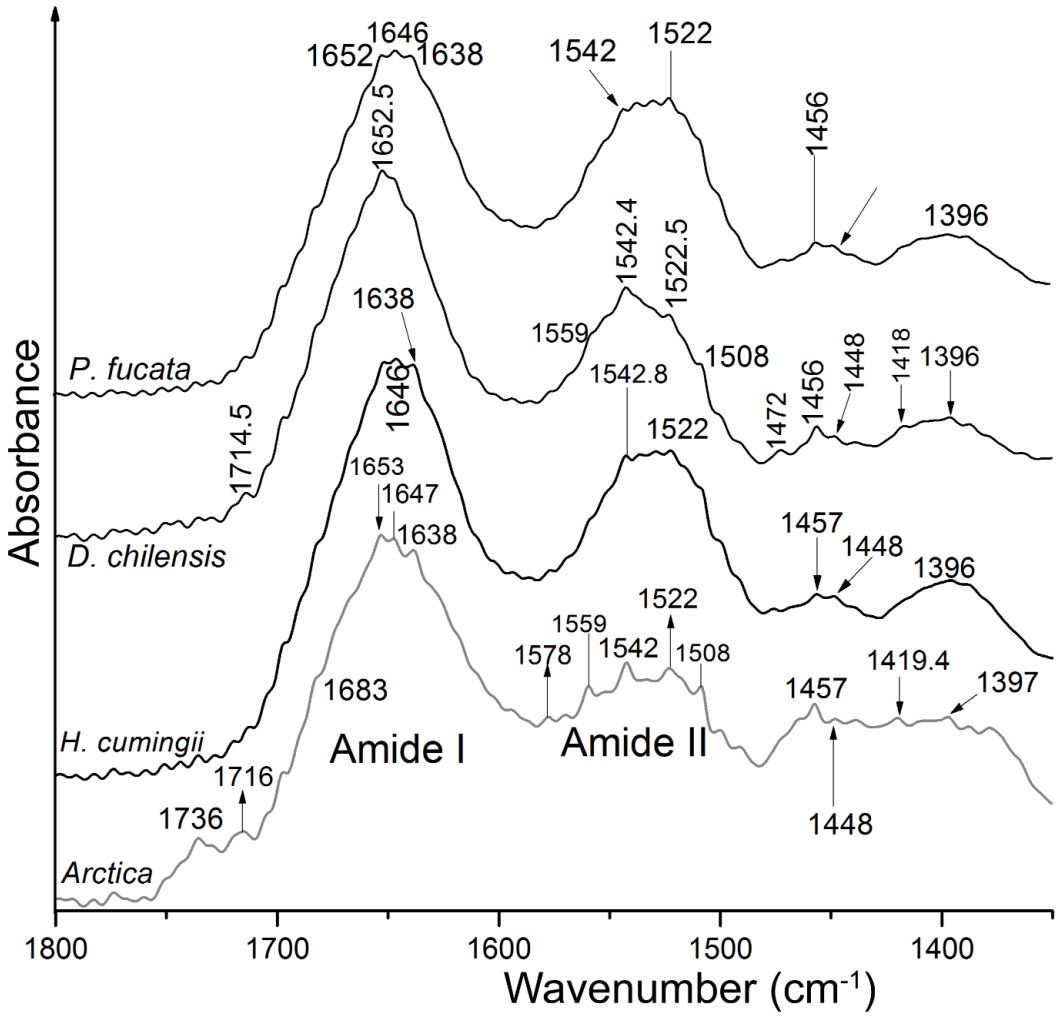

Figure 2.2b. Detailed FTIR spectra for the shaded area from Figure 2.2a showing the different bands in the range 1800-1400 cm^{-1}.

It is possible that the strong amide A, I and II peaks from proteins are also due to the presence of sugars as shown by the spectra of chondroitin sulfate A [23]. Contrarily, the absorption bands at 1000-1150 cm^{-1}, which are usually considered as characteristic for sugars, are absent from protein spectra. Strong peaks are present at 1050-1063 cm^{-1} (Figure 2.2a) and are assigned to

the sugar region. Peaks in this region are more prominent in the *A. islandica* spectrum compared with other samples and imply higher sugar contents in this shell compared with the nacre-prism samples. This is supported by the amino acid composition, which shows high concentrations of proline (15%; Supplementary Figure 2.1). In contrast, the peak at 1050-1063 cm^{-1} in ASM extracts may point to the presence of glucosaminoglycans [4].

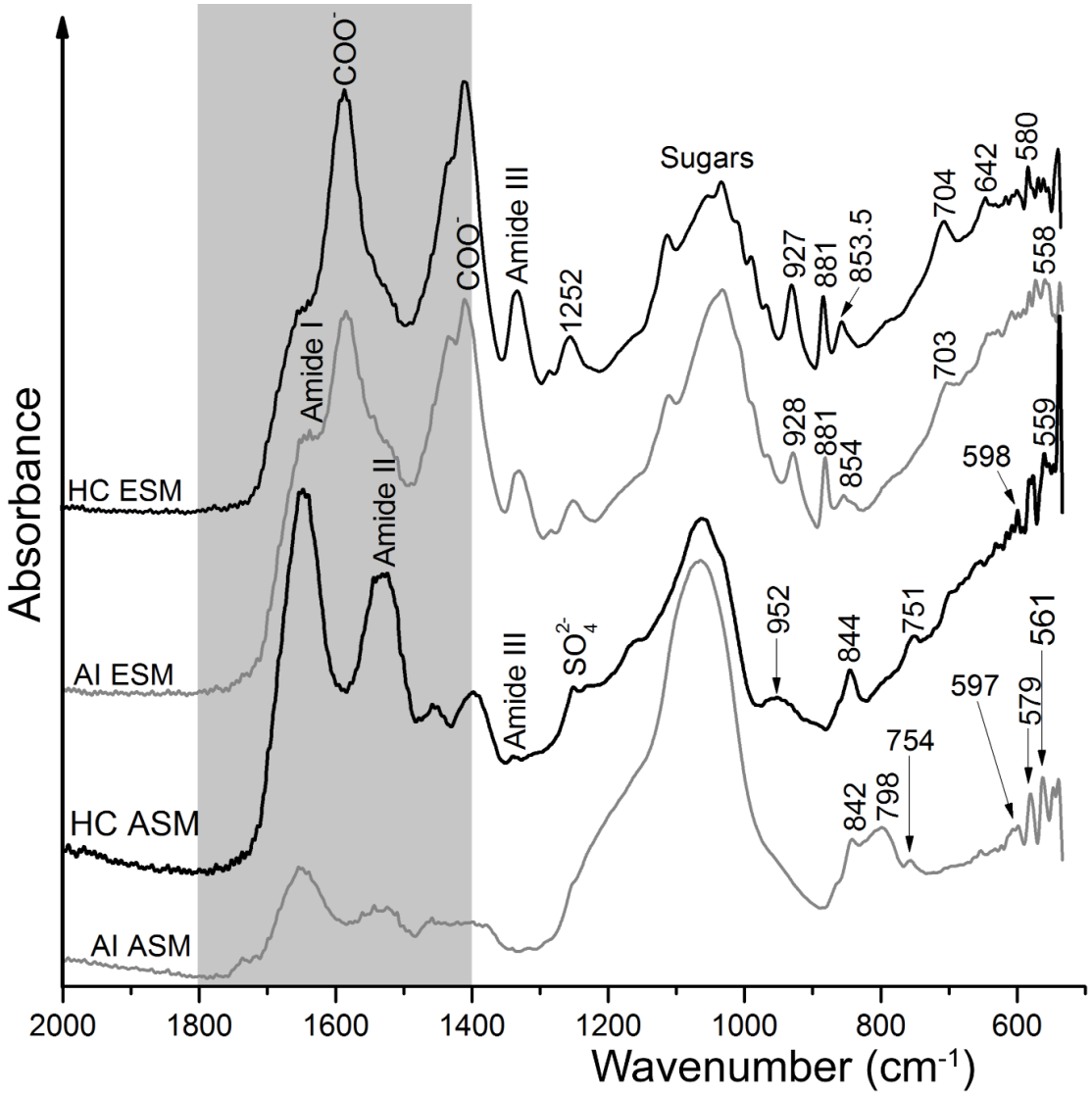

Figure 2.3a. FTIR spectra of Acid-Soluble Organic Moiety (ASM) and EDTA-Soluble Moiety (ESM) of AI (*Arctica islandica*) and HC (*Hyriopsis cumingii*) showing bands in the range 2000-500 cm^{-1}. The grey bar indicates the wavenumber region between 1800 and 1400 cm^{-1}, which contains bands for amide I, II and the secondary structure of proteins. The shaded area is depicted in more detail in Figure 3b.

2.3.2.2 Functional groups in the soluble organics and comparison of EDTA and acid extracts

Detailed infrared spectra were collected in the range 2000-500 cm^{-1} to identify the functional groups in both ESM and ASM extracts (Figure 2.3a). In ESM, prominent asymmetric (1583 cm^{-1}) and symmetric (1409-1408 cm^{-1}) carboxylate bands, amide III band at 1330 cm^{-1}, sulfate peaks, probably O-sulfate groups, near 1282.5, 1252, 927 and 854 cm^{-1} could be assigned (Figure 2.3a). Similarly, a sulfated peak appeared at 1252 cm^{-1} for *H. cumingii* (ASM) and a broad shoulder in this area in *A. islandica* (ASM, see Figure 2.3a) could be identified. Amide I carbonyl group with bands at 1646 cm^{-1} (*H. cumingii*) and 1653 cm^{-1} (*A. islandica*) in ASM can also be assigned as a weak band in ESM (Figure 2.3a). Specific interpretations of amide I bands are difficult due to an overlap of the α-helical with random coil structures, which both have bands in this region (Figure 2.2b and 2.3b). Depending on their source and particularly on the method of preparation [4, 35], the occurrence of the absorption band in the high-frequency wing of the amide II band can be partly merged with carbonyl stretching group [36]. The peak used for characterisation of amide II appears at 1542-1542.8 cm^{-1} in ASM and is also visible as a shoulder in ESM for both samples (see Figure 2.3b).

The region between 800 and 1200 cm^{-1} was characterized by well-resolved peaks in ESM as compared with ASM extracts and could be assigned to polysaccharide groups (Figure 2.3a). The peaks at 1112 cm^{-1} (*A. islandica*) and 1109 cm^{-1} (*H. cumingii*), present in ESM are usually attributed to the asymmetric in-phase ring stretching mode of C-O-C [37]. Furthermore, the peaks of prominent intensity in the range of 1063-1031 cm^{-1} (Figure 2.3a) for ESM and ASM correspond to the C-O stretching bond in *N*-acetylglucosamine [38, 39]. The small peaks near 963 cm^{-1}, 986 cm^{-1} (ESM) and a broad peak at 952 cm^{-1} (ASM) may be influenced by *N*-acetylglucosamine [39]. Amine and/or alkene groups at 881 cm^{-1} (ESM) and 842-844 cm^{-1} (ASM) could also be identified [39]. All spectra in the fingerprint region (754-500 cm^{-1})

including a broad peak at 798 cm^{-1} (Figure 2.3a) for both ESM and ASM are attributed to polysaccharide moieties, probably *N*-acetylglucosamine [38].

The *A. islandica* spectra show some acidic protein bands, which cannot be found in nacroprismatic shells. Prominent peaks in the sugar region for the samples studied may correspond to the glucosaminoglycans.

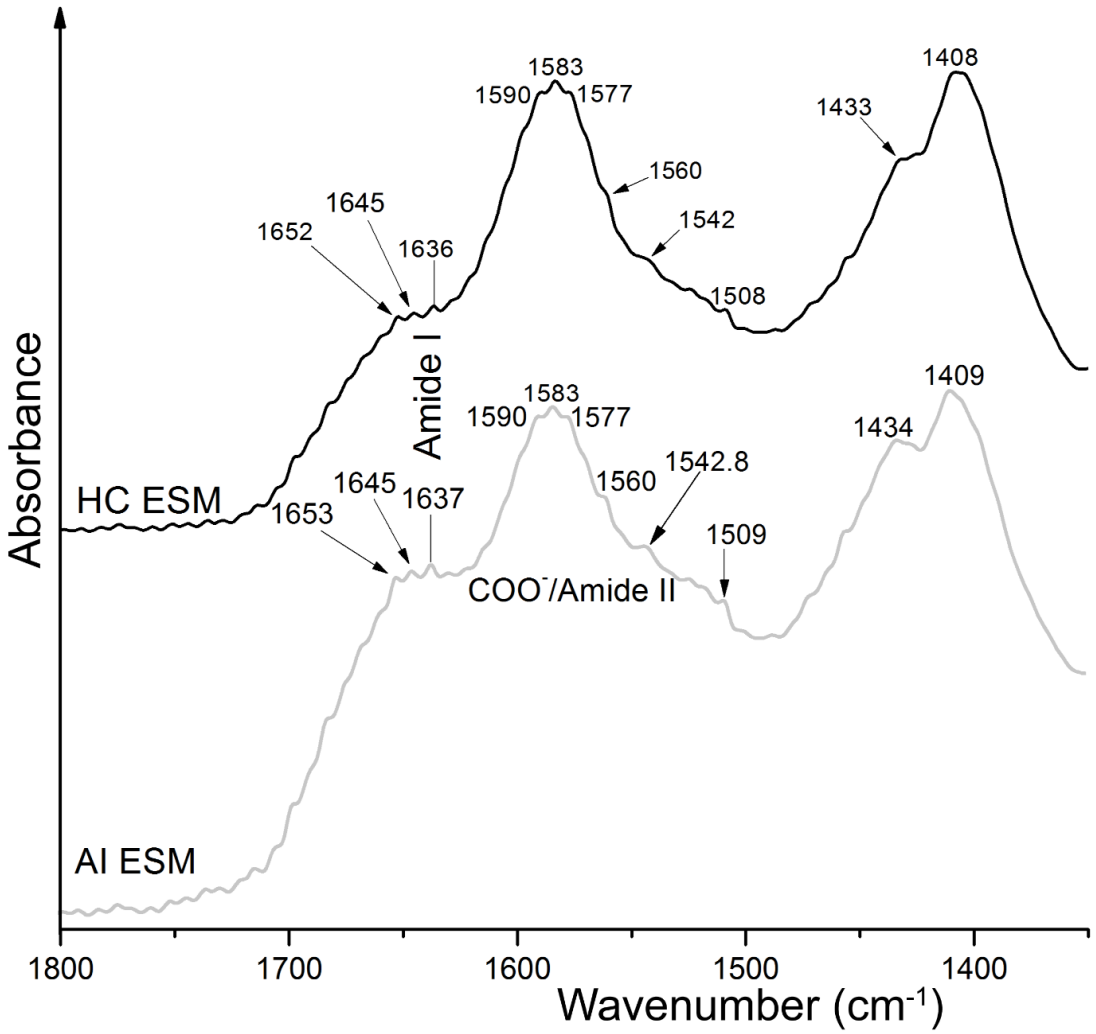

Figure 2.3b. Detailed FTIR spectra for the shaded area from Fig. 3a showing the range 1800-1400 cm^{-1} for ESM of *H. cumingii* and *A. islandica.*

2.3.3 Amino acid composition

Amino acid compositions are shown in Tables 2.1 and 2.2. Glycine, aspartate and proline residues make up ca 40% of the total amino acids in *A. islandica* followed by glutamate (ca

8.5%) (Bulk, AIM, EIM and ESM; Table 2.1). The charge to hydrophobic ratio in ASM is lower (C/HP = 0.59) than in ESM (C/HP = 0.85). In ASM, glycine and proline (31% of the total amino acids) are the main components followed by aspartate, alanine, threonine and glutamate (Supplementary Figure 2.1). These four residues constitute 34% of the total amino acid compositions in ASM (Table 2.1). Comparing the results with published data for *Mercenaria stimpsoni* shells with homogeneous microstructure [27], the composition is similar to *A. islandica* with about 37% of the total amino acid composition consisting of aspartate, alanine, threonine and glutamate (Supplementary Figure 2.1c). The proportions of proline and glycine are higher in *A. islandica* than in *Mercenaria stimpsoni* shells; possibly these differences can be attributed to sampling preparation techniques and/or the different biological taxonomy of these calcareous biominerals. Nonetheless, other microstructures such as crossed lamellar reveal relatively higher proportion (40% in total; [27]).

Table 2.1 Amino acid composition (mole %) in undecalcified (bulk), soluble and insoluble organic matrices

	Arctica islandica					*Hyriopsis cumingii*				
Amino Acid	Bulk	AIM	ASM	EIM	ESM	Bulk	AIM	ASM	EIM	ESM
His[a]	1.0	LOR	0.4	LOR	0.6	0.8	0.7	0.4	0.7	0.7
Ser[b]	5.3	5.4	5.8	5.1	5.6	8.0	8.5	6.9	8.4	7.2
Arg[a]	6.9	5.4	4.7	5.5	5.1	3.8	3.6	2.6	3.5	3.3
Gly	14.9	15.8	16.0	20.3	13.9	28.7	28.3	33.5	27.7	27.5
Asx[a]	11.7	12.0	9.3	10.9	12.9	8.3	8.7	6.9	8.5	10.0
Glx[a]	8.2	9.2	7.3	8.2	8.5	3.7	4.1	3.6	4.2	6.3
Thr[b]	6.4	6.3	8.0	5.8	6.3	2.0	2.2	2.6	2.1	3.2
Ala[c]	6.7	6.6	9.7	6.4	7.8	20.9	20.7	19.0	20.8	14.0
Pro[c]	13.0	12.6	15.0	12.1	13.1	2.9	2.9	3.3	2.9	3.5
Lys[a]	6.1	4.7	3.4	4.6	4.8	2.6	2.5	1.3	2.4	3.1
Tyr[b]	3.8	6.0	3.1	6.9	4.7	3.1	3.0	1.3	3.4	2.1
Met[c]	2.1	LOR	2.9	LOR	2.5	0.9	0.8	1.8	1.0	1.9
Val[c]	5.7	5.1	5.3	4.5	5.5	3.7	3.2	4.0	3.2	4.6
Ile[c]	2.8	4.3	3.1	3.8	2.6	2.2	2.1	2.6	2.6	2.9
Leu[c]	2.8	4.3	4.0	3.7	3.5	4.7	5.0	6.9	5.2	6.0
Phe[c]	2.7	2.3	2.2	2.2	2.6	3.7	3.6	3.5	3.5	3.6
C/HP[d]	**0.94**	**0.89**	**0.59**	**0.89**	**0.85**	**0.49**	**0.51**	**0.36**	**0.49**	**0.64**

[a] Total charged; [b] Total uncharged; [c] hydrophobic residues of amino acid; [d] Ratio of charged to hydrophobic residues; LOR: Limit of reporting. Bulk: undecalcified sample; AIM: Acid-Insoluble Organic Moiety; ASM: Acid-Soluble Organic Moiety; EIM: EDTA-Insoluble Moiety; ESM: EDTA-Soluble Moiety

The nacroprismatic shells are generally characterized by high amounts of glycine and alanine, followed by polar amino acids (aspartate and glutamate) and serine (Table 2.1, 2.2). The composition of the marine nacroprismatic sample (*P. fucata*) is close to that of the freshwater samples, except that the proportion of glycine is higher (33% compared to ~28%), while the proportion of hydrophobic amino acids (i.e. alanine) is lower (16% compared to ~21%). Comparing the results with published data for other shells from the same taxonomical orders studied here, Unionoida [20] and Pterioida [4], about 50% of the total amino acid composition is in glycine-alanine form (Supplementary Figure 2.1).

Table 2.2 Amino acid composition (mole %) in undecalcified (bulk), soluble and insoluble organic matrices

	Diplodon chilensis patagonicus			*Pinctada fucata martensii*		
Amino acid	Bulk	AIM	ASM	Bulk	AIM	ASM
His[a]	0.5	0.7	0.4	0.6	0.7	0.3
Ser[b]	9.3	8.0	6.9	6.4	6.7	6.0
Arg[a]	3.9	2.9	2.3	3.8	3.3	2.0
Gly	27.1	35.6	34.8	32.9	33.1	36.3
Asx[a]	8.9	7.2	5.6	9.5	9.5	5.5
Glx[a]	3.8	3.4	3.9	3.1	3.2	3.5
Thr[b]	1.6	1.3	2.1	1.5	1.8	1.8
Ala[c]	24.8	18.8	19.9	16.3	14.1	17.5
Pro[c]	2.0	2.3	3.1	3.1	3.7	4.0
Lys[a]	2.7	2.2	1.2	2.3	2.0	1.4
Tyr[b]	1.5	4.7	1.9	4.1	5.0	2.7
Met[c]	1.0	0.9	2.1	1.5	1.0	1.0
Val[c]	2.8	2.3	2.7	3.9	4.4	4.5
Ile[c]	2.0	1.7	2.7	2.7	3.3	2.9
Leu[c]	4.6	4.2	6.3	5.9	5.8	8.1
Phe[c]	3.5	3.8	4.1	2.4	2.4	2.4
C/HP[d]	**0.49**	**0.48**	**0.33**	**0.54**	**0.54**	**0.31**

Global amino acid compositions show some individual differences in the nacroprismatic shells (Supplementary Figure 2.2). The freshwater shell samples (*H. cumingii* and *D. chilensis*) have a C/HP ratio of 0.49, while the marine sample (*P. fucata*) yields a slightly higher ratio of 0.54. ASM extracts of the nacre-prism shells contain a large proportion of hydrophobic amino acids (C/HP = ~0.33) and are glycine-alanine rich (54%±1). These characteristics are

significantly different to the results for *A. islandica*, which is rich in aspartate and glutamate (21%), has a higher C/HP of ca. 0.90 and a high proline content (ca 13%; Table 2.1).

2.3.4 Protein size determination

Various organic fractions of nacre-prism and homogeneous shell structures were analysed by SDS-polyacrylamide gel electrophoresis (SDS-PAGE) and staining with CBB G-250 and/or silver nitrate (Supplementary Figures 2.3, 2.4), and Alcian blue and/or modified silver nitrate (Figures 2.4, 2.5). Staining with CBB G-250 did not reveal any protein bands in the samples and incubation of the polyacrylamide gel with traditional silver nitrate demonstrated only a few protein bands for the ASM and ESM extracts. The unsatisfactory response to routine staining methods (including combined silver nitrate and CBB G-250) led us to adapt and develop new fixing and staining methods (as described in *Materials and Methods*) to enhance the visibility of protein bands on the polyacrylamide gel.

For the *A. islandica* shell (ESM), modified silver nitrate staining visualized prominent protein bands at around 40, 26, 17, 14 and 10 kDa, and weaker bands above 160 and at around 55 kDa (Figure 2.4a, Lane 1). The sugar moiety was confirmed by a specific glycoprotein staining in the *A. islandica* organic matrix (Figure 2.4b, Lane 1). The very broad bands at around 26 kDa and 17 kDa visible in all staining methods may correspond to post-translational modifications (glycosylation, phosphorylation or sulfatation) of proteins in *A. islandica*, however, no protein band was observed in shells of *M. stimpsoni* and *M. lusoria* [27], which also have homogeneous microstructure.

For the ESM extract of *H. cumingii*, the fractionation by SDS-PAGE using modified silver nitrate staining (Figure 2.4a; Lane 2) showed protein bands with molecular masses ranging from 5 to 50 kDa along with a smear from 15 to 30 kDa, probably related to the effect of glycosaminoglycans. Weaker bands with molecular weights of 36, 38 and 40 kDa could also

be visualized. ESM extracts of *A. islandica* and *H. cumingii* (Figure 2.4; Supplementary Figure 2.4) both showed similar bands at around 5 to 10 kDa and at 40 kDa.

Alcian Blue and or modified silver nitrate staining of ASM extracts (Figure 2.5) revealed many bands in the range 5-110 kDa for all shells. *A. islandica* shows apparent bands at 21, 31, 40 and 55 kDa, respectively (Figure 2.5a, Lane 1). *P. fucata* revealed a prominent band at 40 kDa (Figure 2.5bs, Lane 1), as well as *H. cumingii* (Figure 2.5bs, Lane 3). Other bands for *H. cumingii* appear around 21, 31, 45, 58, 63 and 110 kDa, respectively, when silver nitrate enhanced Alcian Blue is used (Figure 2.5b+, Lane 3). Similarly, *D. chilensis* revealed prominent bands at around 10 and 14 kDa (Figure 2.5bs, Lane 2). The band at 40 kDa, however, has not been observed in nacroprismatic samples before [4, 20].

The SDS-PAGE of soluble organic matrix extracts (ASM, ESM) in the studied shells revealed many discrete bands of proteins, some of them are reported here for the first time (e.g. proteins in *A. islandica* and *D. chilensis* shells). Two new glycoprotein bands at around 20 and 63 kDa (Figure 2.4b; Lane 2) are found in ESM extracts of *H. cumingii* using combined Alcian Blue/silver nitrate staining and are attributed to a novel acidic sulfated glycoproteins for *H. cumingii*. Freshwater (*H. cumingii* and *D chilensis*) and marine shells (*A. islandica*) exhibit similar bands in the range 5-10 kDa. The band at 40 kDa is prominent in *H. cumingii*, *A. islandica* and *P. fucata*, respectively.

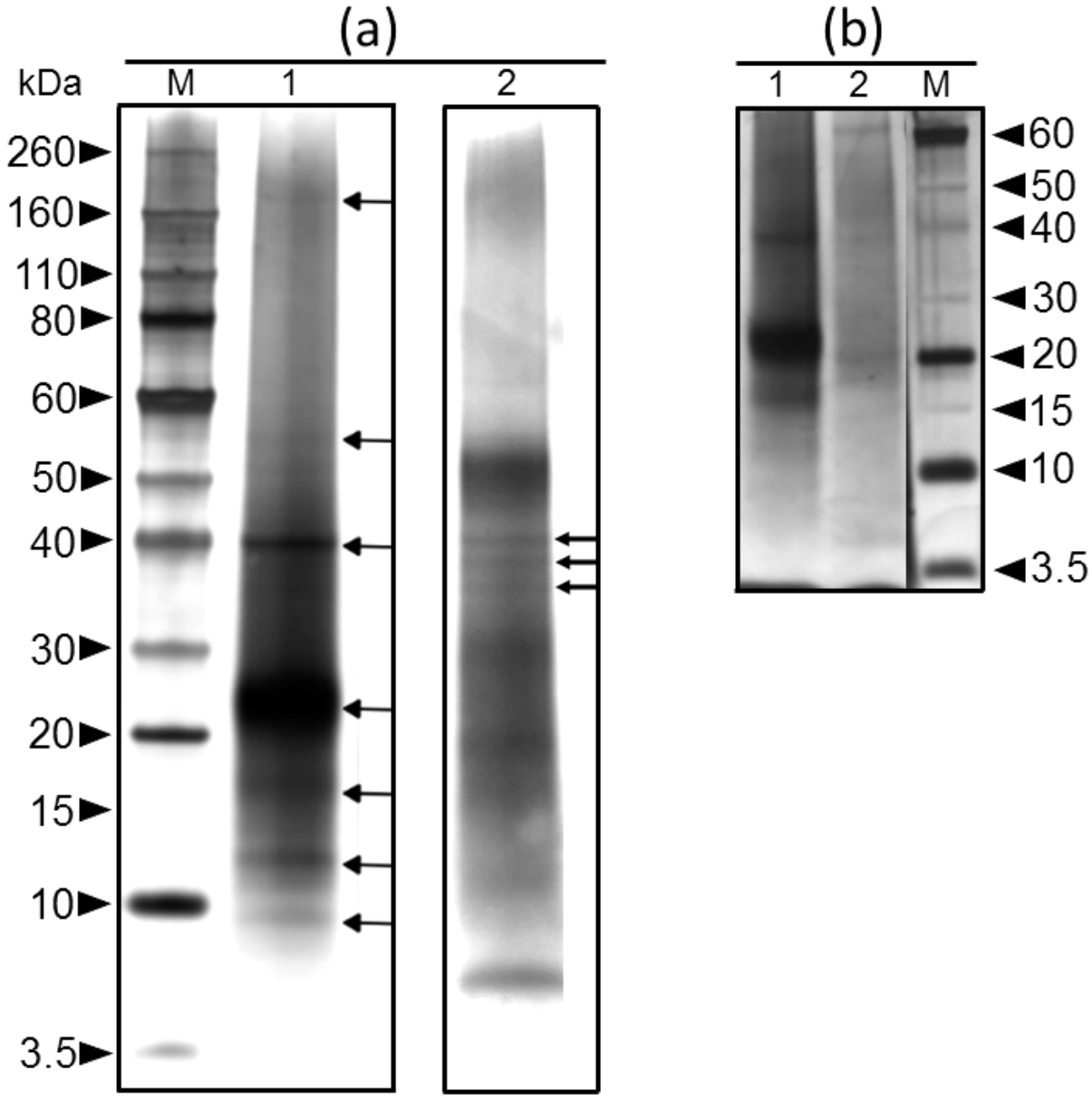

Figure 2.4. (a) SDS-PAGE of ESM soluble matrix (100 µg each) stained with silver nitrate + 50 µL formaldehyde. Lane 1: *A. islandica*; Lane 2: *H. cumingii*; Lane M: Standard molecular weight (5 µL). The arrows in Lanes 1 and 2 indicate relative molecular weights at 10, 14, 17, 26, 40, 55 and above 160; and 36, 38 and 40 kDa. (**b)** SDS-PAGE of ESM, silver nitrate (silver nitrate + 50 µL formaldehyde) enhanced Alcian Blue. Lane 1: *A. islandica* (100 µg); Lane 2: *H. cumingii* (100 µg); Lane M: Standard molecular weight (5 µL). Bands around 17 and 26 kDa for *A. islandica* may be associated with the phosphorylated and/or sulfated structure of the carbohydrate-protein-linkage extracted

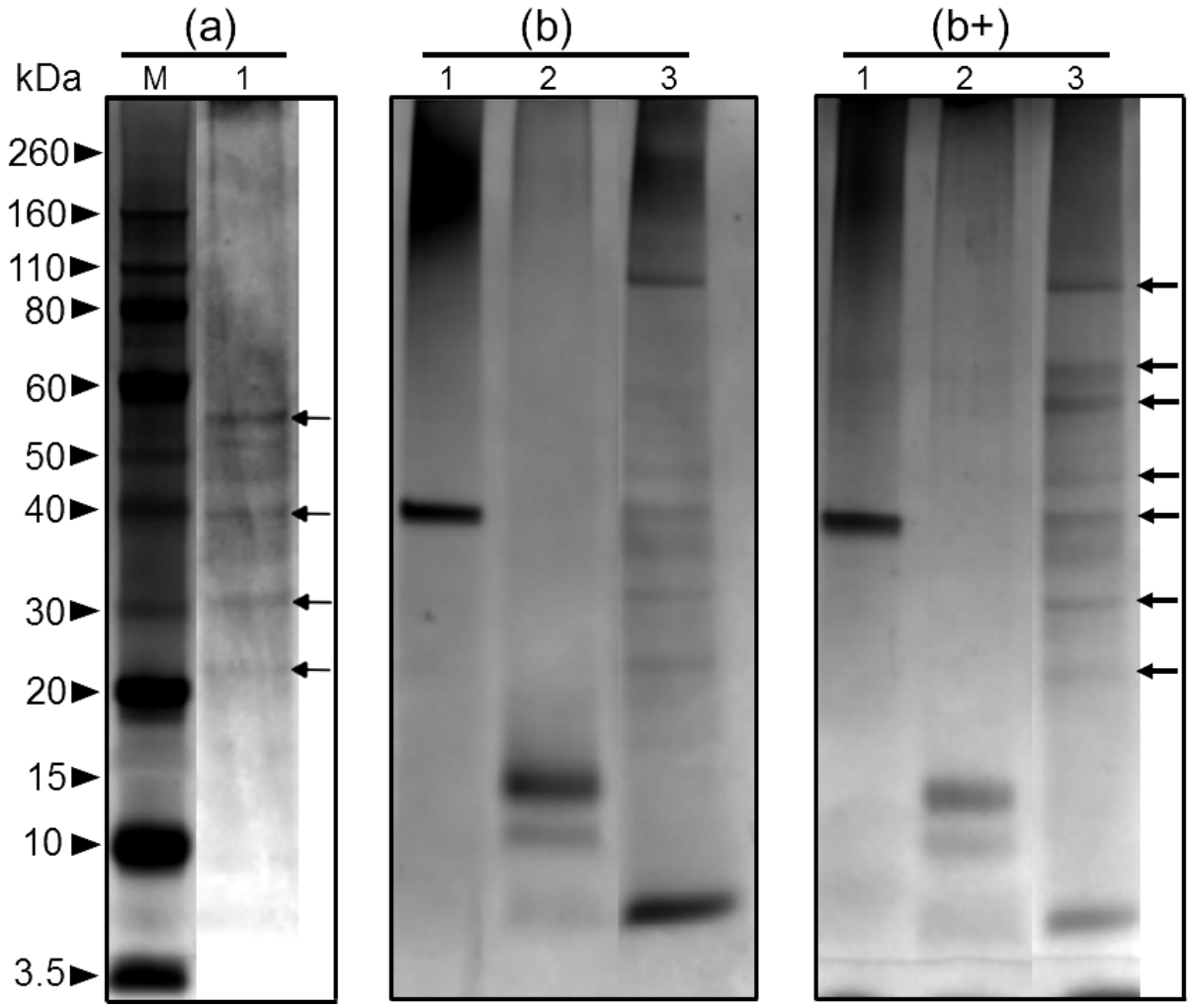

Figure 2.5. SDS-PAGE of ASM homogeneous (a) and nacroprismatic shells (b and b+) soluble matrix. (a) and (b) (20 µL respectively) stained with silver nitrate + 50 µL formaldehyde, while (b+) stained with Alcian Blue enhanced with silver nitrate + 50 µL formaldehyde. Lane M: Standard molecular weight (5 µL); Lane 1A: ASM of *A. islandica*; Lane 1b and 1b+: *P. fucata*, 2b and 2b+: *D. chilensis* and, 3b and 3b+: *H. cumingii*. A distinct band at 40 kDa for *A. islandica*, *P. fucata* and *H. cumingii* (see Fig. 4 and Fig. 4S Suppl.) agrees well with a similar band at 40 kDa found in nacre (Yan et al. 2007). The arrows in (a) indicate the relative molecular weights at around 21, 31, 40 and 55 kDa, while the arrows in (b+) designate the relative molecular weights at around 21, 31, 40, 45, 58, 63 and 110 kDa.

2.3.5 Comparison of EDTA and acid decalcification methods

Two complementary dissolution methods were used to optimize recovery, particularly of the soluble organic fraction (e.g. [19]. Our modification of the traditional EDTA decalcification method (see method section) was efficient in removing most residual EDTA from the extracted soluble organic matrix, which is otherwise a common problem. For instance, comparing the

EDTA fractions with literature data, results for acid-extraction [20] match well with the amino acid composition of *H. cumingii* shells except for a difference in alanine, for which a higher concentration is reported in the literature (See Supplementary Figure 2.1b).

The EDTA extracts in our study yielded higher amounts of polar amino acid and higher C/HP ratios (Table 2.1) compared to the acid extract. Also, protein bands are more prominent in the soluble moiety extracted with EDTA, while the acid extracts generally have higher molecular weights (Figure 2.5). This most likely indicates that some constituents, as for example silk-like constituent, which is rich in glycine and/or alanine [4, 25], remain in the insoluble moiety when the shell is dissolved with EDTA (Table 2.1 and 2.2; Supplementary Figure 2.1).

2.4 Discussion

The soluble protein portion in *A. islandica* shells (ASM and ESM extracts) depict eight major apparent molecular masses: of 10, 14, 17, 21, 26, 31, 40 and 55 kDa (Figure 2.4 Lane 1; Figure 2.5a Lane 1). CBB-G250 fails to stain these proteins bands well and the protein bands ranging from 5 to 10 kDa show strong negative bands (Supplementary Figure 2.4). As CBB-G250 predominantly stains the acidic shell proteins, this suggests that a large portion of the organic macromolecules in *A. islandica* shells is non-acidic [40]. CBB-G250 and Alcian Blue enhanced with silver nitrate stained three major bands at around 14, 26 and 17 kDa, respectively. We propose that these bands (26 and 17 kDa) are associated with sulfated polysaccharides. A band stained at around 55 kDa (ASM, Figure 2.5a; Lane 1) may be a proteoglycan band, which are glycosaminoglycans associated to a core protein.

We firstly observed two discrete glycoprotein bands at 20 kDa and 63 kDa amongst the soluble organic macromolecules in nacroprismatic *H. cumingii* shells (EDTA extract; Figure 2.4b, Lane 2). Similar bands are reported for other molluscs: a 20 kDa protein band was observed in the bivalve *Pinctada maxima* [4, 41] and a 63 kDa acidic glycoprotein was found

in the cephalopod *Nautilus macromphalus* [42]. CBB-G250 and silver nitrate combined stained protein bands between 30 and 50 kDa in this extract (Supplementary Figure 2.4, Lane 2). Similar bands at 48kDa and 50kDa were observed in freshwater cultured pearls [43] and nacre [20] of *H. cumingii*, respectively. These findings are in accordance with the observation of a calcium-binding glycoprotein of an apparent molecular mass of 50 kDa in the bivalves *Unio pictorum* [24] and in *Anodonta cygnea* [44] that belong to the same taxonomic order as *H. cumingii* (Unionida).

The soluble organic fraction after acid extraction (ASM) of two nacroprismatic shells (*D. chilensis patagonicus* and of *H. cumingii*) shells show bands at around 14 kDa and 58 kDa. The matrix proteins N14 (pearline) [45] and MSI60 [46] have similar sizes, but detailed proteomics would be necessary to further clarify the identity of the bands observed here. Both protein bands have also been found in the nacreous layer of *Pinctada* shells [21], but we did not observe these bands in the *P. fucata* shells studied here (Figure 2.5b; Lane 1). Instead, a prominent peak at 40 kDa stains in gels from *P. fucata* is also identified in *A. islandica* and *H. cumingii* shells. This band is inferred to be a conventional "insoluble matrix protein" [47].

Comparison of the organic macromolecules in *A. islandica* shells with nacroprismatic samples exhibit several important differences: The overall organic content is lower in *A. islandica* shells compared with the nacroprismatic samples (Figure 2.1), it contains a higher C/HP ratio (Table 2.1 and 2.2), and hence more polar components (aspartate and glutamate) compared with the nacroprismatic shells. The composition of *A. islandica* shells is comparable to those of *M. stimpsoni* except that the total proportion of the polar amino acids as a group, namely aspartate, glutamate, threonine, serine and arginine, is relatively higher (42.8% in *M. stimpsoni* compared of 38.4% in *A. islandica*, see Supplementary Figure 2.1c). We further compared the composition of those five residues above with the shells of crossed lamellar microstructure [27]. The composition of crossed-lamellar bivalve shells is relatively close

(36.0% vs 38.1%) compared to homogeneous *A. islandica* shell. However, unlike our study that reveals many prominent protein bands in *A. islandica*, shells of *M. stimpsoni* with homogeneous and other bivalve shells with crossed lamellar microstructure showed no protein band [12, 27].

The nacroprismatic shells contain higher amounts of organic scaffolding macromolecules, including *β*-chitin lamellar sheets and silk-like fibroin gel [3] than *A. islandica*. This is supported by acidic bands of *A. islandica* in the FTIR spectra at 1736 cm^{-1}, 1716 cm^{-1} as well as by amide II bands (Figure 2.2b), none of which are present in the nacroprismatic samples. Moreover, glycine and alanine are the main fractions in the nacroprismatic samples (Tables 2.1, 2.2), while *A. islandica* depicts lower amounts of these molecules (Table 2.1), even when considering all proline, glycine and aspartate in their glycine-alanine-rich forms. Furthermore, *A. islandica* demonstrates distinct polysaccharide bands in the FTIR spectra (Figure 2.2a). These could be a result of higher contents of proline (15%; Table 2.1) in *A. islandica*, which by far exceed those in the nacroprismatic organic matrices (ca 3%; [20, 40]).

The composition of the Ca-binding biomolecules in the soluble fractions of the nacroprismatic samples obtained by both decalcification methods are similar; they comprise glycine, threonine, serine, glutamate and aspartate (ca 54%; Supplementary Figure 2.2) with a large proportion of glycine, alanine and serine (ca 60%; Table 2.1 and 2.2) characteristic of silk fibroin-like proteins [48]. These findings agree well with the composition of organic matrices in the nacre of other molluscs [4, 19, 20, 48] and is similar to the composition of insoluble spider silk [49]. Proteins with this amino acid composition are able to form a *β*-sheet structure, which has been proposed to be a key scaffolding constituent in the shell [50].

Previous studies on bivalve nacre established a major role for acidic amino acids, namely aspartic and glutamic acid in biomineralization [5, 40] based on their Ca-binding function. However, compared to nacroprismatic shells, the amounts of aspartate and glutamate in *A. islandica* shells are lower (≤ 16% vs >25%), suggesting that this role is not limited to acidic

proteins, but extends to other compounds of the organic matrix. Glycosylated proteins with the potential to bind Ca^{2+} ions containing lower amounts of acidic properties (Asx + Glx < 22%) but high amounts of hydrophobic proteins (≤ 50%) were identified from *Unio pictorium* shells [24] and cultured pearls of *H. cumingii* [43, 51]. Previous works [47, 51, 52] suggested that aragonite crystal nucleation takes place at a preferential site on the surface of nonacidic matrix proteins and other non-proteinaceous macromolecules. This site is identified as rich in sulphur, probably in the form of sulfate groups [24].

Samata [27] analysed the Ca-binding glycoproteins in molluscan shells with different microstructures and found the compositions similar between homogeneous and crossed lamellar structures. In our study both homogeneous- and nacroprismatic- shells are nonacidic, though glycine-alanine forms are prominent in nacroprismatic shells. We suggest that the composition of the Ca-binding glycoproteins may vary predominantly according to shell structure and/or species. It is obvious that no hydrophobic and/or acidic proteins appear to be specific to certain molluscan shell microstructures [27].

2.5 Conclusions

We report the first analysis of shell-associated biopolymers for *Arctica islandica* shells and distinguish the homogeneous *Arctica islandica* shells from nacroprismatic shells. New staining methods for electrophoretic fractionations remove some major problems and improve the analysis of shell macromolecules. We show that impregnation of gels with silver nitrate solution containing formaldehyde (50 µl in 100 mL) before development can facilitate the visualisation of proteins on the gel. Using these newly adapted fixations and staining protocols we show that the choice of decalcification method significantly influences the sizes as well as the number of protein bands observed on the gels.

Many protein bands (e.g. around 20 and 63 kDa) are revealed in *H. cumingii* here for the first time. We show that shells with homogeneous and nacroprismatic microstructures have

some protein band(s) in common: *A. islandica*, *P. fucata* and *H. cumingii* show a prominent protein band at 40 kDa. *P. fucata* demonstrates just one band at 40 kDa, which is a nonacidic-matrix-protein [47]. Moreover, the shell macromolecules of all studied samples are overall non-acidic, containing low amounts of aspartate and glutamate (21% for homogeneous and 16% for nacroprismatic shells).

Acknowledgements Mark Tran and Dr Christopher McRae are well-appreciated for their incessant technical supports. OBAA acknowledges Emily Gibson and Dr Bhumika Shah (Chemistry and Biomolecular Sciences, Macquarie University) for teaching him the basic techniques of gel electrophoresis.

2.6 References

1. Weiner, S. and P.M. Dove, *An overview of biomineralization processes and the problem of the vital effect.* Reviews in Mineralogy and Geochemistry, 2003. **54**(1): p. 1-29.
2. Farre, B. and Y. Dauphin, *Lipids from the nacreous and prismatic layers of two Pteriomorpha Mollusc shells.* Comparative Biochemistry and Physiology Part B: Biochemistry and Molecular Biology, 2009. **152**(2): p. 103-109.
3. Levi-Kalisman, Y., et al., *Structure of the nacreous organic matrix of a bivalve mollusk shell examined in the hydrated state using cryo-TEM.* Journal of Structural Biology, 2001. **135**(1): p. 8-17.
4. Pereira-Mouriès, L., et al., *Soluble silk-like organic matrix in the nacreous layer of the bivalve Pinctada maxima.* European Journal of Biochemistry, 2002. **269**(20): p. 4994-5003.
5. Addadi, L. and S. Weiner, *Biomineralization: mineral formation by organisms.* Physica Scripta, 2014. **89**(9): p. 098003.
6. Arivalagan, J., et al., *Shell matrix proteins of the clam, Mya truncata: Roles beyond shell formation through proteomic study.* Marine Genomics, 2016. **27**: p. 69-74.
7. Marin, F. and G. Luquet, *Molluscan biomineralization: The proteinaceous shell constituents of Pinna nobilis L.* Materials Science and Engineering: C, 2005. **25**(2): p. 105-111.
8. Giuffre, A.J., et al., *Polysaccharide chemistry regulates kinetics of calcite nucleation through competition of interfacial energies.* Proceedings of the National Academy of Sciences, 2013. **110**(23): p. 9261-9266.
9. Hamm, L.M., et al., *Reconciling disparate views of template-directed nucleation through measurement of calcite nucleation kinetics and binding energies.* Proceedings of the National Academy of Sciences, 2014. **111**(4): p. 1304-1309.
10. Agbaje, O., et al., *Architecture of crossed-lamellar bivalve shells: the southern giant clam (Tridacna derasa, Röding, 1798).* Open Science, 2017. **4**(9): p. 170622.
11. Carter, J.G., *Skeletal biomineralization: patterns, processes and evolutionary trends*. Vol. 1. 1990: Wiley Online Library.
12. Dauphin, Y. and A. Denis, *Structure and composition of the aragonitic crossed lamellar layers in six species of Bivalvia and Gastropoda.* Comparative Biochemistry and Physiology Part A: Molecular & Integrative Physiology, 2000. **126**(3): p. 367-377.

13. Philipp, E.E., et al., *Gene expression and physiological changes of different populations of the long-lived bivalve Arctica islandica under low oxygen conditions.* PLoS One, 2012. **7**(9): p. e44621.
14. Ropes, J., S. Murawski, and F. Serchuk, *Size, age, sexual, maturity, and sex-rati in ocean quahogs, Arctica-islandica linne, off Long-Island, New-York* Fishery Bulletin, 1984. **82**(2): p. 253-267.
15. Weidman, C.R. and G.A. Jones, *The long-lived mollusc Arctica islandica: A new paleoceanographic tool for the reconstruction of bottom temperatures for the continental shelves of the northern North Atlantic Ocean.* Journal of Geophysical Research: Oceans, 1994. **99**(C9): p. 18305-18314.
16. Taylor, J.D., *The structural evolution of the bivalve shell.* Palaeontology, 1973. **16**(3): p. 519-534.
17. Ropes, J.W., et al., *Documentation of annual growth lines in ocean quahogs, Arctica islandica Linne.* Fish Bull, 1984. **82**(1): p. 1-19.
18. Bevelander, G. and H. Nakahara, *An electron microscope study of the formation of the nacreous layer in the shell of certain bivalve molluscs.* Calcified Tissue Research, 1969. **3**(1): p. 84-92.
19. Bédouet, L., et al., *Proteomics analysis of the nacre soluble and insoluble proteins from the oyster Pinctada margaritifera.* Marine Biotechnology, 2007. **9**(5): p. 638-649.
20. Ma, Y., et al., *What is the difference in organic matrix of aragonite vs. vaterite polymorph in natural shell and pearl? Study of the pearl-forming freshwater bivalve mollusc Hyriopsis cumingii.* Materials Science and Engineering: C, 2013. **33**(3): p. 1521-1529.
21. Kono, M., N. Hayashi, and T. Samata, *Molecular mechanism of the nacreous layer formation in Pinctada maxima.* Biochemical and Biophysical Research Communications, 2000. **269**(1): p. 213-218.
22. Miyashita, T., et al., *Complementary DNA cloning and characterization of pearlin, a new class of matrix protein in the nacreous layer of oyster pearls.* Marine Biotechnology, 2000. **2**(5): p. 409-418.
23. Dauphin, Y., *Soluble organic matrices of the calcitic prismatic shell layers of two pteriomorphid bivalves Pinna nobilis and Pinctada margaritifera.* Journal of Biological Chemistry, 2003. **278**(17): p. 15168-15177.
24. Marie, B., et al., *The shell matrix of the freshwater mussel Unio pictorum (Paleoheterodonta, Unionoida).* FEBS Journal, 2007. **274**(11): p. 2933-2945.
25. Addadi, L., et al., *Mollusk shell formation: a source of new concepts for understanding biomineralization processes.* Chemistry-A European Journal, 2006. **12**(4): p. 980-987.
26. Carter, J.G. and R.C. Aller, *Calcification in the bivalve periostracum.* Lethaia, 1975. **8**(4): p. 315-320.
27. Samata, T., *Ca-binding glycoproteins in molluscan shells with different types of ultrastructure.* The Veliger, 1990. **33**(2): p. 190-201.
28. Shirai, K., et al., *Assessment of the mechanism of elemental incorporation into bivalve shells (Arctica islandica) based on elemental distribution at the microstructural scale.* Geochimica et Cosmochimica Acta, 2014. **126**: p. 307-320.
29. Zaitoun, M.A. and C. Lin, *Chelating behavior between metal ions and EDTA in sol-gel matrix.* The Journal of Physical Chemistry B, 1997. **101**(10): p. 1857-1860.
30. Rahman, M.A., et al., *Analysis of proteinaceous components of the organic matrix of endoskeletal sclerites from the alcyonarian Lobophytum crassum.* Calcified Tissue International, 2006. **78**(3): p. 178-85.
31. Cohen, S.A. and D.P. Michaud, *Synthesis of a fluorescent derivatizing reagent, 6-aminoquinolyl-N-hydroxysuccinimidyl carbamate, and its application for the analysis of hydrolysate amino acids via high-performance liquid chromatography.* Analytical Biochemistry, 1993. **211**(2): p. 279-287.
32. Truong, H.H., et al., *Performance of broiler chickens offered nutritionally-equivalent diets based on two red grain sorghums with quantified kafirin concentrations as intact pellets or re-ground*

mash following steam-pelleting at 65 or 97 C conditioning temperatures. Animal Nutrition, 2015. **1**(3): p. 220-228.
33. Morrissey, J.H., *Silver stain for proteins in polyacrylamide gels: a modified procedure with enhanced uniform sensitivity.* Analytical Biochemistry, 1981. **117**(2): p. 307-310.
34. Wall, R.S. and T.J. Gyi, *Alcian blue staining of proteoglycans in polyacrylamide gels using the "critical electrolyte concentration" approach.* Analytical Biochemistry, 1988. **175**(1): p. 298-299.
35. Brine, C.J. and P.R. Austin, *Chitin variability with species and method of preparation.* Comparative Biochemistry and Physiology Part B: Comparative Biochemistry, 1981. **69**(2): p. 283-286.
36. Roeges, N.P., *A guide to the complete interpretation of infrared spectra of organic structures*. 1994: Wiley.
37. Lavall, R.L., O.B. Assis, and S.P. Campana-Filho, *β-Chitin from the pens of Loligo sp.: Extraction and characterization.* Bioresource Technology, 2007. **98**(13): p. 2465-2472.
38. Cárdenas, G., et al., *Chitin characterization by SEM, FTIR, XRD, and 13C cross polarization/mass angle spinning NMR.* Journal of Applied Polymer Science, 2004. **93**(4): p. 1876-1885.
39. Stankiewicz, B.A., et al., *Biodegradation of the chitin-protein complex in crustacean cuticle.* Organic Geochemistry, 1998. **28**(1): p. 67-76.
40. Gotliv, B.A., L. Addadi, and S. Weiner, *Mollusk shell acidic proteins: in search of individual functions.* ChemBioChem, 2003. **4**(6): p. 522-529.
41. Bédouet, L., et al., *Soluble proteins of the nacre of the giant oyster Pinctada maxima and of the abalone Haliotis tuberculata:: extraction and partial analysis of nacre proteins.* Comparative Biochemistry and Physiology Part B: Biochemistry and Molecular Biology, 2001. **128**(3): p. 389-400.
42. Marie, B., et al., *Nautilin-63, a novel acidic glycoprotein from the shell nacre of Nautilus macromphalus.* FEBS Journal, 2011. **278**(12): p. 2117-2130.
43. Natoli, A., et al., *Bio-vaterite formation by glycoproteins from freshwater pearls.* Micron, 2010. **41**(4): p. 359-366.
44. Lopes, A., et al., *Functional studies on the shell soluble matrix of Anodonta cygnea (Bivalvia: Unionidae).* Nautilus, 2014. **128**(4): p. 105-113.
45. Miyashita, T., et al., *Complementary DNA cloning and characterization of Pearlin, a new class of matrix protein in the nacreous layer of oyster pearls.* Marine Biotechnology, 2000. **2**(5).
46. Sudo, S., et al., *Structures of mollusc shell framework proteins.* Nature, 1997. **387**: p. 563-564.
47. Yan, Z., et al., *N40, a novel nonacidic matrix protein from pearl oyster nacre, facilitates nucleation of aragonite in vitro.* Biomacromolecules, 2007. **8**(11): p. 3597-3601.
48. Keith, J., et al., *Comparative analysis of macromolecules in mollusc shells.* Comparative Biochemistry and Physiology Part B: Comparative Biochemistry, 1993. **105**(3): p. 487-496.
49. Lombardi, S.J. and D.L. Kaplan, *The amino acid composition of major ampullate gland silk (dragline) of Nephila clavipes (Araneae, Tetragnathidae).* Journal of Arachnology, 1990. **18**: p. 297-306.
50. Weiner, S. and W. Traub, *X-ray diffraction study of the insoluble organic matrix of mollusk shells.* FEBS letters, 1980. **111**(2): p. 311-316.
51. Ma, Y., L. Qiao, and Q. Feng, *In-vitro study on calcium carbonate crystal growth mediated by organic matrix extracted from fresh water pearls.* Materials Science and Engineering: C, 2012. **32**(7): p. 1963-1970.
52. Zhang, C., et al., *A novel matrix protein p10 from the nacre of pearl oyster (Pinctada fucata) and its effects on both CaCO3 crystal formation and mineralogenic cells.* Marine Biotechnology, 2006. **8**(6): p. 624-633.

Supplementary Material for Chapter 2

Organic macromolecules in shells of *Arctica islandica*: comparison with nacroprismatic bivalve shells

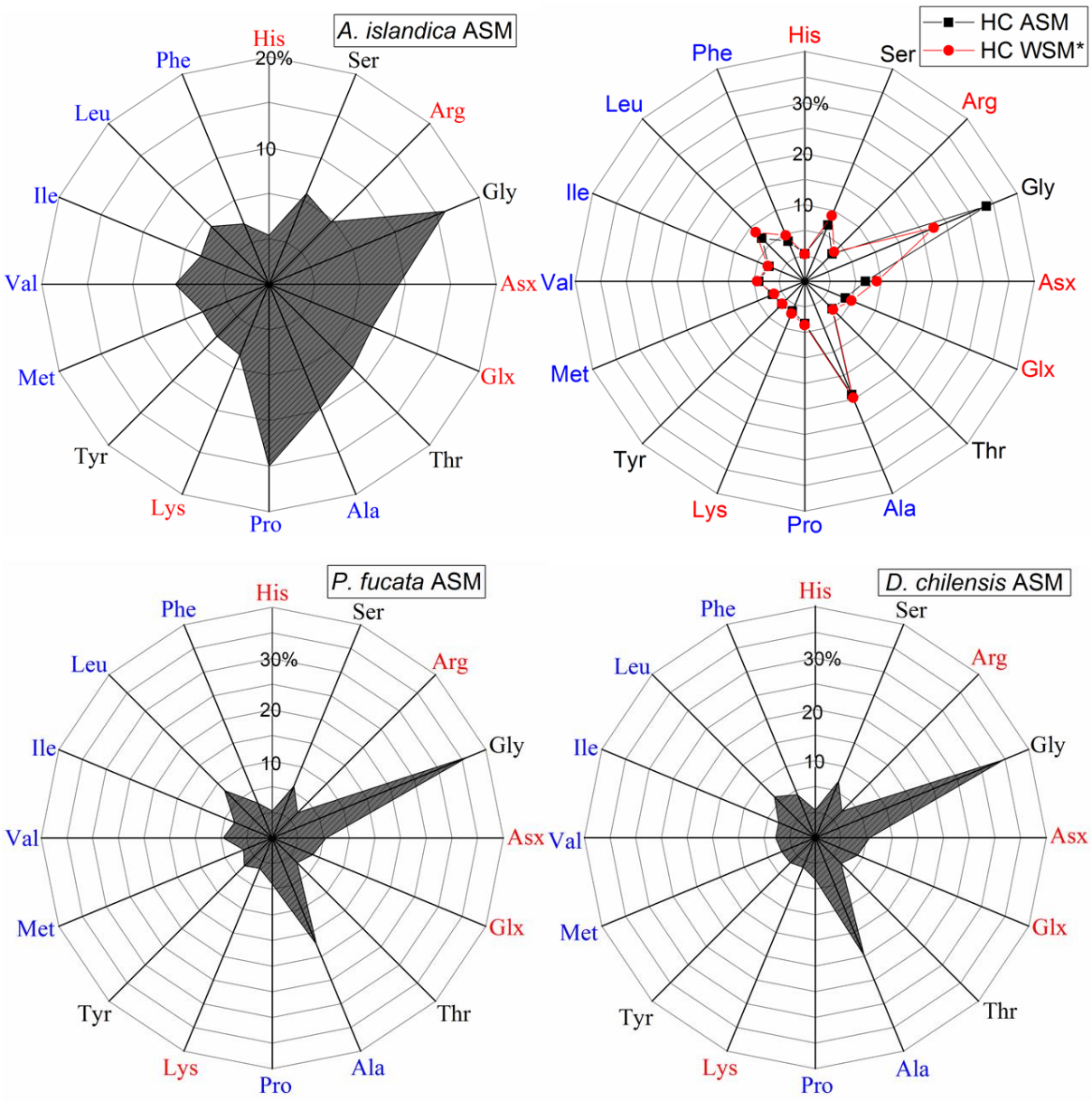

Supplementary Figure 2.1a. Amino acid compositions of ASM in *A. islandica*, *H. cumingi*, *D. chilensis* and *P. fucata* shells. HC WSM* represents *H. cumingii* water soluble organic matrix from ref. [20]. Blue, red and black colours represent non-polar (hydrophobic), polar (charged) and polar (uncharged) except glycine.

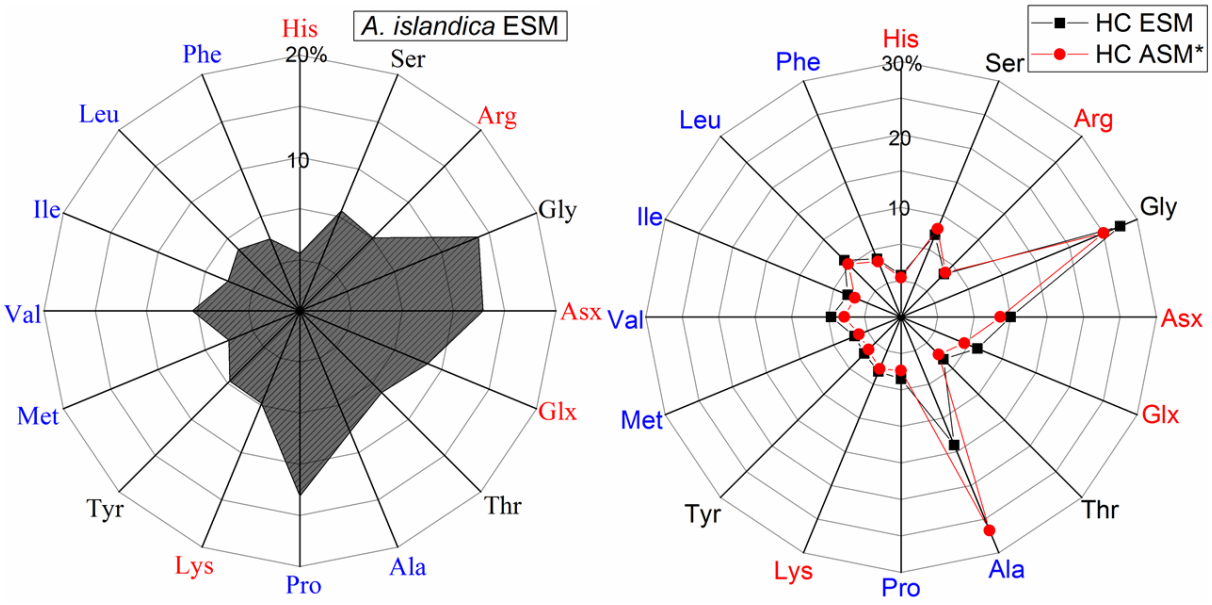

Supplementary Figure 2.1b. Amino acid compositions of the EDTA soluble organic matrices (ESM) in shells of *A. islandica* and *H. cumingii*. HC ASM* represents *H. cumingii* acid soluble organic matrix from ref. [20].

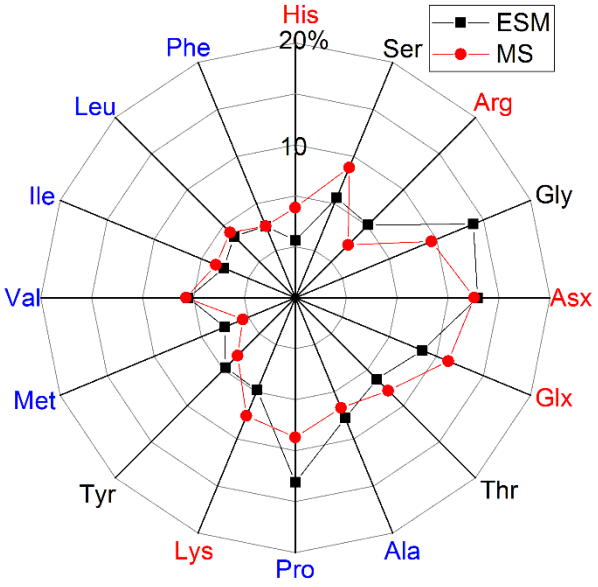

Supplementary Figure 2.1c. Amino acid compositions of the EDTA soluble organic matrices (ESM) in shells of *A. islandica* comparing with shells of homogeneous-type. MS represents *Mercenaria stimpsoni* soluble organic matrix from ref. [27]. In *A. islandica*, glycine and proline are more prominent compared with *M. stimpsoni* soluble organic matrix. The aspartate (Asx) is strikingly analogous despite to the differences in biological taxonomy and preparation techniques. See text for the detail.

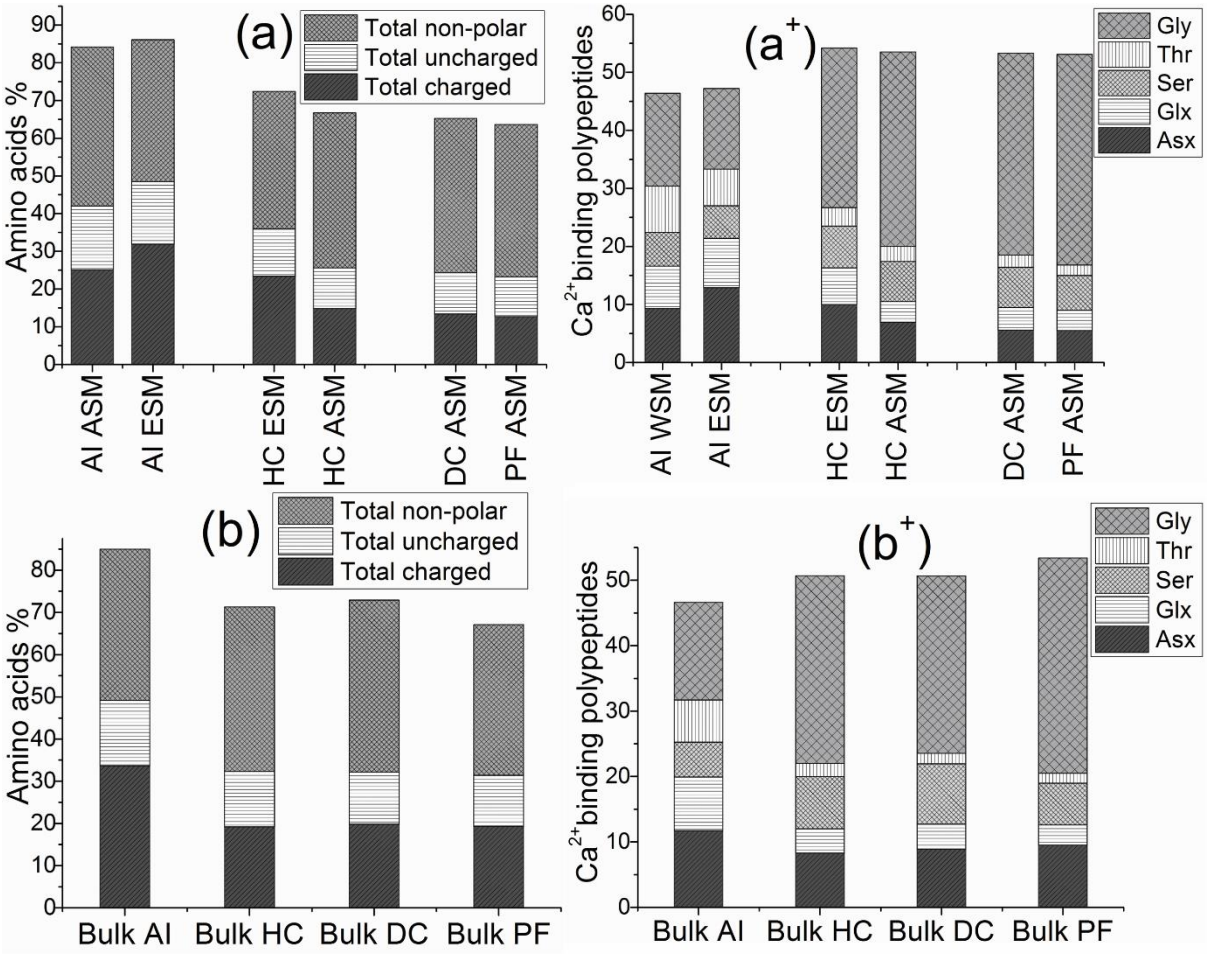

Supplementary Figure 2.2. Comparative analysis of the total amino acid of soluble organic matrix (a), bulk (undecalcified) organic matrix (b) and percentage of Ca^{2+} binding polypeptides from the soluble matrix (a^{+}) and the bulk (undecalcified) matrix (b^{+}). Acid soluble matrix (ASM) and EDTA-soluble matrix (ESM) of AI (*Arctica islandica*), HC (*Hyriopsis cumingii*), DC (*Diplodon chilensis patagonicus*) and PF (*Pinctada fucata martensii*).

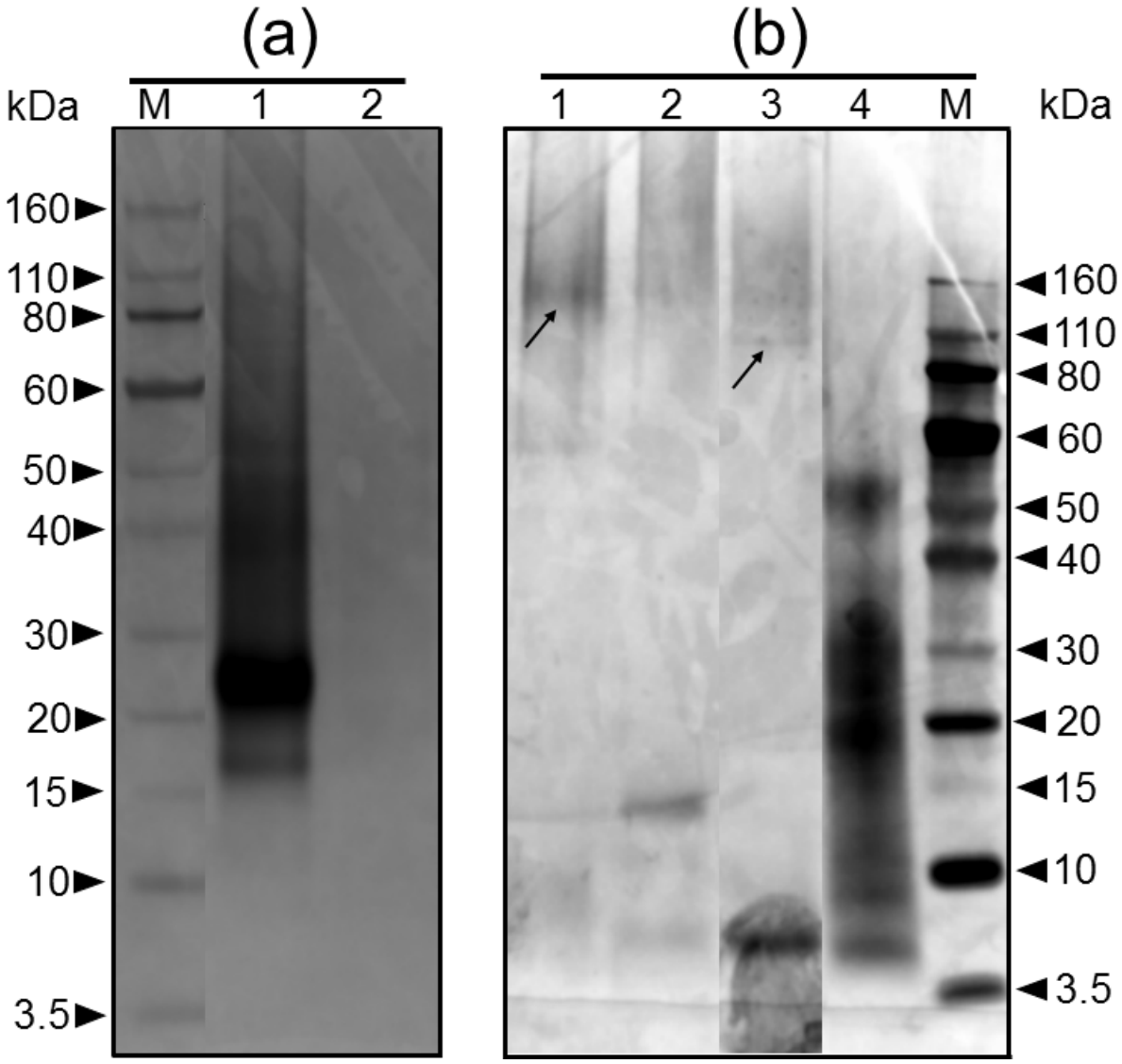

Supplementary Figure 2.3. SDS-PAGE comparison of EDTA and acid soluble matrices from shells stained with silver nitrate. (a) *A. islandica* soluble matrix, Lane 1: ESM (8 µL aliquots of the sample). Note: 20 µL aliquots of the sample was used and the same bands were observed; Lane 2: ASM (20 µL aliquots of the sample), no protein bands were revealed. (b) nacroprismatic shells, each lane was loaded with 20 µL except Lane M (molecular weight) with 10 µL. Lane 1: ASM *P. fucata*; Lane 2: ASM *D. chilensis*; Lane 3: ASM *H. cumingii*; Lane 4: ESM *H. cumingii*; Lane M: Standard Molecular weight. The arrows on lane 1 and 3 indicate weak bands at around 160 and 110 kDa respectively.

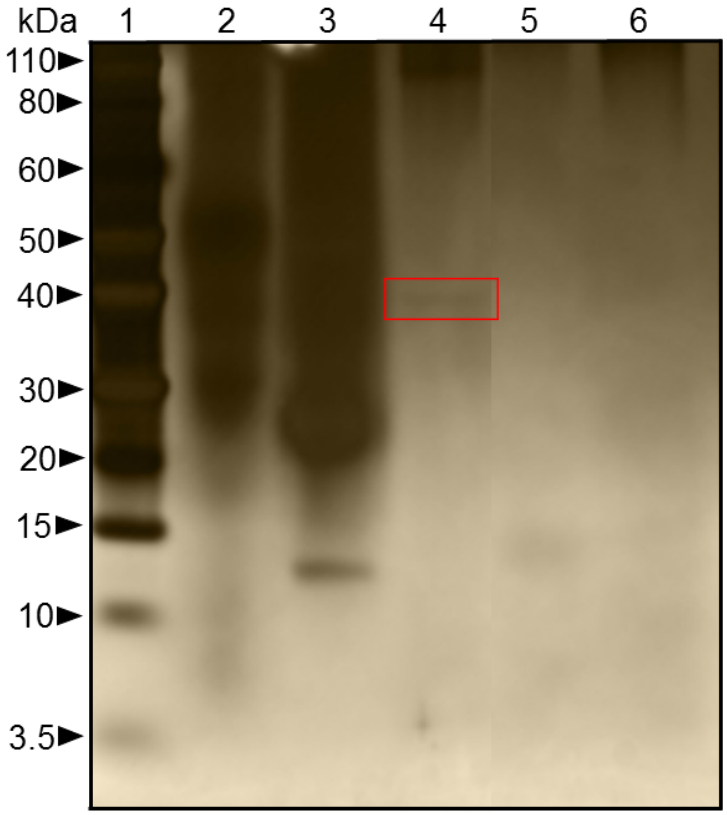

Supplementary Figure 2.4. SDS-PAGE comparison of ESM and ASM, silver nitrate enhanced Coomassie Blue R-250 staining. Each lane was loaded with 20 µL except MW with 10 µL. Lane 1: Standard molecular weight; Lane 2: ESM *H. cumingii*; Lane 3: ESM *A. islandica*; Lane 4: ASM *H. cumingii*; Lane 5: ASM *D. chilensis patagonicus*; Lane 6: ASM *P. fucata martensii*. Note: No protein bands were revealed for ASM *A. islandica* (not shown). The rectangular box on Lane 4 denotes the band at 40 kDa. This is the only staining technique that revealed protein band at around 14 kDa for ESM *A. islandica*.

Silk-based Fibres vs Collagenous Gel: Major Organic Components of Bivalve Shells Revealed by Solid-State NMR

Oluwatoosin Bunmi A. Agbaje[†], Ira Ben Shir[‡], David B. Zax[¥], Asher Schmidt[‡] and Dorrit E. Jacob[†]

[†]Department of Earth and Planetary Sciences, Macquarie University, Sydney, NSW2109, Australia

[‡]Schulich Faculty of Chemistry and Russell Berrie Nanotechnology Institute Technion-Israel Institute of Technology, Technion City, Haifa 32000, Israel

[¥]Department of Chemistry, Cornell University, Ithaca, New York 14853 USA

ABSTRACT Shells of bivalve are nanocomposites consisting of inorganic-organic components, and thus exhibit stiffness higher than that of their pure inorganic counterparts. Identifying a three-dimensional shell biopolymer is therefore a crucial step in improving our understanding towards the formation of biominerals. Here, the biopolymers from nacreous layer of shells *Pinctada maxima*, *Alathyria jacksoni*, *Hyriopsis cumingii* and *Cucumerunio novaehollandiae*, and homogeneous *Arctica islandica* shells have been studied by solid-state NMR. In the organic matrix of nacre, taken as a group, the chemical shifts found for the alanine and glycine carbon atoms classify their local environment as extended *β*-pleated sheets, one of the hallmarks of the important structural protein, which is called silk fibroin fibres. However, in homogeneous *Arctica islandica* shells, ^{13}C CP MAS spectrum exhibits gelatin—a degraded form of collagen. Scanning electron microscope imaging of the organic extract of the *Arctica islandica* demonstrates the mesh networks formed by type IV collagen which is quite unlike the silk-like fibrous structure found in the nacre. While we show that the organic scaffolds in nacre and homogeneous are species-specific, this work presumes the 20 naturally occurring amino acids are the essential 'toolkit' for the formation of a three-dimensional assembly of organic matrix in calcareous biominerals.

KEYWORDS: Polyamino acids, *β*-pleated sheets, Chitin, Crossed lamellar, Biomineralisation.

3.1. INTRODUCTION

Biominerals are inorganic-organic nanocomposites with material properties that outperform those of their inorganic mineral counterparts. The calcareous, aragonitic or calcitic shells of bivalves, for example, show stiffness that is 3000 times higher than that of their pure inorganic counterparts [5]. The organic matter occluded in the shell-bearing calcium carbonate while comprising less than 5 wt% of the total [160] plays an important role in the nucleation and growth of the mineral phase[2, 3] as well as in optimization of the material properties at all spatial scales [161, 162]. Included in most bivalve shells is a significant fraction of insoluble biomacromolecules which serve as scaffolding [57].

Biopolymers occurring in nature are built from monomers based on either nucleic acids, sugars or peptides [163, 164]. Biocarbonates such as mollusk shells show no evidence for the former. In animal species the sugar monomers are chemically modified, most commonly by amination [165-168] and the resulting polymers are referred to as chitin or chitosan depending largely on the degree of subsequent acetylation. Of course, macromolecules based on peptides (including fibrous, tubular, helical, layered, cellular, and intermediate structures) are present throughout the animal taxa [163], as either functional or structural proteins.

In nacre, the aragonitic inner layer of the shells of many bivalve species, the organic scaffolding is proposed to consist of highly ordered planar arrays of β-chitin fibers [57, 89] coated by active soluble acidic macromolecules and embedded in a silk protein hydrogel [85, 89, 94]. That such constructs are reasonable is supported by the observation of β-chitin fibers as a minor protein-associated component in the silk ducts of both the spider *Nephila* genus and the silkworm *Bombyx mori* [168].

While the effort to characterize shell-associated biopolymers has an extensive history much of that effort has focussed macromolecules rich with acidic sidechains[79, 83, 91] and chitin[95-97] and less attention has been devoted to the (typically) hydrophobic proteins, and their interaction with the major components of the shells. Total organic content can be measured

by thermal gravimetric analysis (TGA) and typically finds a total organic content of < 5%wt, but the separation and identification of individual components of the organic matrix is a considerable analytical challenge. Solid-State Nuclear Magnetic Resonance Spectroscopy (SSNMR) is appropriate to address such details[39, 98], as it can probe molecular structures both within intact shells[169, 170] or, after selective extraction, separated from the inorganic matter [169, 171, 172].

In order to characterize the composition of the shell-associated biopolymers in greater detail, we have studied the shells of 7 species from 6 molluscan families by SSNMR in combination with other techniques. The shell samples are classified as nacroprismatic (*Hyriopsis cumingii*, *Cucumerunio novaehollandiae, Alathyria jacksoni, Pinctada maxima*), homogeneous (*Arctica islandica*) and crossed-lamellar (*Tridacna gigas*, *Callista kingii*), based on their shell microstructures [9]. Results are complemented with Fourier Transform Infrared spectroscopy (FTIR), scanning electron microscope (SEM) imaging and saccharide analysis to yield a detailed characterisation of the hydrophobic organic shell matrix, which shows that, contrary to current belief, silk fibroin and not chitin is the major organic component in the shells of these diverse bivalve species.

3.2. MATERIAL AND METHODS

3.2.1. Materials. Recently alive shells of freshwater (*Hyriopsis cumingii* (Unionidae; Lea, 1852), *Cucumerunio novaehollandiae* (Hyriidae; Gray, 1834), *Alathyria jacksoni* (Hyriidae; Iredale, 1934)*)* and marine bivalves (*Pinctada maxima* (Pteriidae; Jameson, 1901), *Arctica islandica* (Arcticidae; Linnaeus, 1767), *Tridacna gigas* (Tridacnidae; Linnaeus, 1758) and *Callista kingii* (Veneridae; Gray in King, 1827)) were used in this study. Except for *P. maxima* shells, all shells are entirely aragonitic. The shells of the first four species are nacroprismatic, consisting of an outer layer with prism-shaped $CaCO_3$ grains and an inner shell layer of mother-of-pearl or nacre [9, 59, 89]. *Arctica islandica* shells have a homogeneous microstructure of mostly granular aragonite with only few distinctive features [9]. *Tridacna gigas* and *Callista*

kingii shells have crossed lamellar microstructures consisting of lath-shaped and fibrous aragonite grains, respectively, interlayered at a constant angle and reminiscent of plywood [9, 51, 69]. Except for *T. gigas*, all shells have a periostracum, which is an organic layer of ≥4 mm in thickness that covers the outside of the shell. *Tridacna* shells consist of a ca. 10 mm thick massive outer layer and a slightly translucent inner layer with visible growth increments [128].

3.2.2. Sample Preparation.

The organic periostracum covering the outside of some of the shells was removed with a scalpel and the outer prismatic shell layer of *H. cumingii, P. maxima, C. novaehollandiae* and *A. jacksoni,* and the periostracum covering the outside layer of homogeneous shell *A. islandica* were removed with a DREMEL tool (Wisconsin, USA, **Figure 3.1**) before analysis. For the *Tridacna* shell, the outer shell layer, which showed considerable overgrowth and evidence for boring, was removed with a diamond rock saw before analysing the remaining inner shell layer. After mechanical cleaning, the shells were soaked in H_2O_2 (Merck KGaA, 64271 Darmstadt; Germany) for 1 h. All samples treated in this way were split into two batches, one of which was powdered using mortar and pestle ('the intact samples'), while the other batch was coarsely crushed and demineralized. Varied procedures have been described to achieve various degrees of demineralization and extraction of the organic matter [173]. Herein, shell pieces (after mechanical removal of the periostracum) was demineralized slowly in strong mineral acid (6N HCl, at 21±1^{o}C) while monitoring the *p*H and adjusting it gradually to a ca. *p*H 4 by adding Milli-Q water. After 24 hrs once the reaction was complete, the procedure was repeated between three to five times until decalcification was complete. Under this treatment some subset of the biomacromolecules aggregate/accumulate in a water-insoluble gel-like fraction that is collected, leaving in the aqueous fraction the acid or water-soluble organic matter, primarily low molecular weight and possible acid hydrolysis products, and some remaining shell fragments and some soluble proteinaceous material. The acid-insoluble organic fraction was

soaked in water overnight at 4˚C to remove any traces of water-soluble components and then lyophilized. For the *T. gigas* and *C. kingii* shells, essentially no insoluble gel was isolated after decalcification, and thus no extracts were available for further study. For all other shells these extracts would appear to contain the majority of the organic insoluble found in the intact shells. These we refer to below as water-insoluble acid extracts.

As a check on our ability to measure low levels of chitin in the bivalve shells and to measure chitin durability through the acid extraction procedure, commercially available chitin extracted from shrimps (Sigma-Aldrich) was mixed with finely ground geological aragonite (from the mineral collection of the Department of Earth and Planetary Sciences, Macquarie University) to produce 'model shell' mixtures containing 1, 5 and 10 wt% chitin, respectively. These mixtures were homogenised by dry centrifugation (at 14,500 rpm (20 min), followed by mixing with a laboratory mixer at 4^{o}C (3 h).

Solid-State NMR. MAS NMR spectra were acquired for all samples using ^{1}H-X **C**ross-**P**olarization (CP; X = ^{13}C, ^{31}P) and **D**irect **E**xcitation (DE).

Cross-**P**olarization (CP) transfers polarization from hydrogen atoms to nearby nuclei, e.g. ^{13}C or ^{31}P in this work, therefore enhancing their peak intensities when reside in hydrogen-rich environments, so yielding high S/N spectra. When combined with Magic-Angle Spinning (CP-MAS), both resolution and sensitivity are improved which significantly increase SSNMR applicability to nuclei with low natural abundances such as ^{13}C [169-171].

As the rates of polarization transfer may vary with differing chemical environments the peak intensities in such spectra do not simply reflect the relative abundance of the different chemical species. Of course, the matrix carbonate species which are distant from any organics and water containing H atoms will be absent from CP spectra. Under carefully chosen experimental conditions the DE technique may yield quantitative spectra (where the experimental repetition

delays are sufficiently long so that all species of ^{13}C are fully relaxed), however at the cost of lowered sensitivity (S/N) or, equivalently, a heavier investment of spectrometer time.

^{1}H, ^{13}C, ^{31}P NMR measurements were carried out on an *AVANCE III* (Bruker) spectrometer using a 4 mm triple-resonance MAS NMR probe with 4 mm zirconia rotors. Samples were spun at 5000 ± 2 Hz. Cross polarization (CP) magic angle spinning (MAS) echo experiments (CP being indirect excitation) were carried out with 5.0 μs π/2 and 10.0 μs π pulse widths, an echo interval τ (200 μs) identical to the rotor period T_R, a ^{1}H decoupling level of 100 kHz. Hartmann-Hahn rf levels were matched at 50 kHz, with contact times (ct) of 0.7- 2.0 ms for ^{13}C and 2 ms for ^{31}P; ^{13}C and ^{31}P CP MAS measurements employed relaxation delays of 3 and 4 s, respectively. Up to 16k transients were acquired, corresponding to approximately one day of spectrometer time in the case of low signal-to-noise samples.

Direct ^{13}C excitation echo experiments (DE) were carried out with a 5.0 μs π/2, a 10.0 μs π pulse widths, an echo interval τ equal to the rotor period T_R (200 μs), a ^{1}H decoupling level of 100 kHz, and a relaxation delay of 2400 s (2400 s to fully relaxed) for ^{13}C. Direct excitation ^{13}C spectra acquired with recycling delay of 2400 s yield fully relaxed spectra [171].

Saccharide analysis. To quantify neutral and aminated sugars, aliquots of the lyophilized samples of the acid-extracted water insoluble organic fraction were acid-hydrolyzed in 2 M trifluoroacetic acid (TFA) at 100°C for 4 h and 8 M HCl at 100°C for 6 h, respectively. In TFA neutral sugars are more readily hydrolyzed, while aminated sugars require stronger and longer hydrolytic condition [166, 174]. Samples were reduced to dryness under vacuum and the residue was re-dissolved by adding to 100 μM 2-deoxy-D-glucose in aqueous solution, the dissolved glucose serving as an internal standard. The sugar contents of the hydrolysates were determined on a high-performance anion-exchange chromatograph system with pulsed amperometric detection (HPAEC-PAD) fitted with a BioLC amino trap guard column (3 x 50 mm) connected to a CarboPac PA10 column (4 x 250 mm) (Dionex Corp., Sunnyvale, CA,

USA) held at 25°C. The cartridge was activated with sodium hydroxide solution passed at a flow-rate of 0.5mL/min. The analytes detected were quantified via an internal calibration which provides for the quantification of glucosamine, galactosamine, xylose, mannose, galactose, glucose and fucose under these conditions.

Fourier Transform Infrared Spectrometry (FTIR). FTIR analyses were recorded using a Thermo Nicolet iS10 ATR-FTIR spectrometer (Nicolet, MA, USA) equipped with a smart performer accessory between 4000 to 500 cm^{-1} in air with 64 accumulations and a resolution of 4 cm^{-1}. Background spectra were measured at the start of the analysis.

SEM imaging. Lyophilised samples were mounted on SEM sample holders and gold-coated using an EMITECH K550 sputter coater (Emitech Ltd, Ashford, UK). Scanning electron micrographs were taken with a JEOL JSM-7100F Field Emission Scanning Electron Microscope (FE-SEM) using an accelerating voltage of 10kV and a current of 75 µA.

3.3. RESULTS AND DISCUSSION

3.3.1. The inorganic matrix of the shells

In all seven shells crystalline aragonite is the dominant component, as demonstrated by the characteristic ^{13}C NMR peak found at 171.0 ppm ($\delta\nu$ = 0.3-0.5 ppm) in the fully relaxed ^{13}C DE quantitative [171] spectra of the 'intact samples' (**Figure 3.1**, Supplemental Data **Figure S3.1**). As the organic matter is present at only low abundance in these shells (ca. 1.65-4.2 wt%; [175]), its characteristic peaks are unobserved in the DE spectra, and its presence must be addressed by both other NMR excitation schemes as well as other spectroscopic techniques.

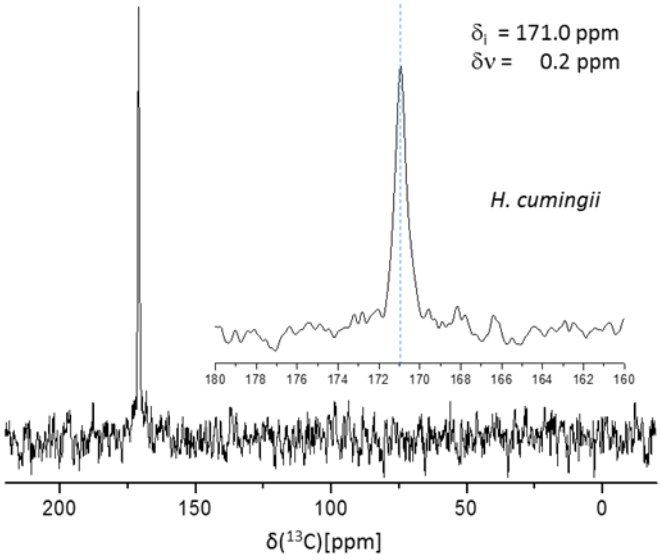

Figure 3.1: Representative 75.4 MHz ^{13}C DE MAS spectrum of the powdered shell ('intact sample') of *H. cumingii* showing the aragonitic carbonate peak as the only detectable component. Using a repetition delay of 2400 s makes the relative peak intensities in the DE spectra quantitative (fully relaxed conditions such that only a small underestimate of the carbonates is possible due to their long $^{13}C(T_1)$).[176] The narrowness of the lines reflects the uniformity of the local order throughout the lattice, as reflected in the narrow range of electronic environments giving rise to the observed carbonate chemical shifts.

3.3.2. The organic content of the shells: proteinaceous biomacromolecules

While the organic matter is a minor fraction of the total mass of the intact shells it can nonetheless be observed by SSNMR, even in the intact shell, (**Figure 3.2a**) by taking advantage of the ^{1}H atoms which are an intrinsic part of the bioorganics – small and high molecular weights alike. The cross-polarization magic angle spinning NMR technique, CP MAS, selects only those ^{13}C sites in close proximity to ^{1}H atoms for detection, and at significantly enhanced sensitivity [177]. As the only ^{1}H atoms in the intact shells are associated either with the organic matter, or are present as trapped water molecules largely associated with the organic matter, CP MAS spectra preferentially observes the ^{13}C sites in the organic matter and in interfacial carbonates nearby. While CP spectra are not precisely quantitative, the relative amounts of different organic materials within the aragonitic matrices may be estimated with some care, assuming the CP dynamics are similar throughout the sample [176].

The ^{13}C CP MAS spectra of all seven intact samples (**Figure 3.2**, left) are poorly resolved, which is hardly surprising given the inherent heterogeneity of the organic components (structural and compositional) of the shell. The advantage of the spectra of intact shells is that they represent all the ^{13}C-containing species found in the shell. Though individual peaks cannot be readily assigned and there are compositional differences from shell to shell, we can still suggest that the peak patterns are consistent with a mainly proteinaceous organic composition (left), in that there the vast majority of the resonances are found in either the carbonyl region (165-180 ppm) and the aliphatic region (15-75 ppm); there are weak absorbances in the phenyl ring region (120-150 ppm) which are consistent with a low abundance of Tyr (as the multiple chemical shifts associated with the partially substituted ring are all observed). Notably absent are the shifts associated with sugar rings, which most often appear as a set of lines in the chemical shift range from 60-110 ppm—many of which are poorly separated from the vast majority of the other spectral lines, but at least the anomeric carbons (90-100 ppm) should be well separated from the bulk; a reference spectrum of chitin is observed at the bottom right of **Figure 3.2**. There is (are) no obvious such peak(s) observed in any of the intact shells, which suggests that the concentration of chitin in these samples is quite low.

The nacreous shells contain the largest fraction of organic matter with similar distribution of amino acids,(SI Figure S3.2) while neither the crossed lamellar (*T. gigas* and *C. kingii*) or homogeneous (*A. islandica*) shells contain sufficient organic material to assign any ^{13}C shifts (other than the interfacial carbonates). The ^{13}C CPMAS intensities in these samples are 1/3 those of the nacreous shells, in agreement with the higher amounts of organic matter found in the latter [175].

3.3.3. Water-insoluble acid extracts: Proteins trapped in the shells

Finer characterization of the chemical details of the organic matter in the intact shells is hindered by the vast excess of inorganic (calcium) carbonate that comprises over 96 wt% of the

samples. Removal of the inorganic matrix enables us to concentrate the organic matter, leading to an increase in spectroscopic sensitivity and, as the extraction selects only a subset of the total organic component, to perhaps better characterize its structure and composition. These water-insoluble acid extracts (see Methods) were observed by CP MAS NMR after lyophilization. In each of the five shell extracts, the CP-MAS spectra (**Figure 3.2b**) show the anticipated improvement in sensitivity, and with the further advantage of improved resolution, which we associate with removal of a fraction of the very heterogeneous organic matter in the soluble fraction. The remainder yields NMR spectra similar to the untreated shells (**Figure 3.2a**), but due to the vast improvement in spectral quality it is more easily assigned to specific amino acids and secondary structures. The extracts have also been subjected to FTIR and, in some cases, amino acid analysis (see Supplemental Data, **Figure S3.2**).

Extracts from the nacreous shells appear quite similar both to one another and to silks found widely distributed in nature [178, 179]. In *H. cumingii* (Supplementary, **Figure S3.2**) we find that nearly half the amino acid residues in the acid-insoluble fraction are either Ala or Gly; the SSNMR spectrum reveals strong peaks at the chemical shifts appropriate to these amino acids with the additional information that these residues are found in *β*-pleated sheets (large peaks of Ala-C_β at 15-20 ppm, Ala-C_α at 49 ppm and Gly at 42 ppm). Similar identification might be provided by x-ray diffraction of silk fibers [180] where one should observe the characteristic *d*-spacings of 4.7 and 5.3Å.

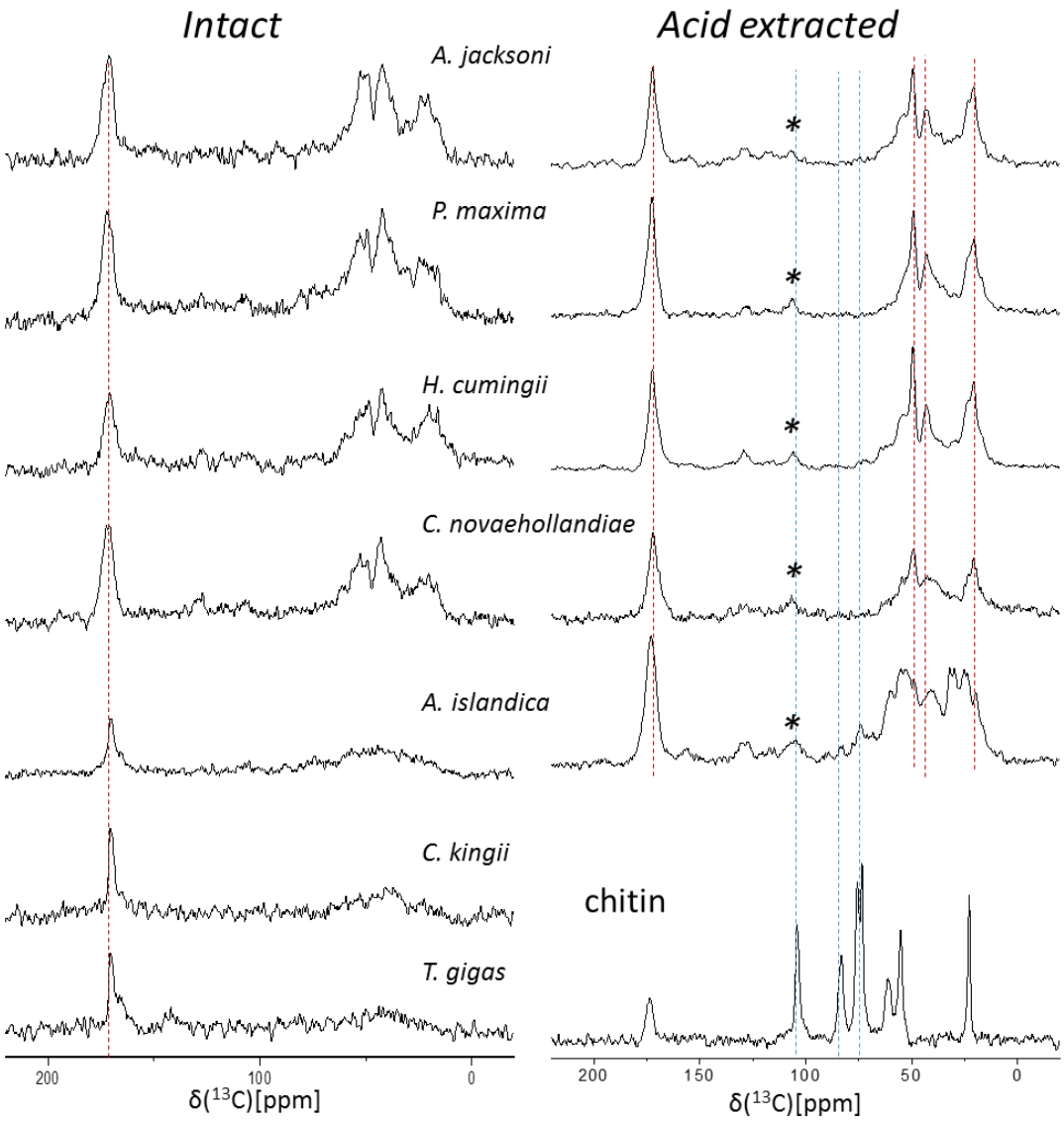

Figure 3.2: 75.4 MHz ^{13}C CP MAS spectra: a) intact samples (powdered shell), b) nacreous and homogeneous shells extracts (water insoluble acid extracts) and pure chitin as a reference. (a) The intact nacreous shells of *P. maxima*, *A. jacksoni*, *H. cumingii* and *C. novaehollandiae* show > 3-fold higher organic content than the other shells. The red line marks the chemical shift of aragonite carbonates. (b) The acid extracts exhibit a mostly proteinaceous content with the characteristic fingerprints of Ala and Gly rich silk-like fibrils in the nacreous, and collagen-like content in *A. islandica*. No significant peaks are detected that could be assigned to chitin or other polysaccharides, except for possibly in the *A. islandica* samples. The blue lines in (b) mark significant peaks in the NMR spectrum of chitin; the red lines are characteristic absorptions of Gly and Ala when found in *β*–pleated sheets. The spectra in (a) are normalized per sample weights and number of scans.

Based on amino acid abundances and the secondary structure information we associate the acid-insoluble fraction of the nacreous shells with a silk-like protein. In four out of five of the

samples we have analysed peaks that could be assigned to Tyr (which has a unique chemical shift signature including aromatic peaks at 119, 129 and 154 ppm) and which in silks typically appears in the more flexible spacers found between crystalline β-sheet units [181]. The aromatic Tyr peaks, which are well-removed from most other interfering chemical shifts, represent typically 4% (3.8% for *H. cumingii*) [175] or less of the amino acid residues in the acid-insoluble fraction, and therefore even less than 4% of the total organic matter. Nonetheless it is easily seen in three of the nacreous samples (*A. jacksoni*, *P. maxima*, *H. cumingii*) and at intensities. We contrast the ease of observation of Tyr in these samples with the significantly weaker signature of possible chitinous absorptions in these same samples. While all samples seem to exhibit a strong peak near 105 ppm which falls in the range of the anomeric ^{13}C shifts, this peak is an experimental artefact resulting from the mechanical rotation of the sample; this peak is a spinning sideband representing intensity borrowed from the carbonyl peaks near 175 ppm. So as to monitor possible chitin in the acid-insoluble fraction we instead prefer to look to the peaks near 73-76 and 83 ppm—which are unobserved in these samples.

In contrast, the shell of *A. islandica* shows little organic content in the intact shell and little or no hint of resolved peaks (**Figure 3.2a**). Once demineralized and separated from the soluble components, the macromolecular content is much better resolved, and neither does the amino acid composition nor the NMR spectrum suggest a significant concentration of silk (**Figure 3.2b**). Amino acid analyses of the isolatable macromolecules in the *A. islandica* shell reveal relatively high concentrations of proline, glycine and aspartate (ca 40%; SI Figure S3.2; [175]), a composition which is more reminiscent of collagen than of silk;[182] similarly, the SSNMR spectrum shows characteristic peaks as are seen in gelatin—a degraded form of collagen where partial hydrolysis and/or degradation of the secondary structure leads to increased heterogeneity of local environments, which is reflected in the NMR spectrum as increased linewidths in the spectrum [183]. Whether this heterogeneity is inherent, or a result of the processing details, is unclear.

Unlike in the nacreous extracts, in the acid-insoluble organic isolate from *A. islandica* shells we do observe weak peaks at 74 ppm and 83 ppm (**Figure 3.2b)** that might be assignable to chitin (while the remaining anticipated chitin chemical shifts are in spectral regions where the amino acids in the proteinaceous matter also appear)—although hydroxylproline, which is uniquely abundant in collagen, has a carbon line in the low seventies. Thus although we can not rule out a small fraction of chitin in this sample—again, the amplitudes of the sugar peaks (if such they are) are weaker than those of the Tyr in the proteinaceous fraction of the same sample. As the Tyr is, again found at less than 4% of the total amino acid content of the sample we can put a similarly low upper bound (< 1%) on the chitin content of the acid-insoluble isolate from *A. islandica* shells. Above we have suggested that the combination of amino acid abundances and the secondary structure described by chemical shifts of specific sites in amino acids can help define the classes of proteins found in the acid-insoluble fraction. Infrared spectroscopy and in particular the vibrational frequencies of the amide I (C=O stretching) and amide II (N-H in-phase bending and C-N stretching) modes are also diagnostic for secondary structure in proteins [184]. The FTIR spectra of the lyophilised water-insoluble acid extracts of the nacreous shells (*P. maxima, A. jacksoni, H. cumingii* and *C. novaeholladiae*) confirm high levels of β-sheet conformation. The amide I and amide II peaks at 1625 cm^{-1} and 1518 - 1522 cm^{-1} are consistent throughout the entire group (Figure 3.3, SI Figure S3.3) and are comparable to those found in silk, such as of *N. clavipes* native dragline silk [185]. These data are consistent with the ^{13}C CP MAS NMR spectra and further support our association of the dominant macromolecule in the acid-insoluble fraction with silk (Table S3.1) [186].

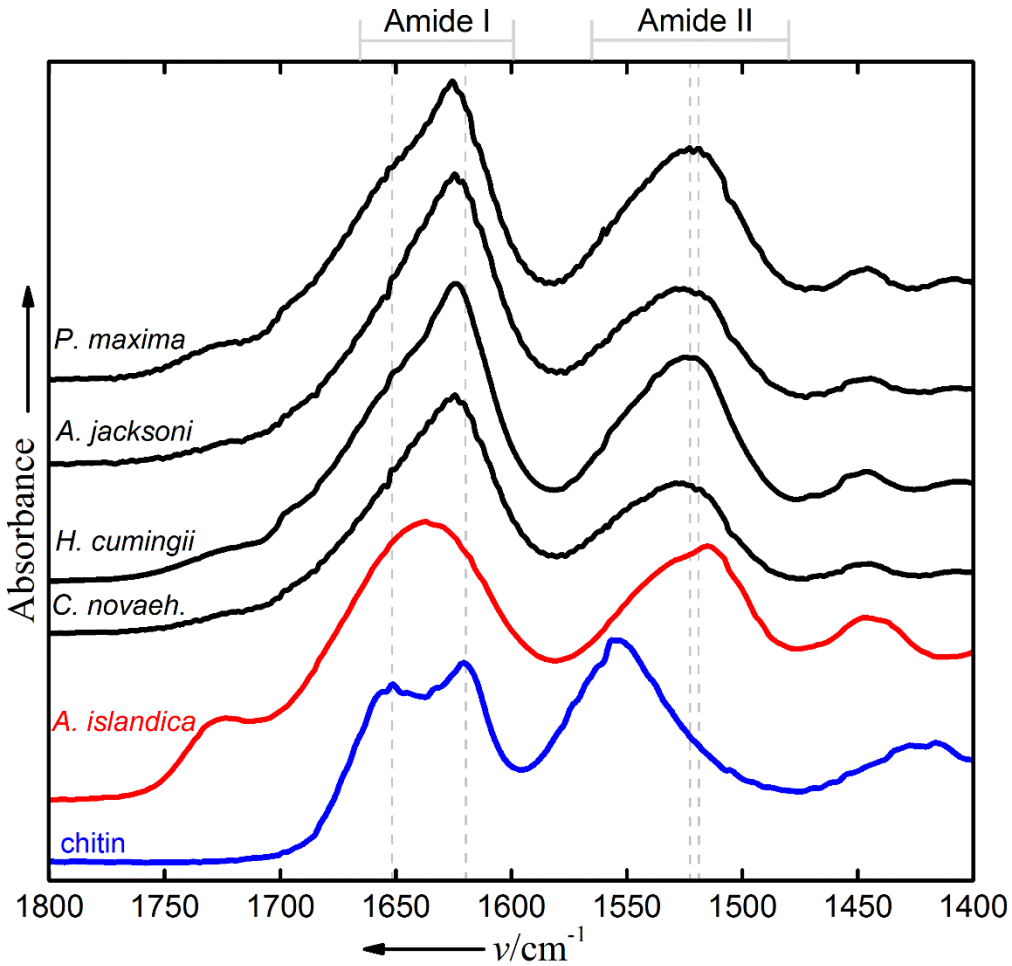

Figure 3.3: FTIR spectra of the shell extracts (acid extracted, water insoluble) and chitin reference. Shell extracts show characteristic absorptions of *β*–pleated sheets at 1625 cm^{-1} (amide I) and 1518, 1522 (amide II) for nacreous (black lines), and at 1638 cm^{-1} (amide I) and 1516 cm^{-1} (amide II) for homogeneous (*A. islandica*) shells. Chitin has α-helix structure shown by the amide I (1652 and 1620 cm^{-1}) and amide II (1556 cm^{-1}) bands. See Supplementary Information (Table S1) for peak assignment. The broader amide II peaks for shell extracts may indicate 'less crystalline' domains. NB: *C. novaeh.* Stands for *C. novaehollandiae*.

In *A. islandica*, we again find that amide I and II absorption peaks are instead shifted to 1638 cm^{-1} and 1516 cm^{-1} compared to those in the nacreous extracts (at 1625 and 1520 cm^{-1}, respectively) (**Figure 3.3**) which suggest a more significant helical component—as in, for example, collagen—than is found in the nacreous extracts. Typical amide I and II peaks in FTIR spectra of collagens appear at slightly higher ranges than observed here, namely at 1650-1660 cm^{-1} and at 1550-1560 cm^{-1} [187]. However the heterogeneity of organic matrix in the *A. islandica* shells or a result of the processing details—which would account for the broad lines observed by SSNMR—would account for the shift of the amide I peak to frequencies lowered

by as much as 30 cm^{-1}. The peak at around 1638 cm^{-1} is compatible with a left-handed collagen helix (probably type IV collagen) in the denatured state with bound water [187-189] (**Figure 3.3**; **SI Figure S3.3**) [190]. While the IR and NMR spectra clearly suggest that the biopolymers found in the shells of *A. islandica* differ from the nacreous shells, in neither class of shells is chitin detected, by either IR or NMR spectroscopy.

3.3.4. Morphology of the insoluble organic extracts

In the Field Emission Scanning Electron Microscopy (FE-SEM) the lyophilised water-insoluble acid extracts of the nacreous shells of *P. maxima, A. jacksoni, H. cumingii* and *C. novaehollandiae* reveal fiber-like patterns typical of silk-based fibers (**Figure 3.4a-d**) [102, 191]. These fibers have a fibrillar structure, but their morphology relatively varies from shell to shell: The fiber structures of *P. maxima* (Figure 3.4a) exhibit cross-sections of fine twisting filaments with smooth surface, while they contain levels of twisted hierarchy (**see SI Figure S4**) in *A. jacksoni* (**Figure 3.4b**). *H. cumingii* depicts filament-like structures (**Figure 3.4c**), and *C. novaehollandiae* shows fibrous layer of organic matrix (**Figure 3.4d**). The ability of arthropods to produce structural silk protein fibers is ancient [100, 101]. Due to the extraordinary mechanical performances, including extensibility, stiffness and high tensile strength [192, 193], silk fibroin fibers of dragline spider silk and Bombyx mori cocoon silk have been studied extensively [102-104]. Though only the latter contain sericin, all silk fibroin fibers are considered to be part of a family of common motif consisting of two phases: β-sheets crystalline and non-crystalline areas with amorphous domains characterised by the presence of amino acids with side chains [102, 103, 194].

In contrast, the organic extract of the *A. islandica* shell (**Figure 3.4e**) exhibits a net-like fibrous matrix, which is quite unlike the silk-like fibrous structure found in the nacreous shells (**Figure 3.4a-d**), but instead has a structural composition typical to chain interlocked network-forming collagen – type IV structure [195, 196]—neither of which resembles what is observed for similarly treated chitin (**Figure 3.4f**).

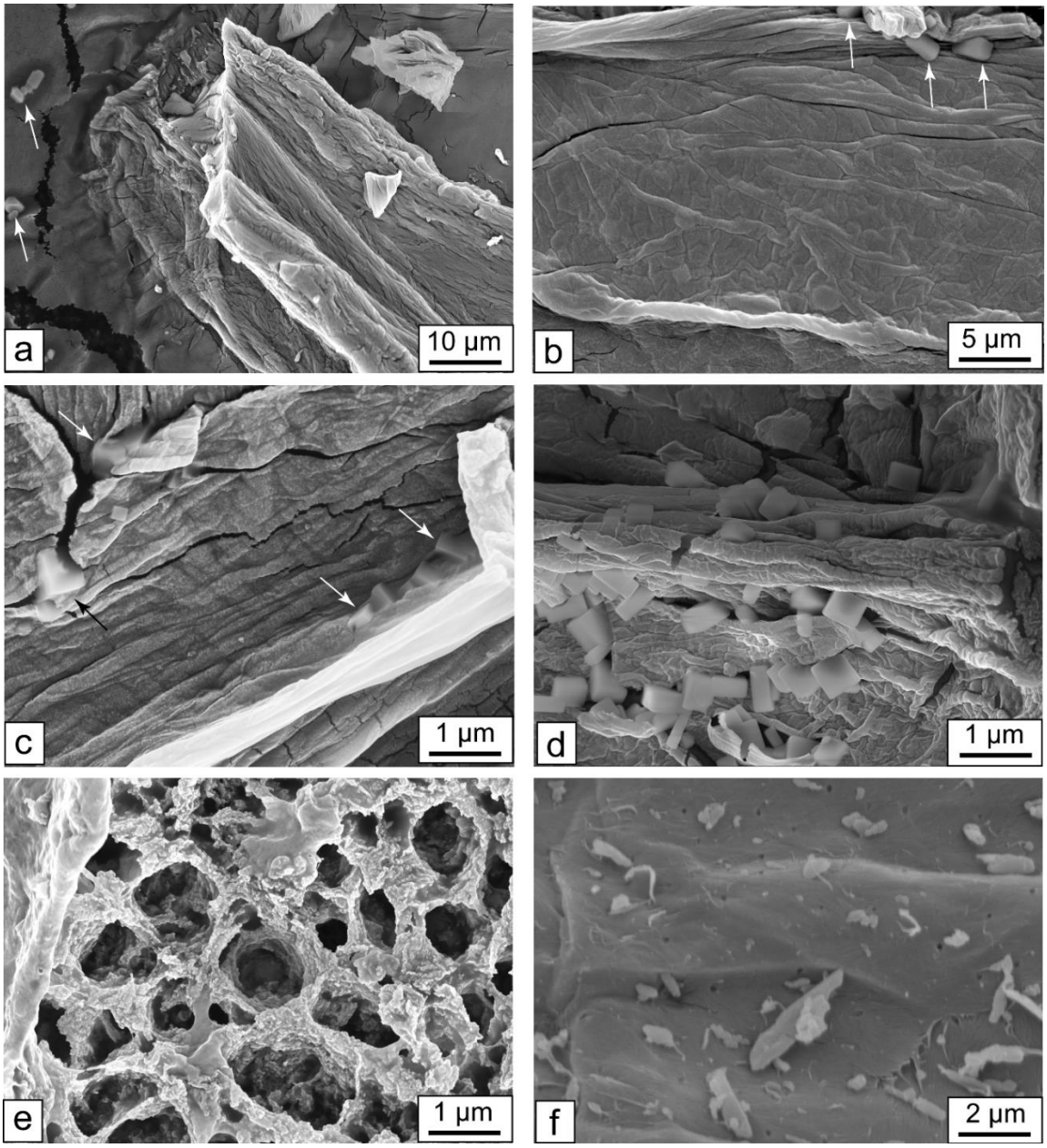

Figure 3.4: FE-SEM images of the acid insoluble lyophilized organic matrix in nacreous shells (a-d) depicting silk-like fibrils: a semi-amorphous regions (fibers) and angular nanocrystals (arrows) probably *β*-sheet crystalline. The nanocrytals are arranged within the fibers and along the cracks in (b) *Alathyria jacksoni*, (c) *Hyriopsis cumingii* and (d) *Cucumerunio novaehollandiae*. (a) *Pinctada maxima* fibers showing nanocrystals (arrows) not embedded within the fibers. (e) homogeneous *Arctica islandica* shell exhibits a net-like fibrous matrix. (f) Chitin reference treated identical to the shell samples shows a distinctly different morphology.

3.3.5. Abundance of Sugars in the shells (or, how much chitin is there in shells?)

^{13}C solid state NMR has previously been used to detect chitin in biominerals such as the brachiopod shells *Lingula anatina* and *Discinisca tenuis*[197] as well as in the gastroliths of the

fresh water crayfish *Cherax quadricarinatus* [176] and in the siliceous diatoms *Thalassiosira pseudonana* [198] The literature on shells returns repeatedly to suggest the importance of chitin and/or chitosan in shells, and therefore we assumed that these species might be straightforwardly observed as the ^{13}C spectrum is well-known and consists of a family of characteristic peaks in the spectral region between 55 and 105 ppm corresponding to the different carbon environments in the sugar rings, many of which are well-removed from the chemical shifts where most organic biomolecules are found (as well as other, less diagnostic peaks, such as at 15 ppm where the $–CH_3$ group on the chitin sidechain appears) (bottom right) **[199].** Were there chitin at detectable levels, each of the characteristic peaks should be observed (bottom right). In none of the intact shells in this study have we observed either chitin, or any other polysaccharide, by ^{13}C NMR. The solid state NMR sensitivity is sufficient to identify, conservatively, as low as 0.5 wt% of chitin in the intact shell and 3 wt% in the acid-insoluble extracts (Supplementary Figure S3.5, S3.6, spectra of chitin-spiked physical mixtures).

While the demineralization process involves harsh chemical treatment which might be suspected of degrading polysaccharides, the supporting information reports on our efforts to ‘‘demineralize’’ a physical mixture of chitin and aragonite–and found that chitin largely survives this study’s extraction procedure (See Supporting Information). Neither is there FTIR evidence (in the amide region) for detectable levels of chitin (**Figure 3.3**). As the total organic content is 4% or less, 3 wt% detection level of chitin in the extracts would correspond to observation of chitin in the shell if it is present at about 0.05 wt% in the worst case scenario that only 50% of the chitin is isolated in the acid-insoluble extract.

Lyophilised extracts after acid hydrolysis were analysed for both neutral and aminated sugars in the nacreous (*P. maxima, A. jacksoni* and *C. novaehollandiae*) and homogeneous (*A. islandica*) shells. As a saccharidic fraction of the total insoluble organic content, we found sugars comprised ≤ 0.59 wt% for acid-insoluble extracts from the nacreous shells yet ≤ 3.50

wt% for the acid extract from *A. islandica* (**Table 3.1**). In all our nacreous samples, glucosamine (the monomer which upon acetylation is the basis of chitin) constitutes the large majority of sugar moieties. Mannose is found at lower, but still significant, concentration. As chitin is normally a polymer of glucosamine, its abundance provides an upper bound to the fraction of chitin. As the maximum glucosamine content in the extracts of the nacreous shells is less than 0.43% the chitin content of the extract, and therefore of the total organic matrix in *nacreous shells* must be below 0.5 wt%.

The *A. islandica* shell is, again, significantly different from the nacreous shells presented above. Its amino acid abundances and NMR spectrum are quite distinct from the nacreous shells; its SEM suggests an entirely different morphological network in the organic extract, and the fraction of sugars in that is quite a bit higher. While the reported sugar content is dominated by glucosamine, this would not appear to be an indication of chitin in the sample. Nearly all the remainder of the reported sugar content is comprised of the otherwise unusual sugar-derivative, galactosamine. Based on the same data used to identify the biopolymer in the nacreous extracts as silk, we have identified the scaffolding material in *A. islandica* to be suggestive of collagen-like matter. Normally collagen is found to be glycosylated with a glucosylgalactose disaccharide at as much as a few percent of the amino acids; in the mesh networks formed by type IV heparin sulfates and keratanasulfates are standard accompaniments (see Figure 4e above) rather that the more typical fibrillar form [200, 201]. These sulfonated sugars are not quantified in ours assays; nonetheless, the unusual galactose abundance and higher sugar content in *A. islandica* shells appears associated with the standard biochemistry of collagen—and not a marker for chitin.

Thus while the saccharide analysis shows clear differences in abundance and composition between the nacreous shells and homogeneous shell, in none of these shell samples is the sugar abundance high, neither is there convincing evidence for chitin. While there may well be

additional sugars in the acid-soluble or water-soluble extracts, these too would seem unlikely to contain polysaccharides. We therefore conclude that in these shell samples the abundance of chitin is beneath our detectable limits, which we conservatively estimate at less than 0.5% of the mass of the organic matter.

Table 3.1

Monosaccharide composition of water insoluble acid extracts of the shells.

Monosaccharide	*A. islandica*		*C. novaehollandiae*		*A. jacksoni*		*P. maxima*	
	ng/mg	%	ng/mg	%	ng/mg	%	ng/mg	%
Galactosamine	11692	34.0	246	5.7	585	9.9	49	1.4
Glucosamine	21216	61.6	3097	71.9	4339	73.5	2754	77.3
Fucose	TR	-	40	0.9	120	2.3	50	1.4
Galactose	1273	3.7	135	3.1	186	3.2	86	2.4
Xylose	235	0.7	279	6.5	175	3.0	135	3.8
Mannose	TR	-	512	11.9	495	8.4	488	13.7
Glucose	TR	-	TR	-	TR	-	TR	-
Total	34416	100.0	4309	100	5900	100.0	3562	100.0
Total %	3.44%		0.43%		0.59%		0.36%	

The values are presented in ng/mg of total acid-extracted matrix and percentage of identified sugar compounds from within all saccharides. Total % denotes wt% of all saccharides (aminated and neutral) within the acid-extracted organics. The *H. cumingii* acid extract yielded too little sample to determine the saccharide.

3.3.6. Phosphorous content - ^{31}P CP MAS NMR

^{31}P NMR studies have demonstrated that phosphorous can be post-translationally incorporated into silk fibers, though there is no consensus on the role of any such transformation. However, the strong affinity between phosphate groups and divalent cations, such as Ca^{2+}, lead to the expectation of their structural significance [202]. This expectation is strengthened by the recent observation that in the absence of Ca^{2+} the caddisfly silk β-sheet formation is suppressed [203].

Figure 3.5 shows the ^{31}P CP MAS NMR spectra of three intact nacreous shells *H. cumingii*, *A. jacksoni* and *C. novaehollandiae*, demonstrating that there is a measurable phosphorous content at a consistent chemical shift of 3.7 ppm. We estimate that the *H. cumingii* yields 2-3 times the concentration of P/gram as is found in the *C. novaehollandiae* or *A. jacksoni* shells.

The absence of ^{31}P CP MAS peaks in the spectra of the other four shells rules out similar levels of phosphate occurrence. The evidence for the phosphate content in two of the extracts (*H. cumingii* and *A. jacksoni*) suggests it is a part of the insoluble proteinaceous content. The role or identity of phosphorous in these materials is unclear, although, it has previously been demonstrated that a small fraction of either Ser or Tyr residues in *N. clavipes* major ampullate gland spider silk is phosphorylated[178] and that the resulting solids NMR spectrum observed under similar conditions has an isotropic chemical shift of σ_{iso}= 0.6 ppm. This position of the peak is sensitive to local pH additional to the specific molecular identity.

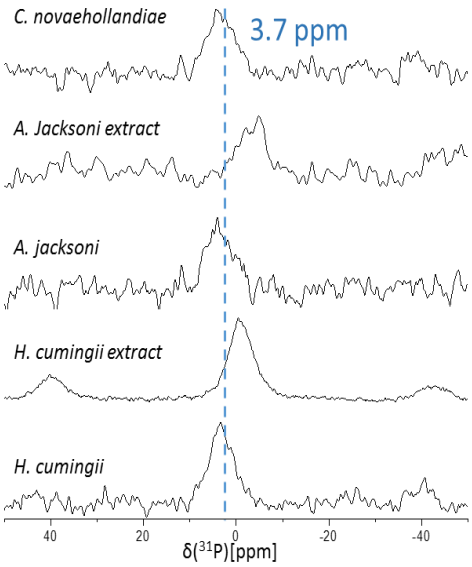

Figure 3.5: 121.4 MHz ^{31}P CP MAS of *H. cumingii* and *A. jacksoni* intact shell and shell extracts and *C. novaehollandiae* intact samples. Significant phosphorous contents exist in these shells, however, it is affected by treatment. No phosphorous content was observed in *C. novaehollandiae* acid extract.

The significant changes to the phosphorous chemical shift after acid extraction treatment, may be the result of the reduced *p*H and of different cation coordination environments. Nonetheless the implications of phosphorylation in calcification clearly depends strongly on the specific system and remains to be more fully explored.

3.3.7. Periostracum organic content - ^{13}C CP MAS NMR

We close our discussion of the experimental results with a brief review of our studies of the periostractum found on the surface of many of our shells. Mature periostracum, the outermost layered architectural pattern common to many bivalve shells, consists of insoluble biopolymers [204] and seems to play a critical role both in the growth and maintenance of the calcareous exoskeleton. It is formed in a specific section of the bivalve epithelial cells and provides the substrate onto which the mineralized part of the shell is deposited; once the shell has grown, it prevents decalcification and mechanical damage to that shell [204]. This structure is an example of a scleroprotein and has been presumed to be cross-linked with variable amounts of chitin,[93, 95] and relatively high concentration of aspartic acid [2]. The high proportion of aspartic acid suggests that mature periostracum also contains shell proteins [2, 205], some of which are characteristically rich in aspartic acid [81, 206, 207].

Periostracum samples were mechanically separated from the shell in the nacreous species *H. cumingii*, *A. jacksoni* and *C. novaehollandiae*. Figure 3.6 represents the ^{13}C CP MAS NMR spectra of each. The spectra are remarkably similar to one another, in that each is dominated by the proteinaceous motif where Gly (43 ppm) and Tyr (see the intense peaks at 36, 54, 119 129, and 156 ppm) amino acids are most abundant--as has previously been found for multiple species [208]. FTIR spectra of the periostracum also suggest the presence of β–pleated sheets (**SI Figure S3.7**).

In none of the three periostracum samples studied is there any definitive suggestion of chitin, although in *A. jacksoni* periostracum, peaks at 71 and 88 ppm may hint at the presence of saccharides (yet not chitin). Recurring peaks, which have not been assigned, appear at 136, 30 and 25 ppm; the latter two appear in valine and isoleucine, but need not necessarily derive from amino acids at all. In these studies we have found no chitin in the periostracum at detectable

levels, which, given the excellent signal to noise ratios, suggests that the chitin content of the periostracum, is (again) less than 0.5 wt%, and possibly much lower.

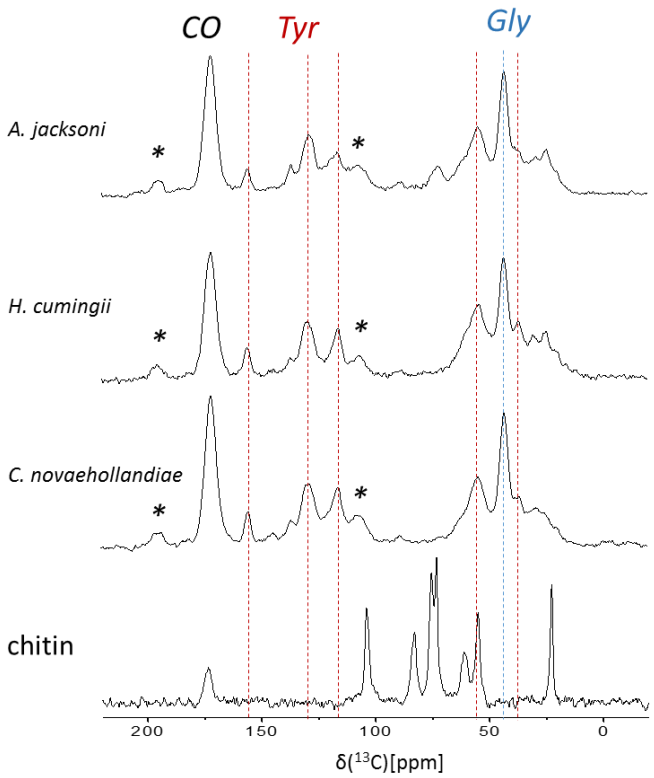

Figure 3.6: 75.4 MHz ^{13}C CP MAS periostracum of nacreous shell. All samples exhibit general pattern of proteinaceous organic content dominated by Gly and Tyr. Spinning sidebands are labelled by *. Repetition delay 3s, ct = 1 ms for all samples.

3.4. Conclusions

Solid state MAS NMR spectroscopy was applied to seven bivalve shells with three types of structures: nacreous, homogeneous and crossed lamellar, as well as to the water-insoluble acid extracts of the homogeneous and nacreous shells, and to periostracum samples from three nacreous samples. The NMR spectra expose selectively (CP MAS) the bioorganic content in the shells, hence reporting 3-fold higher mol% of organics in the nacreous vs. either the homogeneous or the crossed lamellar shells, consistent with our TGA analysis [128, 175]. The higher abundance of bioorganics in the nacreous shells allows us to determine that the bioorganic content is primarily proteinaceous.

The NMR signature of the bioorganic content within the nacreous shells studied herein, particularly after isolation via demineralization, suggests a significant fraction of macromolecular proteinaceous content dominated in abundance by the simplest amino acids, Ala and Gly. In the extracts the chemical shifts found for the Ala and Gly carbon atoms identify their local environment as extended β-pleated sheets, one of the hallmarks of the important structural protein, which is called silk. SEM imaging of the recovered gel-like material in these samples are strikingly reminiscent of silk fibers. Despite the low bioorganic content in the shell of *A. islandica*, its extract clearly showed proteinaceous content that is not characteristic of silk-like proteins, different to that identified for the nacreous shells. Its content, as reflected by the NMR and the amino acid analysis is richer in Gly, Pro, Asp, apparently compositionally closer to collagen-like, yet not distinctively characteristic of collagen *sensu stricto*. The crossed lamellar shells (*T. gigas* and *C. kingii*) contain less total organic matter and in a form which is not easily characterized with our analytical tools. In none of the intact shells, nor in the extracts studied, have we found indisputable evidence for abundant polysaccharides, and those that we have demonstrated using a well-established anion-exchange assay, occur at quite low abundances (**Table 3.1**).

While abundance is not necessarily a surrogate for importance, most models which attempt to explain the development of shells would appear to assign chitin a role which the small amounts we find seem unlikely to support, and to assign the silk-based fibers which dominate the organic matter in nacre shells lesser roles.[89] The silk fibers feature a hierarchical architecture where highly organised, extensively hydrogen-bonded β-sheet nanocrystals are arranged within a semi-amorphous protein in analogy to the spider dragline silk **(Figure 3.7)** [178, 209-211]. As the chemical palette available to form silk-like materials includes many more building blocks (the 20 naturally occurring amino acids) we believe it is worth reconsidering the relative importance of the available biopolymers which assist in the templating and growth of the carbonate-based inorganic matrix in these shells. While it may

certainly be advantageous to exploit available saccharides in the organic matrix, these appear to be present in concentrations not necessarily significantly higher than, for example, phosphates post-translationally inserted into the silk-like fibers. The apparent mismatch between abundance of protein and saccharide moieties found vs. the prevailing model [89] seems to us to suggest that a the experimental evidence tying calcification to chitin in these systems might be usefully reconsidered.

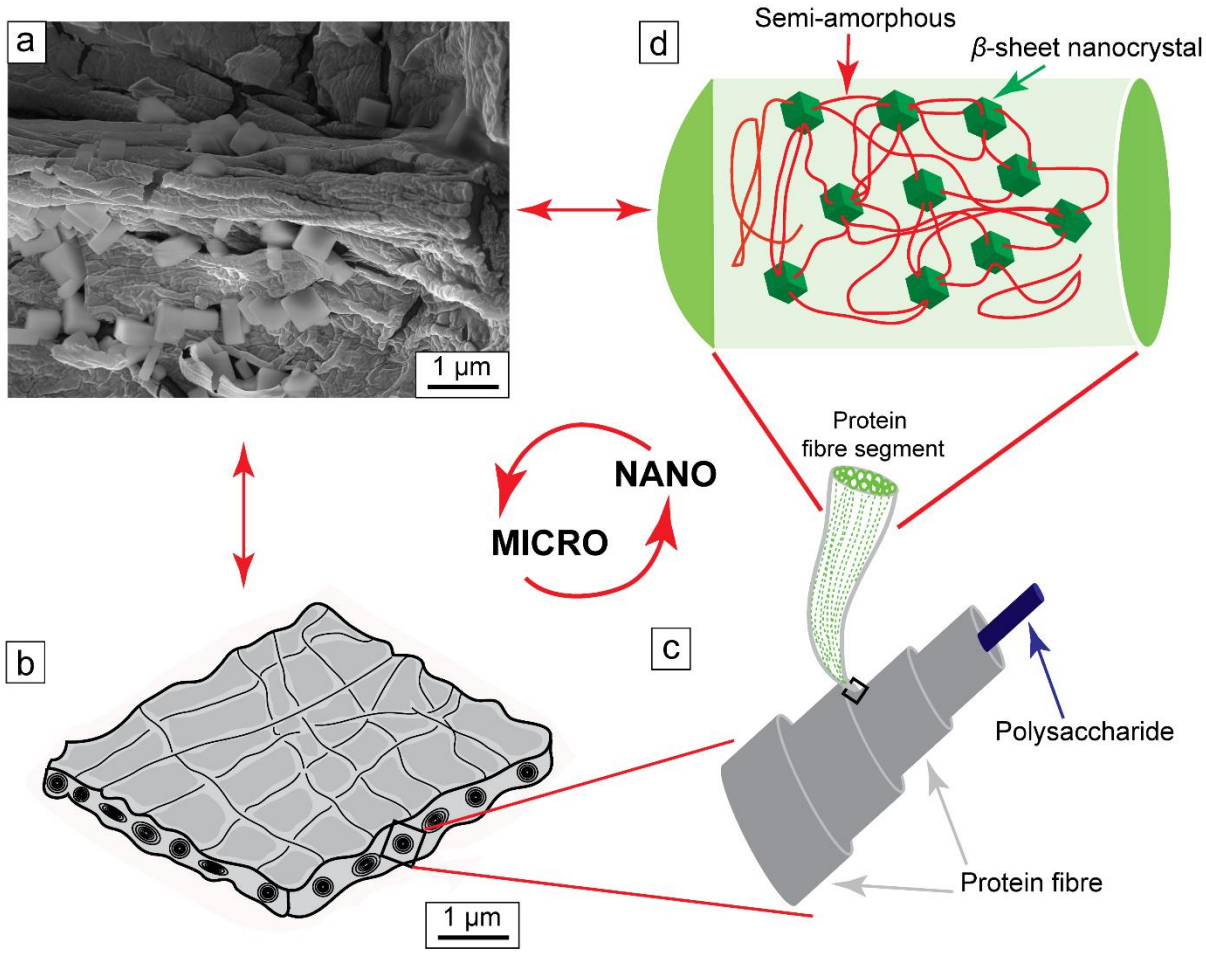

Figure 3.7 : SEM image (a) and schematic diagrams (b, c and d) showing the fibroin fibre. a) shows a representative (*Cucumerunio novaehollandiae*) insoluble organic matrix exhibiting a semi-amorphous regions (fibres) and nanocrystals (propably *β*-sheet crystalline) along the organic cracks. b) Microstructure of three-dimensional organic matrix (the interlamellar sheets) includes fibrous matrix with the long semi-amorphous fibres and crystallites. c) shows the detail of organic matrix ultrastructure. This consists a core polysaccharide within protein-based fibres. Note the protein fibrils segments (green) within protein fibre segment. Polysaccharide is presume as a result of saccharidic composition. d) Cartoon of the proposed model for the molecular arrangement showing a continuous network of semi-amorphous chains cross-linked with the stiff nanocrystals, typical of dragline spider silk.

Our single example of a shell with homogeneous structure (*A. islandica*) clearly shows proteinaceous content that is quite compositionally and morphologically quite different from the silk-like structural proteins found in nacreous samples. Its unusual net-like fibrous architecture as observed by SEM (**Figure 3.4**) requires further study. While compositional variability has already been recognized for the soluble, nacre-forming organic constituents in shells,[59, 79] the remarkable diversity of biomineralization strategies employed in nature may not be amenable to a single unifying description.

These studies have been unable to identify any significant amounts of chitin in shells; neither in the intact samples, the acid-insoluble extracts, or in the periostracum. Assays for sugar content suggest that in most of our shells the sugars are present at less than 0.6% by mass of the total organic content, which itself is typically no more than a few percent of the total shell mass. In particular, neither the shell-associated proteins which appear silk- or collagen-like, nor the samples of intact periostracum composed primarily of a Tyr- and Gly- rich protein, is there evidence for commingled chitin. As this scleroprotein has been presumed to be cross-linked with variable amounts of chitin [93, 95], and to be implicated in the nucleation and growth of the extracellular mineralisation [2], our observations strongly suggest that the structural role of polyamino acids via cooperative hydrogen bonding in support of biomineralization has been underestimated.

Acknowledgements We appreciate the effort of Fei Chi for handling sugar analysis. The work was facilitated in part by the Australian Government's National Collaborative Research Strategy (NCRIS) and its facilities at the Australian Proteome Analysis Facility (APAF).

3.5. References

1. Jackson, A., J. Vincent, and R. Turner, *The mechanical design of nacre.* Proceedings of the Royal Society of London. Series B. Biological Sciences, 1988. **234**(1277): p. 415-440.
2. Sarikaya, M. and I.A. Aksay, *Biomimetics. Design and Processing of Materials*. 1995, Washinton Univ Seattle Dept of Materials Science and Engineering.
3. Lowenstam, H.A. and S. Weiner, *On biomineralization*. 1989: Oxford University Press.

4. Mann, S., *Biomineralization: principles and concepts in bioinorganic materials chemistry*. Vol. 5. 2001: Oxford University Press.
5. Song, F., A. Soh, and Y. Bai, *Structural and mechanical properties of the organic matrix layers of nacre.* Biomaterials, 2003. **24**(20): p. 3623-3631.
6. Currey, J.D., et al., *Mechanical properties of nacre and highly mineralized bone.* Proceedings of the Royal Society of London B: Biological Sciences, 2001. **268**(1462): p. 107-111.
7. Weiner, S. and W. Traub, *X-ray diffraction study of the insoluble organic matrix of mollusk shells.* FEBS letters, 1980. **111**(2): p. 311-316.
8. Naleway, S.E., et al., *Structural design elements in biological materials: application to bioinspiration.* Advanced Materials, 2015. **27**(37): p. 5455-5476.
9. Raven, P.H., et al., *Biology.* Boston; McGraw-Hill, 2002: p. 35-58.
10. Hackman, R., *Studies on chitin IV. The occurrence of complexes in which chitin and protein are covalently linked.* Australian Journal of Biological Sciences, 1960. **13**(4): p. 568-577.
11. Dauphin, Y. and F. Marin, *The compositional analysis of recent cephalopod shell carbohydrates by Fourier transform infrared spectrometry and high performance anion exchange-pulsed amperometric detection.* Experientia, 1995. **51**(3): p. 278-283.
12. Ehrlich, H., et al., *Discovery of 505-million-year old chitin in the basal demosponge Vauxia gracilenta.* Scientific Reports, 2013. **3**: p. 3497.
13. Davies, G.J., D.P. Knight, and F. Vollrath, *Chitin in the silk gland ducts of the spider Nephila edulis and the silkworm Bombyx mori.* PLoS One, 2013. **8**(8): p. e73225.
14. Levi-Kalisman, Y., et al., *Structure of the nacreous organic matrix of a bivalve mollusk shell examined in the hydrated state using cryo-TEM.* Journal of Structural Biology, 2001. **135**(1): p. 8-17.
15. Osuna-Mascaró, A.J., et al., *Ultrastructure of the Interlamellar Membranes of the Nacre of the Bivalve Pteria hirundo, Determined by Immunolabelling.* PLoS One, 2015. **10**(4): p. e0122934.
16. Pereira-Mouriès, L., et al., *Soluble silk-like organic matrix in the nacreous layer of the bivalve Pinctada maxima.* European Journal of Biochemistry, 2002. **269**(20): p. 4994-5003.
17. Gotliv, B.A., et al., *Asprich: A novel aspartic acid-rich protein family from the prismatic shell matrix of the bivalve Atrina rigida.* ChemBioChem, 2005. **6**(2): p. 304-314.
18. Marin, F., et al., *Organic matrices in metazoan calcium carbonate skeletons: Composition, functions, evolution.* Journal of Structural Biology, 2016. **196**(2): p. 98-106.
19. Tsukamoto, D., I. Sarashina, and K. Endo, *Structure and expression of an unusually acidic matrix protein of pearl oyster shells.* Biochemical and Biophysical Research Communications, 2004. **320**(4): p. 1175-1180.
20. Goffinet, G. and C. Jeuniaux, *Distribution et importance quantitative de la chitine dans les coquilles de mollusques.* Cahiers de Biologie Marine, 1979. **20**: p. 341-349.
21. Weiss, I.M., et al., *A simple and reliable method for the determination and localization of chitin in abalone nacre.* Chemistry of Materials, 2002. **14**(8): p. 3252-3259.
22. Cartwright, J.H. and A.G. Checa, *The dynamics of nacre self-assembly.* Journal of the Royal Society Interface, 2007. **4**(14): p. 491-504.
23. Suzuki, M. and H. Nagasawa, *Mollusk shell structures and their formation mechanism 1.* Canadian Journal of Zoology, 2013. **91**(6): p. 349-366.
24. Furuhashi, T., et al., *Molluscan shell evolution with review of shell calcification hypothesis.* Comparative Biochemistry and Physiology Part B: Biochemistry and Molecular Biology, 2009. **154**(3): p. 351-371.
25. Hu, Y.-Y., A. Rawal, and K. Schmidt-Rohr, *Strongly bound citrate stabilizes the apatite nanocrystals in bone.* Proceedings of the National Academy of Sciences, 2010. **107**(52): p. 22425-22429.
26. Martin, R.W. and K.W. Zilm, *Preparation of protein nanocrystals and their characterization by solid state NMR.* Journal of Magnetic Resonance, 2003. **165**(1): p. 162-174.
27. Ben Shir, I., et al., *Exposed and buried biomineral interfaces in the aragonitic shell of Perna canaliculus revealed by solid-state NMR.* Chemistry of Materials, 2013. **25**(22): p. 4595-4602.

28. Nassif, N., et al., *Amorphous layer around aragonite platelets in nacre.* Proceedings of the National Academy of Sciences of the United States of America, 2005. **102**(36): p. 12653-12655.
29. Carter, J.G., *Skeletal biomineralization: patterns, processes and evolutionary trends*. Vol. 1. 1990: Wiley Online Library.
30. Kobayashi, I. and T. Samata, *Bivalve shell structure and organic matrix.* Materials Science and Engineering: C, 2006. **26**(4): p. 692-698.
31. Boggild, O.B., *The shell structure of the mollusks.* Det Kongelige Danske Videnskabernes Selskabs Skrifter, Natruvidenskabelig og Mathematisk, Afdeling, Ser. 9, 1930. **2**: p. 231-326.
32. Kamat, S., et al., *Structural basis for the fracture toughness of the shell of the conch Strombus gigas.* Nature, 2000. **405**(6790): p. 1036-1040.
33. Agbaje, O., et al., *Architecture of crossed-lamellar bivalve shells: the southern giant clam (Tridacna derasa, Röding, 1798).* Open Science, 2017. **4**(9): p. 170622.
34. Younes, I. and M. Rinaudo, *Chitin and chitosan preparation from marine sources. Structure, properties and applications.* Marine Drugs, 2015. **13**(3): p. 1133-1174.
35. Honda, S., *High-performance liquid chromatography of mono-and oligosaccharides.* Analytical Biochemistry, 1984. **140**(1): p. 1-47.
36. Agbaje, O.B.A., et al., *Organic macromolecules in shells of Arctica islandica: comparison with nacroprismatic bivalve shells.* Marine Biology, 2017. **164**: p. 208.
37. Akiva-Tal, A., et al., *In situ molecular NMR picture of bioavailable calcium stabilized as amorphous CaCO3 biomineral in crayfish gastroliths.* Proceedings of the National Academy of Sciences, 2011. **108**(36): p. 14763-14768.
38. Ben Shir, I., et al., *Molecular Level Characterization of the Inorganic− Bioorganic Interface by Solid State NMR: Alanine on a Silica Surface, a Case Study.* The Journal of Physical Chemistry B, 2010. **114**(18): p. 5989-5996.
39. Hijirida, D.H., et al., *13C NMR of Nephila clavipes major ampullate silk gland.* Biophysical Journal, 1996. **71**(6): p. 3442-3447.
40. Simmons, A., E. Ray, and L.W. Jelinski, *Solid-state 13C NMR of Nephila clavipes dragline silk establishes structure and identity of crystalline regions.* Macromolecules, 1994. **27**(18): p. 5235-5237.
41. Slotta, U., et al., *Spider silk and amyloid fibrils: a structural comparison.* Macromolecular Bioscience, 2007. **7**(2): p. 183-188.
42. Izdebski, T., et al., *Structure and dynamics of aromatic residues in spider silk: 2D carbon correlation NMR of dragline fibers.* Biomacromolecules, 2009. **11**(1): p. 168-174.
43. Shoji, A., et al., *Conformational characterization of solid polypeptides by carbon-13 NMR recorded by the cross polarization-magic angle spinning method: conformation-dependent carbon-13 chemical shifts of oligo-and poly (γ-benzyl L-glutamates) and sequential copolymers of γ-benzyl and γ-methyl L-glutamates and qualitative evaluation of side-chain orientation.* Macromolecules, 1984. **17**(8): p. 1472-1479.
44. Aliev, A.E., *Solid-state NMR studies of collagen-based parchments and gelatin.* Biopolymers, 2005. **77**(4): p. 230-245.
45. Haris, P.I. and D. Chapman, *The conformational analysis of peptides using Fourier transform IR spectroscopy.* Biopolymers, 1995. **37**(4): p. 251-263.
46. Paquet-Mercier, F., et al., *Evidence by infrared spectroscopy of the presence of two types of β-sheets in major ampullate spider silk and silkworm silk.* Soft Matter, 2013. **9**(1): p. 208-215.
47. Boulet-Audet, M., F. Vollrath, and C. Holland, *Identification and classification of silks using infrared spectroscopy.* Journal of Experimental Biology, 2015. **218**(19): p. 3138-3149.
48. Payne, K. and A. Veis, *Fourier transform IR spectroscopy of collagen and gelatin solutions: deconvolution of the amide I band for conformational studies.* Biopolymers, 1988. **27**(11): p. 1749-1760.
49. Ozaki, Y., A. Mizuno, and F. Kaneuchi, *Structural differences between type I and type IV collagen in biological tissues studied in vivo by attenuated total reflection/Fourier transform infrared spectroscopy.* Applied Spectroscopy, 1992. **46**(4): p. 626-630.

50. Rabotyagova, O.S., P. Cebe, and D.L. Kaplan, *Collagen structural hierarchy and susceptibility to degradation by ultraviolet radiation.* Materials Science and Engineering: C, 2008. **28**(8): p. 1420-1429.
51. Chirgadze, Y.N., O. Fedorov, and N. Trushina, *Estimation of amino acid residue side-chain absorption in the infrared spectra of protein solutions in heavy water.* Biopolymers, 1975. **14**(4): p. 679-694.
52. Trancik, J., et al., *Nanostructural features of a spider dragline silk as revealed by electron and X-ray diffraction studies.* Polymer, 2006. **47**(15): p. 5633-5642.
53. Lewin, M. and E.M. Pearce, *Handbook of Fiber Chemistry, Revised and Expanded*. 1998: Crc press.
54. Scott, H., *A new East African Species of Urodon (Coleoptera) bred from Gladiolus, with Notes on the Biology of the Genus.* Entomologist's Monthly Magazine, 1930.
55. Trogus, C. and K. Hess, *Studies on Natural Silk and Its Behavior with Acids and Alkalies.* Biochem. Z, 1933. **260**: p. 376.
56. Cranford, S.W., et al., *Nonlinear material behaviour of spider silk yields robust webs.* Nature, 2012. **482**(7383): p. 72-76.
57. Nova, A., et al., *Molecular and nanostructural mechanisms of deformation, strength and toughness of spider silk fibrils.* Nano Letters, 2010. **10**(7): p. 2626-2634.
58. Simmons, A.H., C.A. Michal, and L.W. Jelinski, *Molecular orientation and two-component nature of the crystalline fraction of spider dragline silk.* Science, 1996: p. 84-87.
59. Rousseau, M.-E., et al., *Study of protein conformation and orientation in silkworm and spider silk fibers using Raman microspectroscopy.* Biomacromolecules, 2004. **5**(6): p. 2247-2257.
60. Byrom, D., *Biomaterials: novel materials from biological sources*. 1991: Springer.
61. Nakazata, K., et al., *Gelation of the lens capsule type IV collagen solution at a neutral pH.* The Journal of Biochemistry, 1996. **120**(5): p. 889-894.
62. Yurchenco, P.D. and G. Ruben, *Type IV collagen lateral associations in the EHS tumor matrix. Comparison with amniotic and in vitro networks.* The American Journal of Pathology, 1988. **132**(2): p. 278.
63. Neary, M.T., et al., *Contrasts between organic participation in apatite biomineralization in brachiopod shell and vertebrate bone identified by nuclear magnetic resonance spectroscopy.* Journal of the Royal Society Interface, 2011. **8**(55): p. 282-288.
64. Brunner, E., et al., *Chitin-based organic networks: an integral part of cell wall biosilica in the diatom Thalassiosira pseudonana.* Angewandte Chemie International Edition, 2009. **48**(51): p. 9724-9727.
65. Heux, L., et al., *Solid state NMR for determination of degree of acetylation of chitin and chitosan.* Biomacromolecules, 2000. **1**(4): p. 746-751.
66. Sage, H., R.G. Woodbury, and P. Bornstein, *Structural studies on human type IV collagen.* Journal of Biological Chemistry, 1979. **254**(19): p. 9893-9900.
67. Sage, H. and P. Bornstein, *Characterization of a novel collagen chain in human placenta and its relation to AB collagen.* Biochemistry, 1979. **18**(17): p. 3815-3822.
68. Michal, C.A., et al., *Presence of phosphorus in Nephila clavipes dragline silk.* Biophysical Journal, 1996. **70**(1): p. 489-493.
69. Addison, J.B., et al., *Reversible assembly of β-sheet nanocrystals within caddisfly silk.* Biomacromolecules, 2014. **15**(4): p. 1269-1275.
70. Checa, A., *A new model for periostracum and shell formation in Unionidae (Bivalvia, Mollusca).* Tissue and Cell, 2000. **32**(5): p. 405-416.
71. Peters, W., *Occurrence of chitin in Mollusca.* Comparative Biochemistry and Physiology Part B: Comparative Biochemistry, 1972. **41**(3): p. 541-550.
72. Waite, J., *Quinone-tanned scleroproteins.* The mollusca, 1983. **1**: p. 467-504.
73. Gotliv, B.A., L. Addadi, and S. Weiner, *Mollusk shell acidic proteins: in search of individual functions.* ChemBioChem, 2003. **4**(6): p. 522-529.
74. Weiner, S., *Aspartic acid-rich proteins: major components of the soluble organic matrix of mollusk shells.* Calcified Tissue International, 1979. **29**(1): p. 163-167.

75. Weiss, I.M., et al., *The chitin synthase involved in marine bivalve mollusk shell formation contains a myosin domain.* FEBS letters, 2006. **580**(7): p. 1846-1852.
76. Hunt, S., *Amino acid compositions of periostracal proteins from molluscs living in the vicinity of deep sea hydrothermal vents: an unusual methionine-rich structural protein.* Comparative Biochemistry and Physiology Part B: Comparative Biochemistry, 1987. **88**(3): p. 1013-1021.
77. Keten, S., et al., *Nanoconfinement controls stiffness, strength and mechanical toughness of [beta]-sheet crystals in silk.* Nature Materials, 2010. **9**(4): p. 359-367.
78. Seidel, A., O. Liivak, and L.W. Jelinski, *Artificial spinning of spider silk.* Macromolecules, 1998. **31**(19): p. 6733-6736.
79. Poza, P., et al., *Fractographic analysis of silkworm and spider silk.* Engineering Fracture Mechanics, 2002. **69**(9): p. 1035-1048.

Supplementary Material for Chapter 3

1. Aragonitic composition of the shells: ^{13}C DE MAS NMR

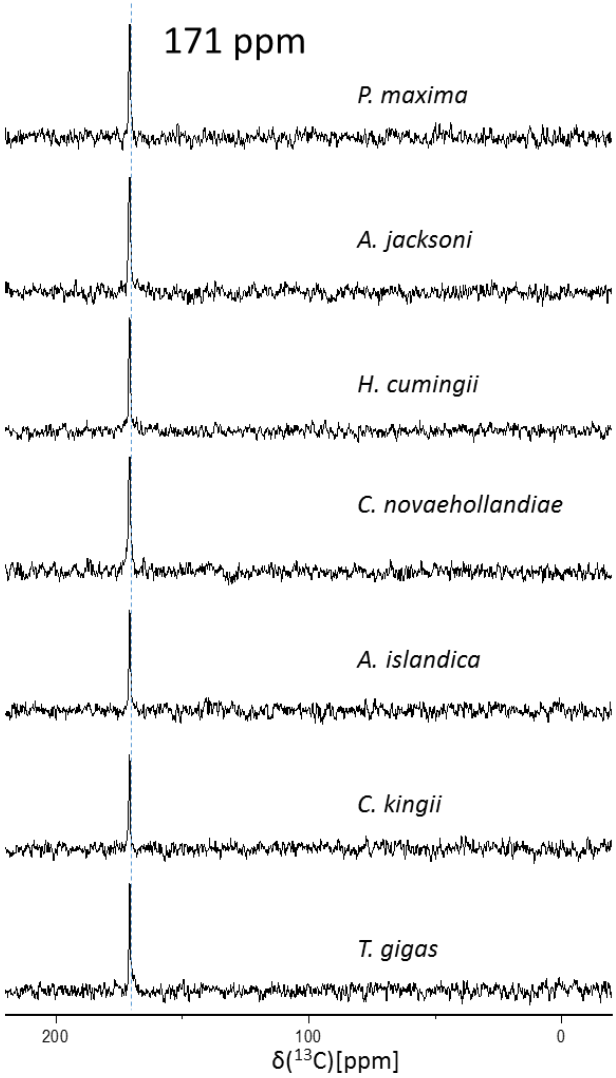

Figure S3.1: 75.4 MHz ^{13}C DE MAS spectra of seven intact shells (powdered, after mechanical removal of the periostracum). The only significant peak is found at 171.0 ppm, which is characteristic of aragonite. While the bio-organic materials in the shell compose as much as 4% of the total mass of the shell [1], the ^{13}C absorbance peaks associated with the organic matter are found over a broad range of chemical shifts—and therefore are not observed at this sensitivity level in the quantitative DE spectra. Nacreous shells: *P. maxima, A. jacksoni, H. cumingii* and *C. novaehollandiae;* homogeneous shell – *Arctica islandica;* and crossed lamellar shells – *Callista kingii* and *Tridacna gigas*.

Characterisation of organics and SEM images

2. Amino acid composition

The amino acid compositions of the shells (analysed without decalcification) differ significantly (**Figure S3.2**). In the nacreous shell of *H. cumingii*, glycine and alanine dominate the composition, with a total amount of 49.6%, followed by aspartate (8.3%) and serine (8.0%).

In the homogeneous shell of *A. islandica* glycine, proline and aspartate occur at high concentrations (39.6% of the total amino acids) followed by glutamate, arginine, threonine, alanine and lysine.

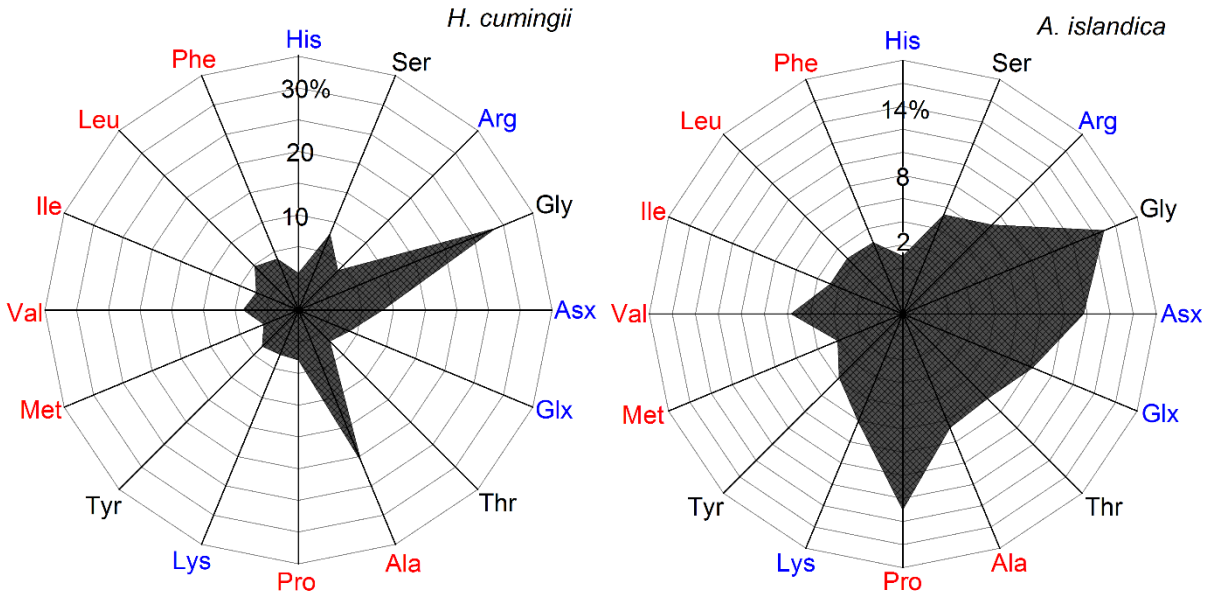

Figure S3.2: Representative amino acid compositions (powdered shells, periostracum mechanically removed). From Agbaje et al. [1].

FTIR spectroscopy

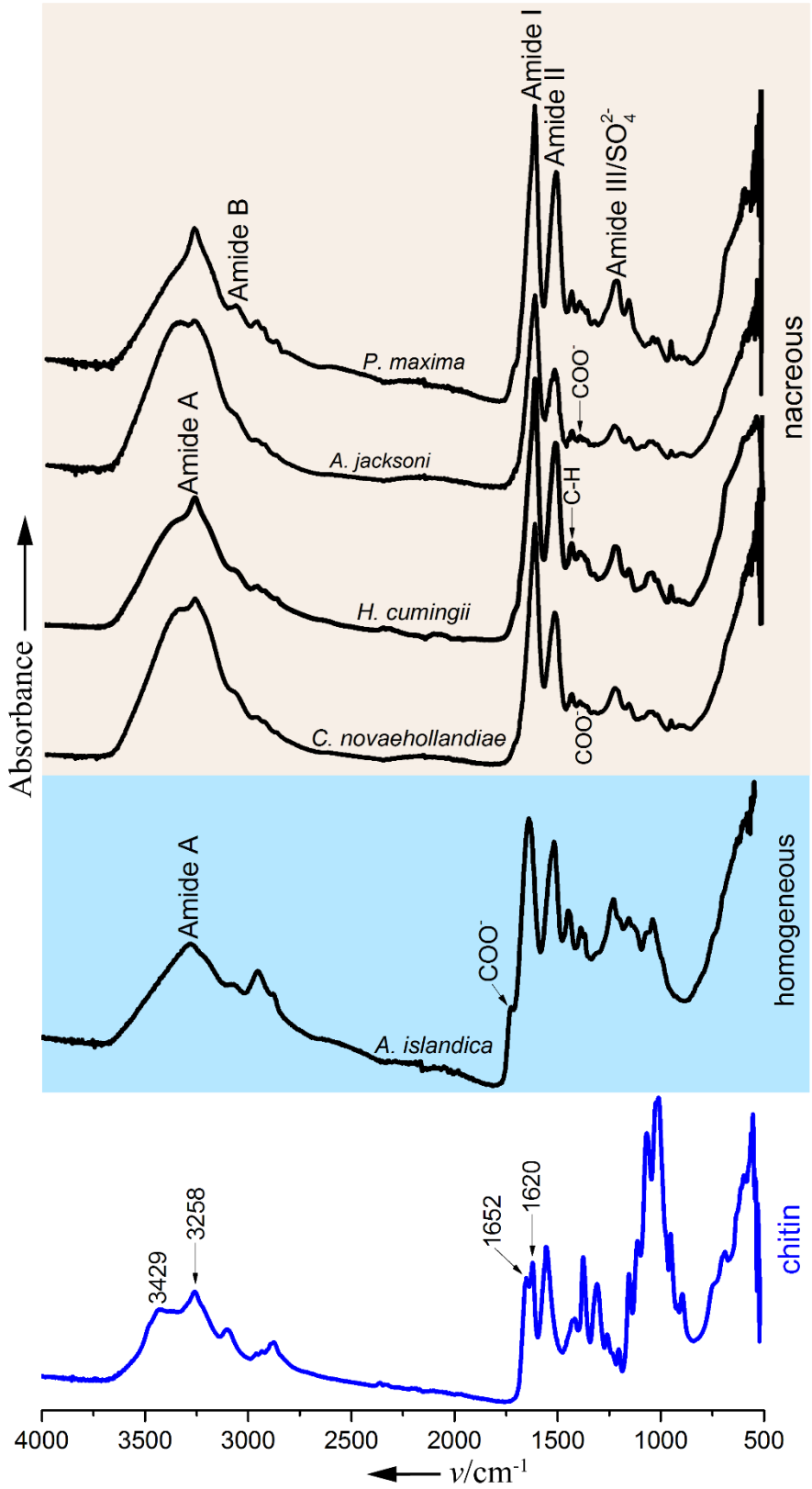

Figure S3.3: FTIR spectra of lyophilized water-insoluble acid extracts from five of the seven shells, in the range 4000-500 cm^{-1}. Chitin spectrum (shrimp chitin, Sigma Aldrich) is shown for comparison. Shell extracts showed characteristic absorptions of β–pleated sheets at around

1625-1638 cm^{-1}, chitin depicts α-helix structure at amide I (1652 and 1620 cm^{-1}). See Table S3.1 for peak assignment.

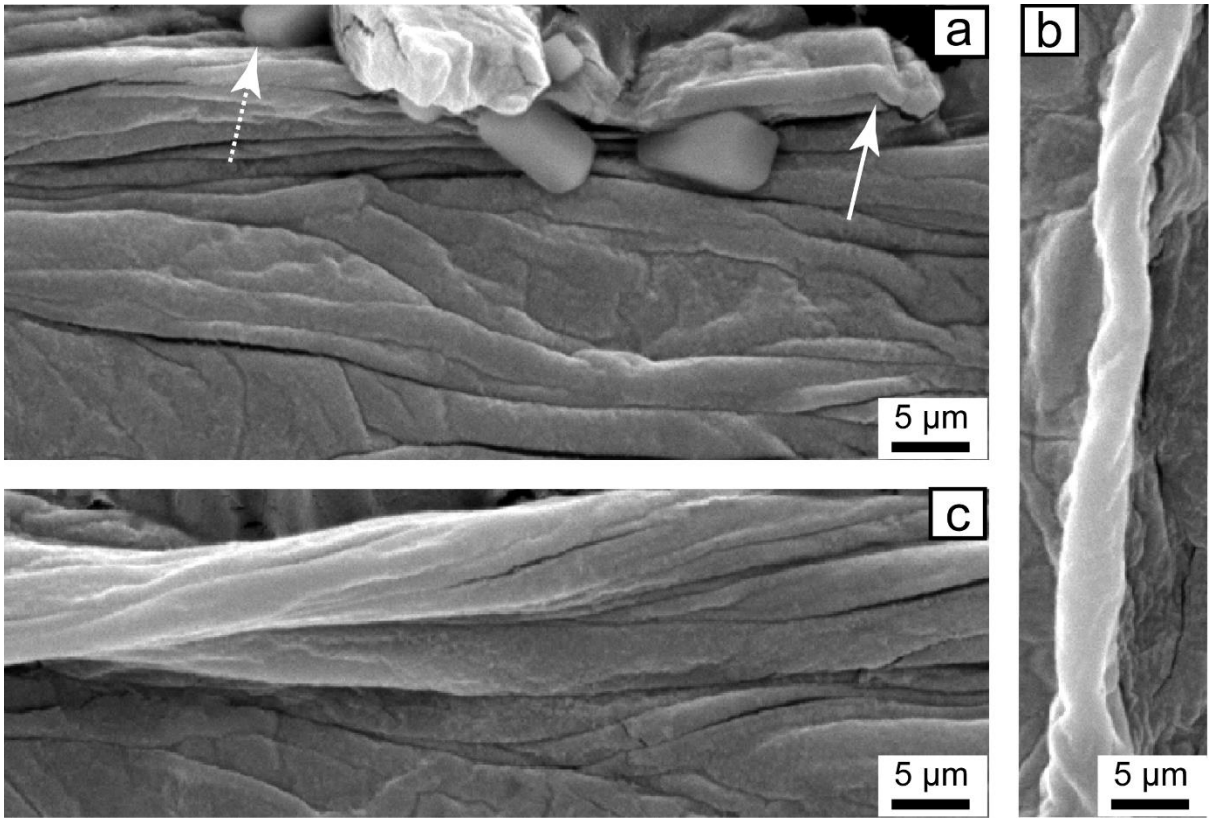

Figure S3.4: SEM images of hierarchical structures of the acid-extracted organic framework in a series of bivalve shells. a-c depict key structural features of silk fibre derived from nacreous shells of *Alathyria jacksoni*. The nanocrystals (dashed line with arrow) embedded within the disrupted fibre (arrow) and semi-amorphous regions. The silk cords in (b) and (c) consist of twisted micro-fibrils. These images depict that identification of chitin based on morphology alone might be unreliable.

3. Limits of detection levels of chitin by ^{13}C CP MAS NMR: A study of a chitin-spiked aragonite 'model shell'

In order to assess the limit of detectability of chitin by NMR in bivalve shells, we have prepared "model shell" samples comprised of physical mixtures of geological aragonite (from the mineral collection of the Department of Earth and Planetary Sciences, Macquarie University) and chitin at 1, 5, and 10 wt% levels. The mixtures were homogenised prior to further experiments (*Experimental* section). At these levels the solid state ^{13}C CP MAS NMR spectra of chitin-spiked aragonites (Error! Reference source not found.) show the characteristic chitin peaks with a good signal to noise ratios (S/N); 1024 and 4096 transients were collected

for 10% and 1% chitin-spiked aragonites, in less than 1 and 3 hours, respectively. The S/N quality and the data acquisition conditions, as they are far less challenging than those used for the intact shells (**Figure 3.2**). Thus, we conclude that the sensitivity of CPMAS NMR is more than sufficient to detect chitin at levels as low as 0.5 wt% (of the total sample) in the intact shells (Error! Reference source not found.) (~160 mg sample weight in the MAS rotor), or as low as 3.0 wt% (of the total organic content) within the extracts (<40 mg sample weight in the MAS rotor). Absent any evidence for the pattern of chitin peaks in any of the studied samples - *intact* shells and acid-extracted bioorganics alike, we conclude that chitin, if it exists, comprises less than 0.5 wt% of the total shell before chemical degradation of the aragonite, and/or less than 3 wt% of the total organic left after removal of the inorganic carbonate.

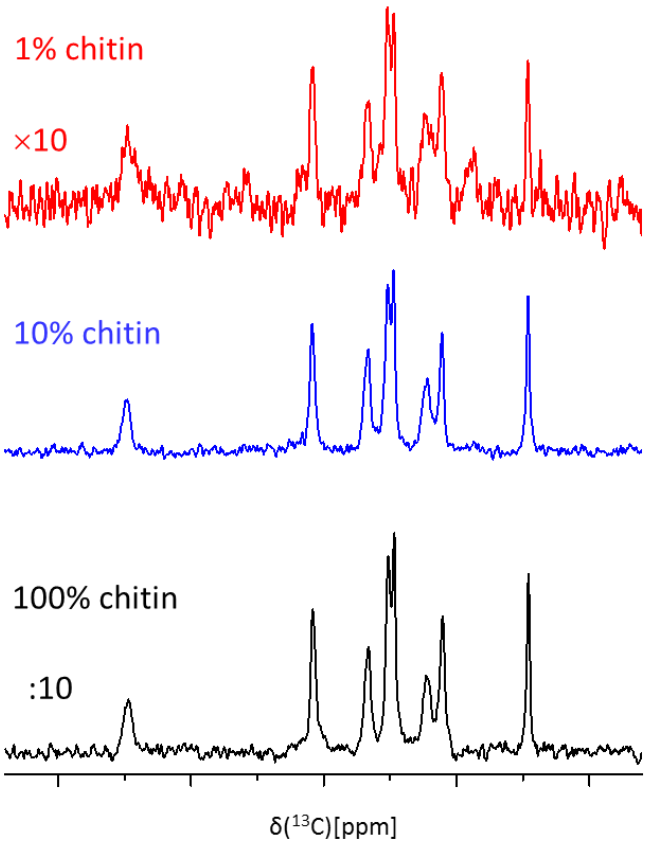

Figure S3.5: 75.4 MHz ^{13}C CP MAS of pure chitin (black), and 10% (blue) and 1% (red) chitin spiked in geological aragonite. The spectra confirm the more than adequate CP MAS NMR sensitivity to detect chitin abundances of 0.25 wt%. The spectra were collected with 2048, 1024, and 4096 scans/spectrum, respectively, with 1 ms CP contact time and 3s repetition time.

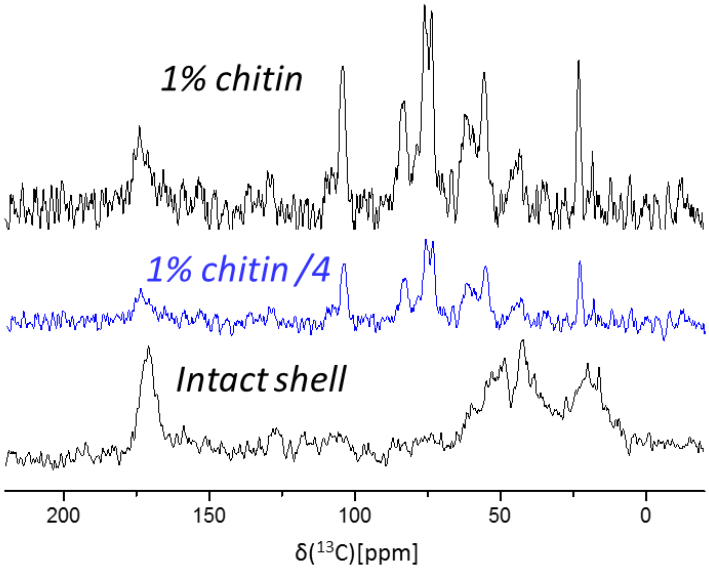

Figure S3.6: 75.4 MHz ^{13}C CP MAS spectra of intact shell *H. cumingii* (bottom), 1% chitin-spiked aragonite (top). The 1% chitin (spiked in aragonite) spectrum divided by 4 is redrawn in blue for a reference to visualize the NMR sensitivity to quantities as low as a fraction of a percent.

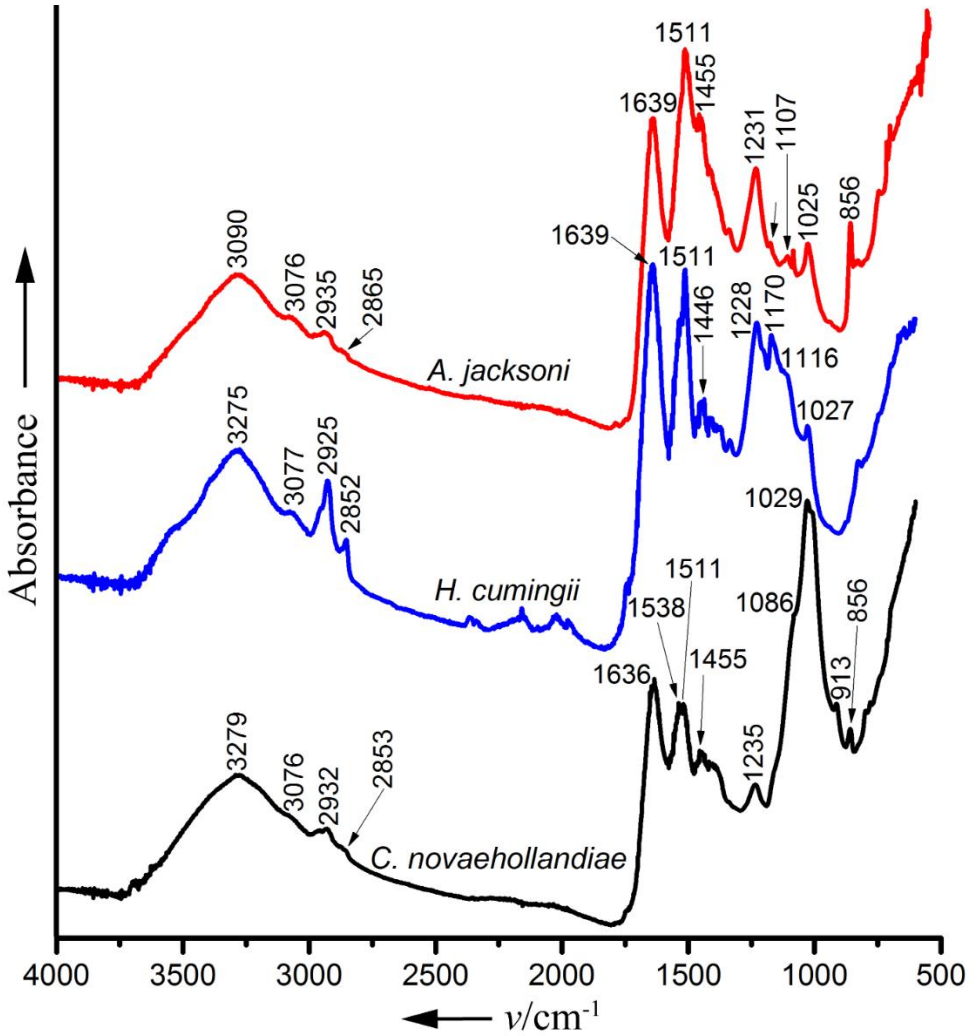

Figure S3.7: FTIR spectra of three samples of periostracum, in the range 4000-500 cm^{-1}. The periostracum exhibits characteristic absorption bands corresponding to *β*–pleated sheets, at

1639 cm^{-1} for *Alatyria jacksoni* and *Hyriopsis cumingii* shells and at 1636 cm^{-1} for *Cucumerunio novaehollandiae* shells.

4. Does Chitin survive the extraction procedure?

In order to assess how our chemical treatment(s) might impact the assessment of chitin in shells, chitin-spiked aragonite samples and pure chitin were tested to measure the response of chitin to the chosen acid- and acid-base extraction. Acid extraction is one of the traditional methods for isolation of the organic matter separate from the calcium carbonate matrix [2]. Subsequent base extraction may be applied to hydrolyse and solubilize the proteinaceous organic matter [2].

Each sample, namely 5% chitin-spiked, pure chitin and the powdered shell ('intact sample') of *H. cumingii* (**Figure S3.8**), was initially immersed in 6 N HCl with the *p*H sustained at around 4 and kept at 4˚C or at room temperature (21±1ºC), respectively, for 24 h. Mixtures were centrifuged to separate the acid-insoluble and the acid-soluble fractions. The latter is assumed to contain most of the small organic molecules. The acid-insoluble precipitate, which is assumed to contain both proteins and polysaccharides, was washed thoroughly with milli-Q water until neutral, thus terminating the acid-extraction procedure. The acid-insoluble fraction was then purified by reflux in sodium hydroxide solution [3], kept for 12 h at room temperature and subsequently at 100°C for another 5 h (12 h in total at 100°C). The resulting insoluble material, acid-base-insoluble, was washed with milli-Q water until neutral. The insoluble products of both procedures were allowed to dry at room temperature in air. After drying, samples were weighed and subjected to NMR characterization.

With ~ 2.0 g total starting weight of the 5 wt% chitin-spiked aragonite, the chitin weight is 100 mg, setting it as the maximum yield. The remaining weights following the acid and acid-base treatments are 154 mg and 124 mg, respectively - which suggests that the geological aragonite material is not completely dissolved and recovered along with the chitin. Using the chitin-spiked aragonite (1% and 10% samples) CP MAS NMR peak intensities as a quantitative

reference (chitin peaks intensities calibrated per mg of chitin in a sample), we have determined that each weighing in total 64 and 52 mg (40 wt%) appears to be chitin. The 40 wt% of chitin indicating a recovery of 60% (or 50%) of the chitin was possible. As in each treatment the initial chitin weight is 100 mg, these values directly correspond to 64% and 52% chitin recovery.

Upon subjecting pure chitin to the acid treatment 87% recovery is demonstrated (80% after acid-base treatment). These tests demonstrate that a significant fraction of chitin present in the shells should be recovered after acid, two treatments; on the contrary, they confirm that most of the initial chitin is recoverable.

As the conditions described above are harsher than those applied so as to obtain the acid-extracts of the shells, we feel confident that in our shell extracts, recovery of chitin should be no worse than, and almost certainly greater than, that demonstrated in the "model" shells. Thus, these tests further validate that the absence of "chitin" identified by the NMR measurements is not an artefact of the preparative sequence. Where no chitin peak pattern is observed, either in the spectra of the intact shells or of the extracts, confirms their low abundance. The chitin concentration, if any at all is present, must be below 3 wt% of the (acid-)insoluble bioorganic content.

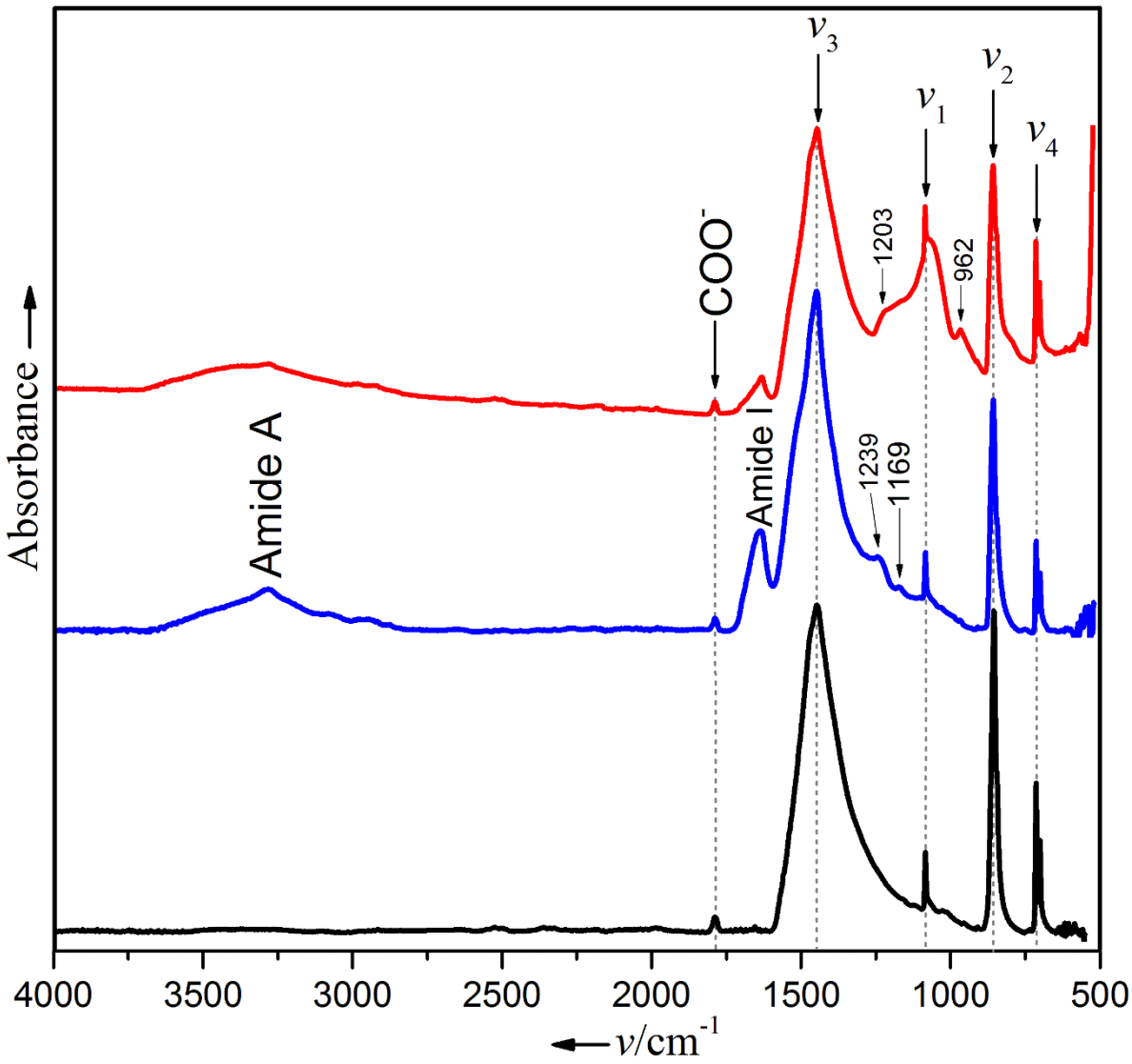

Figure S3.8: Red line: *H. cumingii* shell, powdered and decalcified in 6 N HCl and subsequently deproteinized in 5% NaOH; Blue line: *H. cumingii* shell, powdered and decalcified in 6 N HCl. Black line: Spiked-chitin: geological aragonite spiked with chitin ('Model shell') untreated. ν_1: 1082 cm^{-1}; ν_2: 855 cm^{-1}; ν_3: 1445 cm^{-1}; ν_4: 712, 700 cm^{-1}. Amide I appeared at 1629 cm^{-1} (red) and 1636 cm^{-1} (blue). The relative absorption peak of amide I is reduced after acid-base treatment (red) as compared to the acid treatment (blue).

Acid-base extracts

The nacreous powdered shells were demineralized in 1 M HCl for 7 d and the extraction followed the procedure as described above.

The insoluble fraction derived from the shells after sequential acid- and base- extraction was similarly characterized by ^{13}C CP MAS NMR. After 16k transients no significant signal was observed suggesting that these shells contained no biopolymer (**Figure S3.9** Middle; *H.*

cumingii as representative example) while ^{13}C DE MAS NMR yielded only the characteristic aragonite peak (171 ppm), whose intensity is similar to that found in the intact shell samples, indicating that the extract consisted primarily of aragonite (**Error! Reference source not found.S3.9**, top). We expect that this reflects the original shell; either aragonite remains undissolved after the acid treatment, or may represent recrystallization in base. Our observations regarding this treatment are in accordance with the findings reported by Osuna et al.[4] and Nudelman et al.[5]

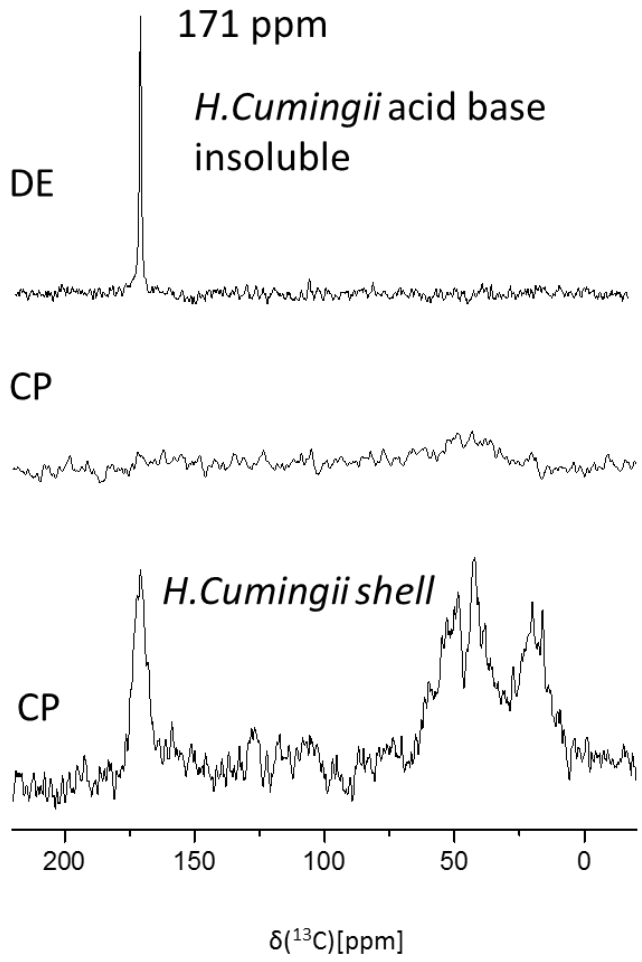

Figure S3.9: Representative 75.4 MHz ^{13}C CP MAS NMR of nacreous shell demonstrating DE (top) and CP (middle) of acid-base insoluble fraction, and CP (bottom) of the powdered shell (‘intact sample’) of *H. cumingii*. The spectra indicate that acid-base insoluble fraction consists of aragonite and some remainders of organic matter. 8 and 16k scans for DE and CP, respectively.

Table S3.1

Peak assignment for the FTIR spectra (cm^{-1}) of chitin, organic macromolecules (lyophilized water-insoluble acid extracts) and Periostracum grouped by shell microstructure. *A. islandica* denotes homogeneous (*Arctica islandica*) shells, nacreous shells are: *Pinctada maxima* (*PM*), *Alathyria jacksoni (AJ), Hyriopsis cumingii (HC)* and *Cucumerunio novaehollandiae (CN).* Peak assignment carried out using data from; Focher et al.[6]; Cárdenas, et al.[7]; Boulet-Audet et al.[8]; Chirgadze et al.[9]; * = shoulder

Chitin (cm^{-1})	*A. islandica* (cm^{-1})	*PM, AJ, HC, CN* (cm^{-1})	Periostracum *AJ, HC, CN* (cm^{-1})	Peak assignment
3429	-	3354/69	3534*	ν_{OH}
3258	3276	3272/4	3275/90	$\nu^{as}_{N\text{-}H}$
3099	3065	3072	3076/7	$\nu^{s}_{N\text{-}H}$
2959	2950	2964/8	2958*	$\nu^{as}_{C\text{-}H}$ of alkyl
2935	-	2932/5	2925/35	$\nu^{s}_{C\text{-}H}$ of methylene
2877	2873	2876	2852/65	$\nu^{s}_{C\text{-}H}$ of alkyl
-	1727	-	-	$\nu^{as}_{COO^-}$
1652, 1620	1638	1625	1636/39	$\nu_{C=O}$ (Amide I)
1556	1516	1518,1522/5	1538, 1511	$\nu_{C\text{-}N}$ (Amide II)
1416	1447	1445/6	1446/55	$\delta_{C\text{-}H}$ of alkyl
-	-	1403/6	1410	$\nu^{s}_{COO^-}$
1376	1386,1367	1367/70	-	$\delta_{C\text{-}H} + \delta_{C\text{-}C\text{-}H}$ of alkyl
1308	1314*	1333/6	1337	$\delta_{C\text{-}N} + \delta_{N\text{-}H}$ (Amide III)
-	1228	1228/35	1228/35	$\nu^{s}_{S=O}$ (Sulfate)
1260	-	-	-	$\delta_{N\text{-}H}$
1203	-	-	-	$\nu_{C\text{-}O}$
1154	1153	1170	1170/4	$\nu^{as}_{C\text{-}O\text{-}C}$ (ring)
1112	1125	-	1107/16	$\nu_{C\text{-}O}$
1068	1070	1052/6	1083/6	$\nu_{C\text{-}O}$
1009	1038	1028/32	1025/29	$\nu_{C\text{-}O}$
952	-	965, 921	913	$\gamma_{C\text{-}H}$ of methylene
895	-	897	856	$\gamma_{C\text{-}H}$ (C1 axial) (β bond)
689	-	-	-	$\gamma_{N\text{-}H}$

References – Supplementary Material for Chapter 3

1. Agbaje, O.B.A., et al., *Organic macromolecules in shells of Arctica islandica: comparison with nacroprismatic bivalve shells.* Marine Biology, 2017 164:208.
2. Younes, I. and M. Rinaudo, *Chitin and chitosan preparation from marine sources. Structure, properties and applications.* Marine drugs, 2015. **13**(3): p. 1133-1174.
3. Darmon, S. and K. Rudall, *Infra-red and X-ray studies of chitin.* Discussions of the Faraday Society, 1950. **9**: p. 251-260.
4. Osuna-Mascaró, A.J., et al., *Ultrastructure of the Interlamellar Membranes of the Nacre of the Bivalve Pteria hirundo, Determined by Immunolabelling.* PloS one, 2015. **10**(4): p. e0122934.

5. Nudelman, F., et al., *Forming nacreous layer of the shells of the bivalves Atrina rigida and Pinctada margaritifera: an environmental-and cryo-scanning electron microscopy study.* Journal of structural biology, 2008. **162**(2): p. 290-300.
6. Focher, B., et al., *Structural differences between chitin polymorphs and their precipitates from solutions—evidence from CP-MAS 13C-NMR, FT-IR and FT-Raman spectroscopy.* Carbohydrate Polymers, 1992. **17**(2): p. 97-102.
7. Cárdenas, G., et al., *Chitin characterization by SEM, FTIR, XRD, and 13C cross polarization/mass angle spinning NMR.* Journal of Applied Polymer Science, 2004. **93**(4): p. 1876-1885.
8. Boulet-Audet, M., F. Vollrath, and C. Holland, *Identification and classification of silks using infrared spectroscopy.* Journal of Experimental Biology, 2015. **218**(19): p. 3138-3149.
9. Chirgadze, Y.N., O. Fedorov, and N. Trushina, *Estimation of amino acid residue side-chain absorption in the infrared spectra of protein solutions in heavy water.* Biopolymers, 1975. **14**(4): p. 679-694.

Architecture of crossed-lamellar bivalve shells: The Southern Giant Clam (*Tridacna derasa*, Röding, 1798)

O. B. A. Agbaje[1], R. Wirth[2], L. F. G. Morales[3], K. Shirai[4], M. Kosnik[5], T. Watanabe[6], D. E. Jacob[1]

[1]Department of Earth and Planetary Sciences, Macquarie University, Sydney, NSW2109, Australia

[2]Helmholtz-Centre Potsdam, German Research Centre for Geosciences GFZ, 14473 Potsdam, Germany

[3]Scientific Center for Optical and Electron Microscopy (ScopeM), ETH Zürich. Auguste-Piccard-Hof 1, HPT D9, 8093, Zürich, Switzerland

[4]International Coastal Research Center, Atmosphere and Ocean Research Institute, The University of Tokyo, 5-1-5, Kashiwanoha, Kashiwa-shi, Chiba, 277-8564 Japan,

[5]Department of Biological Sciences, Macquarie University, Sydney, NSW 2109 Australia

[6]Department of Natural History Sciences, Hokkaido University, N10W8, Kita-ku, Sapporo 060-0810, Japan

Abstract *Tridacna derasa* shells show a crossed lamellar microstructure consisting of three hierarchical lamellar structural orders. The mineral part is intimately intergrown with 0.9 wt% organics, namely polysaccharides, glycosylated and un-glycosylated proteins and lipids, identified by Fourier Transform Infrared Spectrometry. Transmission Electron Microscopy shows nanometer-sized grains with irregular grain boundaries and abundant voids. Twinning is observed across all spatial scales and results in a spread of the crystal orientation angles. Electron backscatter diffraction analysis shows a strong fiber texture with the [001] axes of aragonite aligned radially to the shell surface. The aragonitic [100] and [010] axes are oriented randomly around [001]. The random orientation of anisotropic crystallographic directions in this plane reduces anisotropy of the Young's modulus and adds to the optimization of mechanical properties of bivalve shells.

Keywords: Bivalvia, Tridacnidae, TEM, EBSD, aragonite, Young's modulus

4.1 Introduction

Bivalve shells are complex biocomposites consisting of calcium carbonate intimately intergrown at the nanoscale with organic macromolecules [57, 214]. This composite nature creates enhanced material properties, for example high mechanical strength [69] and fracture toughness [5, 70], which optimize shell stability and protective function for the organism [215]. Much recent research has focussed on the nacreous shell structure in molluscs, while other shell structures in this phylum, such as the most widespread crossed lamellar structure [51], are yet to receive comparable attention. Here, we present one of the first in-depth characterisations of both the inorganic and the organic parts in *Tridacna derasa* (Southern Giant Clam) shells. Furthermore, we combine here Electron Backscatter Diffraction (EBSD) with TEM analysis to identify some of the multiscale strategies for the optimization of mechanical properties across all structural hierarchies in the shell.

4.1.1 *Structure and micro-texture of Tridacna derasa shells*

Tridacna derasa shells are entirely aragonitic and consist of a ca. 10 mm thick massive outer layer and a slightly translucent inner layer with visible growth increments (Figure 4.1a, c). The shell comprises crossed lamellar shell structure, which is the most common structure of mollusc shells and has been described in detail by a number of authors (e.g. [9, 51, 65, 216-219]). With very few exceptions, shells with this structure are aragonitic rather than calcitic [129]. Crossed lamellar shells from different species vary in structural arrangement but bear a basic architectural similarity [68]: aragonite grains are arranged in hierarchically organised lamellae (Figure 4.1b, d) with alternating orientations at an angle of ca. 70-90˚ depending on the species [51, 65]. Three or four hierarchical orders can be identified and growth twinning of the aragonite crystals is very common (e.g. [64, 65]).

The first structural hierarchy in *T. derasa* shells comprises a series of undulating aragonite bands 20 to 50µm thick (first order lamellae, Figure 4.1b) consisting of nanometer-thin stacked second-order lamellae. These sheets of stacked lamellae are oriented at an angle of ca. 70˚ to

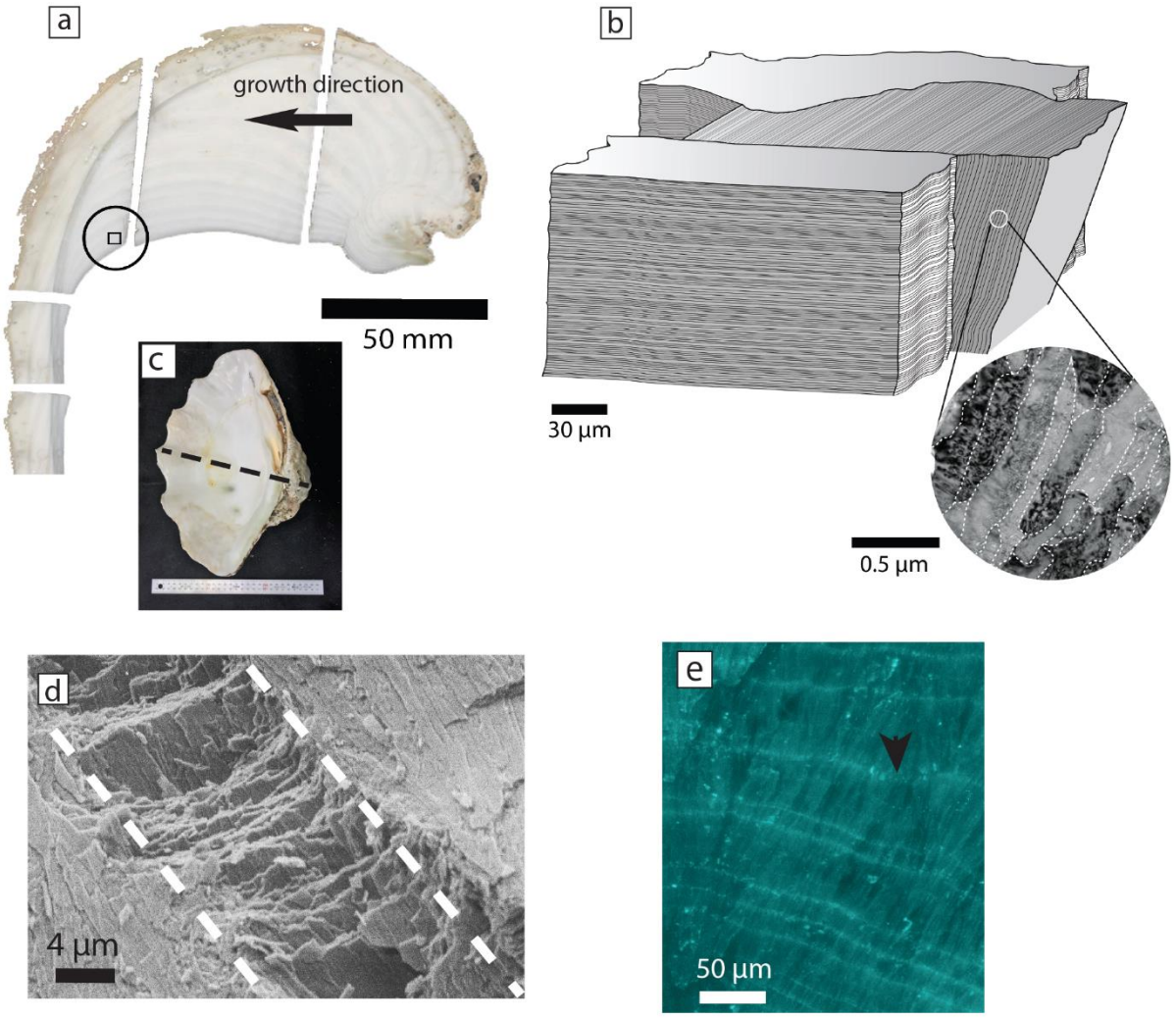

Figure 4.1. (a) Sectioned shell of *Tridacna derasa* showing the location of the EBSD map (circled box). The outer layer, extending ca. a further 10 cm was cut off at the level of the inner shell layer. (b) Schematic sketch of the hierarchical lamellar shell structure. An enlargement showing third order grain is taken from Figure 6c with grain boundaries outlined by the dashed line. (c) Complete valve of the shell with the dashed line indicating where the shell was sectioned. (d) SEM image of a fractured surface of the shell shows the first order lamellae (dashed line) consisting of second order laths. (e) Organic daily growth lines stained with Calcofluor White (arrows) transect the aragonitic lamellae.

each other and are perpendicular to the shell surface. Each sheet of second-order lamellae, in turn, consists of nanometer-sized parallel aragonite laths, which form the third order of hierarchy (Figure 4.1b).

Tridacna species are known to form daily growth lines [220, 221] with growth increments around 15µm in width. Growth lines in molluscs usually have increased organic content

compared to the increments between a set of lines and can be visualized using histochemical staining methods (Figure 4.1e).

4.2 Materials and Methods

The Southern Giant Clam, *Tridacna derasa* (Röding 1798), (Mollusca: Bivalvia), is the second largest species in the family Tridacnidae, reaching shell lengths of up to 520 mm [222]. Tridacnidae occur naturally in the tropical and subtropical waters of the Indo-Pacific and host photosymbiotic algae in their tissues [223]. Shells of *T. derasa*, cultured on Ishigaki Island, Okinawa, Japan (for environmental details see [221]) were used for structural analyses of the inorganic part of the shells, while organic matrix analysis was performed using a recently alive shell from One Tree Island, Queensland, Australia.

4.2.1 *Scanning Electron Microscopy (SEM) and Electron Backscattered Diffraction (EBSD)*

Broken pieces of shell were imaged with a Leo Gemini 1530 Field-Emission Secondary Electron Microscope (FE-SEM) (Carl Zeiss, Germany) at the Max-Planck Institute for Chemistry, Germany. Samples were mounted on aluminum stubs using conductive carbon tape. All samples were studied uncoated with an accelerating voltage of 5 kV, a sample current of 2 pA, and a vacuum pressure of $5x10^{-6}$ mbar.

Crystallographic preferred orientations (CPO) in the shell were determined by automated indexation of electron backscattered patterns (EBSD) in a scanning electron microscope [224, 225] using an EDAX TSL Digiview 3 EBSD camera and an OIM DC 5.0 detector. The sample was polished using standard methods with diamond pastes of different grain sizes down to 0.25 µm and a final step of chemical-physical polishing using a neoprene polishing cloth and an alkaline solution of colloidal silica for 1 hour. The EBSD measurements were conducted in an area of the shell along the axis of maximum growth (Figure 4.1a). Analyses were carried out under low vacuum (10 Pa of H_2O) using the following parameters on the SEM: 15 kV accelerating voltage; 8 nA beam current; 12 mm working distance; step size of 1 µm and 70°

sample tilt. At these conditions, the electron beam size is 4 nm and ca. 90% of all diffraction patterns could be indexed.

Post-acquisition treatment included the standardization of the confidence index (CI) of different points and CI correlation between neighbouring points. 'Grain' dilation was carried out in three steps considering the grain tolerance angle of 10° and a minimum grain size of 10 pixels. Grain sizes as observed by Transmission Electron Microscopy are usually in the nanometer range in biominerals (e.g. Figures 4.4 - 4.6), hence the chosen 'grain' size cut-off for EBSD defines domains of several crystallographically well-aligned nanograins, rather than individual aragonite grains. These domains have misorientation angles <10˚ and are here termed 'first-order domains'.

The pseudohexagonal symmetry effect on aragonite caused by a rotation of 60° around [001] was also corrected. Data with CI >0.1 are plotted in pole figures (Fig. 2d, 9b), which are stereograms with axes defined by an external reference frame using the shell length growth direction (GD), the direction of the growth lines (GL) and the axis normal to these features. Accumulation of points around a specific direction in the pole figures (pole maxima) shows a degree of texture in the polycrystalline material, quantified according to the colour scales in the figures. The rotations of the crystallographic dataset and plots of pole figures were carried out using the MTEX toolbox for Matlab [226, 227].

4.2.2 *Transmission Electron Microscopy*

Transmission Electron Microscopy (TEM) foils ca. 10 by 15 µm in length and 0.15–0.20 µm thickness were cut from the polished section of the sample using the FEI FIB200 focused ion beam device (FIB) following procedures given in Wirth [228]. Six foils were cut from the inner and outer layers of the shell, either parallel or perpendicular to the growth lines. Samples were placed on a carbon coated Cu grid without further carbon coating (*ex situ* lift out method). The FIB milling method involves sputtering the material surrounding the platinum-protected target area with gallium ions. This process can heat the target area, and drive amorphisation

through Ga implantation in the surface of the material [229]. Sample heating is proportional to the beam current, and the extent of amorphisation is proportional to the beam energy; both depend on the angle of beam incidence during milling [230]. To avoid heating of the sample, we used 30 keV with a beam current of 11pA and an angle of incidence of 1.2˚. At these conditions beam heating during FIB milling is less than 10K [231] and sample amorphisation is minimal. As the foils are thicker than 100 nm, the major part of the foil is thus not affected by ion implantation. If amorphisation were a significant problem in the foils, Debye-Sherrer diffraction rings would be present in all collected diffraction patterns, but these features were not observed.

TEM imaging and analysis were undertaken with a FEI Tecnai™ G2 F20 X-Twin transmission electron microscope with a field emission gun source, operating at 200 kV acceleration voltage. A Gatan Tridiem™ filter allowed energy-filtered imaging, applying a 20 eV window to the zero-loss peak for all Bright-Field images in this study. Images were taken either in STEM mode or in High Angle Annular Dark Field (HAADF) mode with 330 mm camera length. At these conditions imaging is possible with z-contrast, diffraction, thickness and density contrast.

Great care was taken to minimize radiation damage to the material during TEM analysis. This involved low-dose analysis and a visual monitoring protocol developed for biominerals [36, 232]: Foils were analyzed in STEM mode, rapidly scanning using a small spot size and assigning the beam between to areas outside the sample to avoid electron irradiation damage. At the start of the analytical session for each FIB foil, a rapid overview picture was taken using a defocused beam and this was repeated after STEM scanning and HREM analysis and at the end of each analytical session to scan for beam damage. All high-resolution TEM (HRTEM) analyses were carried out at the end of the analytical session for each foil, using exposure times of 0.2 secs and a spot size of 5. Using this protocol, irradiation damage was only observed on a few occasions, manifested either as holes from the electron beam or as localized small

amorphizised areas where a STEM scan had been carried out. Analyses and images from these areas were discarded from the dataset.

4.2.3 Organic matrix characterisation

4.2.3.1 *Thermogravimetry*

The total amount of organic shell matrix was determined by thermogravimetric analysis (TGA) with a TGA 2050 Thermogravimetric Analyzer (TA Instruments, USA) at the Department of Chemistry and Biomolecular Sciences, Macquarie University. Approximately 30 mg of powdered and sieved sample from the inner part of the shell (250 µm mesh size) was measured in a temperature interval from 30˚C up to 1000˚C at 10˚C/min steps under a nitrogen atmosphere.

4.2.3.2 *Extraction methods*

To characterise the organic matrix, the shell was decalcified in 6N HCl after cutting and removing its outermost part, followed by a cleaning step that involved immersing the shell in 30% H_2O_2 (Merck KGaA, 64271 Darmstadt; Germany) and rinsing with Milli-Q water. The solution was stored at 4ºC after decalcification. The supernatant was extracted twice, first with dichloromethane (DCM) and then with butanol (BuOH), both fractions were combined and reduced to dryness before storage at -35˚C.

The lipid–lipoprotein fraction was extracted with methanol/dichloromethane (2/1) at room temperature for 40 h, ultrasonicated and dried down in a nitrogen atmosphere.

An aliquot of the total organic matrix extract was taken up in dimethylacetamide containing 5% lithium chloride [233], centrifuged and filtered. The specific optical activity of the filtrate was analysed with a JASCO P-1010 Polarimeter (JASCO, Tsukuba, Japan) at the Department of Chemistry and Biomolecular Sciences, Macquarie University. A cell line of Sodium D at 589 nm was used as the filter at room temperature of 21±1ºC.

4.2.3.3 *Infrared Spectroscopy*

Fourier Transform Infrared (FTIR) spectra of different extracted and dried organic matrix fractions were measured with a Thermo Nicolet iS10 FTIR spectrometer (Nicolet, MA, USA) equipped with Attenuated Total Reflection along with a smart performer assessor at the Department of Chemistry and Biomolecular Sciences, Macquarie University. Spectra were acquired between 4000 and 500 cm^{-1} with a resolution of 8 cm^{-1} and 64 accumulations. Backgrounds were recorded at the beginning of the analytical session and approximately every half hour.

4.3 Results

4.3.1 *Electron Backscattered Diffraction analysis*

Electron Backscattered Diffraction (EBSD) was carried out on a polished area of the inner layer of the shell situated between, but not overlapping with, two organic-rich annual growth lines (approximate location outlined in Figure 4.1a). Figure 4.2a shows a crystal orientation map for this area. The map is coloured according to the orthorhombic inverse pole figure colour scheme for aragonite (inset), assuming the reader's perspective. Areas in red have their crystallographic [001] axis pointing towards the reader, green denotes the [100] axis and blue the [010] axis. Intermediate colours are crystallographic orientations intermediate between these three extremes. Adjacent areas with a misorientation angle >10˚ define a boundary outlined in grey in Figure 4.2a. These boundaries, however, do not delineate single grains, but rather domains of co-oriented smaller aragonite crystals with grain sizes beyond the spatial resolution of the EBSD method. They are termed here 'first-order domains' (see Materials and Methods).

Two first order lamellae are outlined with dashed lines in Figure 4.2a, and a similar area in the shell is shown in Figure 4.2b, where first order lamellae (dashed lines) consisting of second order lamellae are arranged in alternating orientation. Twinning is commonly observed at this level of hierarchy in the shell and amounts to ca. 26% of the 'grain' (i.e. first order domain)

boundaries (Figure 4.2c). This value is derived from analysis of the boundaries between first order domains with a misorientation angle of 60˚ in the CPO map (Figure 4.2a), which is close to the angle of twinning on {110} in aragonite. It should be noted that the estimated value of 26% is a lower limit for the total amount of twin boundaries, because its precision is determined by the measurements conditions and the spatial resolution of the EBSD analysis. Nevertheless, even this rough estimate shows that aragonite twinning is very common in the shell across all structural hierarchies.

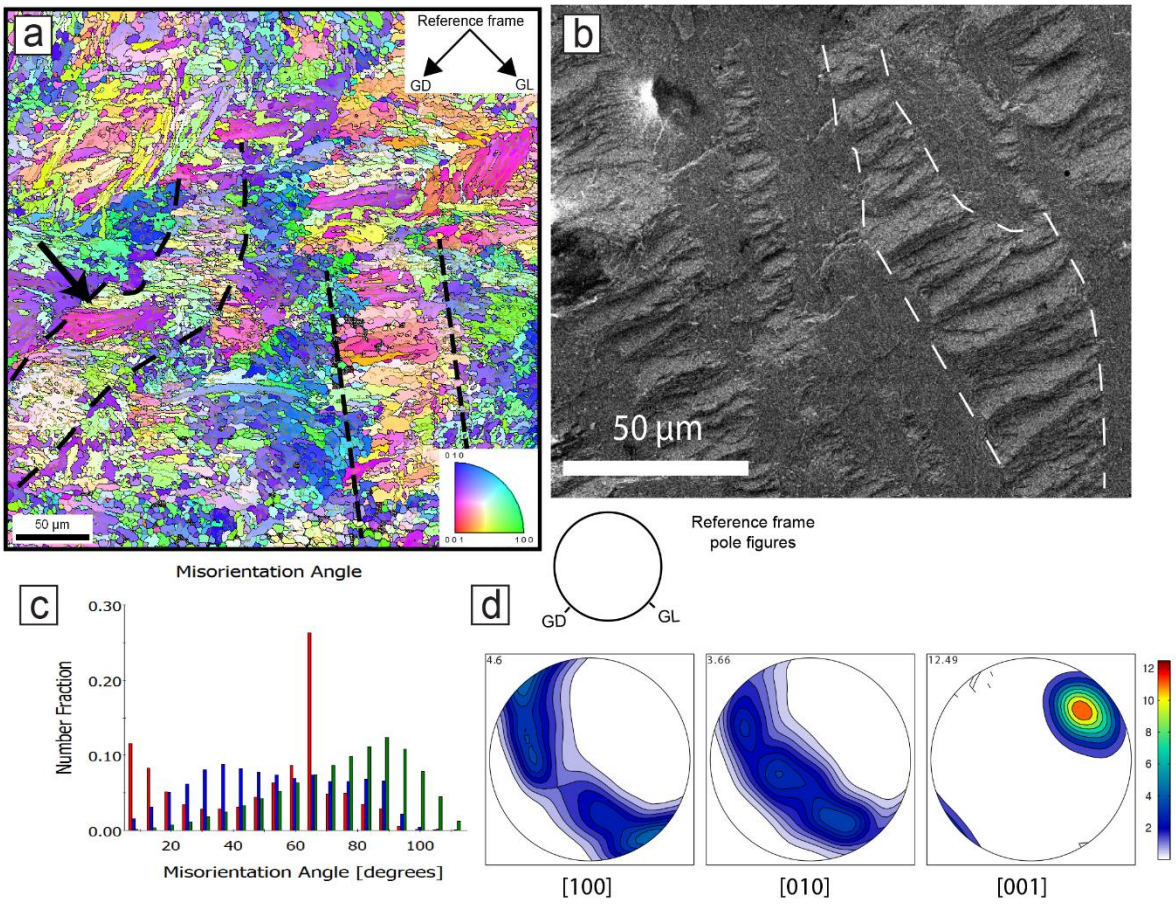

Figure 4.2. (a) Crystallographic orientation map coloured according to the aragonite inverse pole figure colour code (inset). The reference frame (upper right) points out the overall growth direction of the shell (GD) and the direction of the growth lines (GL). For a red domain in the map, the [001] c-axis is pointing to the reader; if green, it is the a-axis [100], and if blue, it is the b-axis is [010]. Dashed lines outline some first order lamellae. First order domains are separated by low-angle boundaries within the domains (grey lines) and by high-angle boundaries between different co-oriented areas (black lines). The arrow points to the co-oriented area detailed in Fig. 3. **(b)** SEM image (fractured shell surface) of a similar area, first order lamella outlined with dashed line. **(c)** Histogram of misorientation angles for neighbour (red bars) and non-neighbour (blue bars) grains. Note the predominance of low angle grain

boundaries (misorientations <15°) for neighbouring crystals, which is not observed between non-neighbour grains. Both distributions of neighbours and non-neighbour grains are distinctly different from the expected misorientation angles for random grain boundaries (green bars). **(d)** Pole figures of the [100], [010] and [001] axes of aragonite (lower hemisphere of the stereographic projection), showing a strong crystallographic preferred orientation of the [001] axes around the growth direction (GD), with the [100] and [010] axes forming a single broad girdle parallel to the plane that contains the direction of growth lines (GL, see the inset in (a) for the external reference frame). The maximum density of the [001] axes is 12.49 times uniform (value in upper left corner, compare to scale).

The CPO of the shell shows a strong alignment of [001] axes parallel to the growth direction of the shell (GD) as seen in the pole figures (Figure 4.2d), with a maximum of about 12x the uniform distribution. The [100] and [010] axes are distributed at random along continuous and broad single girdles normal to GD, with a weak tendency for [100] to be parallel with the growth line direction (GL). Hence, the aragonite crystals are strongly co-aligned in the [001] axial direction but random in radial direction (i.e. concerning their [100] and [010] axes). These are the typical characteristics of a fiber texture.

Figure 4.2a shows that first-order domains forming several second order lamellae within a given first order lamella are co-oriented, forming areas of uniform or similar colour (arrow in Figure 4.2a). These larger areas with small internal misorientation angles are generally around 50µm in size and are separated from each other by high-angle first-order domain boundaries (misorientation angle >15˚, black lines).

Analysis of one such large area (Figure 4.3a, marked with an arrow in Figure 4.2a) shows misorientation angles of ca. 15˚ across the entire area of ca. 50µm (Figure 4.3b). Notably, the misorientation axes within this first-order domain vary considerably (Figure 4.3c), i.e. they are parallel to different crystal directions that can diverge by as much as 90°. This shows that individual aragonite particles (or groups of particles) within this large area are misoriented to different degrees along individually differing misorientation axes, confirming the particulate nature of the area below the spatial resolution of the EBSD method.

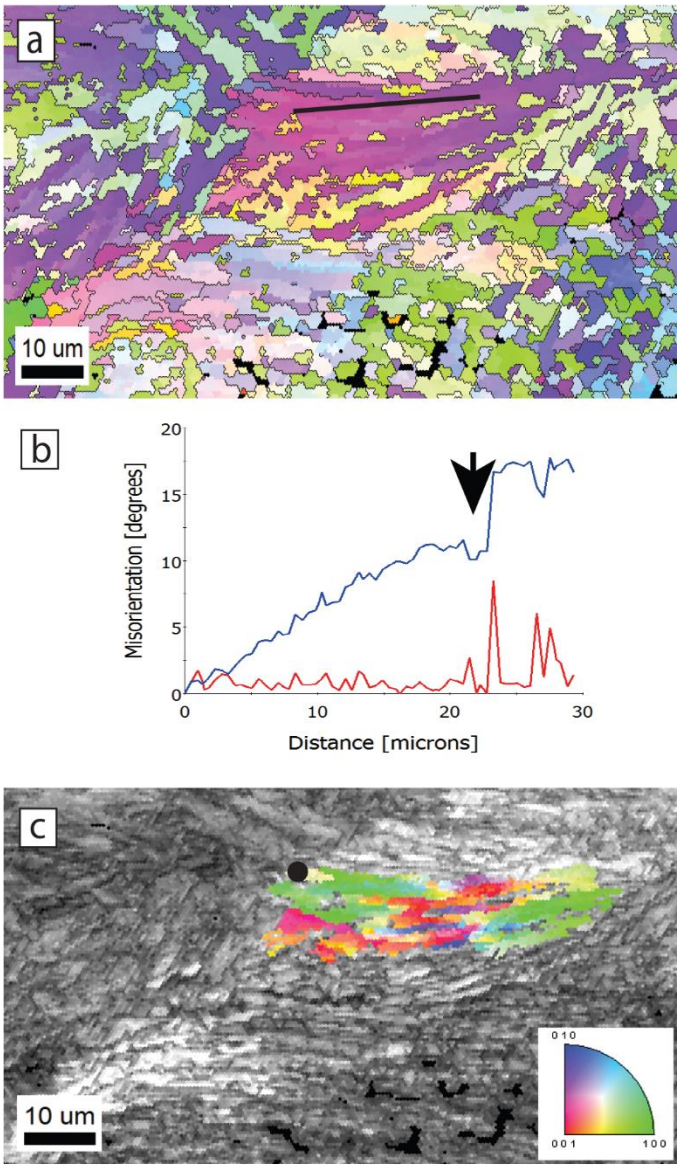

Figure 4.3. Region of interest marked with a black arrow in Fig. 2a. **(a)** Crystallographic orientation map coloured according to the aragonite inverse pole figure colour code (inset in d) and detailed in Fig. 2. **(b)** Misorientation profile (black line in Fig. 3a) showing change in crystal orientation with a misorientation angle of ca. 15˚ across approximately 30 µm. Red curve = point to point values, blue curve = point to origin values. Arrow indicates a subdomain boundary. **(c)** Image quality map where different levels of grey indicate the EBSD pattern quality – clear, high quality patterns in light grey, lowest quality patterns in dark grey. In colour, the 'grain' reference orientation deviation axes, showing the deviation of crystallographic orientation relative to the black point in the map (colour reference as inset).

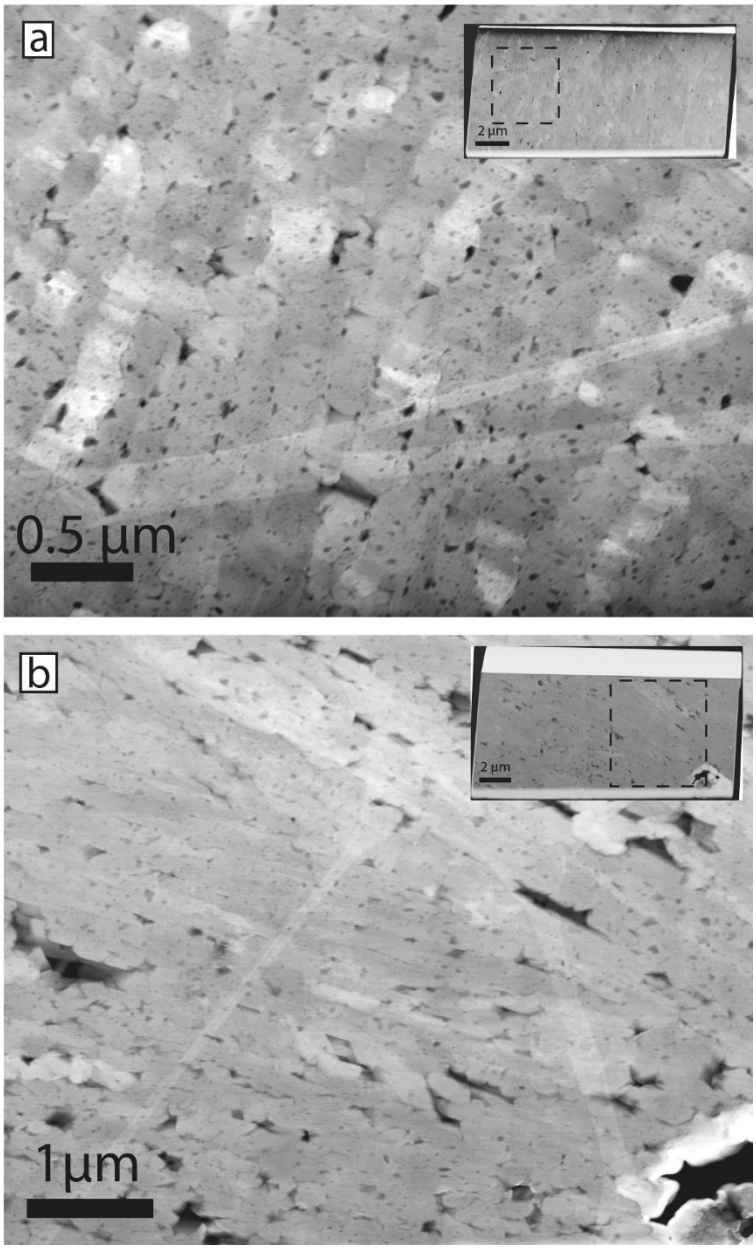

Figure 4.4. High Angle Annular Dark Field (HAADF) images of TEM foils cut perpendicular (a) and parallel (b) to the outer surface of the shell in the outer shell layer (Fig. 1a). Insets show the entire TEM foils with black squares marking the locations of the areas enlarged in (a) and (b). Note the small aragonite laths cut perpendicular (a, b) and parallel (c, d) to their longest axes and the numerous multiscale voids.

4.3.2 *Transmission Electron Microscopy*

We analysed six TEM foils cut from the same polished section for which EBSD measurements were performed (Figure 4.1a). Prominent characteristics observed in the TEM analyses are the typical particulate nature, well-described for natural biominerals (e.g. [36, 234, 235] associated with multi-scale porosity throughout the shell (Figure 4.4 – 4.6). The outer shell

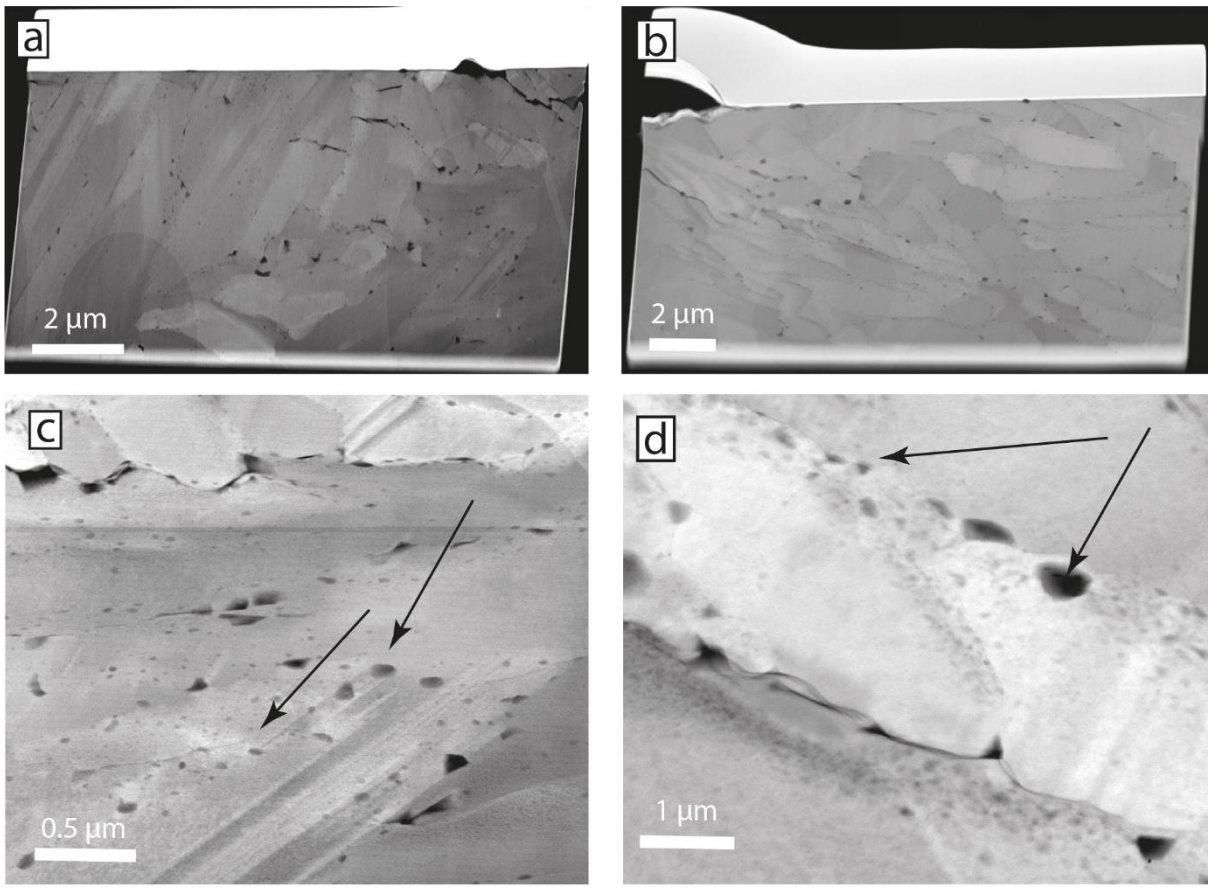

Figure 4.5. High Angle Annular Dark Field (HAADF) images of foils cut by Focussed Ion Beam milling parallel (a, c) and perpendicular (b, d) to the outer surface of the shell in the inner shell layer (Fig. 1a). The lath-shaped aragonite grains are cut perpendicular (a) and parallel (b) to their longest axes. Note the voids along laths boundaries and within the laths (c, d). Polycylcic twinning is common (c). The different grey shades of the aragonite crystals are differences in diffraction contrast due to different crystal orientations.

layer (Figure 4.4) displays micrometer-sized cavities between the third order laths (Figure 4.4a, b), while the inner shell is less porous at the micrometer scale (Figure 4.5a, b). In contrast, the inner shell shows submicron porosity *within* the third order aragonite laths (Figure 4.5c, d), which we found less frequently in the foils cut from the outer part of the shell. We observed numerous and variably sized, irregular voids (ca. 30-130 nm in size) rimming the third order lath boundaries, with smaller voids (ca. 5-15 nm in size) *within* these aragonite laths (Figure 4.5c, d, arrows). They appear to be focused along the outer areas of the laths in the inner shell layer, resulting in irregular 50-100 nm-wide concentration zones of voids. While the foil cut perpendicular to the long axis of the aragonite laths (Figure 4.5c) shows these voids apparently

distributed at random, the rims of the laths cut parallel to their longest axes in Figure 4.5d are not completely enclosed by a focus zone of voids. It is possible that this apparent preferential focus in Figure 4.5d is a sectioning effect from foil preparation.

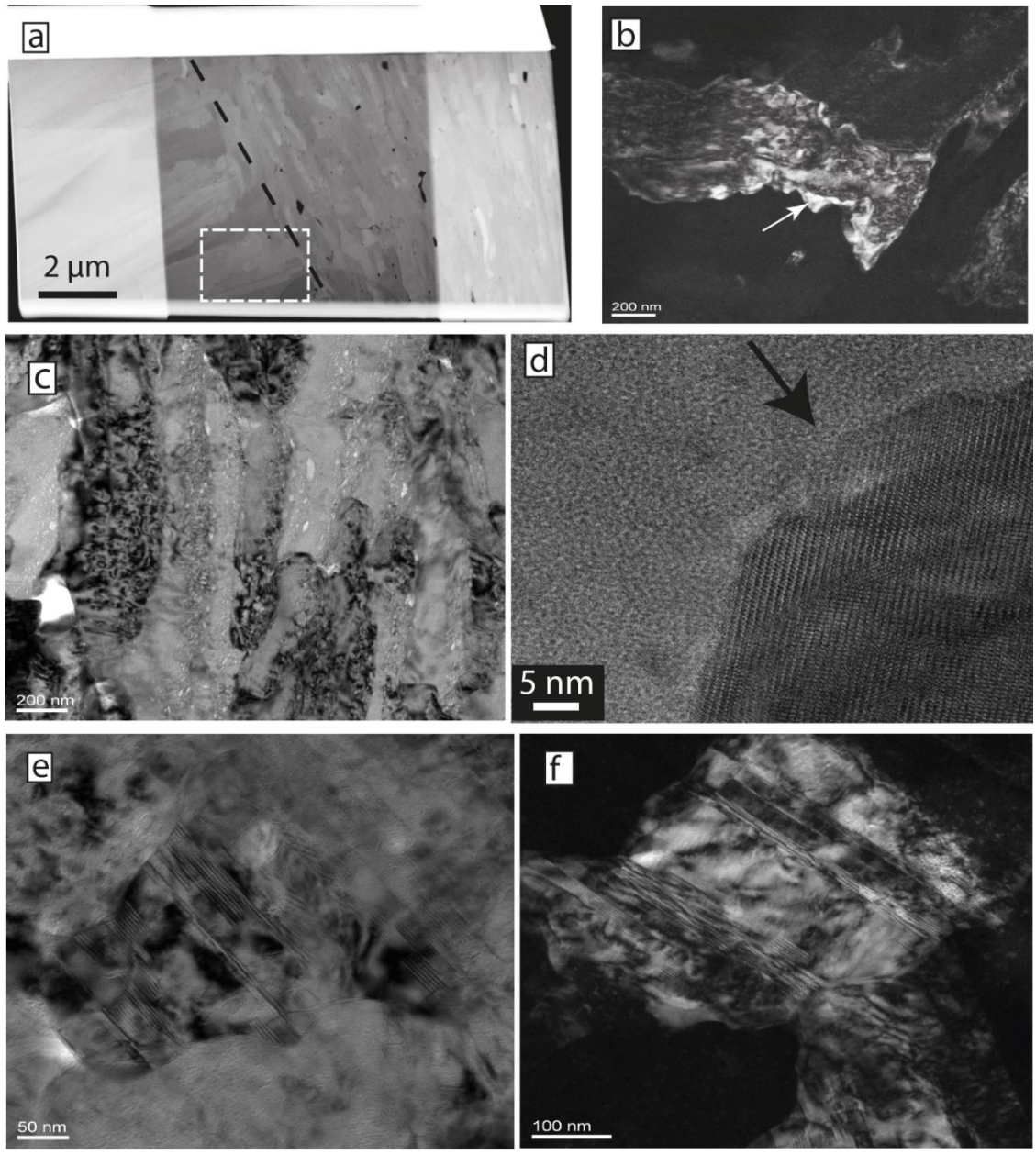

Figure 4.6. TEM foil cut perpendicular to the growth lines in the shell and across an interface (black dashed line) between two first order lamellae containing second order lamellae of different orientation (a, foil thinned in the central part, HAADF image, inner shell layer). (b) Dark Field image of an aragonite grain outlined with the white dashed box in (a). Note the irregular shape and 'speckled' diffraction contrast. (c) Bright Field Image showing numerous inter- and intragranular voids similar to those shown by STEM imaging in Fig. 5c, d. High Resolution TEM images of the tip (d) of a third order lath shows crystal lattice fringes up to the edges of the grain (arrow), no amorphous phases (neither inorganic nor organic) are detected here. (e) Irregularly shaped aragonite grain (Bright Field Image) with polycyclic twinning lamellae, (f) Dark Field Image of the same grain (foil #2592).

Crystal shapes in both layers of the shell are highly irregular (Figure 4.6a - f) and aragonites commonly display a variable and strongly ‘speckled’ diffraction contrasts in TEM bright and dark field imaging, where different areas within an individual grain display sharply different diffraction contrasts (e.g. Figure 4.6b, arrow). Polycyclic/polysynthetic twinning is common at the nano-scale in both shell layers (Figure 4.5c, 4.6e, 4.6f).

All areas studied by High Resolution TEM were found to be crystalline, even the rim areas of the grains (Figure 4.6d), which contrasts with nacro-prismatic shells, where amorphous areas are observed [172, 232], amounting to 10 at% in some shells [15]. Nevertheless, results from Solid-State Nuclear Magnetic Resonance Spectroscopy on the same *T. derasa* shell sample indicate an overall amount of 3-7 at% of amorphous calcium carbonate [15], showing that while this phase is present in the shell, it was apparently not sampled by any of the TEM foils in this study.

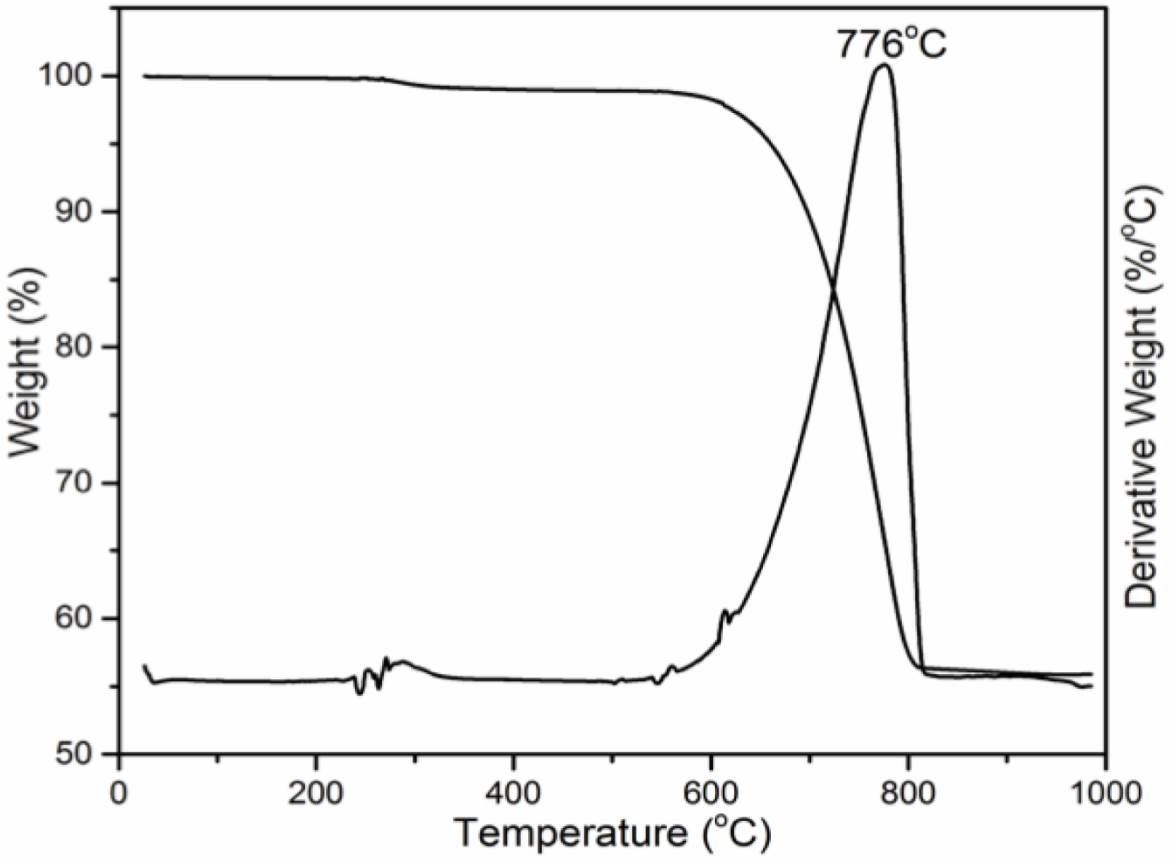

Figure 4.7. Differential thermal analysis (DTA) and thermogravimetric analysis (TGA). The range 150–500°C was used for calculation of the total organic matrix content. The peak at 776°C marks the decomposition of calcium carbonate and release of CO_2.

4.3.2 *Thermogravimetric analysis*

Thermogravimetry was used to quantify water and organic contents in a powdered sample of the shell. The total organic matrix amounts to 0.94 wt.% as calculated from the integrated mass loss in the temperature range 150-500ºC (Figure 4.7). Peaks at around 300˚C are attributed to the decomposition of organic macromolecules. Aragonite converts to calcite at ca. 500˚C, as verified by FTIR spectrometry, and decomposition to CaO and CO_2 is completed at around 800ºC (Figure 4.7).

4.3.3 *FTIR spectroscopic characterization of the organic matrix*

Fourier Transform (FTIR) analysis of the total organic matrix extract of the shell reveals prominent structural chitin-protein bands (Table 4.1): bands indicative for amide A (3000–3500 cm^{-1}), amide B (2800–2990 cm^{-1}), amide I (1600–1700 cm^{-1}), amide II (1300–1590 cm^{-1}) and amide III (1190–1290 cm^{-1}) are present. Strong broad bands between 3200 and 3450 cm^{-1} (Figurre 4.8a) are characteristic for OH and/or NH stretching modes. The band at 1403 cm^{-1} (Figure 4.8a) is assigned to the C=O stretching of structural proteins and amino acids. Other major bands at 1113 cm^{-1}, 1067 cm^{-1} and 1028 cm^{-1} represent sugars in the chitin structure [149, 150] (Table 4.1). The band at 1626 cm^{-1} corresponds to the C=O stretch in amide I and indicates β-sheet structure of the chitin [236]. The β-sheet structure was confirmed by measuring the optical activity of the soluble organic matrix in solution where the chitin was found to have a stable negative optical rotation of -25^{o} after seven days [237].

A well-defined band at 1461 cm^{-1} (Figure 4.8a) is attributed to amide II (Table 4.1), while bands at 1203 cm^{-1} and 1255 cm^{-1} are the carbonyl stretching and amide deformation vibrations of amide III (Table 4.1). The OH and/or NH functional groups for amide A and the C-H stretching modes for amide B have many prominent bands in the soluble organic matrix, for example at 3487 cm^{-1}, 2959 and 2872 cm^{-1}.

Major bands between 1000 and 1150 cm^{-1} [85, 110], and 952-980 cm^{-1} [150] are indicative of sugars. The carbonyl bands (C-O-H) between 1113 cm^{-1} and 1028 cm^{-1}, and C-H vibrational

bands between 946 to 987 cm^{-1} (Table 4.1) are most likely C-O stretching vibrations in *N*-acetylglucosamine in the sugars [150]. The bands at 845 cm^{-1} and 902 cm^{-1} are characteristics of the β-configuration in the anomeric centre [238], confirming the presence of polysaccharides.

The extracted lipids and lipoproteins (Figure 4.8b), show indicative bands at 3394 cm^{-1} (O-H), 1682 cm-1 (Amide I) and 1619.5 cm^{-1} (C=C), while sugar bands are seen between 1150 and 1000 cm^{-1} and are strong in the fingerprint region at 666 cm^{-1} and 593 cm^{-1}.

4.4 Discussion

4.4.1 *Characteristics of the multiscale shell architecture and orqanic moiety*

Compared to the prism-nacre microstructure of mollusc shells, the crossed-lamellar architecture of the *T. derasa* shell is highly mineralized with only 0.9 wt% total organic content compared to >3 wt% in nacre [175]. Its structure is distinctly different and overall more complex than the nacro-prismatic structure [65], with three hierarchy orders of aragonite laths creating an interlocking fabric reminiscent of plywood (Figure 4.1; [9, 51]). Some authors have interpreted polycyclic aragonitic growth twins occurring in the third order structure as a fourth hierarchical order (e.g. [68, 239, 240].

In *T. derasa* shells, the first order lamellae run approximately perpendicular to the growth layers (GL in Figure 4.2), and radially with respect to the shell surface. They comprise thin particulate lamellae with high aspect ratios (second and third order structures: Figure 4.1b), showing voids along grain boundaries, and within grains at the nanoscale (Figure 4.5c, d) that contain organic macromolecules [241]. In contrast to nacro-prismatic bivalve shells, whose architecture consists of well-defined inter-crystalline organic matrix (the so-called interlamellar membranes) interlayered with mineral incorporating intra-crystalline organic matrix molecules, the crossed-lamellar *T. derasa* shell does not show a similarly prominent organic inter-crystalline framework [242].

Within the first order lamellae, the CPO map (Figure 4.2a) shows areas of second order lamellae that are highly co-oriented, meaning that crystal co-orientation of aragonites for these

areas is coherent across the organic layers between the aragonite laths as well as the organic growth lines shown in Fig. 1e. Similar aragonite tablets highly co-aligned across their organic envelopes occur in nacre [243] and are thought to form by a combination of epitaxial crystallization via mineral bridges across the organic envelopes [244] as well as due to competition for space upon growth [245]. It is conceivable that a similar model could be proposed for the formation of the domainal organization in crossed-lamellar structures.

Voids are a characteristic feature of biominerals and are common in bivalve shells irrespective of their microstructure [69, 241, 246, 247]. The voids shown by the TEM analysis (Figure 4.4 – 4.6), have larger diameters along the grain rims, are smaller within the aragonites (Figure 4.5c) and are more common and larger in the outer shell layer (Figure 4.4) than in the innermost layer of the shell (Figure 4.5). Voids in nacre platelets are smaller (2-40 nm) than found in this study [241, 246, 247]. They are focused towards the inner part of the nacre platelets and form a ca. 50 nm wide void-depleted zone along the outer platelet rim adjacent to the interlamellar organic sheets [241]. This contrasts with our observations, where small voids are more common along the outer areas of each grain (Figure 4.5c, d).

While mollusc shell microstructures differ distinctly at the micron and millimeter scale, a common structural motif exists at the nano-scale. It is an almost universal characteristic of biominerals that they are granular at the nano-scale [15]. The granular features have sizes in the range of tens of nanometers, are embedded in an intergranular organic medium (or cortex), and are easily observed by phase contrast Atomic Force Microscopy (AFM) (e.g. [216, 234, 248, 249]), and their presence is supported using Transmission Electron Microscopy (e.g. [36, 232]): Irregular grain boundaries (Figure 4.5c, 4.6b, e, f) and small voids (Figure 4.5c, d) outline the shapes of the nanogranules in the TEM images. This granular nano-structure in mollusc shells is a consequence of their colloid-mediated, nonclassical mode of growth [21, 250].

The organic shell matrix in *T. derasa* consists of a mixture of polysaccharides as well as glycosylated and un-glycosylated proteins and lipids (Figure 4.8a), which is a rather typical

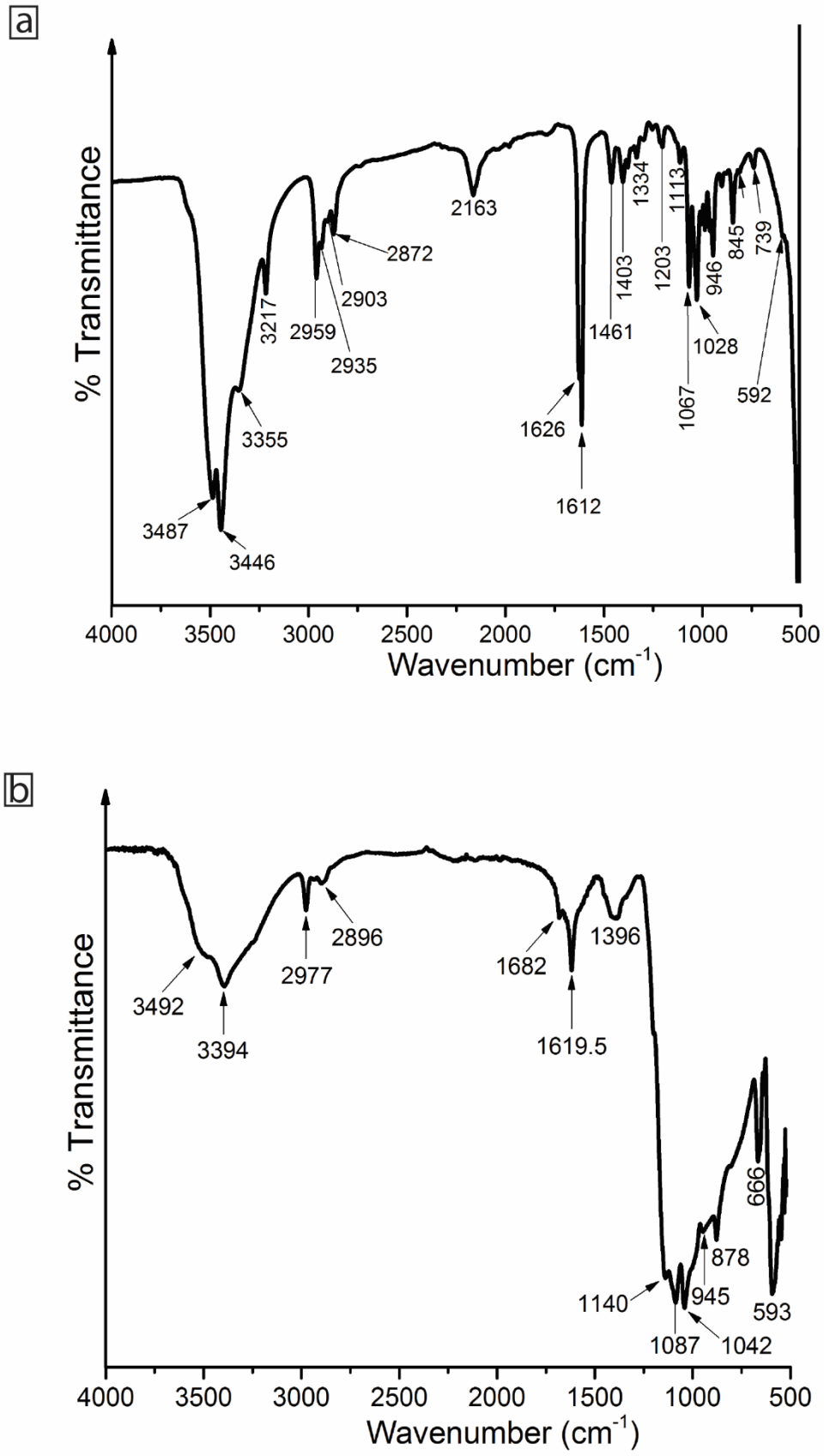

Figure 4.8. (a) FTIR spectra of the total organic matrix in the range of 4000-500 cm^{-1}. (b) FTIR spectrum of lipids and lipoproteins extracted from the shell sample. For band assignments see Table 1.

general organic assemblage in mollusc shells [57, 251]. The polysaccharides play a major role providing organic 'scaffolding' for the mineralized part (e.g. [57, 89]), but may also have an active function of lowering the energy barriers for mineral nucleation [108]. The presence of polysaccharides, not only in nacro-prismatic mollusk shells but also in shells with crossed-lamellar microstructure, reiterates the applicability of the general biomineralization models that promote polysaccharides as the major organic template in this process (e.g. [124]).

4.4.2 *Aspects of mechanical properties of the crossed-lamellar microstructure*

The strength and toughness of shells are specifically distinct and superior to non-biogenic aragonite [5], with the crossed-lamellar shell microstructure displaying the highest fracture toughness [69]. These emergent mechanical properties of shells are a consequence of a combination of parameters including (but not limited to) the complex, multi-order hierarchy [69], their nano-granular texture [252], the organic-inorganic nano-composite nature of the material [253, 254], and high flaw tolerance at the nanoscale [255].

Crystallographically, the crossed-lamellar structure of the *T. derasa* shell belongs to a family of similar, but not identical structures. In a comprehensive study of forty mollusc species including a closely related species, *Tridacna gigas*, Almagro et al. [65] distinguished five crystallographic groups of crossed-lamellar structures. Among these, *Tridacna* shells display a strong fiber texture with highly oriented crystallographic c-axes, and randomly oriented a and b axes (Figure 8.2c). In fact, the texture of *Tridacna derasa* (see Figure 8.2d for scale of textural index) ranges amongst the strongest mollusc shell textures (e.g. [65, 256, 257]).

The aragonite crystallographic c-axes ([001]) in the *Tridacna derasa* shell are oriented perpendicular to the growth lines (GL in Figure 4.2c), thus, are radially oriented with respect to the shell surface. Aragonite single crystals are elastically anisotropic [258], with the anisotropy of the Young's modulus reaching values around 50% between the weakest and stiffest axis (Figure 4.9a). The stiffest axis is [100] with a Young's modulus value of *ca.* 140

GPa, whereas the [010] and [001] axes are considerably weaker with values of around 80 GPa (Figure 4.9a).

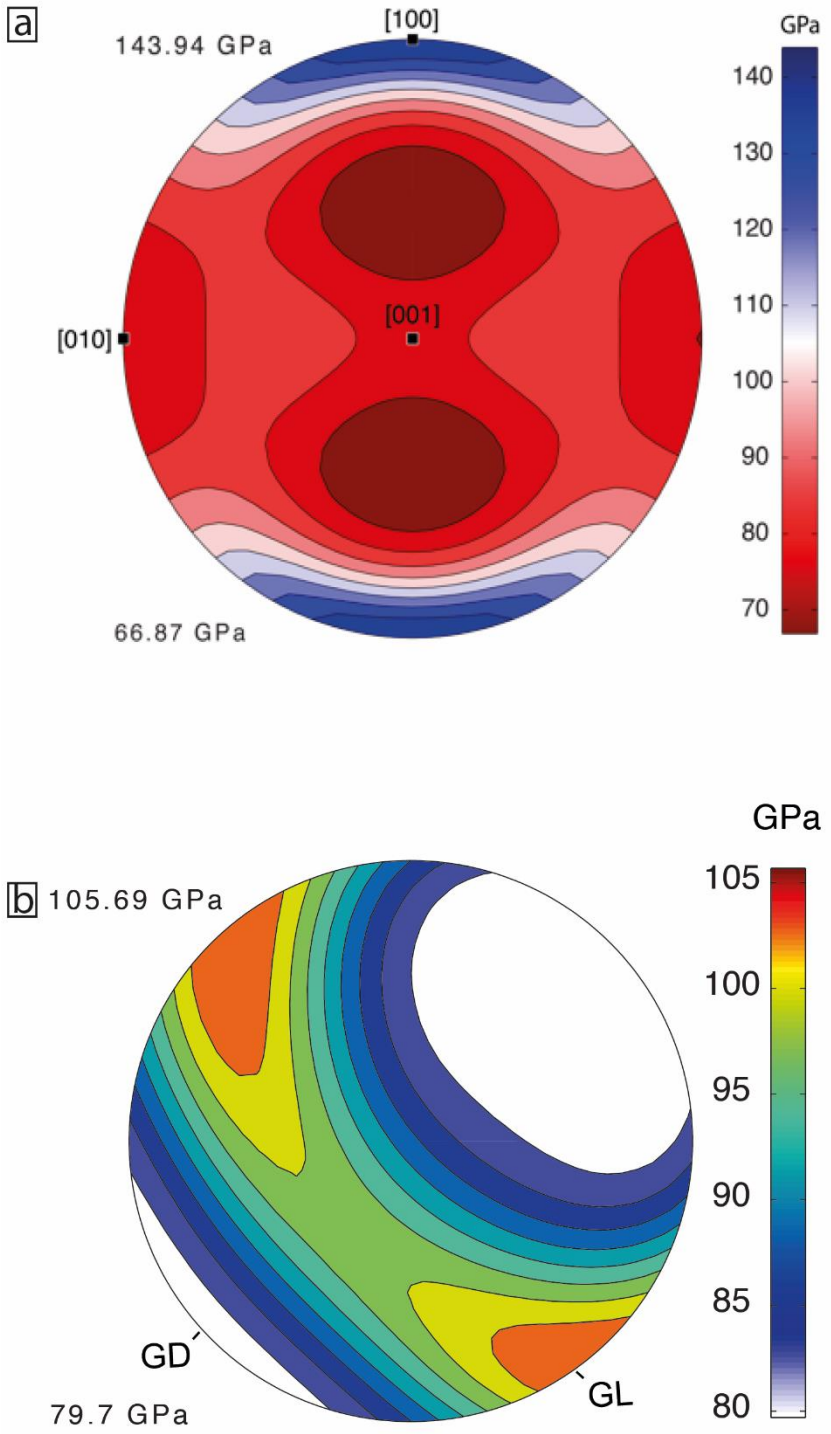

Figure 4.9. Young's modulus derived from the crystallographic preferred orientation for the *Tridacna derasa* shell. **(a)** Young's modulus for a single crystal of aragonite calculated via the Voigt-Reuss-Hill averaging scheme based on the aragonite elastic constants by De Villiers [259]. (b) Young's modulus for the EBSD orientation map in Figure 4.2a via Voigt-Reuss-Hill averaging scheme for the aggregate elastic constant (using the single crystal elastic constants of De Villiers, [259]). Note the development of a plane of isotropy following the distribution of aragonite [100] and [010] axes, leading to the optimization of general stiffness in all

directions along the growth lines. Numbers in GPa are Young's modulus maximum and minimum values (cf. scale).

The weakest direction in an aragonite single crystal lies at an intermediate position between [100] and [001]. By averaging the elastic constant of the *T. derasa* shell based on its crystallographic preferred orientation, it is possible to estimate the general stiffness of the shell based on the elastic properties of the aragonite single crystals. The CPO shows that [100] and [010] are orientated along a girdle around [001]. Such a CPO leads to the development of a plane of quasi-isotropy of the Young's modulus parallel to the girdle of the stiff axis [100] and the weak axis [010] (Figure 4.9b). This minimizes the natural elastic anisotropy of aragonite in this plane while optimizing the general stiffness and resistance of the shell in all directions. Ouhenia et al. [260] recognized a similar strategy for shells of the gastropod *Charonia lampas lampas*: These shells consist of a stack of three different crossed-lamellar layers, whose alternated orientations maximize the stiffness coefficients in all directions of the whole shell. This mechanical effect is further enhanced by the crystal orientation angle spread due to twinning. The combined use of TEM and EBSD shows that twinning, which is common at the nanoscale, remains a prominent structural motif across all hierarchical orders with at least 26% twin boundaries (as detected at the millimetre scale across the CPO map by EBSD, Figure 4.2b). Most likely, this complex architectural design is aimed at increasing isotropy [215], adding to other strategies aimed at optimizimg mechanical properties and providing a significant evolutionary advantage by generating higher rigidity and wear resistance that is beneficial to the organism's protection.

4.5 Conclusion

Tridacna derasa shells are highly mineralised bio-ceramics consisting of aragonite with around 1 wt% organics, namely polysaccharides, glycosylated and un-glycosylated proteins and lipids. The shells have a crossed-lamellar microstructure with a strong fiber texture in which the aragonite crystallographic c-axes are aligned radially to the shell surface. The spread of

crystal orientation angles due to intense twinning at all hierarchical structures, nano-granularity and random orientation of the aragonitic crystallographic a and b axes, optimize the Young's modulus of the shell in all directions and all spatial scales, thus increasing isotropy. This is one of the first comprehensive studies that identify optimization strategies for mechanical properties across all hierarchal structures in the shell.

Table 4.1: Band assignments for the main bands in the FTIR spectra (cm^{-1}) of the shell organic matrix components for *Tridacna derasa.* Band assignments carried out using data from [36, 70, 71]

Total Organic Matrix	Band assignment
3487,3446	ν_{OH}
3355, 3217	ν_{N-H}
2959	ν^{as}_{C-H} of alkyl
2935	ν^{s}_{C-H} of methylene
2903, 2872	ν^{s}_{C-H} of alkyl
1626,1612	$\nu_{C=O}$
1462	δ_{C-H} of alkyl
1403	$\nu^{s}_{C=O}$
1334	$\delta_{C-N} + \delta_{N-H}$
1379	$\delta_{C-H} + \delta_{C-CH3}$
1255	δ_{N-H}
1203	ν_{C-O}
1298	ν_{C-O}
1028, 1067,1113	ν_{C-O-H}
987	γ_{C-H} of alkyl
962, 946	γ_{C-H} of methylene
902	γ_{C-H}
845	γ^{as}_{C-O} deformation
739	ρ_{C-H} of methylene
592	γ_{C-C}

Acknowledgements

We thank Kenji Iwai for providing the cultured shell sample. J. Huth (MPI Chemistry) is thanked for expert assistance with SEM imaging and we are grateful to A. Schreiber for TEM foil sample preparation.

4.6 References

1. Marin, F., N. Le Roy, and B. Marie, *The formation and mineralization of mollusk shell.* Front Biosci, 2012. **4**: p. 1099-1125.
2. Weiner, S. and W. Traub, *X-ray diffraction study of the insoluble organic matrix of mollusk shells.* FEBS letters, 1980. **111**(2): p. 311-316.
3. Kamat, S., et al., *Structural basis for the fracture toughness of the shell of the conch Strombus gigas.* Nature, 2000. **405**(6790): p. 1036-1040.
4. Currey, J. and A. Kohn, *Fracture in the crossed-lamellar structure ofConus shells.* Journal of Materials Science, 1976. **11**(9): p. 1615-1623.
5. Jackson, A., J. Vincent, and R. Turner, *The mechanical design of nacre.* Proceedings of the Royal society of London. Series B. Biological sciences, 1988. **234**(1277): p. 415-440.
6. Weiner, S. and L. Addadi, *Design strategies in mineralized biological materials.* J. Mater. Chem., 1997. **7**(5): p. 689-702.
7. Boggild, O.B., *The shell structure of the mollusks.* Det Kongelige Danske Videnskabernes Selskabs Skrifter, Natruvidenskabelig og Mathematisk, Afdeling, Ser. 9, 1930. **2**: p. 231-326.
8. Almagro, I., et al., *New crystallographic relationships in biogenic aragonite: the crossed-lamellar microstructures of mollusks.* Crystal Growth & Design, 2016. **16**(4): p. 2083-2093.
9. Böhm, C.F., et al., *Structural commonalities and deviations in the hierarchical organization of crossed-lamellar shells: a case study on the shell of the bivalve Glycymeris glycymeris.* Journal of Materials Research, 2016. **31**(5): p. 536-546.
10. Carter, J.G., *Skeletal biomineralization: patterns, processes and evolutionary trends*. Vol. 1. 1990: Wiley Online Library.
11. Pokroy, B. and E. Zolotoyabko, *Microstructure of natural plywood-like ceramics: a study by high-resolution electron microscopy and energy-variable X-ray diffraction.* Journal of Materials Chemistry, 2003. **13**(4): p. 682-688.
12. Nakahara, H., M. Kakei, and G. Bevelander, *Studies on the formation of the crossed lamellar structure in the shell of strombus gigas.* Veliger, 1981. **23**(3): p. 207-&.
13. CUIF, J.-P., A. Denis, and M.-P. TRICLOT, *Ultrastructure de la couche externe du test d'un Veneracea: Dosinia ponderosa (Gray, 1838)(Mollusque, Lamellibranche).* Bulletin du Muséum national d'histoire naturelle. Section A, Zoologie, biologie et écologie animales, 1985. **7**(4): p. 741-759.
14. Dauphin, Y. and A. Denis, *Structure and composition of the aragonitic crossed lamellar layers in six species of Bivalvia and Gastropoda.* Comparative Biochemistry and Physiology Part A: Molecular & Integrative Physiology, 2000. **126**(3): p. 367-377.
15. Wilmot, N., et al., *Electron microscopy of molluscan crossed-lamellar microstructure.* Philosophical Transactions of the Royal Society B: Biological Sciences, 1992. **337**(1279): p. 21-35.
16. Kobayashi, I. and J. Akai, *Twinned aragonite crystals found in the bivalvian crossed lamellar shell structure.* The Journal of the Geological Society of Japan, 1994. **100**(2): p. 177-180.
17. Bonham, K., *Growth rate of giant clam Tridacna gigas at Bikini Atoll as revealed by radioautography.* Science, 1965. **149**(3681): p. 300-302.
18. Sano, Y., et al., *Past daily light cycle recorded in the strontium/calcium ratios of giant clam shells.* Nature communications, 2012. **3**: p. 761.
19. Lamprell, K., T. Whitehead, and J. Healy, *Bivalves of Australia*. 1992: Crawford House Press.
20. Besley, P., G. Ross, and A. Wells, *Mollusca: the southern synthesis.: Fauna of Australia*. 1998, CSIRO Publishing, Melbourne.
21. Prior, D.J., et al., *The application of electron backscatter diffraction and orientation contrast imaging in the SEM to textural problems in rocks.* American Mineralogist, 1999. **84**(11-12): p. 1741-1759.
22. Randle, V. and O. Engler, *Introduction to texture analysis: macrotexture, microtexture and orientation mapping*. 2000: CRC press.

23. Bachmann, F., et al., *Inferential statistics of electron backscatter diffraction data from within individual crystalline grains.* Journal of Applied Crystallography, 2010. **43**(6): p. 1338-1355.
24. Hielscher, R. and H. Schaeben, *A novel pole figure inversion method: specification of the MTEX algorithm.* Journal of Applied Crystallography, 2008. **41**(6): p. 1024-1037.
25. Wirth, R., *Focused Ion Beam (FIB):A novel technology for advanced application of micro- and nanoanalysis in geosciences and applied mineralogy.* European Journal of Mineralogy, 2004. **16**(6): p. 863-876.
26. Branson, O., et al., *The coordination and distribution of B in foraminiferal calcite.* Earth and Planetary Science Letters, 2015. **416**: p. 67-72.
27. Kato, N.I., *Reducing focused ion beam damage to transmission electron microscopy samples.* Journal of electron microscopy, 2004. **53**(5): p. 451-458.
28. Ishitani, T. and T. Yaguchi, *Cross-sectional sample preparation by focused ion beam: A review of ion-sample interaction.* Microscopy research and technique, 1996. **35**(4): p. 320-333.
29. Jacob, D., et al., *Nanostructure, composition and mechanisms of bivalve shell growth.* Geochimica et Cosmochimica Acta, 2008. **72**(22): p. 5401-5415.
30. Jacob, D., et al., *Amorphous calcium carbonate in the shells of adult Unionoida.* Journal of structural biology, 2011. **173**(2): p. 241-249.
31. Austin, P.R., et al., *Chitin: new facets of research.* Science, 1981. **212**(4496): p. 749-753.
32. Dauphin, Y., *The nanostructural unity of Mollusc shells.* Mineralogical Magazine, 2008. **72**(1): p. 243-246.
33. Hovden, R., et al., *Nanoscale assembly processes revealed in the nacroprismatic transition zone of Pinna nobilis mollusc shells.* Nature communications, 2015. **6**.
34. Nassif, N., et al., *Amorphous layer around aragonite platelets in nacre.* Proceedings of the National Academy of Sciences of the United States of America, 2005. **102**(36): p. 12653-12655.
35. Wolf, S.E., et al., *Nonclassical crystallization in vivo et in vitro (I): process-structure-property relationships of nanogranular biominerals.* Journal of Structural Biology, 2016. **196**(2): p. 244-259.
36. Cárdenas, G., et al., *Chitin characterization by SEM, FTIR, XRD, and 13C cross polarization/mass angle spinning NMR.* Journal of Applied Polymer Science, 2004. **93**(4): p. 1876-1885.
37. Stankiewicz, B.A., et al., *Biodegradation of the chitin-protein complex in crustacean cuticle.* Organic Geochemistry, 1998. **28**(1): p. 67-76.
38. Jackson, M. and H.H. Mantsch, *The use and misuse of FTIR spectroscopy in the determination of protein structure.* Critical reviews in biochemistry and molecular biology, 1995. **30**(2): p. 95-120.
39. Brine, C.J. and P.R. Austin, *Chitin isolates: species variation in residual amino acids.* Comparative Biochemistry and Physiology Part B: Comparative Biochemistry, 1981. **70**(2): p. 173-178.
40. Dauphin, Y., *Soluble organic matrices of the calcitic prismatic shell layers of two pteriomorphid bivalves Pinna nobilis and Pinctada margaritifera.* Journal of Biological Chemistry, 2003. **278**(17): p. 15168-15177.
41. Pereira-Mouriès, L., et al., *Soluble silk-like organic matrix in the nacreous layer of the bivalve Pinctada maxima.* European Journal of Biochemistry, 2002. **269**(20): p. 4994-5003.
42. Zhbankov, R., V. Andrianov, and M. Marchewka, *Fourier transform IR and Raman spectroscopy and structure of carbohydrates.* Journal of Molecular Structure, 1997. **436**: p. 637-654.
43. Agbaje, O.B.A., et al., *Organic macromolecules in shells of Arctica islandica: comparison with nacroprismatic bivalve shells.* Marine Biology. In review., 2017.
44. Nouet, J., A. Baronnet, and L. Howard, *Crystallization in organo-mineral micro-domains in the crossed-lamellar layer of Nerita undata (Gastropoda, Neritopsina).* Micron, 2012. **43**(2): p. 456-462.

45. Younis, S., et al., *Atomic structure and ultrastructure of the Murex troscheli shell.* Journal of structural biology, 2012. **180**(3): p. 539-545.
46. Younis, S., et al., *Inhomogeneity of nacre lamellae on the nanometer length scale.* Crystal Growth & Design, 2012. **12**(9): p. 4574-4579.
47. Erben, H.K. and N. Watabe, *Crystal formation and growth in bivalve nacre.* 1974.
48. Gilbert, P., et al., *Gradual ordering in red abalone nacre.* Journal of the American Chemical Society, 2008. **130**(51): p. 17519-17527.
49. Schäffer, T.E., et al., *Does abalone nacre form by heteroepitaxial nucleation or by growth through mineral bridges?* Chemistry of Materials, 1997. **9**(8): p. 1731-1740.
50. Checa, A.G., T. Okamoto, and J. Ramírez, *Organization pattern of nacre in Pteriidae (Bivalvia: Mollusca) explained by crystal competition.* Proceedings of the Royal Society of London B: Biological Sciences, 2006. **273**(1592): p. 1329-1337.
51. Li, H., et al., *Calcite prisms from mollusk shells (Atrina Rigida): swiss-cheese-like organic–inorganic single-crystal composites.* Advanced Functional Materials, 2011. **21**(11): p. 2028-2034.
52. Gries, K., et al., *Investigations of voids in the aragonite platelets of nacre.* Acta biomaterialia, 2009. **5**(8): p. 3038-3044.
53. Rousseau, M., et al., *Multiscale structure of sheet nacre.* Biomaterials, 2005. **26**(31): p. 6254-6262.
54. Wolf, S.E., et al., *Merging models of biomineralisation with concepts of nonclassical crystallisation: is a liquid amorphous precursor involved in the formation of the prismatic layer of the Mediterranean Fan Mussel Pinna nobilis?* Faraday Discussions, 2012. **159**(1): p. 433-448.
55. De Yoreo, J.J., et al., *Crystallization by particle attachment in synthetic, biogenic, and geologic environments.* Science, 2015. **349**(6247): p. aaa6760.
56. Gower, L.B. and D.J. Odom, *Deposition of calcium carbonate films by a polymer-induced liquid-precursor (PILP) process.* Journal of Crystal Growth, 2000. **210**(4): p. 719-734.
57. Simkiss, K., *The organic matrix of the oyster shell.* Comparative biochemistry and physiology, 1965. **16**(4): p. 427IN9429-428435.
58. Levi-Kalisman, Y., et al., *Structure of the nacreous organic matrix of a bivalve mollusk shell examined in the hydrated state using cryo-TEM.* Journal of structural biology, 2001. **135**(1): p. 8-17.
59. Giuffre, A.J., et al., *Polysaccharide chemistry regulates kinetics of calcite nucleation through competition of interfacial energies.* Proceedings of the National Academy of Sciences, 2013. **110**(23): p. 9261-9266.
60. Weiner, S. and P.M. Dove, *An overview of biomineralization processes and the problem of the vital effect.* Reviews in Mineralogy and Geochemistry, 2003. **54**(1): p. 1-29.
61. Li, X., et al., *Nanoscale structural and mechanical characterization of a natural nanocomposite material: the shell of red abalone.* Nano Letters, 2004. **4**(4): p. 613-617.
62. Fratzl, P., et al., *Hindered crack propagation in materials with periodically varying Young's modulus—lessons from biological materials.* Advanced Materials, 2007. **19**(18): p. 2657-2661.
63. Smith, B.L., et al., *Molecular mechanistic origin of the toughness of natural adhesives, fibres and composites.* Nature, 1999. **399**(6738): p. 761-763.
64. Gao, H., et al., *Materials become insensitive to flaws at nanoscale: lessons from nature.* Proceedings of the national Academy of Sciences, 2003. **100**(10): p. 5597-5600.
65. Chateigner, D., C. Hedegaard, and H.-R. Wenk, *Mollusc shell microstructures and crystallographic textures.* Journal of Structural Geology, 2000. **22**(11): p. 1723-1735.
66. Chateigner, D., et al., *Structural distortion of biogenic aragonite in strongly textured mollusc shell layers.* Nuclear Instruments and Methods in Physics Research Section B: Beam Interactions with Materials and Atoms, 2010. **268**(3): p. 341-345.
67. Han, Y.H., et al., *Knoop Microhardness Anisotropy of Single-Crystal Aragonite.* Journal of the American Ceramic Society, 1991. **74**(12): p. 3129-3132.

68. Ouhenia, S., et al., *Microstructure and crystallographic texture of Charonia lampas lampas shell.* Journal of structural biology, 2008. **163**(2): p. 175-184.
69. Villiers, J.P.R.D., *Crystal structures of aragonite, strontianite, and witherite.* American Mineralogist, 1971. **Vol. 56**: p. 758–767.
70. Marxen, J.C. and W. Becker, *The Organic Shell Matrix of the Freshwater Snail< i> Biomphalaria glabrata</i>.* Comparative Biochemistry and Physiology Part B: Biochemistry and Molecular Biology, 1997. **118**(1): p. 23-33.
71. Focher, B., et al., *Structural differences between chitin polymorphs and their precipitates from solutions—evidence from CP-MAS 13C-NMR, FT-IR and FT-Raman spectroscopy.* Carbohydrate Polymers, 1992. **17**(2): p. 97-102.

Inorganic-organic relationships in the crossed lamellar shells

Oluwatoosin B. A. Agbaje[1*], Denise E.Thomas[2], J. Gabriel J. Dominguez[3], Bernie V. Mclnerney[2], Matthew A. Kosnik[3], Dorrit E. Jacob[1]

[1]Department of Earth and Planetary Sciences, Macquarie University, NSW 2109 Australia
[2]Australian Proteome Analysis Facility (APAF), Macquarie University, NSW, 2109 Australia
[3]Department of Biological Sciences, Macquarie University, NSW, 2109 Australia

Abstract Here we present an in-depth characterisation of two bivalve shells with crossed lamellar microstructure, namely *Tridacna gigas* and *Fulvia tenuicostata*. High-resolution scanning electron microscopy and confocal microscopy imaging reveal a fine structure of nanogranular particles that are inorganic-bioorganic nanocomposites for both, *T. gigas* and *F. tenuicostata*. In *Fulvia tenuicostata*, inorganic-organic components are arranged in a polycrystalline fibre-like fabric. *Tridacna gigas* consists of up to four hierarchical lamellar structural orders; the second order lamellae include elongated nanometer-sized laths (third order lamellae). The total amount of organic matter (1.8 and 1.5 wt%) is lower, and the composition of the organic matrix is variable between the two species. This work shows for the first-time the presence of chitin and its derivatives as well as many prominent protein bands, glycoproteins and/or glycosaminoglycans of unknown size (far above 260 kDa) in bivalve shells with crossed lamellar microstructure. Chitosan (deacetylated chitin) with apparent molecular weights from 18 to 110 kDa for *Tridacna gigas* and from 12 kDa till above 110 kDa for *Fulvia tenuicoststa* are detected in gel-electrophoresis after Calcofluor staining. Our new findings indicate that chitin-protein-complex and lipid-lipoproteins may be essential for shells with different microstructures. The amount of polysaccharides in crossed lamellar may be lower compared to that found in nacroprismatic shells due to the total amount of organics. Identification of chitin-containing carbohydrate from two crossed lamellar shells representing two molluscan orders and families show that this biopolymer is not restricted only to families with nacroprismatic shells.

Keywords: *Tridacna gigas*; *Fulvia tenuicostata*; laths; fibres; chitin deacetylated; Calcofluor White M2R.

5.1. Introduction

Molluscan shells are biocomposites consisting of a mineral phase (aragonite and/or calcite) and organic macromolecules intergrown at the nanoscale [1, 2]. Amongst all different shell microstructures nacre is the most studied to date due to its exceptional toughness [3, 4] and its biocompatibility [5], while comparable knowledge is lacking for shells with non-nacreous microstructures. One of these is the crossed lamellar microstructure, which is the most widespread microstructure in mollusc shells [1].

Compared with nacreous shells, which contain approximately 3 wt% of organics [6], the crossed-lamellar shells are more mineralized with only around 1 wt% organic moiety [7, 8]. As is typical for the architecture of many biominerals, the crossed lamellar structure is hierarchically organized with up to four hierarchical orders [9, 10]. With very few exceptions, shells with this structure are aragonitic rather than calcitic [11, 12]. Crossed lamellar shells from different species vary in structural arrangement but share the architectural similarity [13] of hierarchically organized lamellae consisting of organic-coated aragonitic laths (Fig. 1) or fibers (Fig. 2) with alternating orientations at angles of ca. 70–90° [12, 14, 15].

Macromolecules occluded in the calcareous biominerals play a crucial role in the nucleation and growth of the inorganic calcium carbonate phase [2] as well as in optimizing the intrinsic properties of the inorganic matrix at all spatial scales [3, 16]. While the composition of shell macromolecules varies between different species and shell microstructures, they generally include soluble organic fraction, comprising lipids-lipoproteins [17] and proteins rich in acidic amino acids [18]. The acidic proteins are covalently linked to proteoglycans-glycosaminoglycans, sulfated polysaccharides and/or glycoproteins [19]. Neutral and amino sugars constitute a part of the carbohydrate fraction [20, 21]. Though the exact molecular mechanisms by which the organic biomolecules control the mineralisation are not fully understood, they are linked to the ability of negatively charged polyanionic groups to bind Ca^{2+}

ions [22-24], thus locally increasing super-saturation and initiating hetero-epitaxial nucleation [25]. Organic fibres comprising a chitin-protein-complex are believed to exert a fundamental role in biomineralisation by creating a hydrophobic environment and inhibit non-specific nucleation [23, 26]. However, it is yet unclear whether these specific macromolecules are present in lamellar bivalve shells [12, 26, 27].

Only a few studies have described the organic matrix in mollusc shells with crossed lamellar microstructure and these have mostly focused on the soluble organic matrix of gastropods [12, 15, 20, 21, 28]. One of the fundamental questions concerning the composition of organic matrix in the shells with crossed lamellar structures is whether shell proteins and polysaccharides β-chitin (and its derivatives) are restricted to some micro-textures, such as nacre-prism species. To address this question, we studied *Tridacna gigas* and *Fulvia tenuicostata* shells as examples for shells with crossed lamellar microstructure with newly developed extraction methods for organic macromolecules. We present a detailed biochemical analysis of the shell macromolecules including chitin and its derivatives, shell proteins and saccharidic composition of the shells.

5.2. Materials and methods

5.2.1. Materials

Tridacna gigas (Linnaeus, 1758), (Bivalvia, Veneroida), is the largest species in the phylum Mollusca and the family Tridacnidae, reaching shell lengths of up to ~130 cm with average lifespan in the wild of over 100 years [29]. It occurs throughout Australasia and is an important part of coral reef biodiversity [30]. In April 2014, the Australian Fisheries Management Authority (AFMA) seized ca. 200 *T. gigas* from Fishermen illegally operating in Australian territorial waters of the Timor Sea near Evans Shoal, about 184 nautical miles north of Darwin, Northern Territory. Four of these shells were provided to Macquarie University for use in research projects and teaching activities. Sample 257842-B was used here. The timing and

location of the shells is unknown. However, it is certain that they were collected within a few days of the seizure and most likely, the sourced of the shells were very close to the location where they were seized (09°54'23" South and 129°35'23' East).

The common southern cockle, *Fulvia tenuicostata* (Lamarck, 1819), (Bivalvia: Cardiida), is a member of the cardiidae family and reaches a maximum size of ~6 cm, with average lifespans of about 5 years [31]. *Fulvia tenuicostata* is native to Australia and occurs mostly along the southern parts with Sydney as the current most northern distribution [29]. The shell is generally common in Sydney Harbour death assemblages, but live animals are very rare [31]. Several subfossil *F. tenuicostata* shells (ca. 2000 years old; [31]) from the Sydney Harbour, Australia were used in this study.

5.2.2. Methods

5.2.2.1. Sample Preparation and Thermogravimetry Analysis

The *Tridacna* shell is entirely aragonitic and consist of two major macrolayers: an inner translucent layer with visible growth increments and a massive outer white layer [8]. The outer part of the *T. gigas* shell fragment was removed with a diamond rock saw before analysing the remaining inner translucent layer. Unlike *Tridacna* with massive layers, *F. tenuicostata* shells consist of two thin aragonitic layers and whole shells have been utilised in this study. Fragments of *F. tenuicostata* shells were washed thoroughly in Milli-Q water and immersed in ethanol for 24 h with two ultrasonic treatments before rinsing and drying at room temperature. Both, *Tridacna* and *F. tenuicostata* shells were immersed in 30% H_2O_2 (Merck KGaA, 64271 Darmstadt; Germany) for 2 h at room temperature combined with ultrasonic treatment, washed extensively with Milli-Q water and air-dried. Samples were powdered with a rock crusher before Thermogravimetric analysis (TGA/DTA) was performed using a TGA 2050 Thermogravimetric Analyzer (TA Instruments, USA). About 30 mg of powdered sample was measured at a rate of 10ºC/min in a temperature interval from room temperature (21˚C) up to 1000˚C.

5.2.2.2. Scanning Electron and Fluorescence Microscopy

Shell fragments were etched with EDTA (1% wt/vol), gold-coated and imaged with either a JEOL JSM-7100F Field Emission- Scanning Electron Microscope (FESEM) or a JEOL JSM-6480LA Scanning Electron Microscope. For histochemical staining, broken pieces of shell were submerged in 10% glacial acetic acid for decalcification at 4^{o}C for 7 d. After thorough rinsing with distilled water, the acid-insoluble samples were stained with Calcofluor White M2R (Fluorescent brightener F-3543 Sigma-Aldrich; 0.1%). Images of the stained organic matrix were collected with an Olympus Fluoview FV1000 laser confocal microscope (Olympus, Japan) built around an IX81 inverted microscope fitted with a 60X oil immersion objective and using a laser diode at 405µm and in the UV-spectrum (425-525 µm).

5.2.2.3. Extraction of Shell Macromolecules and Infrared Spectroscopy

About 50 g of powdered sample was decalcified in 1mM HCl (and pH was raised to with Milli-Q water to the ~ 7) and the extracts centrifuged, separating the insoluble organic residue from the soluble organic matrix (SOM) in the supernatant. To characterise the organic moiety in the insoluble matrices, the insoluble residue was lyophilized and then decalcified in 1:1 (pH ~4) of 0.1 N trichloroacetic acid and phosphate buffer (pH 7.4), the resulting extract was termed trichloroacetic acid-phosphate buffer soluble moiety (TPM). Both extracts were concentrated using Sep-Pak C_{18}-2g (Waters Associates Milford, MA, USA) and lyophilized. Afterwards, TPM was desalted twice with cold acetone, centrifuged and air-dried at room temperature. The lipid–lipoprotein contents were extracted in methanol/dichloromethane (2/1) at room temperature for 22 h, sonicated and dried down in nitrogen atmosphere.

Fourier Transform Infrared (FTIR) analyses were conducted on lyophilized soluble organic moieties and lipid-lipoproteins. Spectra were recorded using a Thermo Nicolet iS10 ATR-FTIR spectrometer (Nicolet, MA, USA) equipped with a smart performer accessory between 4000 to 600 cm^{-1} in air with 64 accumulations and a resolution of 4 cm^{-1}. Background spectra were measured at the start of the analysis.

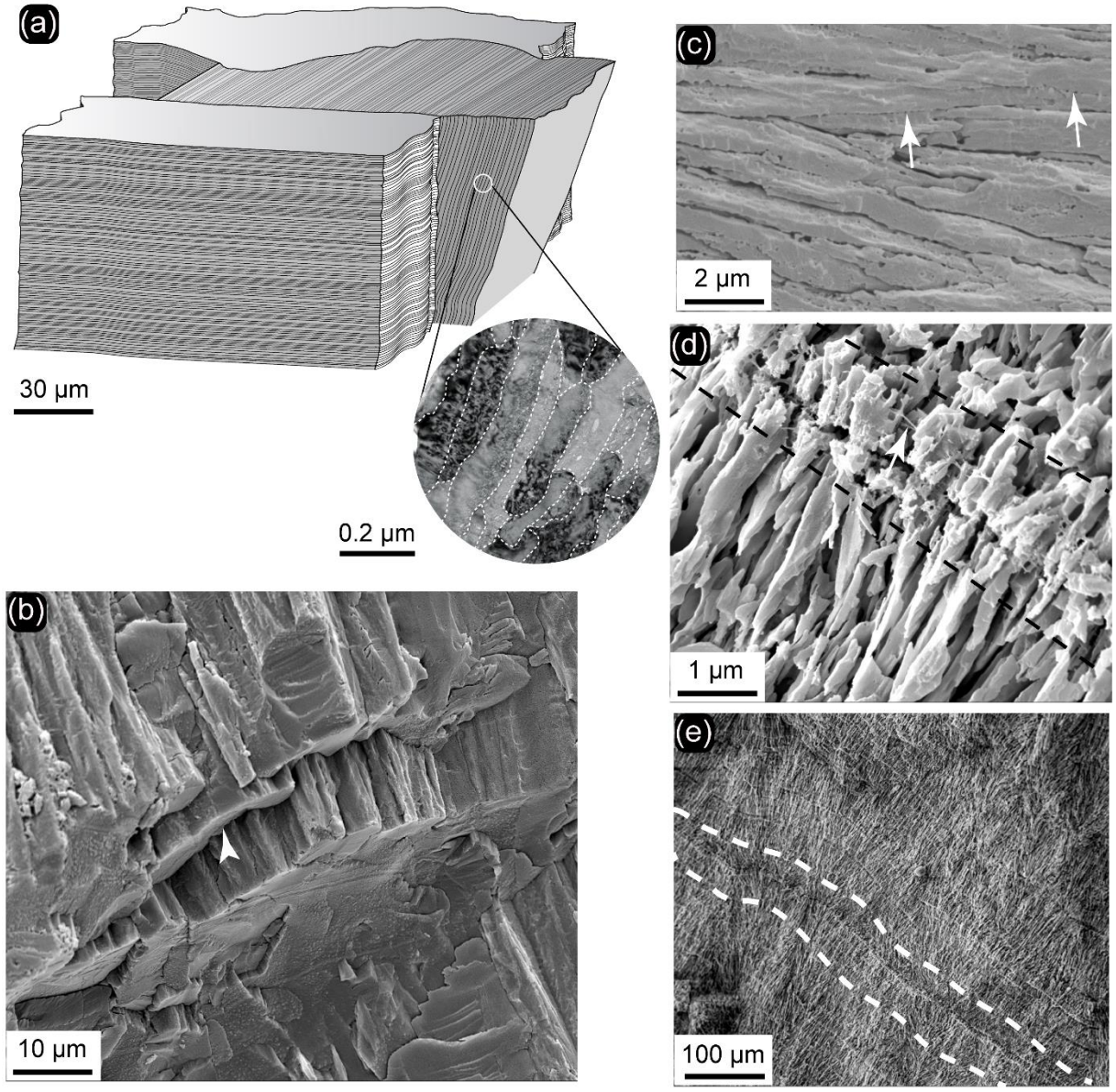

Fig. 5.1: (a) Schematic representation of the crossed lamellar microstructure in a *Tridacna* shells showing hierachical order. An enlargement demonstrating third-order lamellae with grain boundaries sketched by dashed lines (Adapted from ref.[8]). (b) Microstructure of the inner layer of a *Tridacna* shell. Fragment of *Tridacna* shell showing the differently oriented first order lamellae (arrowhead) consisting of second order aragonite lamellae. (c) Close-up image of the second order lamellae within one first order lamella. Arrows in the etched sample exhibit the location of the thin layers of the organic scaffolding between the second order lamellae. Sample was etched with 1% EDTA for 90s. (d) Detail of dashed lines in (e) showing third-order laths. *Tridacna* shell is composed of organic fibrils (arrow) and granules (dashed lines) within the surface of daily growth lines (see Fig. 10a for detail). Sample was etched with 1% EDTA for 180s.

5.2.2.4. Amino acid and monosaccharide analysis

Aliquots of the lyophilized extracts were acid-hydrolysed with 6 M HCl for 24 h at 110˚C under nitrogen following the procedure described in Agbaje et al. [6]. Soluble fractions after gas phase hydrolysis were dissolved in Milli-Q water and an aliquot was derivatized with AQC regent using AccQTag Ultra derivatisation kit (Waters Corporation, Milford, MA, USA). The resulting hydrolysates were separated and quantified using an ACQUITY ultra-performance liquid chromatography (UPLC) system and BEH RP C18 1.7μm column (Waters Corporation, Milford, MA). The amino acid composition was expressed as molar percentage (mole %) of the total amino acids and is the average of duplicate results.

To quantify neutral and amino sugar contents, aliquots were hydrolysed in 2 M trifluoroacetic acid at 100˚C (4 h) and 8 M HCl at 100°C (6 h), respectively. Samples were reduced to dryness under vacuum and the residue was re-dissolved adding 100 μM 2-deoxy-D-glucose solution as an internal standard. The sugar contents of the hydrolysate samples (neutral and amino sugar contents) were determined on a high-performance anion-exchange chromatograph system with pulsed amperometric detection (HPAEC-PAD) fitted with a BioLC amino trap guard column (3 x 50 mm) connected to a CarboPac PA10 column (4 x 250 mm) (Dionex Corp., Sunnyvale, CA, USA) held at 25°C. The cartridge was activated with a basic solvent (NaOH) passed at a flow-rate of 0.5mL/min. These hydrolytic conditions allowed the quantification of fucose, galactose, glucose, xylose, mannose, glucosamine and galactosamine. The sugar contents expressed as an ng/mg, represent the average of duplicate results.

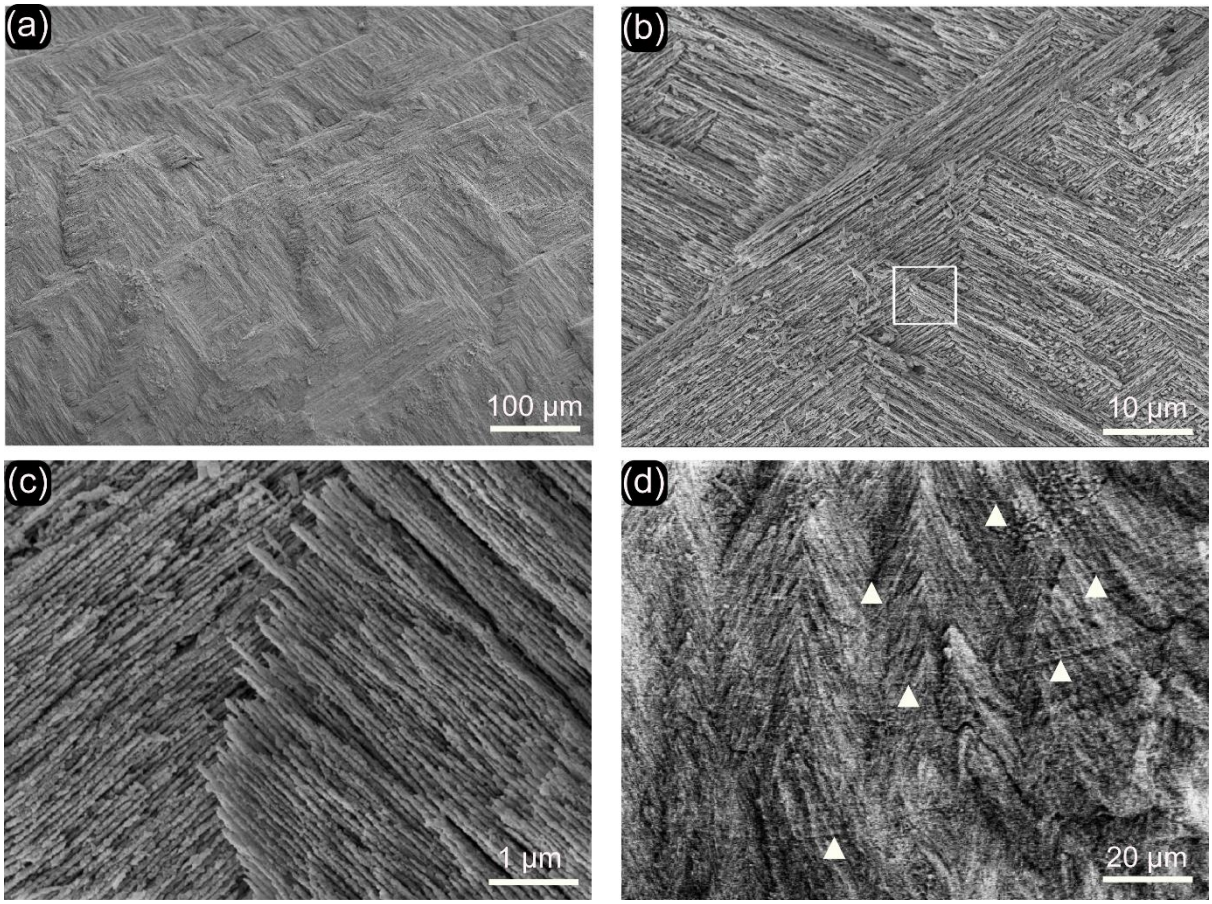

Fig. 5.2: Scanning electron microscopy (SEM) micrographs showing the hierarchical organization of *Fulvia tenuicostata* shells after etching with 1% EDTA for 180s. (a) View of the inner aragonitic layer. Note the higher magnification in (b) and (c). (b) White square depicts the thin elongated fibres of aragonite oriented in different directions thus create the bundle plates in first (outer) and second (middle) layers. Note the higher magnification in (c). The dimension of each fibre is ~ 50-60 nm. (d) Cross-section of the growth bands (arrowheads) and fibrous structure with fan-shaped fibre bundles in the outer shell layer.

5.2.2.5. Determination of shell proteins and chitin deacetylated activity on SDS-PAGE

The organic moieties in the shells were separated under denaturing conditions by conventional 1D electrophoresis using Laemmli sample buffer [32]. Proteins were separated on a pre-cast NuPAGE 4–12% Bis-Tris gel in MES running buffer following protocols supplied by the manufacturer (Invitrogen; Carlsbad, CA, USA). After electrophoresis, gels were stained with silver nitrate following methods detailed in Agbaje et al. [6]. Potential glycosylation in the SOM and TPM extracts were studied using the Wall and Gyi [33] method (modified after Agbaje et al. [6]). Gels were also studied for potential Ca^{2+} binding proteins adapting the

protocol for Stains-all from Osuna et al. [21]. After staining, the gel was treated with 50% ethanol to ensure clear background and subsequently treated following the modified silver nitrate staining method as described in Agbaje et al. [6].

The chitin deacetylated (CDA) activity was analysed after sodium dodecyl sulfate polyacrylamide gel electrophoresis (SDS-PAGE) using a modified Calcofluor White M2R (hereafter Calcofluor) staining [34], followed by silver nitrate staining. The modification to the CDA staining involved fixation of the gel in 50 vol% methanol and glacial acetic acid. The gel was incubated overnight at 4˚C in the dark with a freshly prepared solution of 0.15% (w/v) Calcofluor in 0.5 M Tris-HCl (pH 8.8), and subsequently stained with silver nitrate. The duration for each wash and incubation was identical to that for the combined Alcian Blue/silver nitrate protocol described.

5.3. Results and discussion

5.3.1. Microstructure of crossed lamellar shells

Tridacna genus are closely related [35, 36]; both, *T. gigas* (this study) and *T. derasa* comprise three orders of lamellar hierarchy, as schematically depicted in Fig. 5.1a [8]. The first order hierarchy comprises undulating bands of a ca 50µm thickness (first order lamellae, Fig. 5.1b) that consist of stacked second order lamellae (Fig. 5.1c) perpendicular to the shell surface and oriented at an angle of ca. 90˚ to each other. The second order lamellae consist of elongated nanometer-sized laths (third order lamellae, Fig. 5.1a). Nanometer-scale growth twinning of the aragonites is very common (e.g.[14, 37]) and could be regarded as a fourth hierarchical order [12].

F. tenuicostata shells have a crossed lamellar inner layer (Fig. 5.2a-c) and an outer layer consisting of fan-like shaped fine fibrous prisms (Fig. 5.2d) [1, 38]. In inner layer it is observed that shells depict three sublayers (Fig. 5.2a); the morphologies of this structure are discernible in Fig. 5.2b-c, where thin third-order fibres arranged mutually parallel, thereby forming bundles

of sheet-like organisation of second-order lamellae (Fig. 5.2a, b), which are in turn produce the building blocks of crossed lamellar shell – first-order lamellar (Fig. 5.3).

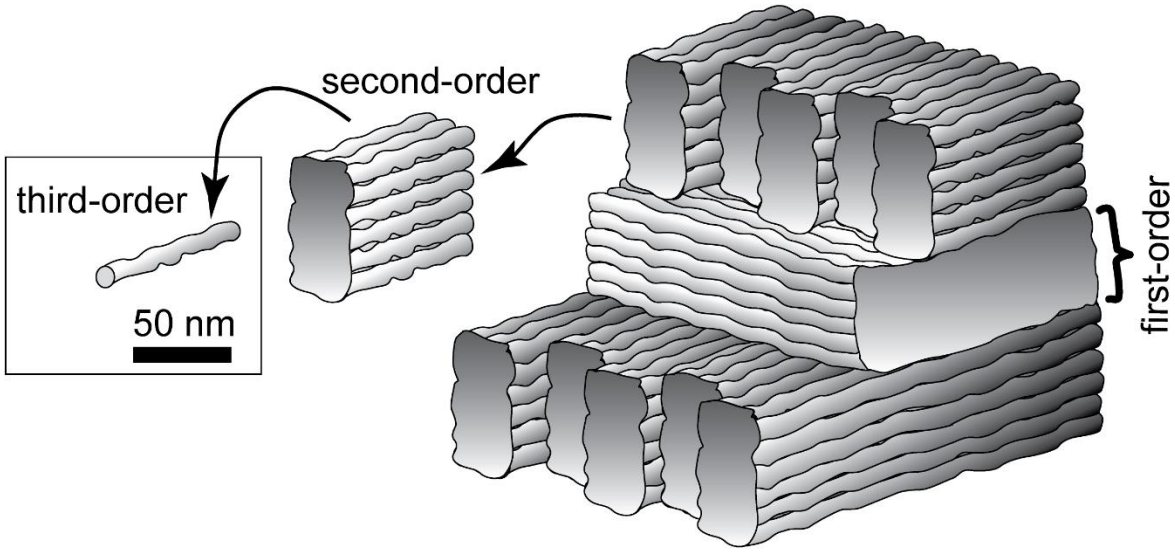

Fig. 5.3: Schematic representation of the crossed lamellar microstructure of *Fulvia tenuicostata* shell. Three orders of hierarchy are visible. The third-order lamellae are fibre-like and are built of nanogranule particles. A bundle of 3rd-order lamellae forms the second-order lamellae and these, in turn, are the building blocks of the first-order lamellae.

5.3.2. Localization and amount of the organic matrix

Growth lines, enriched in organic components transect the shell microstructure [39] and can be visualized using histochemical staining with Calcofluor white M2R (CFW). CFW is a fluorescent marker, and binds specifically to structural β-(1-3)- and β-(1-4)-polysaccharides (cellulose, chitin and chitosan) but not to proteins [40]. Growth lines in *T. gigas* (Fig. 5.1e) are well stained and visible with CFW (Fig. 5.4a). Also, growth lines are visible in the outer shell layer [1] of *F. tenuicostata* (Fig. 5.4b), while the inner parts of the shell shows organic material interlayered with sheets of fibrous aragonite, but no growth lines (Fig. 5.4c).

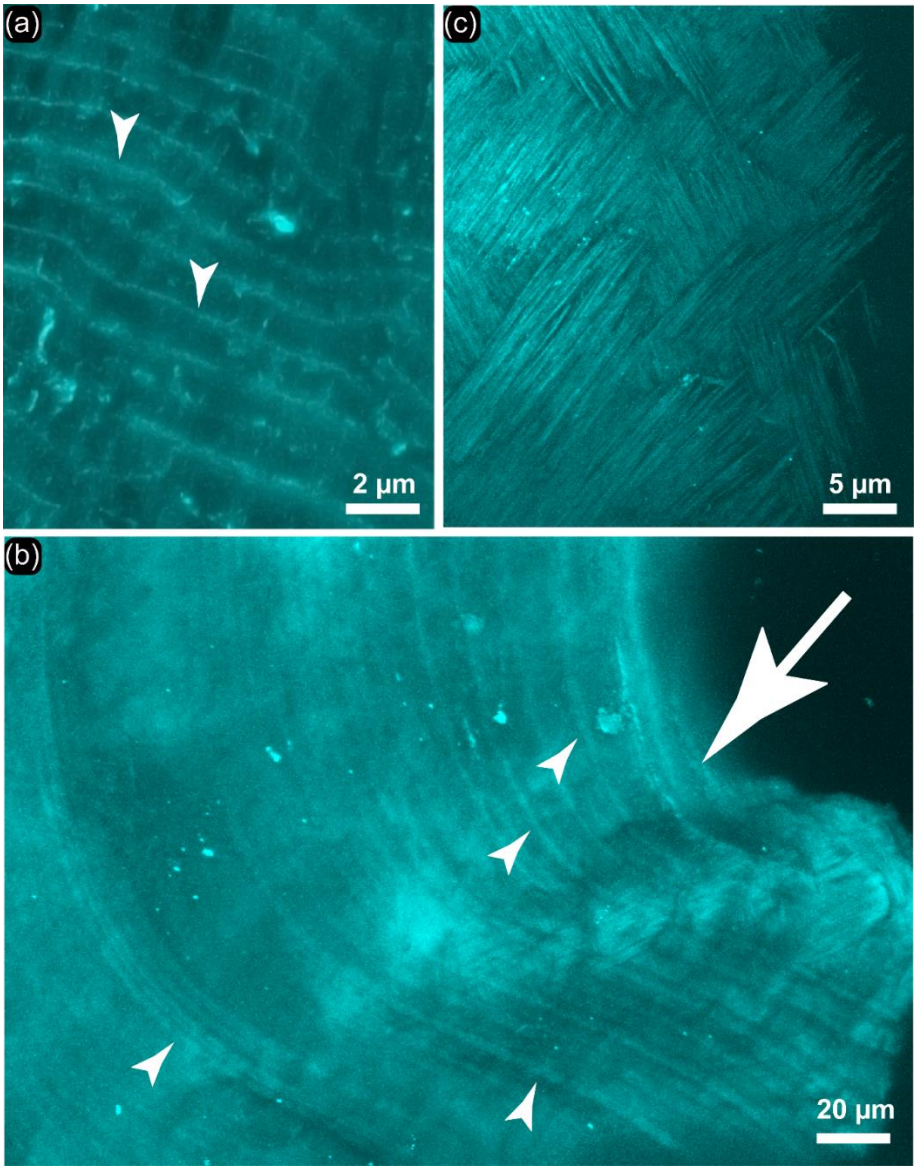

Fig. 5.4: (a) Etched section of *T. gigas* shell indicating the presence of organic fibre (chitin, arrowheads) in the growth bands in the inner shell layer after staining with Calcofluor White M2R. (b) Organic growth bands (arrowheads) in the outer shell layer (*F. tenuicostata*) stained with Calcofluor White M2R. The white arrow designates the outside surface of the shell. (c) Etched cross-section of the inner shell layer of *F. tenuicostata* shows the organic framework interlayered with the aragonite fibres after Calcofluor White M2R staining.

Fig. 5.5 shows Differential Thermogravimetric thermal analyses of the samples studied, which consisted of differential thermal analysis (DTA; Fig. 5.5a) and thermogravimetric analysis (TG; Fig. 5.5b). The DTA exhibits three decompositional steps for both shells. The first occurs at 104^{o}C is caused by loss of water, the second exists in the range 220-462^{o}C and is due to the combustion of the shell macromolecules followed by transformation of aragonite to calcite [8]. The third decomposition step at 761-764^{o}C is attributed to the disintegration of

$CaCO_3$ and hence form CaO and CO_2 [6, 8]. In total the organic matrix amounts to 1.54 wt% in *F. tenuicostata* and 1.83 wt% in *T. gigas.* These amounts are in the same range as for other mollusc species with crossed lamellar microtexture, such as *Glycimeris glycimeris* (1.4 wt%; [7]), and *Murex troscheli* (1.7 wt%; [41]) but are overall distinctly lower than for nacre-prism shells (~ 4.0 wt%; [6]).

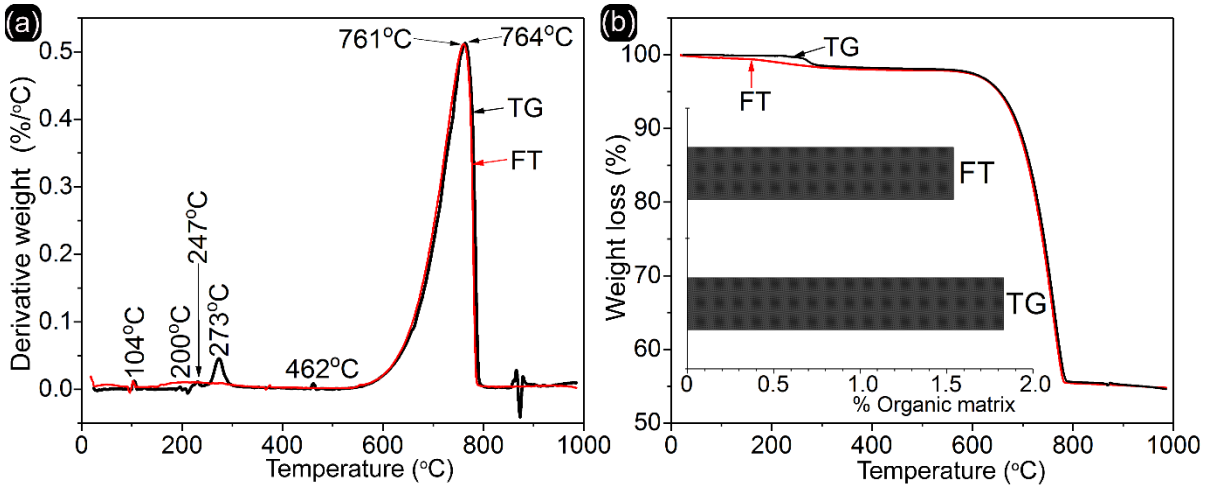

Fig. 5.5: Differential thermogravimetric analysis (a) and Thermogravimetric analysis (b) were used to determine the total organic contents of the shells (TG: *Tridacna gigas* and FT: *Fulvia tenuicostata*). The bar chart inserted in (B) represents the calculated total shell organic content for the range 150–500°C. FT and TG demonstrate 1.54 wt% and 1.83 wt% for total organic content, respectively.

5.3.3. Fourier Transform Infrared (FTIR) Spectroscopy

After decalcification, the composition of the lyophilised Soluble Organic Moiety (SOM) and the TP-Soluble Organic Moiety (TPM, see methods) are characterised with infrared spectroscopy. The main components in the shell macromolecules are proteins, polysaccharides (Fig. 5.6a, b) and lipids-lipoproteins (Fig. 5.6c, see methods). The bands at around 3300 cm^{-1} and between 2957 and 2847 cm^{-1} are attributed to amide A (N-H band) and C-H stretching groups, respectively. The bands at 1657 and 1651 cm^{-1} for *F. tenuicostata*, 1648 and 1651 cm^{-1} for *T. gigas* correspond to amide I C=O stretch (Fig. 5.6a, b).

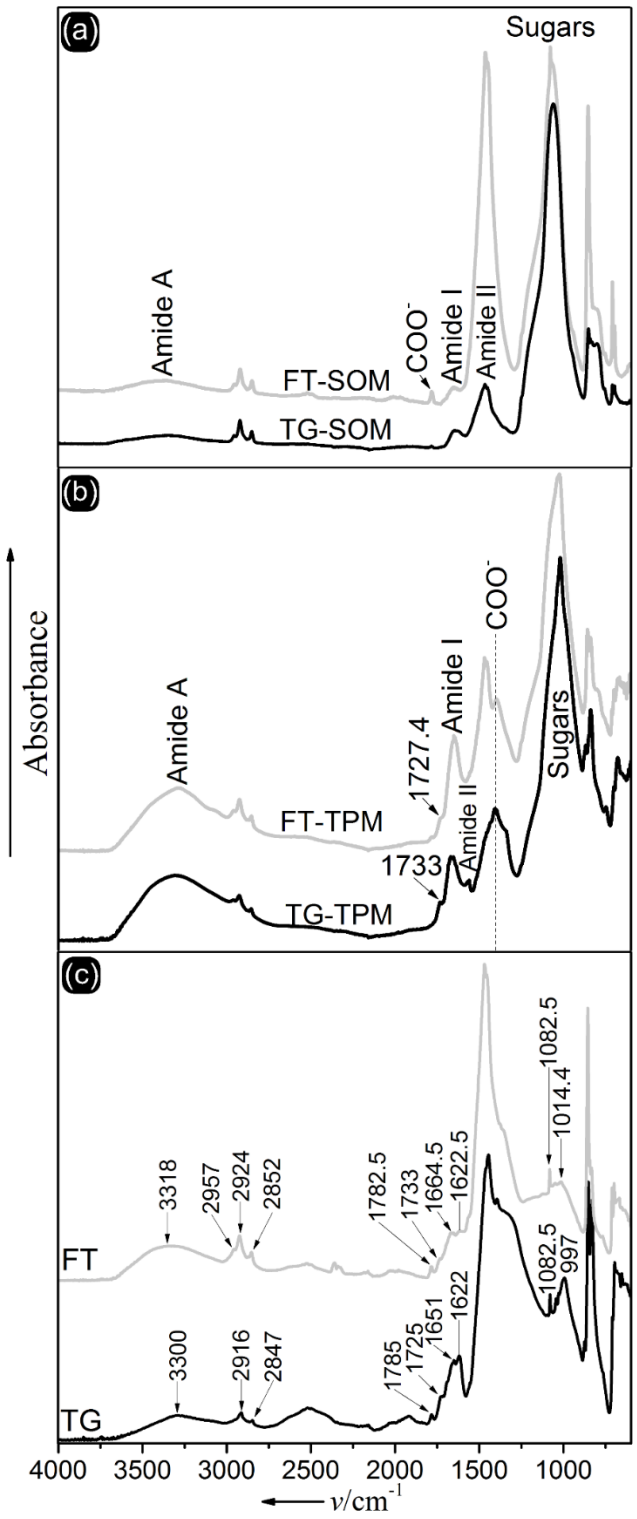

Fig. 5.6: FTIR spectra of the shells (TG: *Tridacna gigas* and FT: *Fulvia tenuicostata*) in the range 4000-600 cm^{-1}. (a): Soluble Organic Moiety (SOM). (b) : Trichloroacetic acid-Phosphate buffer Soluble Moiety (TPM). **(c):** FTIR spectra (4000-600 cm^{-1}) of lipoproteins extracted from *Tridacna gigas* (FT) and *Fulvia tenuicoststa* (FT) shell samples. Bands at around 1622 cm^{-1} exhibit the C=C of lipids and the bands at 1651 and 1664.5 cm^{-1} show the presence of proteins.

The characteristic features in the amide regions of the organic moieties exhibit some significant differences in TPM between the two bivalve species: the amide II band (1557 cm^{-1}) and band at 1668.5 cm^{-1} in TPM of *T. gigas* are assigned to glutamic acid and glutamine [42]. These bands are absent in *F. tenuicostata* shells (Fig. 5.6b). Carboxylate bands and carbonyl esters occur at 1406 and 1733 cm^{-1} (*T. gigas*), 1397 and 1727.4 cm^{-1} (*F. tenuicostata*) are generally absent in SOM (Fig. 5.6a). Bands for C-H vibrations of aliphatic groups (1470-1452 cm^{-1}) are prominent in all organic moieties except for TPM of *T. gigas* that shows only a shoulder at 1434 cm^{-1} (Fig. 5.6b). Stretching vibration of the C-O bonds of the sugars biomolecules show absorption bands at 1082-1019 cm^{-1}.

Lipids and lipoproteins (Fig. 5.6c) have bands at around 3300 cm^{-1} (O-H coupled with N-H group), 2957-2847 cm^{-1} (C-H groups), 1651 for *T. gigas* and 1664.5 for *F. tenuicostata* (Amide I), and 1622 cm^{-1} (C=C). The bands between 1082 and 997 cm^{-1}, 1725 and 1733 cm^{-1}, respectively (Fig. 5.6c), are usually assigned to sugars and C=O stretch vibration as in Fig. 5.6a and b. Lipid is the third constituent of the shell biopolymer after proteins and polysaccharides. Characterization of this constituent in biogenic inorganic solid-state materials are very rare and the exact composition is far from being understood. This finding suggests that the association of lipids and proteins may be of general important for shells with different microstructures [17, 43].

5.3.4. Amino acid composition

Both, SOM and TPM of *F. tenuicostata* shells contain glycine and aspartate, accounting for 26% (in SOM) and 29.2% (in TPM) of total amino acids, followed by proline, alanine, valine, leucine and glutamate (Table 5.1). These five residues constitute around 40% (42.2% in SOM and 40% in TPM) of the total amino acid composition. In comparison, SOM of *T. gigas* exhibits more glycine, proline and leucine (39.1% of total amino acids) than *F. tenuicostata* shells, followed by glutamate and aspartate (15.7% of total amount). The composition of TPM in *T.*

gigas is slightly different to that of SOM and dominated by glycine, glutamate, aspartate, proline and leucine, together 56.2% of the total amino composition.

Table 5.1

Amino acid composition (mole %) of the organic extracts of *Tridacna gigas* and *Fulvia tenuicostata* shells

Amino Acid	*Tridacna gigas*		*Fulvia tenuicostata*	
	SOM	TPM	SOM	TPM
His[a]	0.7	0.6	0.3	0.2
Ser[b]	4.7	5.3	6.2	6.4
Arg[a]	4.3	4.0	3.4	3.2
Gly	12.7	12.6	15.1	13.6
Asx [a] (Asp + Asn)	7.3	10.6	10.9	15.6
Glx[a] (Glu + Gln)	8.4	10.7	7.5	9.1
Thr[b]	3.5	4.5	6.0	6.0
Ala[c]	6.1	7.1	9.5	8.9
Pro[c]	13.3	11.4	8.7	7.5
Lys[a]	5.1	3.9	2.6	3.1
Tyr[b]	2.6	2.3	2.2	2.2
Met[c]	2.1	< 0.4	1.2	1.0
Val[c]	5.4	5.9	8.2	7.5
Ile[c]	6.0	5.9	5.6	5.0
Leu[c]	13.1	10.9	8.3	7.0
Phe[c]	4.7	4.4	4.4	3.8
C/HP	0.51	0.65	0.54	0.77

NB: [a] charged amino acid; [b] uncharged, polar amino acid; [c] hydrophobic amino acid; SOM: Soluble Organic Moiety; TPM: Trichloroacetic acid-Phosphate buffer Soluble Moiety (Extract from Water-Insoluble Moiety); C/HP: charged to hydrophobic ratio.

The soluble moiety (SOM) in the *F. tenuicostata* shells contains 24.6% of glycine and alanine, and has a charge to hydrophobic ratio (C/HP) of 0.54. *T. gigas* has a similar C/HP ration of 0.51, but contains lower amounts of glycine and alanine (18.8%) than *F. tenuicostata*. In TPM of *F. tenuicostata*, glycine and alanine amount to 22.5% and a relatively large C/HP ratio of 0.77. This is significantly different to the C/HP in *T. gigas* (0.65), which contains only slightly more glycine and alanine (19.7% total amount). Using the total amount of the soluble organic moieties (SOM and TPM; Fig. 5.7a), *F. tenuicostata* shells exhibits higher amount of glycine (15.1% for SOM and 13.6% for TPM) and aspartate (10.9% for SOM and 15.6% for TPM) than *T. gigas*. Contrarily, the main amino acids found in *T. gigas* are glycine (12.7% for

SOM and 12.6% for TPM), proline (13.3% for SOM and 11.4% for TPM), leucine (13.1% for SOM and 10.9% for TPM) and glutamate (8.4% for SOM and 10.7% for TPM). The higher amount to glutamate compared with aspartate in *T. gigas* agrees well with the FTIR spectra, where glutamic acid (1557 cm^{-1}) and glutamine (1668.5 cm^{-1}) bands are observed (Fig. 5.6b).

5.3.5. Monosaccharide composition

The soluble organic moieties demonstrate the presence of a set of neutral and amino sugars, including glucose, mannose, xylose, fucose, galactose, *N*-acetyl-D-glucosamine and *N*-acetyl-D-galactosamine (Table 5.2). The most abundant sugar moieties are glucose and xylose. The two sugars exhibit 59.6% (SOM) and 45.3% (TPM) in *F. tenuicostata*, and have higher concentrations of 70.7% (SOM) and 78.2% (TPM) in *T. gigas* (Table 5.2). Also, *F. tenuicostata* exhibits higher amounts of galactosamine, glucosamine and mannose than *T. gigas*. In *F. tenuicostata* shells fucose is present in considerably higher amounts (SOM: 3.7%, TPM: 4.6%) than in *T. gigas* that show only traces (Table 5.2). The total amount of 1.18 wt% sugar content in *F. tenuicostata* shells and 0.52 wt% in *T. gigas* are significantly lower compared with 3.1% found in bivalve species with nacreous microstructure (e.g. Unionoida: [44]). This means that the organic matrix extracts of *T. gigas* and *F. tenuicostata* shells are only weakly glycosylated.

In summary, saccharidic composition of the two shells is distinct (Fig. 5.7b): the total soluble organic moieties (SOM and TPM) of *F. tenuicostata* shells contains higher contents of glucosamine (13.3% for SOM and 21.0% for TPM), galactosamine (12.3% for SOM and 15.7% for TPM), mannose (11.1% for SOM and 13.4% for TPM) and fucose (3.7% for SOM and 4.6% for TPM) compared to *T. gigas*. Instead, *T. gigas* exhibits higher amounts of xylose (28.2% for SOM and 57.3% for TPM) followed by glucose (42.5% for SOM and 20.9% for TPM). Generally, sugars such as xylose and mannose are unusual for mollusc shells [21, 45]. However recently, Osuna et al., [21] reported higher amounts of mannose (32.3%) in the soluble shell macromolecules of the gastropod *Strombus gigas*, while high amounts of xylose (33.64%) were discovered in the soluble shell matrix of gastropod *Rapana thomasiana* [46].

Table 5.2

Monosaccharide composition of organic extracts of *Tridacna gigas* and *Fulvia tenuicostata* shells

Monosaccharide	*Tridacna gigas*		*Fulvia tenuicostata*	
	SOM ng/mg (%)	TPM ng/mg (%)	SOM ng/mg (%)	TPM ng/mg (%)
Galactosamine	171 (5.9)	165 (7.2)	663 (12.3)	1002 (15.7)
Glucosamine	299 (10.3)	139 (6.0)	716 (13.3)	1344 (21.0)
Fucose	TR	TR	199 (3.7)	296 (4.6)
Glucose	1235 (42.5)	481 (20.9)	997 (18.6)	1600 (25.0)
Xylose	820 (28.2)	1319 (57.3)	2203 (41.0)	1302 (20.3)
Mannose	381 (13.1)	199 (8.6)	596 (11.1)	856 (13.4)
Total	2906 (100)	2303 (100)	5374 (100)	6400 (100)
Total %	0.29	0.23	0.54	0.64

TR – trace; SOM: Soluble Organic Moiety; TPM: Trichloroacetic acid-Phosphate buffer Soluble Moiety (Extract from Water-Insoluble Moiety).

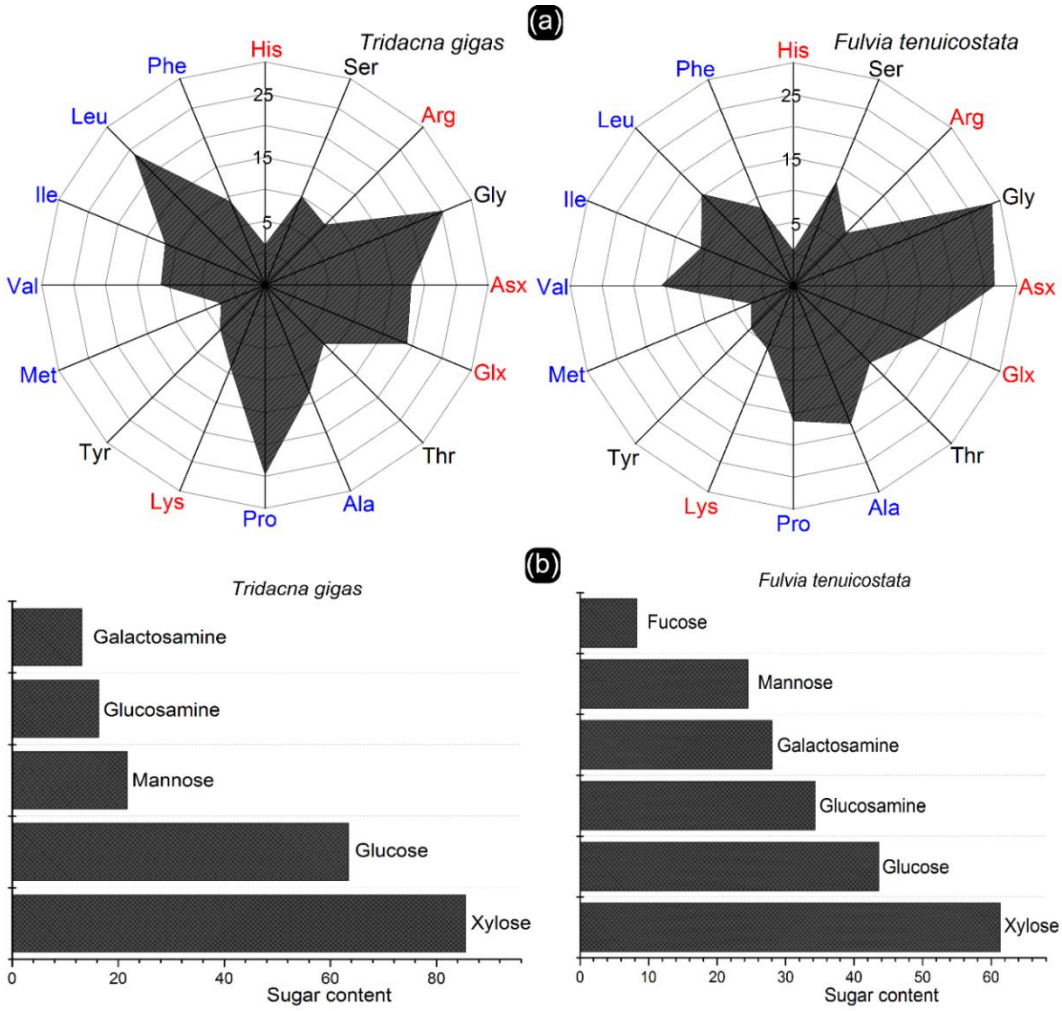

Fig. 5.7: Total amino acid compositions and proportions from combining the soluble (SOM) plus the Trichloroacetic acid-Phosphate buffer soluble moieties (TPM) (a); Total monosaccharide compositions and proportions taken together from the water soluble (SOM) plus the Trichloroacetic acid-Phosphate buffer soluble moieties (TPM) (b). NB: The compositions involved the percentage of two fractions, i.e. SOM and TPM.

It has been argued that structures containing a β1 → 2-linked xylose bound to a β-mannose unit of the carbohydrate core are essential in animal species [46]. Van Kuik et al., [45] for example, showed that xylose is a component of an *N*-linked glycosidic carbohydrate chain in the α-hemocyanin of the gastropod *Helix pomatia*. It has been speculated that these specific glycoproteins exhibit a crucial role in shell developmental processes [47] although the exact role in the biomineralization process is unclear.

5.3.6. The protein signature in the shells

Organic fractions in *T. gigas* and *F. tenuicostata* shells were analysed by mono-dimensional electrophoresis. This technique has been widely used to visualize inorganic-associated proteins, with, however, some technical limitations [12, 27]. In this study, silver nitrate, Stains-all and Alcian blue staining show numerous proteins and/or glycosaminoglycans-glycoproteins bands (Fig. 5.8), their high number probably being caused by the presence of carbohydrate groups linked with the proteins [23, 48, 49].

For both Soluble Organic Moiety (SOM) extracts (Fig. 5.8, Lanes 1, 2), the most prominent and highly reproducible bands for all biochemical assays have an apparent molecular mass of 20 kDa and 36 kDa. Also, a weak band at around 160 kDa is reproducible for the TP-Soluble Organic Moiety (TPM) of *F. tenuicostata* (Fig. 5.8, Lane 3). We observed no protein bands for the TPM of the *T. gigas* shell (Fig. 8; Lane 4).

A number of weaker protein bands are visualized by silver nitrate staining for both SOM samples (Fig. 5.8a). The calcium-binding proteins are confirmed by a specific Stains-all staining method (Fig. 5.8b). Bands at around 140, 110, 80, 60 and 63 kDa could be identified in both SOM samples (Fig. 5.8b, Lanes 1, 2). Alcian Blue combined with silver nitrate staining (Fig. 5.8c) resulted in an increased sensitivity for glycoproteins and/or glycosaminoglycans. The soluble portion of the organic matrix reveals a discrete band with unknown weight (far above 260 kDa) after staining with Alcian Blue (Fig. 5.8c, Lane 1), which was reproducible with silver nitrate and stains-all staining (Fig. 5.8a, b; Lane 1). The band is attributed to sulfated

polysaccharides/glycosaminoglycans (e.g.[28] [9]). Similarly, a number of bands appeared at around 20 up to 160 kDa (Fig. 5.8c, Lane 1, 2). Most of these bands are visualized in SOM of *T. gigas* but are less prominent compared to SOM of *F. tenuicostata*. In addition, bands at around 58 kDa and 63 kDa (Fig. 5.8b, c) for both extracts of *F. tenuicostata* (SOM and TPM) are not visible with silver nitrate staining (Fig. 5.8a; Lane 1, 3). These bands can be attributed to calcium-binding proteins and/or glycoproteins [44, 50]. The two bands were also identified in the soluble organic matrix of the freshwater species *Hyriopsis cumingii* (Unionoida) with nacro-prismatic shell architecture [6].

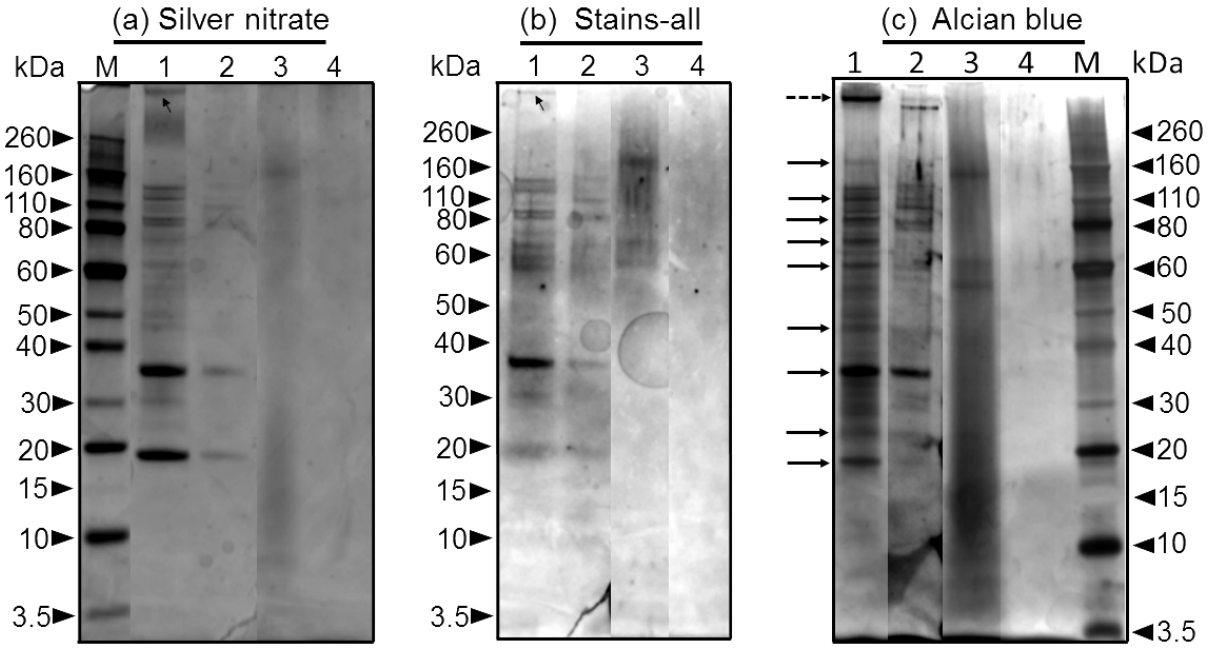

Fig. 5.8: SDS-PAGE of Soluble (SOM) and Trichloroacetic acid-Phosphate buffer Soluble Moieties (TPM). Lane 1: SOM *F. tenuicostata*; Lane 2: SOM *T. gigas*; Lane 3: TPM *F. tenuicostata*; Lane 4: TPM *T. gigas*; Lane M: Molecular weight (Novex Sharp Pre-stained Protein; 5 µL) standards with masses in kDa are indicated. Samples were stained with silver nitrate (0.1% with 50 µL 37% formaldehyde). Each well was loaded with 100 µg. Stains-all and Alcian Blue: samples were visualized with Stains-all and Alcian Blue, and then enhanced with silver nitrate, respectively. For Silver nitrate and Alcian Blue, each well was loaded with 100 µg whereas for Stains-all, each well was loaded with 50 µg. Arrows on Silver nitrate and Stains-all point to the glycosaminoglycans/proteoglycans bands. For Alcian blue, arrows indicated protein bands at around 20, 23, 36, 46, 63, 70, 80, 110 and 160 kDa. Dashed arrow far above 260 kDa points to glycosaminoglycans and/or proteoglycans band.

Calcofluor white (CFW) binds strongly to carbohydrate residues in the polyacrylamide gel [34, 48]. As all extracted organics are disordered species and mixtures, we stained TPM (the

soluble extract of the insoluble shell organic matrix) of both shells with CFW to reveal the deacetylated form of chitin (chitosan), and subsequently enhanced the staining with silver nitrate (Fig. 5.9; Lane 1, 2). Both TPM extracts reveal distinct bands. In *T. gigas* bands at 110, 80, 40 kDa and around 36 and 18 kDa could be identified (Fig. 5.9; Lane 1). As CFW interacts preferentially with the saccharide residues and reveals prominent bands that are unstained with protein stains (Fig. 5.8), we propose the band at around 36 kDa to be an acidic glycoprotein linked with a carbohydrate, because it occurs in all SDS-electrophoresis (Fig. 5.8 and 5.9).

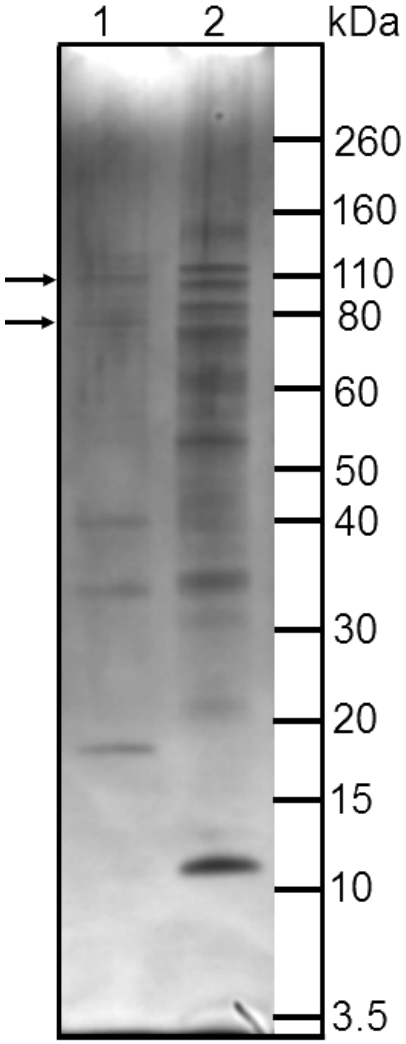

Fig. 5.9: SDS-PAGE of Trichloroacetic acid-Phosphate buffer Soluble Moiety (TPM). Lane 1: *T. gigas*; Lane 2: *F. tenuicostata*. Samples were visualized with Calcofluor white M2R and then enhanced with silver nitrate. Each well was loaded with 100 µg. Arrows depicted the estimated molecular weights of chitin derivatives at 110 and 80 kDa. Numbers on the right denote molecular weight markers in kDa (kilodaltons). This is first time shell-associated macromolecules was stained with Calcofluor White in SDS-electrophoresis.

Similarly, prominent bands at above and below 110 and 80, at around 60, 53, 36 and 12 kDa, and weaker bands at around 21, 30 and 40 kDa occur for *F. tenuicostata* shells (Fig. 5.9; Lane 2). This method was also used for the SOM fraction. No distinct band could be visualized except for a band at around 36 kDa (data not shown), supporting the general absence of chitin (and its derivatives) in the soluble organic matrix fraction. This result agrees well with the known role of amino polysaccharide-chitin as organic scaffolding in the calcareous shell [23]. Moreover, the presence of partial hydrolysis of chitin in the insoluble organic matrix provides evidence independent from FTIR and optical activity studies [8] for the existence of a chitin component in shells with crossed lamellar architecture.

5.3.7 Granular nanostructure

High-resolution imaging reveals a fine structure of nanogranular particles that are inorganic-bioorganic nanocomposites for both, *T. gigas* and *F. tenuicostata* shells (Fig. 5.10). In *T. gigas* the organic fibrils and granular matrix (Fig. 5.10a) intergrown at the central part of the growth surface (Fig. 5.1d and 5.1e). This observation thus followed a universal structural motif for calcium carbonate-based biominerals [51]. Also, the three-dimensional structure and high magnification of *F. tenuicostata* shells show the detail of the hierarchy order lamellae (Fig. 5.10b). Fig. 5.10c depicts clearly that, within each fibre, there is existence of lineation of nanogranules in growth increments, which later leads to the familiar large, crossed lamellar plates (Fig. 5.2 and 5.3). While the most basic level of hierarchy occurs at the nanoscale and involves stacked inorganic constituents in biomineralised structures, it was suggested that the nanostructure should play crucial roles in the overall mechanical properties of composite materials [51, 52]. As is typical to nacro-prismatic bivalve shells [51-53], the granule particles of *F. tenuicostata* shells also increase from a ca 50 nm at the shell surface to granules as large as 110 nm or more at the interface to form ‘continuum fibre’. The factors that determine the dimension of the nanogranules are unknown, as the interface is not well-defined. In some regions, we observed the gradual emergence of intergranular pores (Fig. 5.10d).

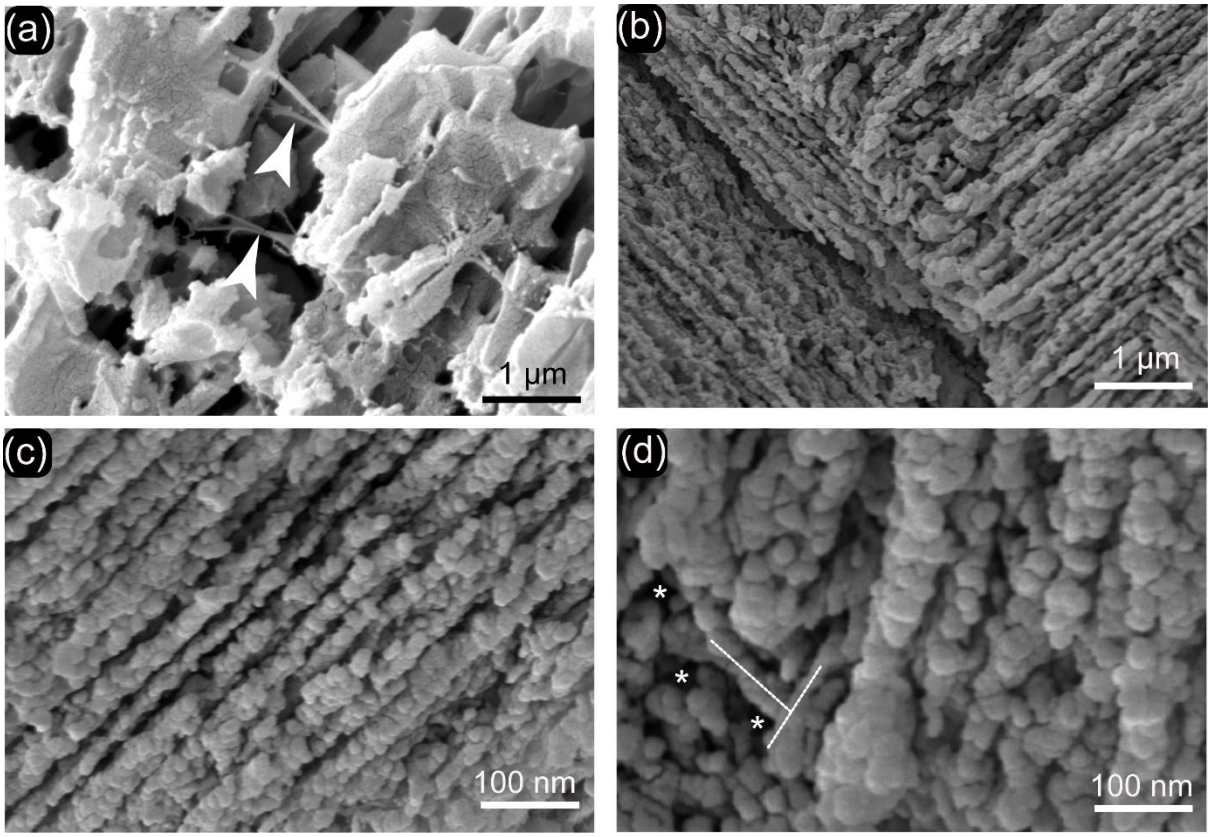

Fig. 5.10: Higher magnification Field Emission Scanning Electron Microscopy (FE-SEM) images of *Tridacna gigas* (a) and *Fulvia tenuicostata* (b-d) shells after etching. (a) Detail of organic fibrils (arrowheads) and granular particles at the surface of shell growth lines (see Fig. 1d and e). (b) Three dimensional structure of the fibres separated by thin layers of organics (see Fig. 5c for the detail of organic layer). (c) Detail of the fibres, revealing the granular arrangement and each fibre is a composite structure (d) A highly magnified image of the granular arrangement, showing that the nanogranules are indeed composites. Note the inner part of the granules revealing the juxtaposition of the several granules that are perpendicular to the fibre length (white dashed lines); also the intergranular pores (Stars).

In calcareous biominerals including nacreous tablets, calcitic prisms of molluscs and other biogenic inorganic solid-state materials [51], the aggregation of granulated calcium carbonate are intimately linked with a fibrous, or needle-like, geometry [52]. The structural motif is feasible due to a template action of the glycopolymers (e.g. [22, 26, 54]). Herein, *in situ* localisations of the organic framework via Calcofluor staining and high-resolution imaging depicts a densely packed organic matrix within the granular fibres at the micron scale in the *F. tenuicostata* shells (Fig. 5.4b, c), which appears less dense in the *T. gigas* (Fig. 5.4a). This difference is following the monosaccharide analysis demonstrating a higher proportion of

amino sugars in *F. tenuicostata* shells. While the differences in the composition of organic matrix (scaffold) persist, both crossed lamellar shells, taken as a group, depict chitin-protein-complex, which, in turn, intercalated within inorganic units.

5.3.8 Chitin-protein complex in calcareous biominerals

The amide I band, which is identified as the main matrix protein, is very prominent in this work. This is contrary to the previous findings [12]. Organic fibres including insoluble *β*-chitin, a constituent of many calcareous shells such as nacre [55, 56], is covalently associated with other macromolecules (for instance proteins) in nature and intergrown with the inorganic matrix to provide structural strength and toughness for the adult molluscs [3]. Our study on the crossed lamellar bivalve shells shows that the chitin-protein-complex exists in *T. gigas* and *F. tenuicostata* and thus stabilising aragonitic crystals of the calcareous biominerals (Fig. 5.4; Fig. 5.8 – 5.10).

The location of the organic template in crossed lamellar shells, in contrast to nacre shells structure, is poorly characterised. Infrared spectroscopy has been used to describe the bioorganic template in crossed lamellar layers and attributed the template mainly to glycoproteins [12]. The evidence for this conclusion was based on soluble shell macromolecules analysis with hydrolysis [12, 27]. That approach, however, was clearly insufficient to distinguish whether the biopolymer in lamellar shells contains insoluble polysaccharide or other components like glycosaminoglycans. Calcofluor White specifically binds to chitin (and its derivatives) and not to proteins, even when staining glycoproteins [40]. Our unambiguous Calcofluor staining (Fig. 5.4; Fig. 5.9) with the results of amino sugars in this work reveals that insoluble chitin fibrils may remain chemically stable enough for paleoclimatic and paleoecological information to be derived from stable isotope analysis (see material section) [31, 57]. The same models exist in other exoskeletons like arthropods, brachiopods and bryozoans [58, 59].

5.4. Conclusion

This work presents first structural imaging of *F. tenuicosata* shells and first detailed organic matrix description on *Tridacna* shells and *F. tenuicostata*. Like other calcareous biominerals, such as nacroprismatic shells [52, 53], we have also evidenced the existence of lineations of nanogranules that subsequently formed the polycrystalline fibre-like fabric, which then fashions the basic building blocks of crossed lamellar bivalve shells *F. tenuicostata*. Also, in *T. gigas* granules and organic fibrils are evidenced at the surface of growth bands. The microstructures and the inorganic matrix of *Tridacna* shells and *F. tenuicostata* are comparable, while the quantities of shell macromolecules (the organic matrices) are variable, and thus follow the previous findings [12]. However, we report here some of the highest resolved electrophoresis results yet for crossed lamellar bivalve shells. Our newly developed fixing and staining methods allowed us to identify many distinct bands in the bivalve shells with the crossed lamellar microstructure for the first time; chitosan (deacetylated chitin) is revealed after staining the SDS-gel with the unambiguous Calcofluor White for the first time and hence support the *in situ* study.

Acknowledgements Fei Chi is well-appreciated for handling sugar analysis. OBAA acknowledges Dr Nadia Suarez-Bosche for teaching him the basic techniques of confocal microscope. The work was facilitated in part by the Australian Government's National Collaborative Research Strategy (NCRIS) and its facilities at the Australian Proteome Analysis Facility (APAF).

5.5. References

1. Carter, J.G., *Skeletal biomineralization: patterns, processes and evolutionary trends*. Vol. 1. 1990: Wiley Online Library.
2. Lowenstam, H.A. and S. Weiner, *On biomineralization*. 1989: Oxford University Press.
3. Jackson, A., J. Vincent, and R. Turner, *The mechanical design of nacre.* Proceedings of the Royal Society of London. Series B. Biological Sciences, 1988. **234**(1277): p. 415-440.
4. Watabe, N., *Studies on shell formation: XI. Crystal—matrix relationships in the inner layers of mollusk shells.* Journal of Ultrastructure Research, 1965. **12**(3): p. 351-370.
5. Westbroek, P. and F. Marin, *A marriage of bone and nacre.* Nature, 1998. **392**(6679): p. 861-862.

6. Agbaje, O.B.A., et al., *Organic macromolecules in shells of Arctica islandica: comparison with nacroprismatic bivalve shells.* Marine Biology, 2017. **164**: p. 208.
7. Böhm, C.F., et al., *Structural commonalities and deviations in the hierarchical organization of crossed-lamellar shells: A case study on the shell of the bivalve Glycymeris glycymeris.* Journal of Materials Research, 2016. **31**(5): p. 536-546.
8. Agbaje, O., et al., *Architecture of crossed-lamellar bivalve shells: the southern giant clam (Tridacna derasa, Röding, 1798).* Open Science, 2017. **4**(9): p. 170622.
9. Boggild, O.B., *The shell structure of the mollusks.* Det Kongelige Danske Videnskabernes Selskabs Skrifter, Natruvidenskabelig og Mathematisk, Afdeling, Ser. 9, 1930. **2**: p. 231-326.
10. Wilmot, N., et al., *Electron microscopy of molluscan crossed-lamellar microstructure.* Philosophical Transactions of the Royal Society B: Biological Sciences, 1992. **337**(1279): p. 21-35.
11. MacClintock, C., *Shell structure of patelloid and bellerophontoid gastropods (Mollusca).* Yale Univ. Peabody Mus. Nat. Hist, Bull., 1967. **22**: p. pls. 1-32.
12. Dauphin, Y. and A. Denis, *Structure and composition of the aragonitic crossed lamellar layers in six species of Bivalvia and Gastropoda.* Comparative Biochemistry and Physiology Part A: Molecular & Integrative Physiology, 2000. **126**(3): p. 367-377.
13. Li, X., et al., *Mechanical Properties of Crossed-Lamellar Structures in Biological Shells: A Review.* Journal of the Mechanical Behavior of Biomedical Materials, 2017.
14. Almagro, I., et al., *New crystallographic relationships in biogenic aragonite: the crossed-lamellar microstructures of mollusks.* Crystal Growth & Design, 2016. **16**(4): p. 2083-2093.
15. Suzuki, M., et al., *Formation of aragonite crystals in the crossed lamellar microstructure of limpet shells.* Crystal Growth & Design, 2011. **11**(11): p. 4850-4859.
16. Currey, J. and A. Kohn, *Fracture in the crossed-lamellar structure ofConus shells.* Journal of Materials Science, 1976. **11**(9): p. 1615-1623.
17. Farre, B. and Y. Dauphin, *Lipids from the nacreous and prismatic layers of two Pteriomorpha Mollusc shells.* Comparative Biochemistry and Physiology Part B: Biochemistry and Molecular Biology, 2009. **152**(2): p. 103-109.
18. Gotliv, B.A., et al., *Asprich: A novel aspartic acid-rich protein family from the prismatic shell matrix of the bivalve Atrina rigida.* ChemBioChem, 2005. **6**(2): p. 304-314.
19. Cusack, M. and A. Freer, *Biomineralization: elemental and organic influence in carbonate systems.* Chemical Reviews, 2008. **108**(11): p. 4433-4454.
20. Marxen, J.C., et al., *Carbohydrates of the organic shell matrix and the shell-forming tissue of the snail Biomphalaria glabrata (Say).* The Biological Bulletin, 1998. **194**(2): p. 231-240.
21. Osuna-Mascaró, A., et al., *The shell organic matrix of the crossed lamellar queen conch shell (Strombus gigas).* Comparative Biochemistry and Physiology Part B: Biochemistry and Molecular Biology, 2014. **168**: p. 76-85.
22. Giuffre, A.J., et al., *Polysaccharide chemistry regulates kinetics of calcite nucleation through competition of interfacial energies.* Proceedings of the National Academy of Sciences, 2013. **110**(23): p. 9261-9266.
23. Nudelman, F. *Nacre biomineralisation: A review on the mechanisms of crystal nucleation*. in *Seminars in Cell & Developmental Biology*. 2015. Elsevier.
24. Suzuki, M., et al., *An acidic matrix protein, Pif, is a key macromolecule for nacre formation.* Science, 2009. **325**(5946): p. 1388-1390.
25. Smeets, P.J., et al., *Calcium carbonate nucleation driven by ion binding in a biomimetic matrix revealed by in situ electron microscopy.* Nature Materials, 2015.
26. Falini, G., et al., *Control of aragonite or calcite polymorphism by mollusk shell macromolecules.* Science, 1996. **271**(5245): p. 67-69.
27. Samata, T., *Ca-binding glycoproteins in molluscan shells with different types of ultrastructure.* The Veliger, 1990. **33**(2): p. 190-201.
28. Marxen, J.C. and W. Becker, *The Organic Shell Matrix of the Freshwater Snail< i> Biomphalaria glabrata</i>.* Comparative Biochemistry and Physiology Part B: Biochemistry and Molecular Biology, 1997. **118**(1): p. 23-33.

29. Lamprell, K., T. Whitehead, and J. Healy, *Bivalves of Australia*. 1992: Crawford House Press.
30. Benzie, J. and S. Williams, *No genetic differentiation of giant clam (Tridacna gigas) populations in the Great Barrier Reef, Australia.* Marine Biology, 1992. **113**(3): p. 373-377.
31. Dominguez, J.G., et al., *Time-averaging and stratigraphic resolution in death assemblages and Holocene deposits: Sydney Harbour's molluscan record.* Palaios, 2016. **31**(11): p. 564-575.
32. Laemmli, U.K., *Cleavage of structural proteins during the assembly of the head of bacteriophage T4.* Nature, 1970. **227**(5259): p. 680-685.
33. Wall, R.S. and T.J. Gyi, *Alcian blue staining of proteoglycans in polyacrylamide gels using the "critical electrolyte concentration" approach.* Analytical Biochemistry, 1988. **175**(1): p. 298-299.
34. Trudel, J. and A. Asselin, *Detection of chitin deacetylase activity after polyacrylamide gel electrophoresis.* Analytical Biochemistry, 1990. **189**(2): p. 249-253.
35. Neo, M.L., et al., *The ecological significance of giant clams in coral reef ecosystems.* Biological Conservation, 2015. **181**: p. 111-123.
36. Su, Y., et al., *Tridacna noae (Röding, 1798)–a valid giant clam species separated from T. maxima (Röding, 1798) by morphological and genetic data.* Raffles Bulletin of Zoology, 2014. **62**.
37. Kobayashi, I. and J. Akai, *Twinned aragonite crystals found in the bivalvian crossed lamellar shell structure.* The Journal of the Geological Society of Japan, 1994. **100**(2): p. 177-180.
38. Popov, S.V., *Composite prismatic structure in bivalve shell.* Acta Palaeontologica Polonica, 1986. **31**(1-2).
39. Bonham, K., *Growth rate of giant clam Tridacna gigas at Bikini Atoll as revealed by radioautography.* Science, 1965. **149**(3681): p. 300-302.
40. Albani, J.R., *Förster energy-transfer studies between Trp residues of α 1-acid glycoprotein (orosomucoid) and the glycosylation site of the protein.* Carbohydrate Research, 2003. **338**(21): p. 2233-2236.
41. Younis, S., et al., *Atomic structure and ultrastructure of the Murex troscheli shell.* Journal of Structural Biology, 2012. **180**(3): p. 539-545.
42. Venyaminov, S.Y. and N. Kalnin, *Quantitative IR spectrophotometry of peptide compounds in water (H2O) solutions. I. Spectral parameters of amino acid residue absorption bands.* Biopolymers, 1990. **30**(13-14): p. 1243-1257.
43. Samata, T. and M. Ogura, *First finding of lipid component in the nacreous layer of Pinctada fucata.* Journal of Fossil Res, 1997. **30**: p. 66.
44. Marie, B., et al., *The shell matrix of the freshwater mussel Unio pictorum (Paleoheterodonta, Unionoida).* FEBS Journal, 2007. **274**(11): p. 2933-2945.
45. Van Kuik, J., et al., *Primary structure of the low-molecular-weight carbohydrate chains of Helix pomatia alpha-hemocyanin. Xylose as a constituent of N-linked oligosaccharides in an animal glycoprotein.* Journal of Biological Chemistry, 1985. **260**(26): p. 13984-13988.
46. Idakieva, K., et al., *Carbohydrate Content and Monosaccharide Composition of Dioxygen-Binding Functional Units from Rapana thomasiana Hemocyaninlsoform RtH2.* Comptes Rendus de l'Academie Bulgare des Sciences, 2001. **54**(10): p. 73.
47. Merry, T. and S. Astrautsova, *Glycoproteins.* eLS, 1996.
48. Kafetzopoulos, D., A. Martinou, and V. Bouriotis, *Bioconversion of chitin to chitosan: purification and characterization of chitin deacetylase from Mucor rouxii.* Proceedings of the National Academy of Sciences, 1993. **90**(7): p. 2564-2568.
49. Tsigos, I. and V. Bouriotis, *Purification and characterization of chitin deacetylase from Colletotrichum lindemuthianum.* Journal of Biological Chemistry, 1995. **270**(44): p. 26286-26291.
50. Marie, B., et al., *Nautilin-63, a novel acidic glycoprotein from the shell nacre of Nautilus macromphalus.* FEBS Journal, 2011. **278**(12): p. 2117-2130.
51. Wolf, S.E., et al., *Nonclassical crystallization in vivo et in vitro (I): process-structure-property relationships of nanogranular biominerals.* Journal of Structural Biology, 2016. **196**(2): p. 244-259.

52. Hovden, R., et al., *Nanoscale assembly processes revealed in the nacroprismatic transition zone of Pinna nobilis mollusc shells.* Nature Communications, 2015. **6**.
53. Jacob, D., et al., *Nanostructure, composition and mechanisms of bivalve shell growth.* Geochimica et Cosmochimica Acta, 2008. **72**(22): p. 5401-5415.
54. Hamm, L.M., et al., *Reconciling disparate views of template-directed nucleation through measurement of calcite nucleation kinetics and binding energies.* Proceedings of the National Academy of Sciences, 2014. **111**(4): p. 1304-1309.
55. Levi-Kalisman, Y., et al., *Structure of the nacreous organic matrix of a bivalve mollusk shell examined in the hydrated state using cryo-TEM.* Journal of Structural Biology, 2001. **135**(1): p. 8-17.
56. Osuna-Mascaró, A.J., et al., *Ultrastructure of the Interlamellar Membranes of the Nacre of the Bivalve Pteria hirundo, Determined by Immunolabelling.* PLoS One, 2015. **10**(4): p. e0122934.
57. Miller, R.F., *Chitin paleoecology.* Biochemical Systematics and Ecology, 1991. **19**(5): p. 401-411.
58. Hackman, R., *Studies on chitin IV. The occurrence of complexes in which chitin and protein are covalently linked.* Australian Journal of Biological Sciences, 1960. **13**(4): p. 568-577.
59. Ehrlich, H., et al., *Discovery of 505-million-year old chitin in the basal demosponge Vauxia gracilenta.* Scientific Reports, 2013. **3**: p. 3497.

Bioorganic-inorganic fibre network in the crossed lamellar bivalve shells: Architecture of shells of *Callista* spp.

Oluwatoosin Bunmi A. Agbaje[1], Gabriel J. Dominguez[2], Dorrit E. Jacob[1]

[1]Department of Earth and Planetary Sciences, Macquarie University, NSW 2109 Australia

[2]Department of Biological Sciences, Macquarie University, NSW, 2109 Australia

Abstract The shells of *Callista disrupta* and *Callista kingii* have a very complex hierarchical architecture and built up of the aragonitic crossed lamellar layers, which are in turn interlayered at a constant angle and reminiscent of plywood. High-resolution electron microscopy imaging exhibit space-filling bodies of nanogranular and acicular substrates. Shell biopolymers consisting of chitin component was revealed on the growth surface of the calcareous biominerals by confocal microscope after staining with Calcofluor White M2R. While thermal gravimetric analysis (TGA) demonstrates total biopolymers of 1.71 wt%, shell macromolecules extracts are dominated by aspartate, glycine and proline (ca 40% in total). Compared to nacre, the saccharidic compositions reveal that the shell-associated matrix is weakly glycosylated. Our SDS-electrophoresis fixing and staining, including unambiguous Calcofluor White, Alcian Blue and/or modified silver staining, show deacetylated chitin and many, if not all of the glycoproteins in the crossed lamellar bivalve shells for the first time. Though the amount of biopolymer is lower compared with nacre (1.7 wt% by TGA vs ~ 4 wt% for nacre), our new findings depict that chitin-protein-complex is not restricted to only nacroprismatic shells.

6.1 INTRODUCTION

The combination of relatively soft bioorganic, comprising proteins, glycoproteins and acidic polysaccharides and brittle inorganic (calcium) carbonate, aragonitic and/or calcitic, demonstrate excellent mechanical properties which are beyond that of the single crystals of the pure materials [1]. The effort to characterise organic macromolecules in nacre has an extensive history and less attention has been devoted to other microstructures, such as crossed lamellar [2, 3].

Crossed lamellar microstructure is the most common of all molluscan microstructures and consisted three or four orders of lamellae [4]. The larger hierarchical units (first order lamella) are composed of smaller bundles of laths (second order lamella) which are in turn further consisting of thin lamellae of about 100 nm thickness that are known as third-order lamellae [2, 5, 6]. Thin layers of biopolymer form coatings on the smallest units [6], and thicker layers of biopolymer are also extant within second order lamellae layers [6]. The microstructure and inorganic composition of crossed lamellar shells between several species are comparable [7-9], whereas the distinctions in crystallographic orientation of the inorganic (calcium) carbonate and level of structural complication remain and very little is known about the organic macromolecules [10, 11]. We present here the first in-depth study of the inorganic matrix and the organic composition in the shells of *Callista* spp. Careful etching observations with Field Emission-SEM analysis enabled us to reveal a universal design motifs – nanogranular composite structure [12]. Our histochemical staining allowed us to depict and characterise shell macromolecules, including organic framework, protein and glycoproteins.

6.1.1 Cross-laminated architecture of *Callista* bivalve shells

Two species of cockle shells are studied: *Callista disrupta* (Sowerby, 1853) and *Callista kingii* (Gray in King, 1827). The structural patterns of *Callista* shells are made of aragonite and reflected optical microscopy shows two shell layers, the outer- and the inner- layers (Figure

6.1a). In the outer layer, stripe patterns run distinctively at a ca 90^{o} to the daily growth lines (Figure 6.1b). These stripes assigned to the irregular shaped first order prisms [13]. Each first order-prism appears to consist smaller bundles of elongated units (second order prisms) that are stacked up diagonally along the stripes (Figure 6.1b) [13, 14].

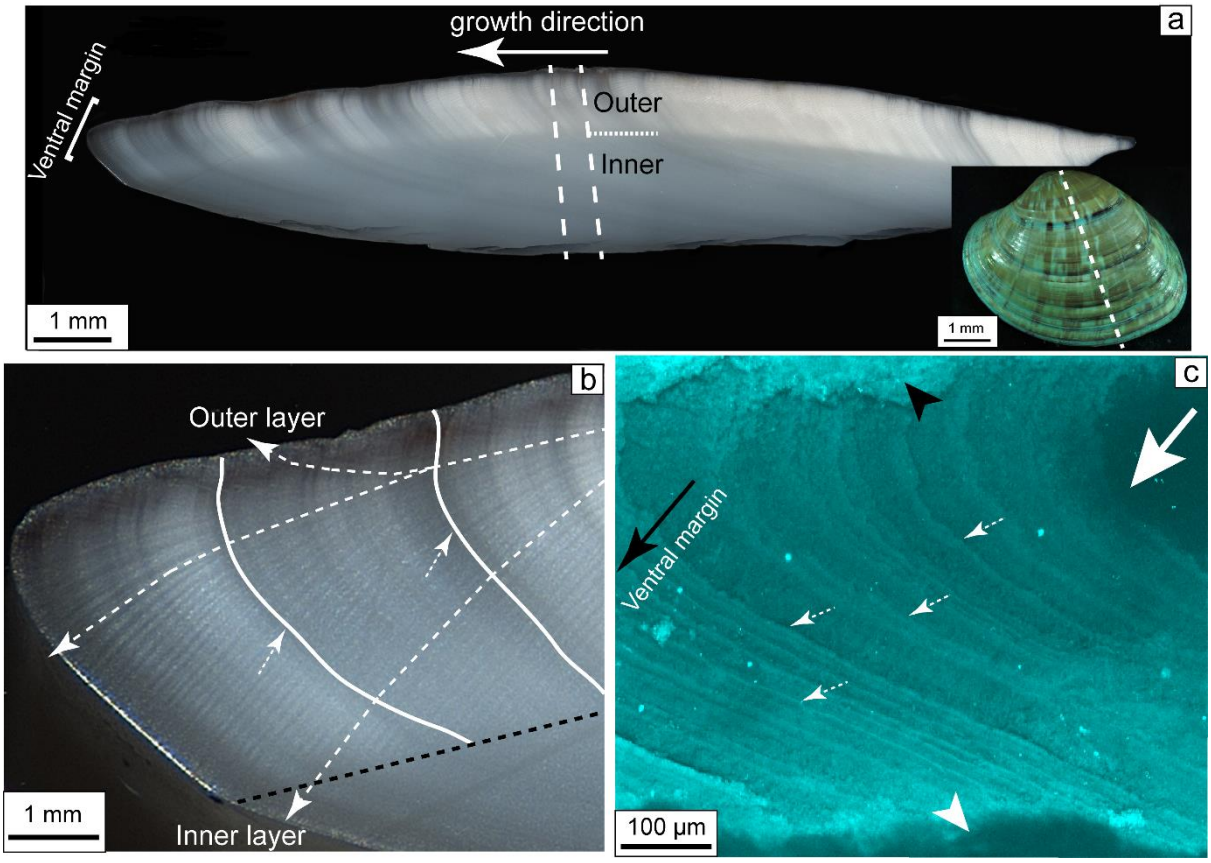

Figure 6.1. Complete valve of the shell of *Callista* species (insert in a). (a) Optical micrograph of *Callista* shell showing growth lines and two layers. (b) Radial section at the ventral margin (growth edge) of the *Callista* shell. Black dotted line depicts outer- and inner- layers. (c) Note the distibution of organics within the growth bands stained with Calcofluor White M2R. The white arrowhead point towards inner and the black arrowhead point towards outer shell layers. The white arrow defines the outside surface of the shell.

Daily growth lines in the shells of mollusc have higher concentrations of organics [3] and can be visualised using fluorescent dye – Calcofluor white M2R (CFW). CFW forms hydrogen bonds with β-(1-3)- and β-(1-4)-linked polysaccharides, and shows a high affinity for carbohydrates [15]. Shell pieces (after etching) was stained with CFW, birefringent organic framework was observed within the shells of *Callista* species (Figure 6.1c; Supplementary

Figure S6.1) and is strikingly comparable to the daily growth lines observed with the optical microscopy (Figure 6.1a, b) and organic fibres observed with Field Emission-SEM (Figure 6.2).

6.2 MATERIAL AND METHODS

6.2.1 MATERIAL

Living specimens of *Callista kingii* (Gray in King, 1827), (Mollusca: Bivalvia), were collected in the Bermagui Harbour of New South Wales, Australia. After capture, the soft tissues of the bivalves were mechanically removed and subsequently washed under running Milli-Q water and hence allowed to dry at room temperature. Empty shells of *Callista disrupta* species (Sowerby, 1853) from unknown origin, Sydney Harbour area.

6.2.2 METHODS

6.2.2.1 Scanning Electron and Confocal Microscopy. Shell sample was broken into fragments of sub-cm in size. For SEM, the fragments were treated with 1% EDTA disodium salt (wt/vol), gold-coated (3 min, 2 angles; Emitech K550) and image with a JEOL JSM-7100F Field Emission Scanning Electron Microscope (FESEM). A fluorescence microscopical investigation of the shells were performed using a Calcofluor white M2R (Sigmal Aldrich; Fluorescent brightener F-3543; 0.1%). Prior to staining, samples were decalcified with 10% glacial acetic acid at 4^{o}C. Birefringent organic framework was observed with an Olympus Fluoview FV1000 laser confocal microscope (Olympus, Japan). A laser diode at 405 µm and UV-spectrum 425-525 µm were used as the filter.

6.2.2.2 Shell preparation and organic matrix extraction. The intact shells were submerged in 30% H_2O_2 (Merck KGaA, 64271 Darmstadt; Germany) for 2 h combined with ultrasonic treatment to remove superficial organic contaminants, washed with Milli-Q water and acetone, air-dried, and then powdered with a rock crusher before bioorganic content was calculated by

using a TGA 2050 thermogravimetric analyser (TA Instruments, USA). The powdered sample was decalcified in 1 mM HCl (*p*H > 5) for 48 h. The entire extract was centrifuged at 10,500 rpm (4^{o}C) for 30 min to separate the supernatant (Soluble Organic Matrix; SOM) and precipitate (insoluble fraction). The lyophilized insoluble fraction was further decalcified in 1:1 (pH > 4) of 0.1 N trichloroacetic acid and phosphate buffer (*p*H 7.4). SOM and soluble organic matrix extracted from the insoluble fraction, termed trichloroacetic acid-phosphate buffer soluble matrix (TPM) were concentrated by using Sep-Pak C_{18}-2g (Waters Associates Milford, MA, USA) and later lyophilized. Then, the TPM was desalted twice with cold acetone, centrifuged at 12,000 rpm (4^{o}C) for 15 min and the pellet was air-dried at room temperature.

6.2.2.3 Characterization of organic matrix. Fourier Transform Infrared (FTIR) spectra were conducted obtained from lyophilized samples (SOM and TPM) at a 4 cm^{-1} resolution with 64 accumulations in the range 4000-600 cm^{-1}, using a Thermo Nicolet iS10 FTIR spectrometer (Nicolet, MA, USA) equipped with a smart performer accessory Attenuated Total Reflection device. A background spectrum was measured at the beginning of the analysis.

Saccharide compositions of the SOM and TPM were quantified following the method described in Chapter 5. Each moiety lyophilisate was hydrolysed in 2 M trifluoroacetic acid at 100°C (4 h) and 8 M HCl at 100°C (6 h), respectively. The sugar contents of the hydrolysate samples: glucosamine, galactosamine, mannose, xylose, fucose, galactose and glucose were determined on a high-performance anion-exchange chromatograph system with pulsed amperometric detection (HPAEC-PAD) fitted with a BioLC amino trap guard column (3 x 50 mm) connected to a CarboPac PA10 column (4 x 250 mm) (Dionex Corp., Sunnyvale, CA, USA) held at 25°C and eluted by using sodium hydroxide at a flow rate of 0.5 mL/min. The sugar contents expressed as an ng/mg, represent the average of duplicate results. For amino acid analysis, aliquots of the shells extracts, SOM and TPM, were acid hydrolysed under nitrogen in 6 N HCl at 110^{o}C for 24 h. Ensuing evaporation of the HCl solution, the resulting

hydrolysates were analysed using an ACQUITY ultra-performance liquid chromatography (UPLC) system and BEH RP C18 1.7μm column (Waters Corporation, Milford, MA)[16].

6.2.2.4 Determination of matrix proteins and chitin derivatives on SDS-PAGE

The shell matrices of *Callista* shells were separated under denaturing conditions by one dimensional SDS-PAGE using a pre-cast NuPAGE 4–12% Bis-Tris gel in MES running buffer according to protocols supplied by the manufacturer (Invitrogen; Carlsbad, CA, USA). After electrophoresis, gels were stained for proteins with silver nitrate and for potential glycosylation with Alcian blue following the protocol described in Chapter 2 and 5. In brief, SOM and TPM of *Callista* shells were stained with Alcian Blue 8GX at *p*H 1 for the very specific acidic sulfated sugars, and subsequently stained with silver nitrate. Chitin deacetylated (CDA) activity was analysed after SDS-PAGE using the protocol described in Chapter 5.

6.3 Results

6.3.1 Shell microstructure observations

Careful etching of shells of *Callista* spp. and observations with FESEM exhibit the internal structure of the calcareous biominerals and what we address as the constituting primary particles. High-resolution SEM imaging of cross-sectional species (Figure 6.2) shows three layers: an outer composite prismatic (Figure 6.2a); a middle layer with crossed lamellar (Figure 6.2b); and an inner layer that includes both homogeneous and fine complex crossed lamellar structures (Figure 6.2c; Supplementary Figure S6.2). As is typical to venerid shells, other studies revealed that the layers consists up to five different microstructures [5, 17].

Within the outer shells layer, *Callista* spp. composed of acicular crystals and arranged parallel with the aggregate of granular particles (Figure 6.2d). Both, acicular crystals and aggregate of granular particles are arranged in a feathery manner and appear perpendicular to the growth lines. In the middle layer, granule-by-granule growth becomes aragonitic rod-type mineral. These rods alternate, and thus form crossed lamellar microstructure (Figure 6.2b, e).

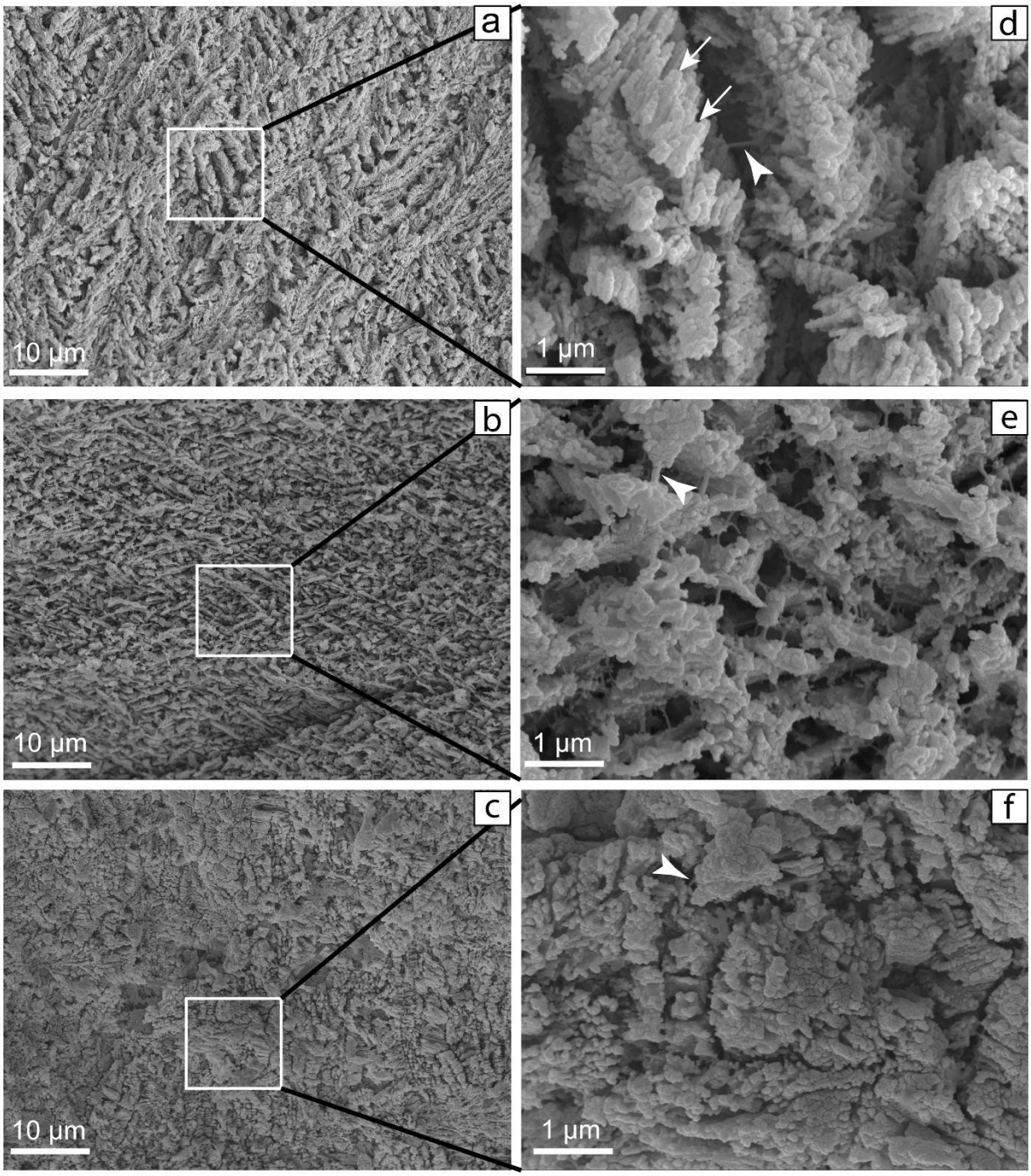

Figure 6.2. Shell microstructure of *Callista* species showing organic fibres (arrowheads). (d), (e) and (f) exhibit the enlargement structure in (a), (b) and (c). d) Composite prismatic outer layer shows a feathery appearance (see Figure S6.2) and mixture of granular and acicular grains (arrows). e) In middle layer, granule-by-granule growth becomes rods and eventually form crossed lamellar layer. Note a network of organic fibres that are consistently intergrown with the inorganic fibres.

Within middle layer, however, careful inspection reveals that randomly homogeneous fibrous structure exists and inner layer exhibits no discernible structure (Figure 6.2c’), typically known

as homogeneous and found in some venerid shells [5, 17-19]. In summary, SEM imaging of the outer- and inner-layers demonstrate structural patterns where organic fibrils and inorganic matrix are arranged in such a distinct fibre network (Figure 6.3) and hence produce such a uniquely formed biomineral.

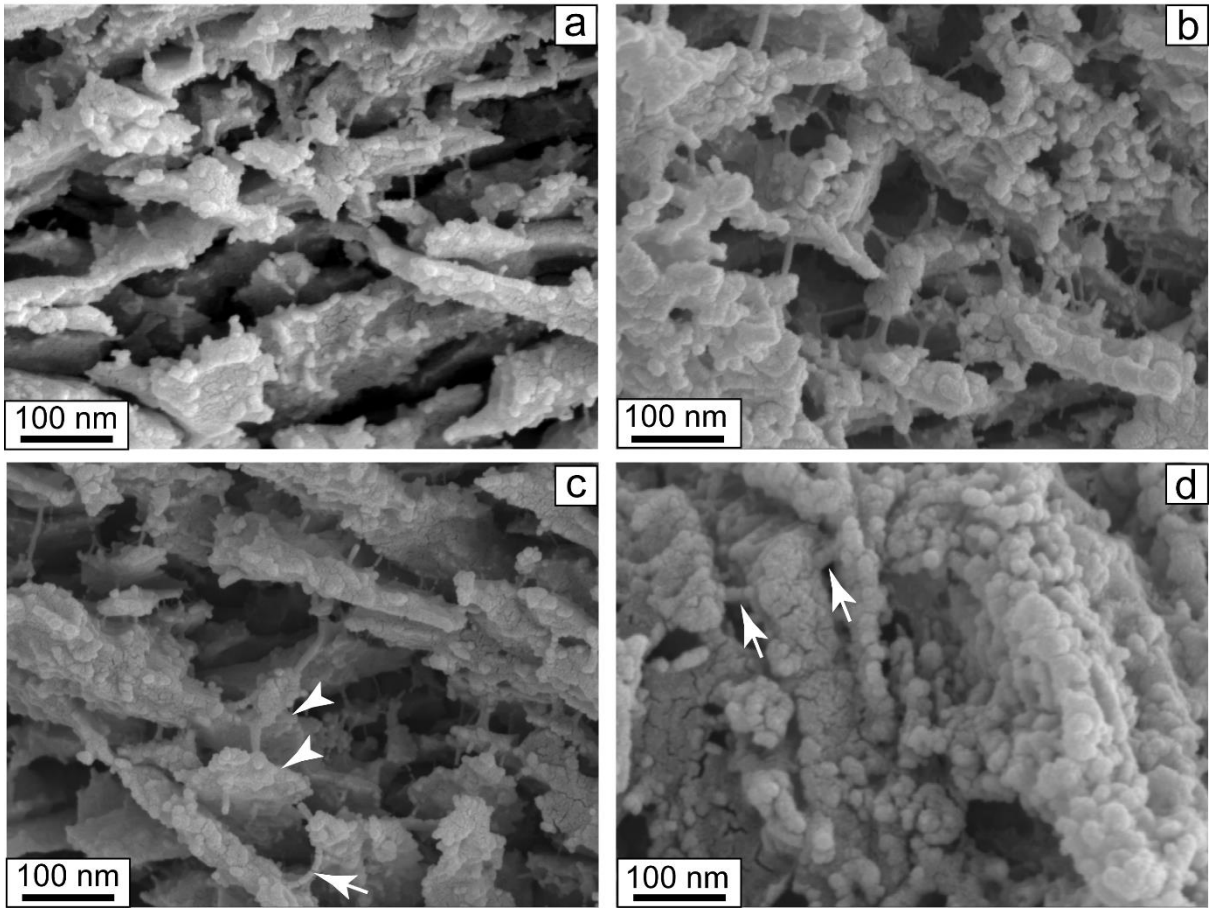

Figure 6.3. Detail showing nanogranules at the middle layer (a-c) and outer layer (d). The organic fibrils (arrows) between the granules become more visible. In (c), organic fibril (arrow) joins nanorod with the granular plates (arrowheads).

6.3.2 Fourier Transform Infrared (FTIR) analysis

Figure 6.4 illustrates the functional properties of the lyophilised samples of the soluble organic matrices (SOM and TPM). Bands at around 3272 cm^{-1}, 3065 cm^{-1} and between 2962 cm^{-1} and 2873 cm^{-1} assign to the N-H bound of amide A, B and C-H stretching groups, respectively. Also, a strong band at around 1640 cm^{-1} is attributed to the C=O of amide I. Different patterns occur in the spectra of SOM and TPM, a well-defined amide II band at 1515 cm^{-1} (C-N bound) and a small amide III band at 1310 cm^{-1} (C-N and N-H bound) for SOM

show small shoulders at around 1529 cm^{-1} and 1320 cm^{-1} in the spectrum of TPM. Also, the carbohydrate band at 1069 cm^{-1} is more prominent in TPM extract. However, strong absorption bands at around 1450 cm^{-1} and 1395 cm^{-1} for both, SOM and TPM, assign to the C-H bending vibration and carboxylate absorption bands, respectively. The assignments in this study agree well with the findings in the literature (Table 6.1). Since sulfate is indicated in between 1250-1200 cm^{-1}, the band near 1236 cm^{-1} can be interpreted as a sulfate band, strongly imply that polysaccharide molecules are sulfated.

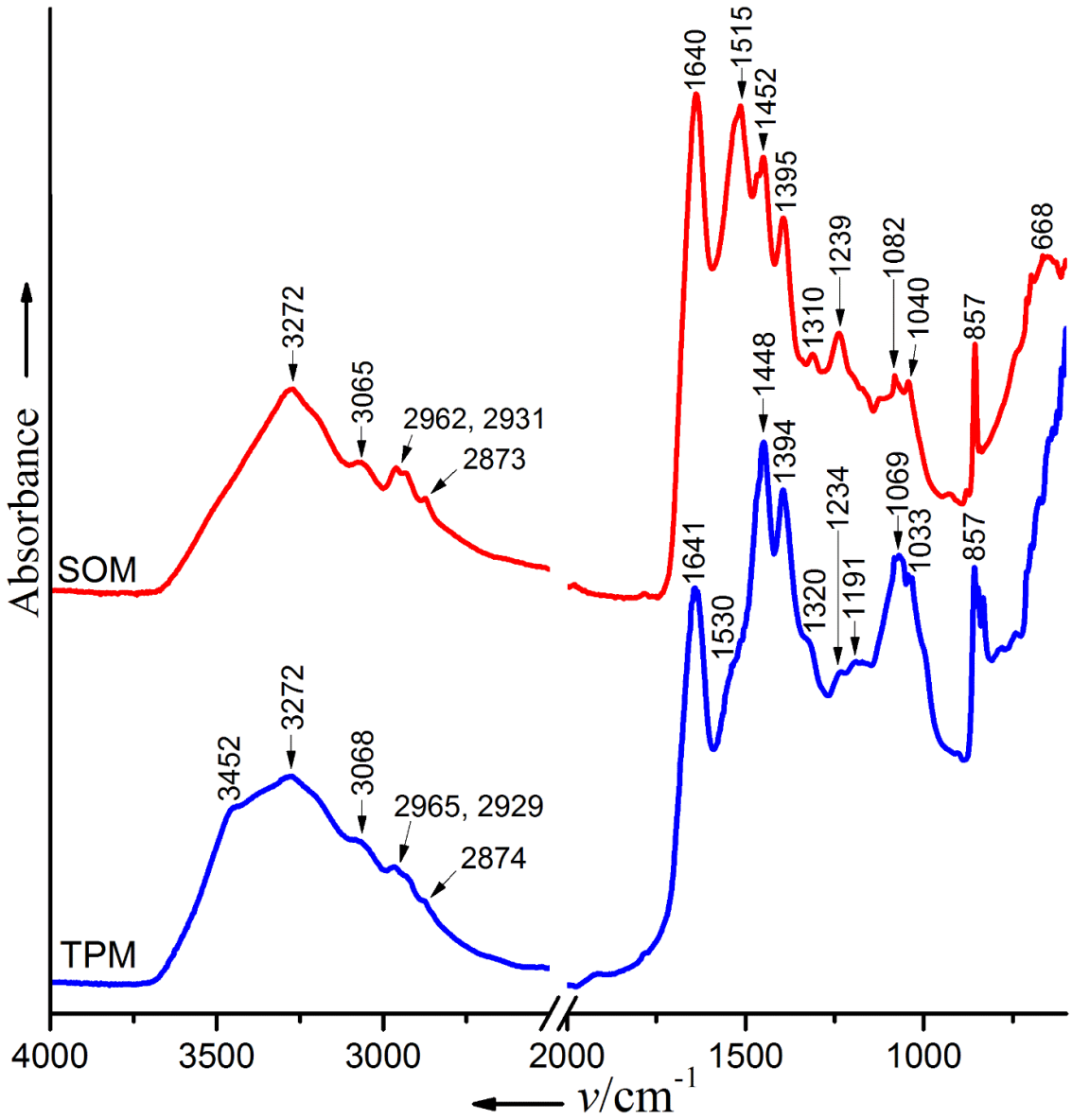

Figure 6.4. FTIR spectra of *Callista* shells in the range 4000-600 cm^{-1}. Soluble Organic Moiety (SOM). Trichloroacetic acid-Phosphate buffer Soluble Moiety (TPM). See Table 1 below for peaks assignment.

Table 6.1

The FTIR band assignments of the shell organic matrices

Soluble Organic Matrix (SOM)	TCA-phosphate buffer soluble matrix (TPM)	Assigned
3272	3272	ν^{as}_{NH} (Amide A)
3065	3068	$\nu^{s}_{N\text{-}H}$ (Amide B)
2962	2965	$\nu^{as}_{C\text{-}H}$ of alkyl
2931	2929	$\nu^{s}_{C\text{-}H}$ of methylene
2873	2874	$\nu^{s}_{C\text{-}H}$ of alkyl
1640	1641	$\nu_{C=O}$ (Amide I)
1515	1530*	$\nu_{C\text{-}N}$ (Amide II)
1452	1448	$\delta_{C\text{-}H}$ of alkyl
1395	1394	$\nu^{s}_{COO^-}$
1310	1320*	$\delta_{C\text{-}N} + \delta_{N\text{-}H}$ (Amide III)
1239	1234, 1191	$\nu^{s}_{S=O}$ (Sulfate)
1082, 1040	1069, 1033	$\nu_{C\text{-}O\text{-}H}$ (Polysaccharide)
857	857	$\gamma_{C\text{-}H}$
668	-	$\gamma_{O=C\text{-}N\ deformation}$

Band assignments using data from Marxen et al. [20]; Stankiewicz et al. [21]; * = shoulder.

6.3.3 Amino acid composition

The amino acid composition of SOM and TPM is presented in Table 6.2A. In SOM extract, glycine, proline and aspartate account for 35.2 mol% of the total amino acids, followed by glutamate, leucine and alanine, making up 22.3%. Contrarily, TPM extract contains a prominent amount of aspartate (17.5%), followed by glycine, glutamate and proline. The last three residues constitute 32.6% of the total amount of the amino acid. In TPM, polar amino acid (aspartate and glutamate) is significantly higher (28.1%) compared to SOM (17.7%). Also, arginine, phenylalanine, valine and isoleucine (23.9% of the total amino acids) are fairly distributed in SOM whereas, threonine, valine, alanine, leucine and isoleucine comprised 27.3% of the total amino acids in TPM. Both, SOM and TPM contain serine at approximately 6%. The lowest amount of histidine in SOM (0.2%) is rather similar to that of TPM (0.4%) (Table 6.2A).

Comparing the results of *Callista* shells with *A. islandica* amino acid, their composition is comparable; the total amino acid comprising of aspartate, glycine, glutamate and proline in soluble organic matrices of *A. islandica* shells, is close to the TPM of *Callista* shells (48.4% in total vs 50.1%; Supplementary Figure S6.3). Though the amount for SOM of *Callista* shells is

relatively lower (42.7% in total), this is strikingly comparable to the soluble organic matrix found in homogeneous shells *Mercenaria stimpsoni* (42.0%; ref.[11]).

Table 6.2

The composition of the organic moieties of *Callista* species. (a) Amino acid composition (mole %) of the SOM and of the TPM extracts. (b) Monosaccharide composition of the SOM and of the TPM extracts. The values are expressed in ng/mg and in wt%. TR, trace.

(a) Percentage of the total amino acid		
Amino Acid	SOM	TSM
His[a]	0.2	0.4
Ser[b]	6.2	6.0
Arg[a]	6.2	4.4
Gly	13.3	11.8
Asx [a] (Asp + Asn)	10.2	17.5
Glx[a] (Glu + Gln)	7.5	10.6
Thr[b]	4.7	5.4
Ala[c]	7.3	6.3
Pro[c]	11.7	10.2
Lys[a]	3.3	4.0
Tyr[b]	2.7	2.6
Met[c]	1.4	0.3
Val[c]	6.1	5.5
Ile[c]	6.1	4.9
Leu[c]	7.5	5.2
Phe[c]	5.5	4.7
(b) Monosaccharide composition [ng/mg of matrix (% of the total matrix composition)]		
Galactosamine	460 (26.1)	643 (16.8)
Glucosamine	327 (18.6)	528 (13.8)
Fucose	TR	TR
Glucose	534 (30.3)	1163 (30.4)
Xylose	219 (12.4)	939 (24.5)
Mannose	220 (12.5)	555 (14.5)
Total	1760 (100)	3828 (100)
Total Sugars	0.17%	0.38%

NB: [a] charged amino acid; [b] uncharged, polar amino acid; [c] hydrophobic amino acid; WSM: Water-Soluble Moiety; TPM: Trichloroacetic acid-Phosphate buffer Soluble Moiety (Extract from Water-Insoluble Moiety)

6.3.4 Monosaccharide composition

The soluble organic matrices, SOM and TPM exhibit the presence of neutral and amino sugars (Table 6.3). In SOM, galactosamine and glucose are the prominent constituents, depict

56.4% of the total amount of the sugar contents followed by glucosamine, mannose and xylose. The sum of the three components represents 43.5% of the total amount of sugar contents. On the other hand, glucose and xylose (54.9% in total) are the prominent sugar contents in TPM, followed by galactosamine, mannose and glucosamine. While the two organic extracts (SOM and TPM) exhibit only traces of fucose, the total amount of neutral and amino sugars in each matrix denotes 0.18% and 0.38% w/w for SOM and TPM. The percentage of the sugar contents in this study does not represent the totality of the carbohydrate in *Callista* shells. After the extraction of organic macromolecules from the insoluble fraction by using trichloroacetic acid-phosphate buffer solution (see the method of extractions), we observed an insoluble fraction that may still contain a considerable amount of carbohydrates. Therefore, it is most likely that the percentage is underestimated. This method of extraction, however, allows us to show that *Callista* shells contain chitin (and its derivatives) with the aid of SDS-PAGE method (see protein signature).

6.3.5 Proteins signature

A sequential soluble organic fraction (SOM and TPM) derived from *Callista* shells are similarly characterised by mono-dimensional gels (Figure 6.5). Using Alcian Blue and/or silver nitrate stains, the total mixture of organic biomolecules in SOM contain many shell proteins that separated in SDS-PAGE gels, bands at around 18, 36, 58, below and above 110, and far above 260 kDa are visualized with silver nitrate stain. On top of those above protein bands mentioned, one additional band stained faintly at apparent molecular weight 78 kDa (Figure 6.5b; lane 1) with Alcian Blue method (see method). The latter staining intensity is relatively higher than silver nitrate, demonstrating that the shell proteins are glycosylated. Contrarily, TPM extract depicts a strong negative staining with silver nitrate (Figure 6.5a; lane 2). The same fixation method was used, and the gel was stained with Alcian Blue and then enhanced with silver nitrate, we exhibit many prominent protein bands (Figure 6.5b; lane 2). Also seen

in this fraction is bands with a higher molecular mass far above 260 kDa (Figure 6.5b; lane 2). This result demonstrates that only silver nitrate does not bind to these glycosylated acidic proteins. This result is consistent with the observation that traditional protein stains such as Coomassie Blue and Silver nitrate bind faintly with proteoglycans and glycosaminoglycans in gels [22] (Chapter 5), however, no protein band was observed in shell of *M. stimpsoni* [23].

Amino polysaccharide wherein their polymers are referred to as chitin or chitosan (depending on the degree of acetylation), is found as one of the organic components of the organic biopolymer in molluscs [24]. The chitin and its derivatives typically found in, such as cell wall of most fungi [25, 26] and the exoskeleton of some arthropods [27], have been investigated by SDS-PAGE. For this study, SOM was characterised by the presence of apparent molecular weights of 36, 58, 78 and 110 (Figure 6.5c; lane 1), indicating that SOM fraction consists shell proteins that are covalently linked with sugar moiety. TPM demonstrates major molecular weights at 110 and 80 kDa, bands at around 5, 36, 40, 45 kDa and additional bands (including bands above 110 and 80 kDa) that stained faintly could be identified (Figure 6.5c; lane 2). Calcofluor white binds specifically to sugar derivatives such as chitin, chitosan and cellulose and not directly with the proteins[28] even when staining glycoprotein[29]; most of the prominent glycoprotein bands in Figure 6.5b are indeed not visible or noticeable with unambiguous Calcofluor staining (Figure 6.5c). For instance, glycosaminoglycans bands far above 260 kDa for both SOM and TPM are not visible in Figure 6.5c. Besides, apparent molecular weights that show negative staining at around 5 and 10 kDa in Figure 6.5b birefringent with fluorescence method (Figure 6.5c). This result reiterates that hydrophobic constituent that acts as an architectural framework onto which hydrophilic components directly associated is indeed intercalated in *Callista* shells (see Figure 6.1, Figure 6.2).

6.4 Discussion

The shells of *Callista* spp. are build solely with an aragonitic inorganic (calcium) carbonated granules. These shells employ a universal structural trait where most biominerals share a nanogranular composite structure [12]. Herein, the shapes of granular particles can be grouped, in the middle- and outer-layers, into polycrystalline fibre-like fabric and platelet-like (Figure 6.3), and are intimately intergrown with the organic fibres.

The shell structures of *Callista* spp. is highly mineralised with a minimal amount of organic content (1.71 wt%; Supplementary Figure S6.4) compared to a ca 4 wt% found in nacre shells [16]. Its structure is entirely different even from other shells with crossed lamellar microstructure [9, 30] and overall more distinct and complex than the nacroprismatic morphology [30, 31]. Contrast with nacroprismatic shells with just two calcified layers, SEM imaging of the samples studied depict four layers, the massive homogeneous structure is secreted very carefully with the fine complex crossed lamellar structure in the inner layer, and in the middle layer, rod-type crossed lamellar structure is discernible. The outer or outermost layer is composed of feathery appearance inorganic matrix, which are in turn diverging from the midst of the layer (Figure 2a). Nanoparticles of this layer are secreted by the acicular crystals in a characteristic ‘cross-stitch’ pattern and co-occur with the granules. While the mechanisms of coexistence in the same layer are challenging to define, the ‘cross-stitch’ pattern in the outer layer of *Callista* spp. may relate to crossed acicular or complex composite prismatic [5, 13, 17].

Our unambiguous staining method revealed the organic fibres that intercalated within and along the elongated inorganic matrix (Figure 6.1). The organic fibres joined inorganic fibres together (Figure 6.2, 6.3; Supplementary Figure 6.1), and thus control the orientation of inorganic (calcium) carbonate [32]. In nacre, minor chitin constituent comprises of very thin organic fibres; each fibre has a protein coat and hence forms a chitin-protein-complex fibre [33]. Herein, total amino acid compositions and proportions from combining the SOM plus

TPM consist relatively higher amount of aspartate (asparagine and aspartic acid), proline, serine and threonine (Supplementary Figure S6.5). These residues are common glycosylation linkers in glycoproteins and associated with a relatively large amount of sugar-derivatives, probably proteoglycans [34]; previous work showed that these aggregates are involved in biomineral nucleation and crystal growth [35]. Though shell macromolecules of the samples studied are weakly glycosylated since the total contents of sugar constituents represent < 1 wt% (Table 6.2b), however, our results identify well-defined glycoprotein bands. A 'doublet' (SOM, lane 1) and 'singlet' (TPM, lane 2) protein bands far above 260 kDa (Figure 6.5) are attributed to the glycosaminoglycan bands. This result agrees well with the previous findings (Chapter 5).

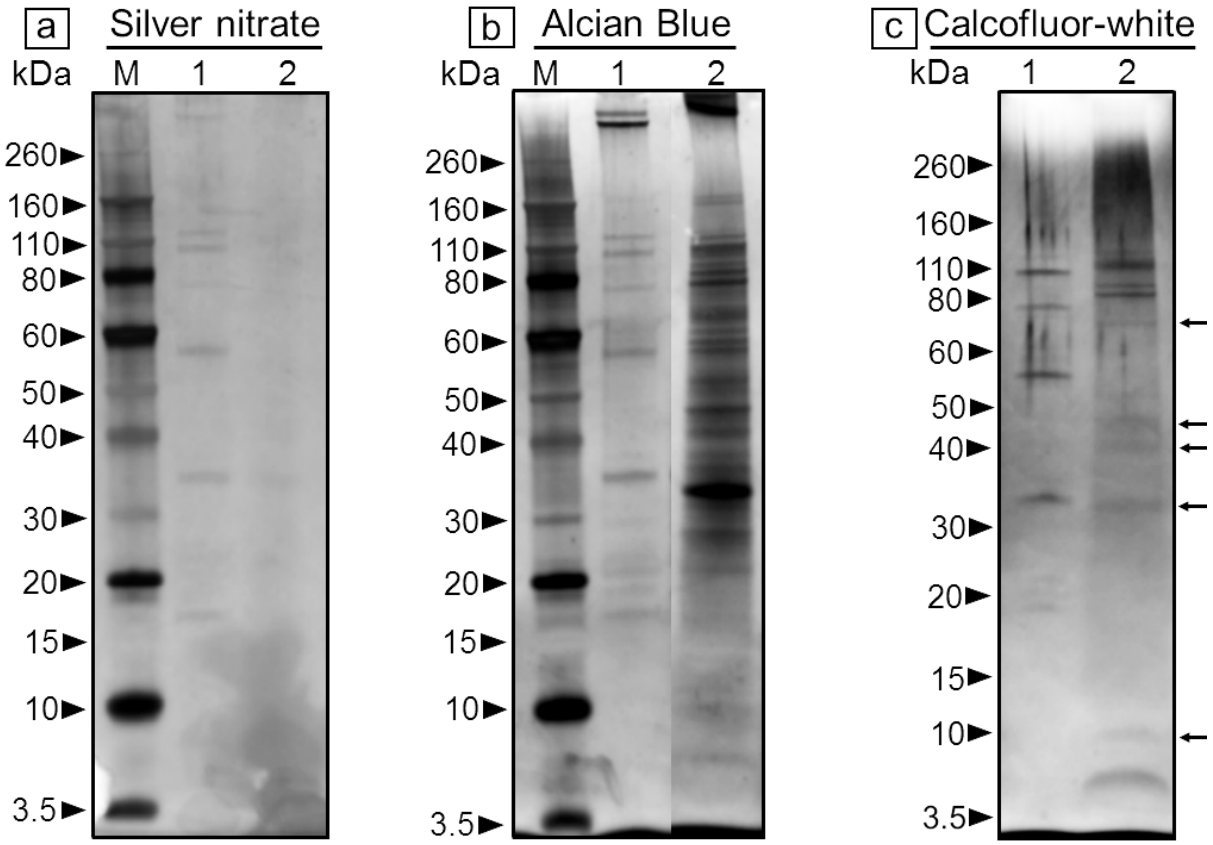

Figure 6.5. SDS-PAGE of SOM (Lane 1) and TPM (Lane 2) extracts. Lane M: Standard marker with masses in kDa. For Alcian Blue and Calcofluor-white, see methods for detail. Arrows depict apparent molecular weights at around 70, 45, 40, 36 and 10 kDa. Relative molecular bands far above 260 kDa (in a and b) point to glycosaminoglycans and/or proteoglycans band. (b) (Lane 1) shows doublet bands far above 260 kDa. Figure **NB:** Standard marker shows negative staining with Calcofluor-white dye.

The many published works of shell proteins that utilised SDS-electrophoresis, however, are thus improbable to be representative of shell macromolecules. Studies have reported that homogeneous and crossed lamellar bivalve shells contain no noticeable protein bands [10, 11], though poor staining might be attributed to insufficient protein concentration[36]. Moreover, nuclear magnetic resonance (NMR) (chapter 3) revealed that homogeneous (and probably crossed lamellar) shells constitute the high amount of proteinaceous type IV collagen, lower amount of chitin (ca 1 wt%) and acidic polysaccharides for instance, glycosaminoglycans (more specifically proteoglycans; [16]). Some of these components are challenging to stain - either diffuse, smear or stain faintly in SDS-electrophoresis [10, 11, 37].

Moreover, biochemical studies of the amino acid composition of homogeneous *A. islandica* shell is apparently similar to the composition of amino acid in *Callista* shells. Primary residues, comprising glycine, aspartate and proline are strikingly similar (39.9% in total vs 39.5%; Supplementary Figure S6.3), and solid state NMR spectra showed only low levels of biopolymers that cannot be assigned to any particular species, other than the interfacial carbonates for undecalcified *A. islandica* and *Callista kingii* shells. However, the insoluble organic moiety of *A. islandica* revealed type IV collagen gel, and thus constitutes higher proportions of glucosamine, galactosamine and galactose, an *O*-glycosylated sugar moiety that play a role in protein folding, interaction, stability, and mobility, as well as in signal transduction [38](Chapter 3). Exploring glycopolymers by using Calcofluor white M2R dye for both *in*-situ and *ex*-situ, we find something comparable as shown in Figure 6.1c and Figure 6.5c. Bioorganic in *Callista* shells is a cross-linked macromolecular assembly primarily made of glycoproteins and polysaccharides. As shown in Table 6.2B, the glycosidic part, together with fairly typical carbohydrates, has a certain amount of aminated biopolymers (Figure 6.1c; Figure 6.5c). Our NMR study (Chapter 3) showed that the amount of sugar moiety in nacreous is smaller compared with the homogeneous shells. Based on the amount of organic matrix (1.71 wt%) and the percentage of total sugar contents in this study, the amount of chitin (and its

derivatives) in the shells of *Callista* spp. could be lower than the one present in nacreous shells. This aspect of organic matrix in non-nacreous shell is new, more scrutinising is needed to further explain the composition of organic moiety in non-nacreous shells most especially in crossed lamellar microstructure.

Acknowledgements. We thank Dr Matthew Kosnik for providing *Callista disrupta* shells. We are grateful to Denise Thomas and Fei Chi for handling amino acid and monosaccharides analyses, respectively. The work was facilitated in part by the Australian Government's National Collaborative Research Strategy (NCRIS) and its facilities at the Australian Proteome Analysis Facility (APAF).

6.5 References

1. Barthelat, F., J.E. Rim, and H.D. Espinosa, *A review on the structure and mechanical properties of mollusk shells–perspectives on synthetic biomimetic materials.* Applied Scanning Probe Methods XIII, 2009: p. 17-44.
2. Boggild, O.B., *The shell structure of the mollusks.* Det Kongelige Danske Videnskabernes Selskabs Skrifter, Natruvidenskabelig og Mathematisk, Afdeling, Ser. 9, 1930. **2**: p. 231-326.
3. Agbaje, O.B.A., et al., *Architecture of crossed-lamellar bivalve shells: The Southern Giant Clam (Tridacna derasa, Röding, 1798).* Royal Society Open Science, 2017. **4: 170622**.
4. Li, X., et al., *Mechanical Properties of Crossed-Lamellar Structures in Biological Shells: A Review*. Journal of the Mechanical Behavior of Biomedical Materials, 2017.
5. Carter, J.G., *Skeletal biomineralization: patterns, processes and evolutionary trends*. Vol. 1. 1990: Wiley Online Library.
6. Uozumi, S., K. Iwata, and Y. Togo, *The ultrastructure of the mineral in and the construction of the crossed-lamellar layer in molluscan shell.* Journal of the Faculty of Science, Hokkaido University. Series 4, Geology and mineralogy = Hokkaido University Faculty of Science, 1972. **15**(3-4): p. 447-477.
7. Wilmot, N., et al., *Electron microscopy of molluscan crossed-lamellar microstructure.* Philosophical Transactions of the Royal Society B: Biological Sciences, 1992. **337**(1279): p. 21-35.
8. Pokroy, B. and E. Zolotoyabko, *Microstructure of natural plywood-like ceramics: a study by high-resolution electron microscopy and energy-variable X-ray diffraction.* Journal of Materials Chemistry, 2003. **13**(4): p. 682-688.
9. Almagro, I., et al., *New crystallographic relationships in biogenic aragonite: the crossed-lamellar microstructures of mollusks.* Crystal Growth & Design, 2016. **16**(4): p. 2083-2093.
10. Dauphin, Y. and A. Denis, *Structure and composition of the aragonitic crossed lamellar layers in six species of Bivalvia and Gastropoda.* Comparative Biochemistry and Physiology Part A: Molecular & Integrative Physiology, 2000. **126**(3): p. 367-377.
11. Samata, T., *Ca-binding glycoproteins in molluscan shells with different types of ultrastructure.* The Veliger, 1990. **33**(2): p. 190-201.
12. Wolf, S.E., et al., *Nonclassical crystallization in vivo et in vitro (I): process-structure-property relationships of nanogranular biominerals.* Journal of Structural Biology, 2016. **196**(2): p. 244-259.

13. MacClintock, C., *Shell structure of patelloid and bellerophontoid gastropods (Mollusca).* Yale Univ. Peabody Mus. Nat. Hist, Bull., 1967. **22**: p. pls. 1-32.
14. Hayashi, A., et al., *Crystallographic characterization of the crossed lamellar structure in the bivalve Meretrix lamarckii using electron beam techniques.* Journal of Structural Biology, 2011. **176**(1): p. 91-96.
15. Burns, E.R., M. Wittner, and F. Faskowitz, *Method for detecting chitin-containing organisms*. 2005, Google Patents.
16. Agbaje, O.B.A., et al., *Organic macromolecules in shells of Arctica islandica: comparison with nacroprismatic bivalve shells.* Marine Biology, 2017. **164**: p. 208.
17. Shimamoto, M., *Shell microstructure of the Veneridae (Bivalvia) and its phylogenetic implications.* 1986.
18. Ropes, J., S. Murawski, and F. Serchuk, *Size, age, sexual, maturity, and sex-rati in ocean quahogs, Arctica-islandica linne, off Long-Island, New-York* Fishery Bulletin, 1984. **82**(2): p. 253-267.
19. Shirai, K., et al., *Assessment of the mechanism of elemental incorporation into bivalve shells (Arctica islandica) based on elemental distribution at the microstructural scale.* Geochimica et Cosmochimica Acta, 2014. **126**: p. 307-320.
20. Marxen, J.C., et al., *Carbohydrates of the organic shell matrix and the shell-forming tissue of the snail Biomphalaria glabrata (Say).* The Biological Bulletin, 1998. **194**(2): p. 231-240.
21. Stankiewicz, B.A., et al., *Biodegradation of the chitin-protein complex in crustacean cuticle.* Organic Geochemistry, 1998. **28**(1): p. 67-76.
22. Moller, H., D. Heinegard, and J. Poulsen, *Combined alcian blue and silver staining of subnanogram quantities of proteoglycans and glycosaminoglycans in sodium dodecyl sulfate-polyacrylamide gels.* Analytical Biochemistry, 1993. **209**(1): p. 169-175.
23. Hayashi, A., T. Watanabe, and T. Nakamura, *Crystalline arrangement and nanostructure of aragonitic crossed lamellar layers of the Meretrix lusoria shell.* Zoology, 2010. **113**(2): p. 125-130.
24. Weiner, S. and W. Traub, *X-ray diffraction study of the insoluble organic matrix of mollusk shells.* FEBS Letters, 1980. **111**(2): p. 311-316.
25. Colussi, P.A., C.A. Specht, and C.H. Taron, *Characterization of a nucleus-encoded chitinase from the yeast Kluyveromyces lactis.* Applied and Environmental Microbiology, 2005. **71**(6): p. 2862-2869.
26. Trudel, J. and A. Asselin, *Detection of chitinase activity after polyacrylamide gel electrophoresis.* Analytical Biochemistry, 1989. **178**(2): p. 362-366.
27. Wang, P. and R.R. Granados, *Calcofluor disrupts the midgut defense system in insects.* Insect Biochemistry and Molecular Biology, 2000. **30**(2): p. 135-143.
28. Ehrlich, H., et al., *Discovery of 505-million-year old chitin in the basal demosponge Vauxia gracilenta.* Scientific Reports, 2013. **3**: p. 3497.
29. Albani, J.R., *Förster energy-transfer studies between Trp residues of α 1-acid glycoprotein (orosomucoid) and the glycosylation site of the protein.* Carbohydrate Research, 2003. **338**(21): p. 2233-2236.
30. Younis, S., et al., *Atomic structure and ultrastructure of the Murex troscheli shell.* Journal of Structural Biology, 2012. **180**(3): p. 539-545.
31. Hovden, R., et al., *Nanoscale assembly processes revealed in the nacroprismatic transition zone of Pinna nobilis mollusc shells.* Nature Communications, 2015. **6**.
32. Addadi, L. and S. Weiner, *Biomineralization: mineral formation by organisms.* Physica Scripta, 2014. **89**(9): p. 098003.
33. Osuna-Mascaró, A.J., et al., *Ultrastructure of the Interlamellar Membranes of the Nacre of the Bivalve Pteria hirundo, Determined by Immunolabelling.* PLoS One, 2015. **10**(4): p. e0122934.
34. Arias, J.L. and M.a.S. Fernández, *Polysaccharides and proteoglycans in calcium carbonate-based biomineralization.* Chemical Reviews, 2008. **108**(11): p. 4475-4482.
35. Gal, A., et al., *Macromolecular recognition directs calcium ions to coccolith mineralization sites.* Science, 2016. **353**(6299): p. 590-593.

36. Keith, J., et al., *Comparative analysis of macromolecules in mollusc shells.* Comparative Biochemistry and Physiology Part B: Comparative Biochemistry, 1993. **105**(3): p. 487-496.
37. Weiner, S., H. Lowenstam, and L. Hood, *Discrete molecular weight components of the organic matrices of mollusc shells.* Journal of Experimental Marine Biology and Ecology, 1977. **30**(1): p. 45-51.
38. Roth, Z., G. Yehezkel, and I. Khalaila, *Identification and quantification of protein glycosylation.* International Journal of Carbohydrate Chemistry, 2012. **2012**.

Supplementary Material for Chapter 6

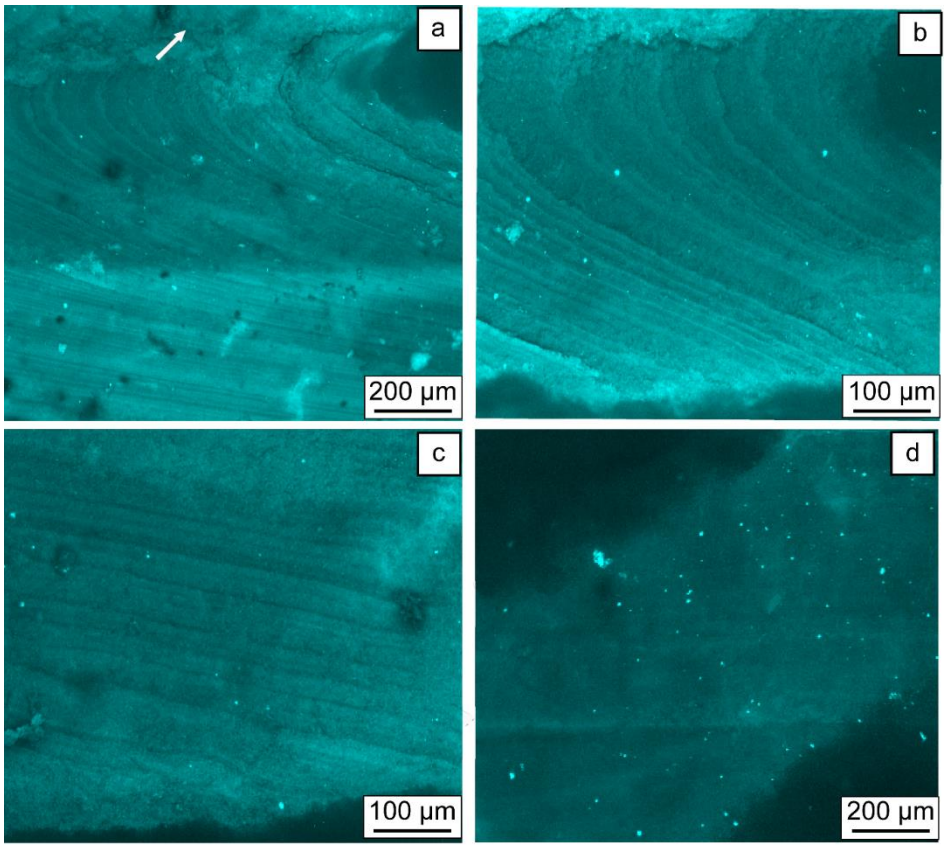

Figure S6.1. The fluorescence of acid-insoluble organic matrix shows three major layers. Calcofluor staining of the outermost layer exhibits the fibrous organic component (a; arrow). The organic layers in form of daily growth lines are clearer in the middle- (b) and inner- (c) layers, where they transect the inorganic matrix. No fluorescence signal of organic material in the control sample (d)

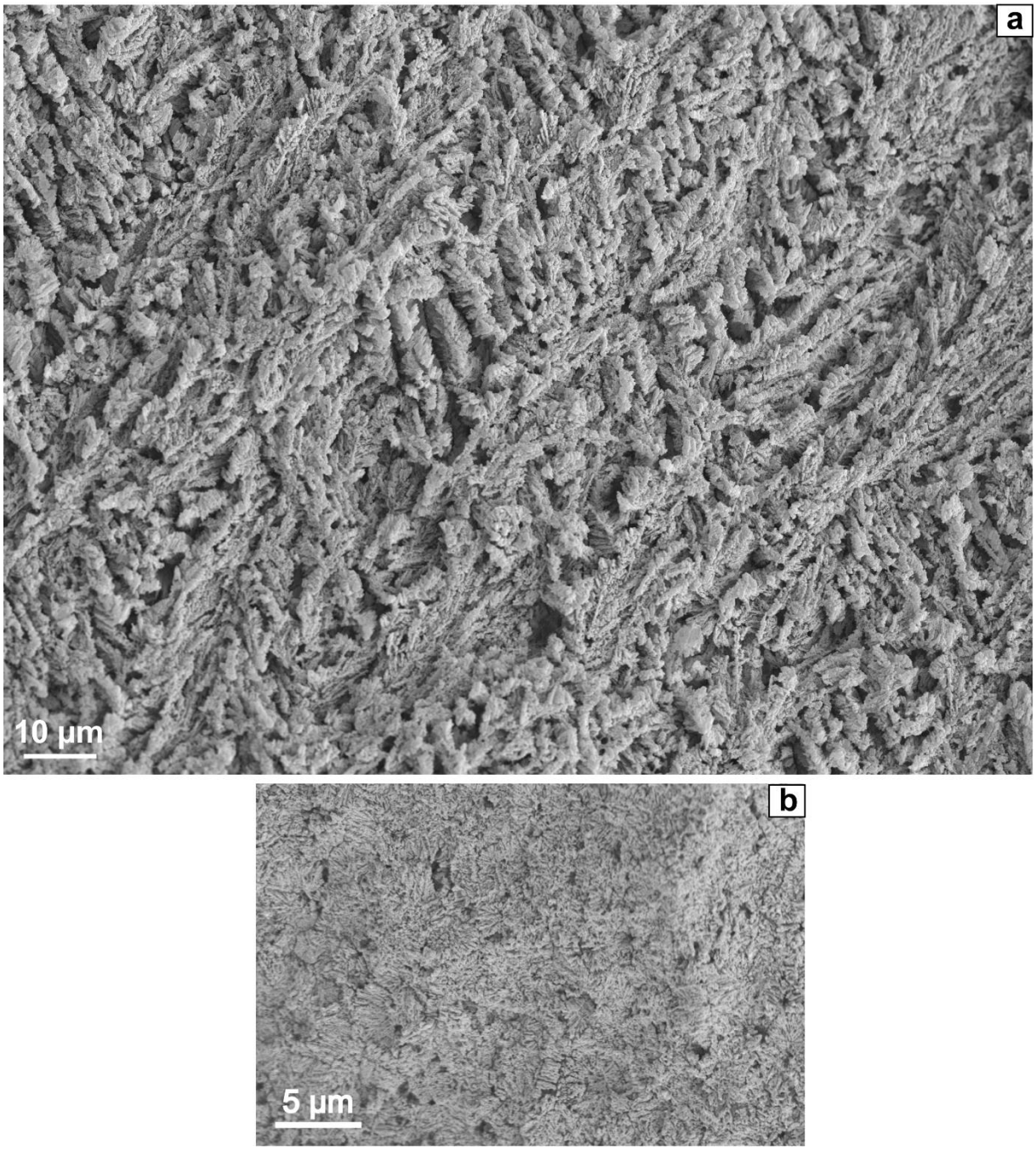

Figure S6.2. (a) SEM micrograph showing feathery appearance in the outer layer of the shells of *Callista spp.* (b) Image of complex crossed lamellar that co-occurs with homogeneous layer.

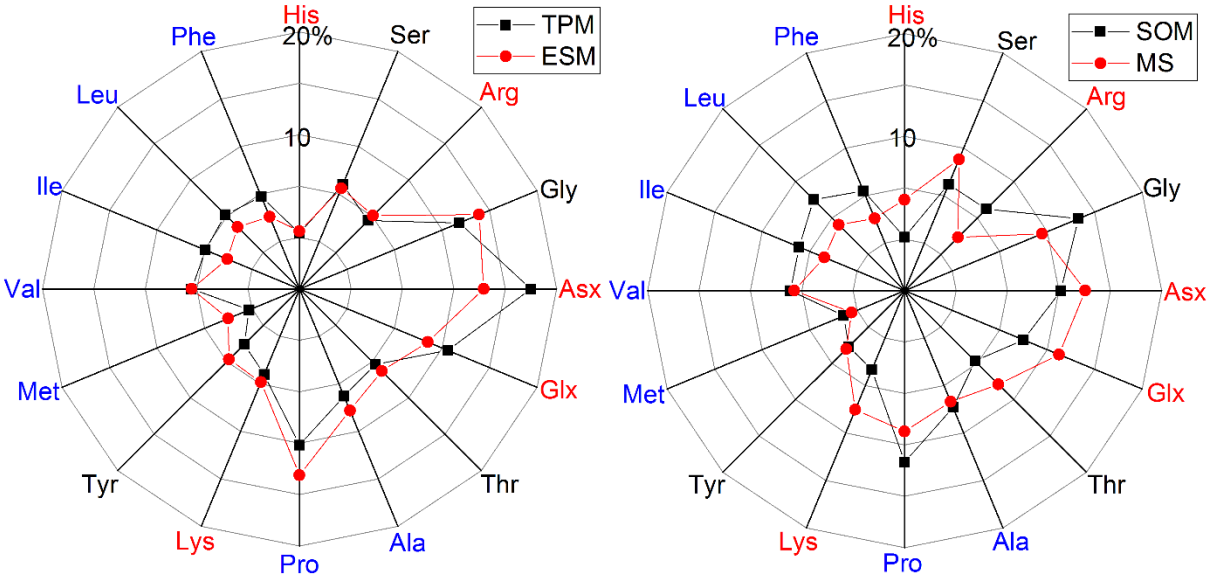

Figure S6.3. Amino acid compositions of TP-Soluble Matrix **(TPM)** and Soluble Organic Matrix **(SOM)**, comparing with the EDTA-Soluble Organic Matrix **(ESM)** in shells of homogeneous *A. islandica* from Agbaje et al. [16] and *Mercenaria stimpsoni* **(MS)** soluble organic matrix from Samata [11]. See text for detail.

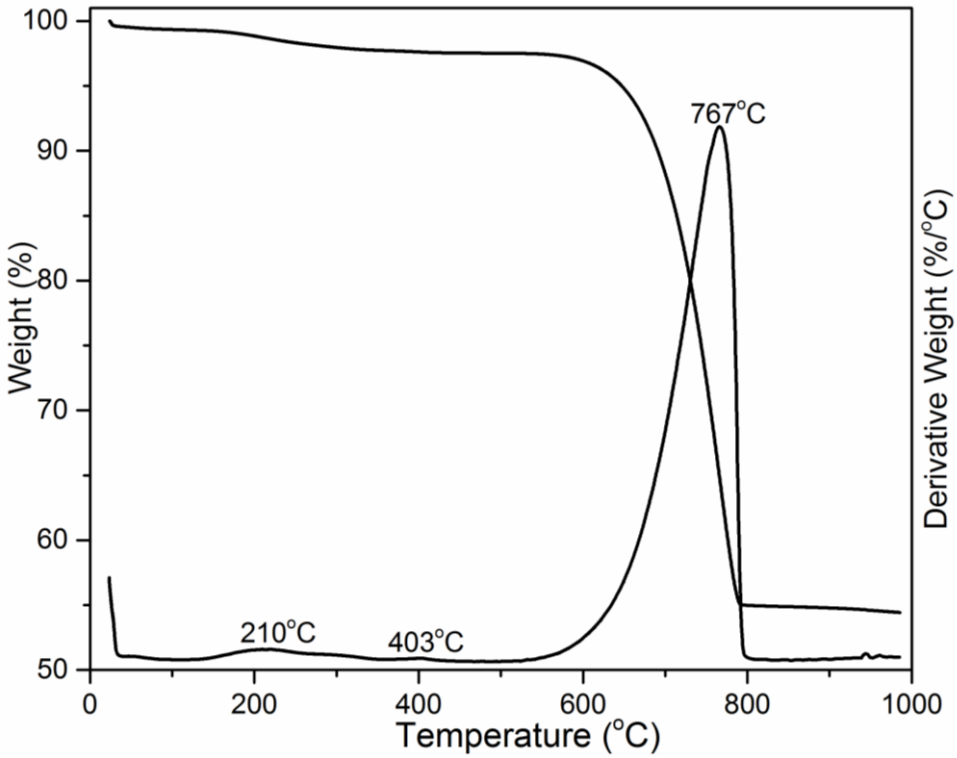

Figure S6.4. Thermal gravimetric analysis (TGA) and differential thermal analysis (DTA) were carried out on the powdered shells using a TGA 2050 thermogravimetric analyser (TA Instruments, USA). At the heating rate of 10°C/min, powdered shell sample (ca 30 mg) was heated under a linear gradient from 21°C to 1000°C. The range 150–500°C was used for calculation of the bioorganic contents. While the broad peak at around 210°C exhibits the release of organic biomolecules, the peak at 403°C depicts transformation of aragonite to calcite and 767°C demonstrates the decomposition of calcium carbonate and release of CO_2.

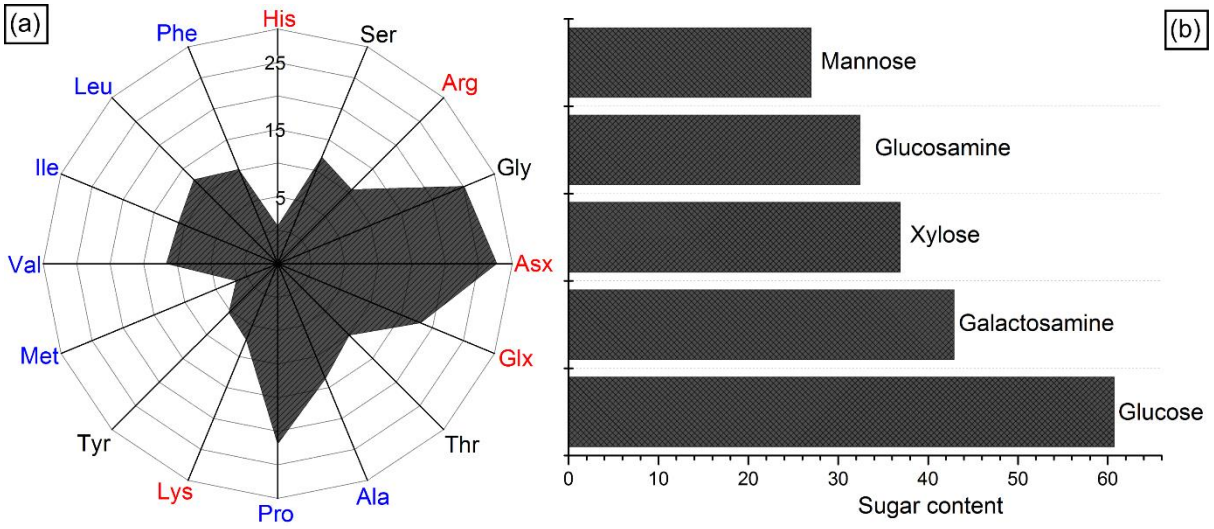

Figure S6.5. Total amino acid compositions of *Callista* shells and proportions from combining the soluble (SOM) plus the Trichloroacetic acid-Phosphate buffer soluble moieties (TPM) (a); Total monosaccharide compositions of *Callista* shells and proportions taken together from the water soluble (SOM) plus the Trichloroacetic acid-Phosphate buffer soluble moieties (TPM) (b). NB: The compositions involved the percentage of two fractions, i.e. SOM and TPM.

Planktic foraminifera form their shells via metastable carbonate phases

D.E. Jacob[1], R. Wirth[2], **O.B.A. Agbaje**[1], O. Branson[3], S.M. Eggins[3]

[1]Department of Earth and Planetary Sciences, Macquarie University, Sydney 2109, NSW, Australia

[2]Helmholtz-Centre Potsdam, German Research Centre For Geosciences GFZ, 14473 Potsdam, Germany

[3]Research School of Earth Sciences, Australian National University, Canberra, 2601 ACT, Australia

Abstract The calcium carbonate shells of planktic foraminifera provide our most valuable geochemical archive of ocean surface conditions and climate spanning the last 100 million years, and play an important role in the ocean carbon cycle. These shells are preserved in marine sediments as calcite, the stable polymorph of calcium carbonate. Here we show that shells of living planktic foraminifers *Orbulina universa* and *Neogloboquadrina dutertrei* originally form from the unstable calcium carbonate polymorph vaterite, implying a non-classical crystallization pathway involving metastable phases that transform ultimately to calcite. The current understanding of how planktic foraminifer shells record climate, and how they will fare in a future high-CO_2 world is underpinned by analogy to the precipitation and dissolution of inorganic calcite. Our findings require a re-evaluation of this paradigm to consider the formation and transformation of metastable phases, which likely exert a significant influence on the geochemistry and solubility of the biomineral calcite.

7.1 Introduction

Planktic foraminifera are among the most important calcifying organisms in the open ocean, contributing as much as half the particulate $CaCO_3$ exported from the surface ocean annually (ca. 2.9 Gt $CaCO_3$ yr^{-1}) [296, 297]. Their calcite shells, preserved in the marine sedimentary record over the last 500 million years [298], provide an unparalleled geochemical archive of past climate in their trace element and isotope chemistry. Translating this archive into useful climatic information requires a systematic understanding of how mineral growth conditions relate to trace element chemistry, historically established by analogy to synthetically produced calcite [299]. However, the geochemistry of foraminiferal shells diverges significantly from inorganic calcite precipitated from seawater-like solutions [300]. These differences have been attributed to vital effects [124, 301], which encompass all the influences that biological processes might exert on foraminiferal calcite composition [300, 302-304].

All existing models of foraminiferal mineralisation assume shell formation proceeds via the direct precipitation of calcite. However, many biologically precipitated carbonates are known to form via complex mineralisation pathways involving metastable intermediate phases that transform stepwise into the final shell mineral [21]. This provides an energetically and kinetically favourable pathway to calcite formation, by employing metastable particles with high surface energy, which have a lower free energy barrier to nucleation [305]. If similar processes are employed by foraminifera, they would provide an alternate mineralogical control on shell geochemistry, and could account for the discrepancies between the chemistry of foraminifera shells and inorganic calcite precipitated from seawater-like solutions. This would alleviate the requirement for complex, energy intensive ion control mechanisms to explain the geochemistry of foraminifera.

Orbulina universa (Figure 7.1a) and *Neogloboquadrina dutertrei* (Figure 7.1b) are two common, well-studied species of planktic foraminifera that are frequently employed in palaeoceanographic [306] and biomineralisation studies [307-309]. *Orbulina universa* is representative of spinose and *N. dutertrei* of non-spinose groups of symbiotic planktic foraminifera. Both construct their shells by the sequential addition of distinct ‘chambers’ [310], which are formed of calcium carbonate with a very low Mg content (0-10 mmol/mol Mg/Ca; [311]). The formation of each chamber begins with the extrusion of a thin, balloon-like organic template in the form of the new chamber. Previous TEM investigations reveal

micron-scale plaques of $CaCO_3$ develop and coalesce to form continuous layers of $CaCO_3$ on both sides of the organic template [312, 313], resulting in a characteristic bilamellar chamber wall construction.

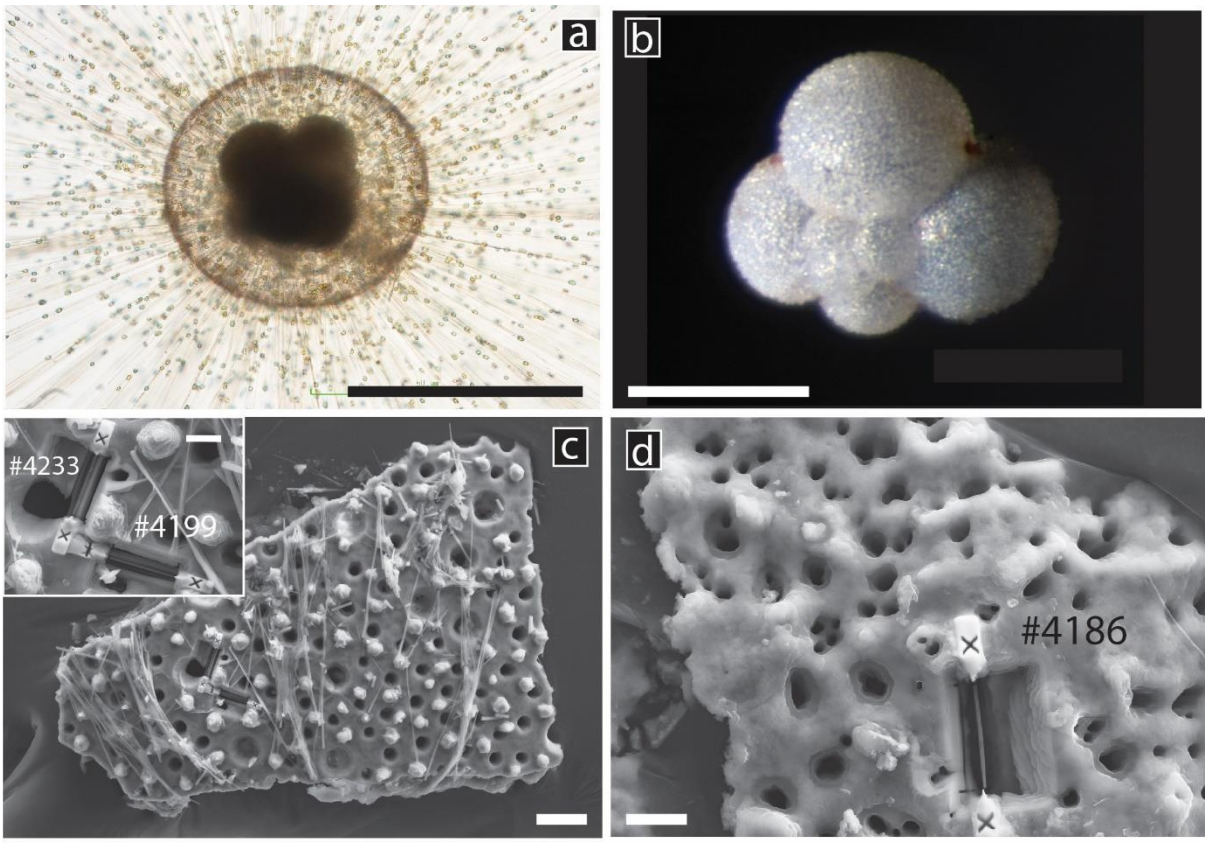

Figure 7.1. The structure of foraminiferal shells. (a) *Orbulina universa* develops a final, large, spherical chamber, which encloses the earlier formed spiral shell of its 'juvenile' stage (dark, centre). The shell supports long radiating mineralised spines that host a sticky network of streaming rhizopodia that are used to trap prey, take up and excrete material, and deploy algal symbionts. This final spherical chamber is initially thin-walled and thickens continuously over 3 to 7 days. Near the end of the foraminifer's life cycle [314], the spines are shed and *O. universa* undergoes a massive release of gametes, leaving an empty shell that sinks rapidly to the sea floor, exporting $CaCO_3$ from the surface ocean. (b) *Neogloboquadrina dutertrei* form trochospiral shells of consecutively larger chambers, and do not have mineralised spines or symbionts. Electron-transparent foils were extracted orthogonally from the outer surface (Session 1) or polished cross sections (Session 2) of pre-gametogenic *O. universa* (c) and *N. dutertrei* (d) shell fragments using a FIB. The pits in the images show the locations of foil extraction with foil identification numbers. Scale bars are 500µm (a), 200µm (b), 20µm (c), 5µm (inset), 5µm (d).

Table 7.1. Details on storage and measurements. The storage time, conditions, measurements conducted and sample preparation for specimens measured in all 4 analytical sessions. Specimens measured during sessions 1-3 were all collected at the same time, and stored in the same conditions. TEM = Transmission electron microscopy; FTIR = Fourier Transform Infra-Red Spectroscopy; XRD = X-Ray Diffraction.

Analytical Session	**Storage**		**Technique**	**Preparation**
	Months	***Conditions***		
1	20	Dry	TEM	Surficial FIB extraction after shell fracture.
2	26	Dry	TEM	Cross-section FIB extraction after resin-mount and polish.
3	39	Dry	FTIR	Unprepared, analysed broken.
4*	1	Wet	XRD	Shells broken open by hand.

*Separate collection of *N. dutertrei* only

The architecture of the shell walls of both species is highly organised, and contains numerous pore channels through which metabolic substrates and products are transported (Figure 7.1c, d). *Orbulina universa* also supports long $CaCO_3$ spines that radiate up to several hundred micrometres from the shell surface and play important functions in foraminiferal biology (Figure 7.1a). *Orbulina universa* is unusual amongst foraminifera in that its final mineralised chamber is large (400-1000 µm diameter) and fully encloses the earlier formed chambers. The formation of this final chamber is likely analogous to chamber wall thickening in other species of foraminifera [308].

We present an *in situ* study of the ultrastructure and mineralogy of *O. universa* and *N. dutertrei*, using Focussed Ion Beam (FIB) supported Transmission Electron Microscopy (TEM) Imaging and Diffraction, and Fourier Transform Infrared (FTIR) Spectrometry.

7.2 Materials and Methods

7.2.1 Sample collection and preparation

Foraminifera were collected from the surface mixed layer and uppermost thermocline (0-50 m depth, 18-20°C) by plankton tow in the San Pedro Channel (California, USA) in August 2013. Individual foraminifera were extracted from plankton concentrates using a wide-bore pipette and sacrificed by transfer into ultrapure water for a period of 1-2 hours. The shells were then dried at room temperature

by placement on absorbent cardboard before being transferred into multi-well micro-paleontology slides. Large pre-gametogenic adult specimens of *Orbulina universa* (sphere stage) and *Neogloboquadrina dutertrei* were selected for further investigation by scanning electron microscopy (SEM) and Focused Ion Beam supported transmission electron microscopy (FIB-TEM) and Fourier Transform Infrared (FTIR) Spectrometry (see below).

FIB-TEM analyses were carried out in two separate sessions in March (3 foils from 2 *O. universa*, 1 foil from *N. dutertrei*) and October 2015 (5 foils from 4 *O. universa*, 4 foils from 3 *N. dutertrei*). Samples studied in the first session were lightly crushed under a binocular microscope, fractured pieces were transferred on carbon paste covered SEM stubs and used for FIB milling without further coating. All TEM foils in this session consisted of vaterite with minor ACC. Samples in the second session were from the same batch, but were mounted in epoxy and polished to expose shell cross-sections for FIB milling. All TEM foils analysed in the second session had transformed to calcite.

7.2.2 Fourier Transform Infrared Spectrometry

Fourier Transform Infrared (FTIR) spectra of single foraminifera shells (two each for *O. universa* and *N. dutertrei*) were measured with a Thermo Nicolet iS10 FTIR spectrometer (Nicolet, MA, USA) equipped with Attenuated Total Reflection along with a smart performer assessor at Macquarie University. Samples were part of the same batch sampled alive in 2013 and FTIR analyses were carried out in November 2016. Spectra were acquired between 1600 and 500 cm^{-1} with a resolution of 4 cm^{-1} and 64 accumulations. Each analysis was duplicated and four resulting spectra for two shells for each species were averaged and are shown in Figure 7.5 and Supplementary Figure 7.4. Backgrounds were recorded at the start and the end of the analytical session. Spicules of *Herdmania momus* consisting of stable vaterite [315] and geological calcite from the mineral collection at the Department of Earth and Planetary Sciences, Macquarie University, were measured as comparisons at identical conditions during the same analytical session. Spectra were normalized to the band intensity at 872 cm^{-1} and band assignments were carried out using data from [316] and are tabulated in Supplementary Table 7.2. Exploiting the linear relationship for relative areas of the bands at 740 cm^{-1} and 712 cm^{-1} in vaterite-

calcite mixtures [317] the *O. universa* shells measured here contained ca. 4.5% vaterite, while the *N. dutertrei* shells contained ca. 3 % vaterite.

7.2.3 Focused Ion Beam sample preparation

Focused Ion Beam milling using a FEI FIB200 instrument (*ex situ* lift out method) at the German Research Centre For Geosciences (GFZ) followed procedures published previously [228, 232]. Foils obtained from non-mounted, resin-free sections in the first analytical session transect the entire chamber wall of *N. dutertrei* and the outer half of the ca. 12µm thick *O. universa* shell. Foils in the second analytical session were cut across resin-mounted sectioned and polished shells.

The FIB-milling method involves sputtering the material surrounding the platinum-protected target area with gallium ions. This process can heat the target area, and drive amorphisation through Ga implantation in the surface of the material [229]. Sample heating is proportional to the beam current, and the extent of amorphisation is proportional to the beam energy, and both depend on the angle of beam incidence during milling [230]. We used 30 keV with a beam current of 11pA and an angle of incidence of 1.2˚. At these conditions beam heating during FIB milling is less than 10K [228] and sample amorphisation is minimal. As the foils are thicker than 100 nm, the major part of the foil is thus not affected by ion implantation. If amorphisation were a significant problem in the foils, Debye-Sherrer diffraction rings would be present in all collected diffraction patterns. These features were only observed in diffraction patterns collected at grain boundaries (Figure 4), which contain clear amorphous regions related to foraminiferal structure.

To date, approximately 5000 FIB foils have been produced at the GFZ TEM facility, of which ca. 1000 foils are of biomineral carbonates and phosphates. Amorphisation introduced by FIB milling across major parts or even the complete thickness of a 100-200 nm thick foil has never been observed. Similarly, transformation of major parts or an entire FIB foil into a different crystalline phase (e.g. calcite to vaterite) using our analytical protocols is considered impossible.

Foils were transferred to individual copper grids coated with holey carbon, before analysis by Transmission Electron Microscopy (TEM) without further carbon coating.

7.2.4 Transmission Electron Microscopy analysis and processing

A FEI Tecnai™ G2 F20 X-Twin transmission electron microscope operated at 200kV acceleration voltage with a field emission gun electron source was used for imaging and analysis, following previously published procedures [228, 232]. Energy-filtered imaging was undertaken with a Gatan Tridiem™ filter applying a 20 eV window to the zero loss peak. Great care was taken to minimize radiation damage to the material during TEM analysis. This involved a low-dose analysis and visual monitoring protocol adapted specifically for the analysis of biominerals and used in previous studies [232]: Foils were analysed in STEM mode, rapidly scanning using a small spot size [302] and assigning the beam between STEM scans to areas outside the sample to avoid electron irradiation damage. At the start of the analytical session for each FIB foil, a rapid overview picture was taken using a defocused beam to identify crystalline and amorphous areas. This overview image was repeated after STEM scanning and HREM analysis and at the end of each analytical session, to confirm that beam damage was not driving sample transformations.

All high-resolution TEM (HRTEM) analyses were carried out at the end of the analytical session for each foil, using exposure times of 0.2 secs. For HREM imaging we used a spot size of 5. Diffraction patterns were collected using Selected Area Electron Diffraction (SAED), which spreads the beam over a larger region, and exposes the sample to a lower radiation dose than more conventional Convergent Electron Beam Diffraction, at the cost of spatial resolution.

Using this protocol, irradiation damage was only observed on two or three occasions and consisted either of holes from the electron beam or of small amorphizised areas where a STEM scan had been carried out. These areas were discarded from the dataset. In no case was transformation from calcite to vaterite or vice versa observed.

In total, thirty different areas on four foils from *O. universa* and *N. dutertrei* were analysed either by High-Resolution TEM (n=17) or by electron diffraction (SAED) using an image plate detector (n=13). No data filtering was applied except for results shown in Fig. 5c. All diffraction indexing was carried out manually.

7.3 Results

7.3.1 Sampling

Shells of *O. universa* (Figure 7.1c) and *N. dutertrei* (Figure 7.1d) were live-collected and analysed using a range of techniques over four analytical sessions after varying time spent stored under wet or dry conditions (Table 7.1).

7.3.2 Shell ultrastructure

Shell ultrastructure was examined by high-resolution transmission electron microscopy (HR-TEM) during our first two analytical sessions (Table 7.1). Electron-transparent foils (ca. 150 nm thick) were extracted from shells of *O. universa* (Figure 7.1c) and *N. dutertrei* (Figure 7.1d) by Focussed Ion Beam milling. For session 1, foils were cut orthogonal to the outer shell surface (Figure 7.1c, d), while for session 2 they were extracted from polished shell cross-sections. All TEM analyses revealed a microstructure of fibrous structures (Figure 7.2a) with abundant, nanometre-sized pores (distinct from the larger structural pore channels that bisect the shell wall; Figure 7.2c, Supplementary Figure 7.2). The fibrous structures are aligned orthogonal to the shell surface, and show similar diffraction contrast (Supplementary Figure 7.4a), indicating a consistent crystallographic orientation. They are approximately 40 nm in diameter in *O. universa* (Figure 7.2b) and 100 nm in *N. dutertrei* (Supplementary Figure 7.3), with undulating, interlocking margins. These characteristics are typical of crystals formed via particle attachment [11, 21], and the nanopores in these crystals may be a consequence of imperfect packing and volumetric changes during particulate assembly and transformation [21]. These nanopores are similar to the abundant voids seen in crystals formed via particle-attachment *in vitro*, although they are likely filled with organic material or water in natural biominerals and these foraminifer shells [246]. The tips of the fibres form a ragged plane of oriented single crystals at the shell's outer surface (Supplementary Figure 7.4b, c) with crystallographic c-axes aligned radially along the shell growth axis, and are protected from the external environment by a *ca.* 30 nm-thick organic layer (Figure 7.2a inset, [313]).

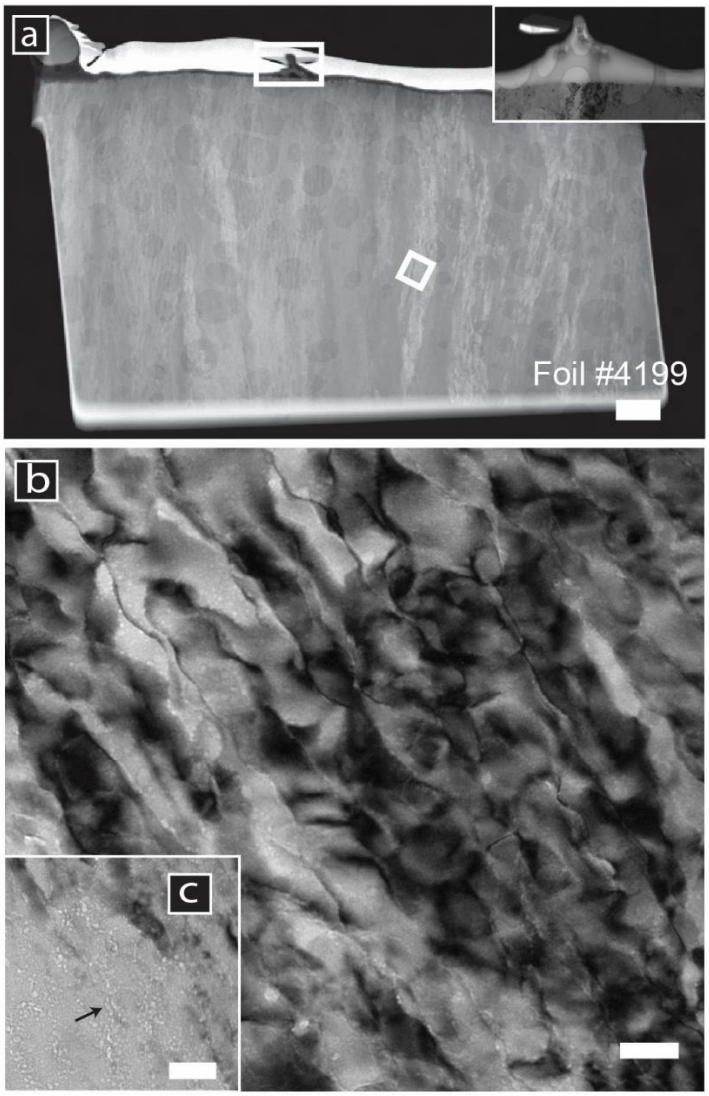

Figure 7.2. Microstructure of *O. universa* shells. (a) High Angle Annular Dark Field (HAADF) image shows the fibrous texture of the chamber and the base of a spine (white rectangle and enlarged in the inset). Note the organic membrane that covers the spine foundation in the inset. The circular features in the sample image are caused by the underlying carbon sample holder. (b) Bright-field image of the particulate fibres that comprise the chamber wall. Scale bars are 1µm (a), 50 nm (b). Analyses were carried out during session 1.

7.3.3 Shell crystallography and Infrared Spectrometry

Thirty electron diffraction patterns were collected from both foraminifer species during our first analytical session. All are consistent with the structure of vaterite, rather than calcite, with hexagonal unit cell parameters $a_0=b_0=0.71239$ nm; $c_0=$ 2.53204 nm [318] (Supplementary Table 7.1, Supplementary Figure 7.1). Vaterite has a complex, layered crystallographic structure, where variations in symmetry between the layers create a number of polytypic structures [315, 316]. The crystallographic

structure of vaterite we observe in these foraminifer shells is one of the most ordered variants and has a six-layer periodicity [315, 316].

Electron diffraction patterns collected from the entire foils during session 1 (Figure 7.3a) reveal a prominent lattice spacing of 0.841 nm (Figure 7.3, Supplementary Table 7.1). This lattice spacing fits neither calcite nor vaterite but rather corresponds to a twinning superstructure, in which vaterite crystals (Figure 7.3b-e) in neighbouring fibres in the shell are twinned by 180˚ rotation around a shared crystallographic c-axis (aligned orthogonal to the shell surface). This twinning structure may enhance the physical properties of the foraminifer shell by averaging out the mechanical anisotropy of the crystals and optimizing the mechanical stability of the shell, as has been observed for Dauphiné twins in quartz [317].

Session 1 HR-TEM analyses further revealed that not all areas within the chamber wall sections were crystalline. Fourier-transform analyses of HR-TEM images of the rim of the vaterite fibres (Figure 7.2b) display diffuse ‘Debye-Sherrer rings’ (Figure 7.4a, b), and lack lattice fringes observed in crystalline materials (Figure 7.4c, d). These are characteristic of non-crystalline materials that could either be regions of amorphous calcium carbonate (ACC), or organic components included within the shell structure [309].

Eighteen additional electron diffraction patterns were collected during analytical session 2. All are consistent with the structure of calcite, in keeping with the long-standing paradigm of foraminiferal mineralogy [311], and contradicting the results from our first analytical session. However, vaterite is highly unstable and its absence in our second set of analyses does not negate our initial results. It is likely that differences in sample treatment caused a vaterite-calcite phase transformation prior to analysis. The only differences between the analytical sessions were an additional six months of storage, prior mounting in resin and the polishing of specimens before FIB extraction for session 2; FIB milling procedures and TEM analytical conditions were identical. An additional six months of storage under similar conditions is unlikely to have induced a phase transformation. Sample mounting and polishing exposes the sample to thermal energy during exothermic resin hardening, and mechanical energy in a hydrous environment during polishing. Any of these processes could have provided the necessary

energy and environment to facilitate a phase transformation. Two additional analyses were conducted to test the veracity of our initial vaterite result, and explore possible conditions that lead to a phase transformation: Fourier Transform Infrared Spectroscopy (FTIR) and X-Ray Diffraction (XRD).

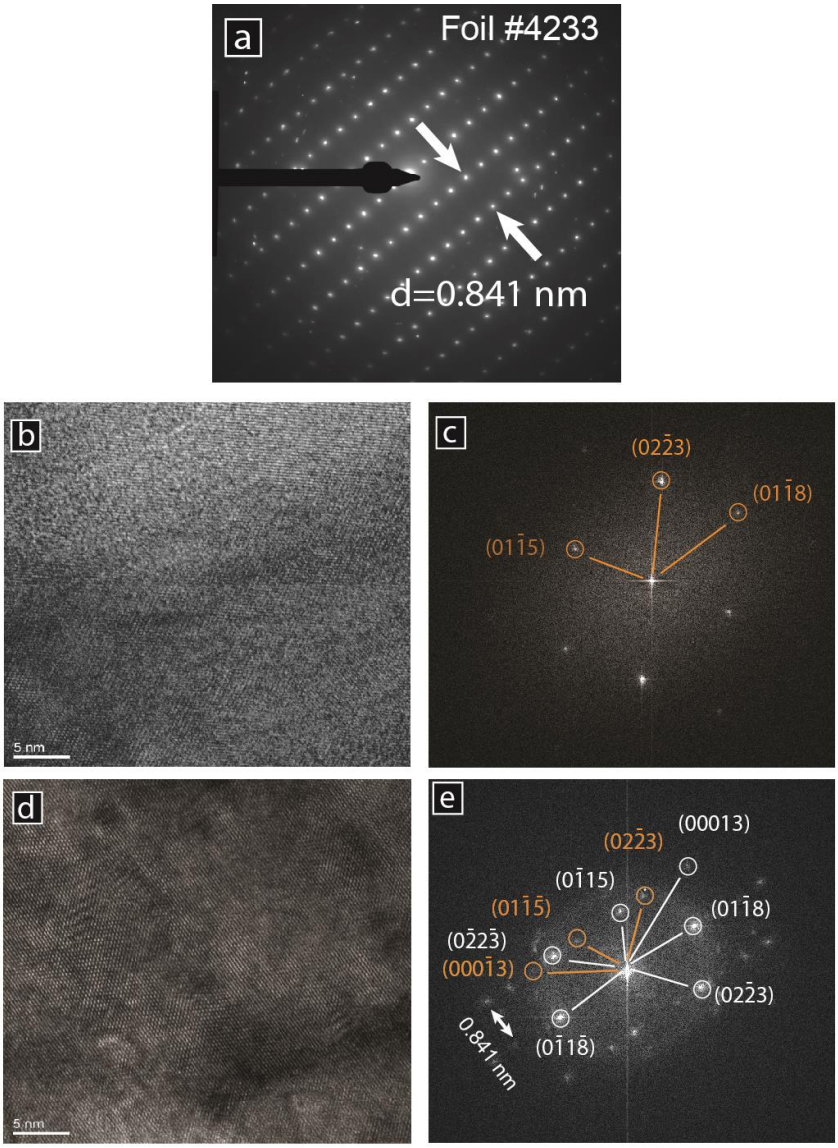

Figure 7.3. Twinned structure of *O. universa* shells. Electron diffraction patterns collected from an entire TEM foil (a) show a prominent lattice spacing of 0.841 nm, which is consistent with neither calcite nor vaterite. High-resolution analysis of a crystallographically uniform region within the foil (b) via Fourier Analysis revealed a characteristic vaterite electron diffraction pattern (c; orange). Similar analysis of a crystallographically complex region within the superstructure (d) revealed that the 0.841 nm lattice spacing observed in the entire foil can be explained by a twinned vaterite structure, with twin pairs rotated 180 along the c-axis (e; orange vs. white). All analyses carried out in analytical session 1.

Two individual shells each of *O. universa* and *N. dutertrei* from the same sample batch measured during session 1 and 2 were measured by Attenuated Total Reflection FTIR (ATR-FTIR; Session 3),

and compared to spectra collected from vateritic spicules of *Herdmania momus* [319] and geological calcite (Figure 7.5, Supplementary Figure 7.5). Vaterite is identified in FTIR spectra by a characteristic shift in the v_4 CO_3^{2-} vibration band from ~712 cm^{-1} in calcite, to ~744 cm^{-1}, caused by changes in the local bonding environment of the CO_3^{2-} group [320]. Based on the relative areas of these diagnostic peaks [321], *O. universa* contained ~4.5% vaterite and *N. dutertrei* contained ~3%. These analyses independently confirm the presence of vaterite in both species. Furthermore, these analyses were conducted on specimens from the same batch as TEM analyses during our first two sessions, indicating that the lack of vaterite in session 2 is most likely attributable to phase transformation during sample preparation, rather than storage conditions. The relatively small percentage of vaterite present in these specimens is at odds with the entirely vaterite composition of FIB foils observed during analytical session 1. This indicates a gradual transformation of vaterite to calcite during storage, leading to a decrease in amount of observable vaterite with time.

To further explore the effect of sample storage on foraminiferal vaterite stability, we analysed newly-collected *N. dutertrei* specimens by X-ray diffraction in analytical session 4. These specimens were stored in wet saline conditions for 1 month, and contained no detectable vaterite on analysis. This preliminary result suggests that a hydrous environment may be important in facilitating a vaterite-calcite phase transformation in foraminifera, and that rinsing in pure water and storage in dry conditions may be responsible for vaterite preservation in our other specimens. A more rigorous study of sample treatment and storage conditions is required to fully evaluate this.

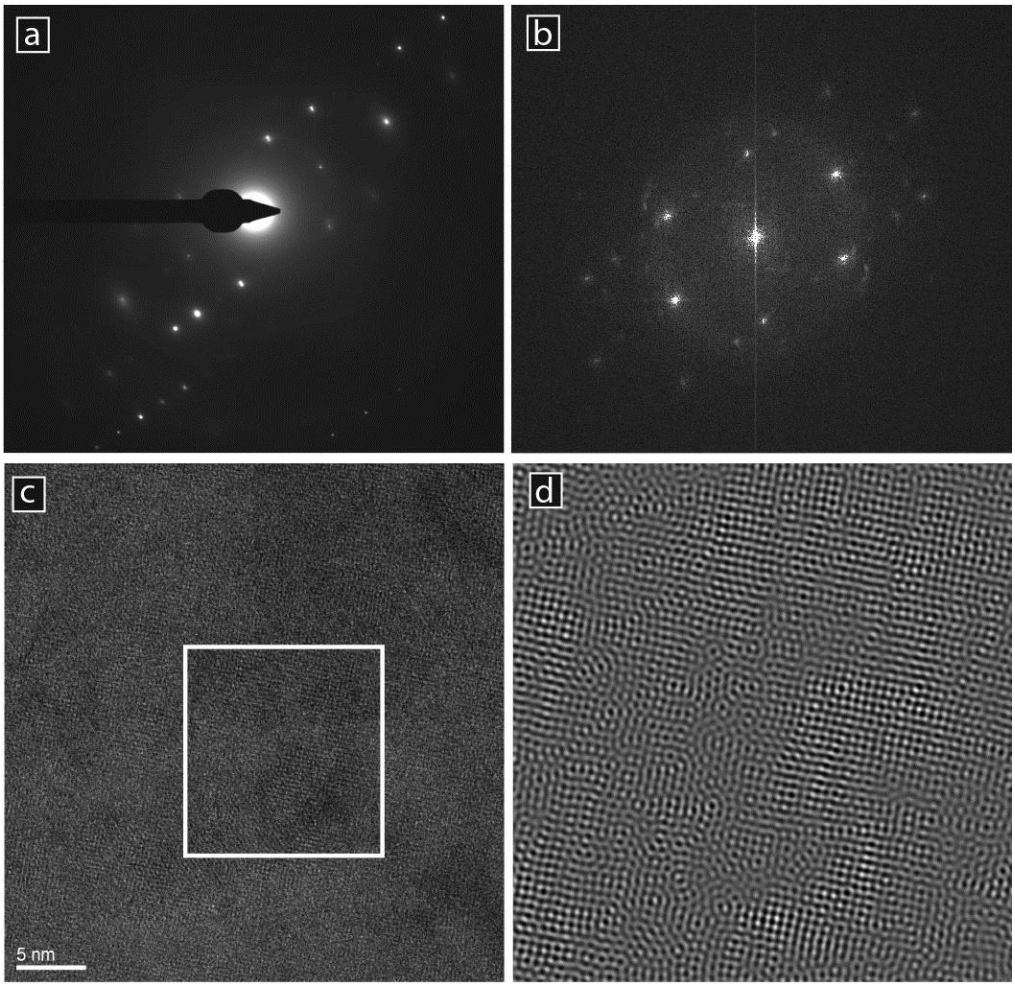

Figure 7.4. Amorphous regions on crystal fringes. Electron diffraction patterns collected from *O. universa* during analytical session 1 (a: image plate detector, b: Fourier Transform analysis of c) display Debye-Scherrer rings (diffuse diffraction patterns around the image centre). These are typical of amorphous material. After filtering and inverse Fourier transformation (d) areas devoid of lattice fringes can be seen that are inconsistent with a crystalline material, but consistent with the presence of either ACC or organic material. Lattice fringes are visible as periodic parallel lines in c and d.

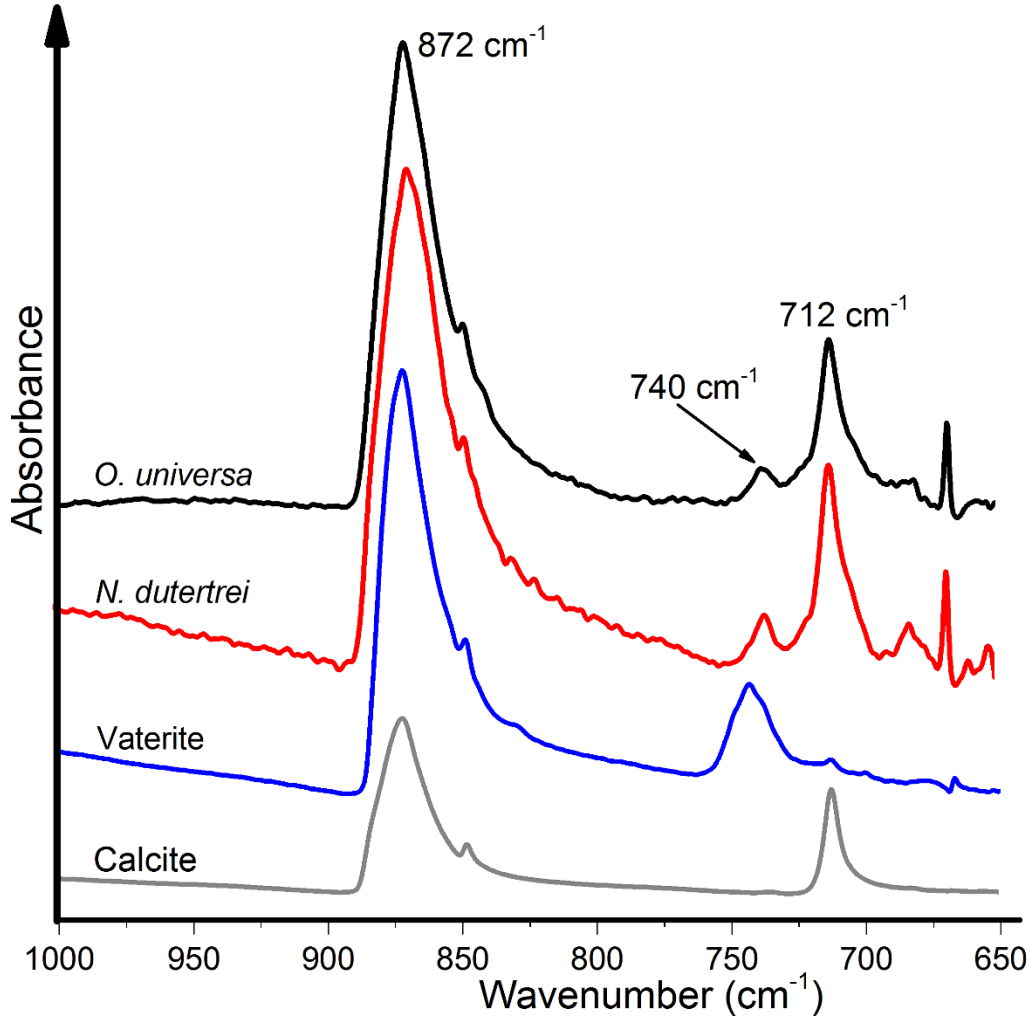

Figure 7.5. Fourier Transform Infrared spectra of geological calcite and vateritic *Herdmania momus* spicules compared to *O. universa* and *N. dutertrei* shells. The absorption bands at ~740 and 712 cm^{-1} are the v_4 vibrational frequencies of in-plane bending of the carbonate ion [320]. The carbonate ion in vaterite has a higher vibrational frequency (~740 cm^{-1}) than in calcite (712 cm^{-1}) because of differences in the bonding environment of the ion, and these bands are diagnostic of the two mineral phases. The ~740 cm^{-1} peak in the foraminiferal specimen is slightly offset from the vaterite peak in *Herdmania momus* (~743 cm^{-1}). These peaks are the same within spectral resolution of the instrument (4 cm^{-1}), although this offset could also indicate subtle differences in vaterite structure. The relative areas of these bands suggests that the foraminifera contain ca. 4.5% vaterite in *O. universa* and 3% in *N. dutertrei* ([321], see Supplementary text 7.2.2). All analyses carried out in analytical session 3.

7.4 Discussion

Our HR-TEM analyses show that the planktic foraminifers *O. universa* and *N. dutertrei* mineralise their calcite shells via vaterite. The presence of vaterite in minimally-prepared, dry-stored samples, and its absence in samples that were either energetically prepared or stored in a wet, saline environment suggests metastable vaterite is an important early phase to form in the organism that subsequently transforms to stable calcite in the natural environment. Thus, these foraminifera employ a non-classical

crystallization pathway that involves the transformation of metastable vaterite into calcite. The presence of vaterite in both species strongly suggests that other foraminifera, which also produce low-Mg calcite shell composition, likely share a similar biomineralization strategy. The highly unstable nature of vaterite has likely contributed to its occurrence in foraminifer shells remaining undiscovered until now. Our findings supersede the longstanding paradigm that planktic foraminifera construct their shells by the direct precipitation of calcite, which has persisted since X-ray diffraction analysis was first applied to foraminifer shells [311]. Our findings add planktic foraminifera to the growing catalogue of calcifying taxa, including sea urchins, molluscs, sponges and crustaceans [232, 322], that employ metastable intermediate phases to form their shells and skeletons [29, 235]

The mechanisms by which vaterite transforms to calcite are unstudied, but a considerable body of work has explored non-classical crystal growth involving the transformation of metastable amorphous calcium carbonate (ACC). *In vitro* transformation of ACC to crystalline calcium carbonate proceeds via dissolution and reprecipitation [32, 33, 323], whereas most *in vivo* studies of skeletal structures reveal a solid-state process involving dehydration and structural re-arrangement [28, 29]. A combination of dissolution-reprecipitation and solid-state transformation processes is possible, with the predominance of either being influenced by the amount of aqueous fluid present [32, 321]. The similarity of the twinned, fibrous microstructure and crystallographic orientation observed in both vateritic (Session 1) and post-transformation calcitic (Session 2) foraminifer shells suggests either a solid-state mechanism, or a highly-localised dissolution-reprecipitation process at the vaterite-calcite boundary [321].

Solid-state transformation from ACC to calcite is common *in vivo* [32, 322], but significant crystallographic differences between vaterite and calcite create a high-energy barrier that makes solid-state transformation between these two phases much less likely. The absence of vaterite in wet-stored specimens (Session 4) suggests a dissolution-reprecipitation transformation facilitated by hydrous environments is most likely. Furthermore, the large calcite single crystal observed bisecting the calcite shell microstructure of a dry-stored *N. dutertrei* sample in analytical session 2 (Figure 7.6) is unlikely to be the product of a solid-state transformation, which is more likely to preserve the micro-crystalline architecture of the vaterite. Together, these observations indicate a dissolution-precipitation transformation mechanism is most likely, similar to that observed in *in vitro* ACC experiments [32]. Our

results do not constrain the exact mechanism or timing of vaterite-calcite transformation, but do indicate that living foraminifera form their calcitic shells via vaterite. It further is possible that vaterite is preceded by another less-stable phase such as ACC, although this has not yet been demonstrated for foraminifera. This has significant implications for our understanding of geochemical proxies [323], and potentially the vulnerability of foraminifera to a future, more acidic ocean.

Our results require a re-evaluation of the incorporation mechanisms of trace elements and isotopes into foraminiferal calcite, to account for the influence of precipitation of a metastable vaterite phase and possible initial ACC phase on shell geochemistry. This is not feasible at present because we lack knowledge of both vaterite geochemistry and the nature of the vaterite-calcite phase transformation. The only existing data that provides insight into the possible influence of vaterite on foraminiferal calcite composition is the fractionation of calcium isotopes during precipitation of synthetic vaterite [324].

Vaterite, calcite and *O. universa* shells are all enriched in ^{40}Ca relative to the fluid they precipitate from [324-326]. *Orbulina universa* shells are most enriched and vaterite is least enriched in ^{40}Ca. This also rules out a solid-state transformation that transfers all the Ca in vaterite to the resulting calcite, which would result in *O. universa* inheriting the Ca-isotope composition of vaterite. Rather, it implies foraminiferal calcite forms via a process that involves multiple fluid-mineral fractionation steps. A vaterite to calcite dissolution-reprecipitation pathway could provide a double-fractionation mechanism, the first on formation of vaterite and a second on transformation to calcite in the presence of a solution phase that is not isolated from the external environment (Figure 7.7). This multistep process is qualitatively consistent with the ^{40}Ca enrichment of calcite, which is of similar magnitude to the difference between vaterite and *O. universa* [324-326].

A multi-step crystallisation pathway involving vaterite, and possibly ACC, would have a significant influence on all aspects of the trace element and isotope geochemistry of foraminiferal calcite (Figure 7.7). The current lack of vaterite and ACC geochemical data prevent us from quantifying this influence, but a double-fractionation process provides a conceptual framework that might account for the significant and unexplained differences between foraminiferal and inorganic calcite geochemistry. Most notable is the order of magnitude lower Mg content of foraminifera (0.1-1.0 mol%) compared to

inorganic calcite (10-20 mol%; [299]). This has attracted the proposal of complex, often contradictory mechanisms involving energetically expensive selective pumping of Mg or Ca ions out of or in to the calcification environment [300, 302-304], and has hindered understanding of the widely-used foraminiferal shell Mg/Ca proxy for past ocean temperature [327]. If Mg partitioning into vaterite is of similar magnitude to calcite, a double fractionation provides a straightforward explanation for the low Mg content of foraminiferal calcite. New experiments investigating the geochemistry of vaterite formation and the vaterite-calcite phase transformation stand to transform our understanding of foraminiferal shell geochemistry.

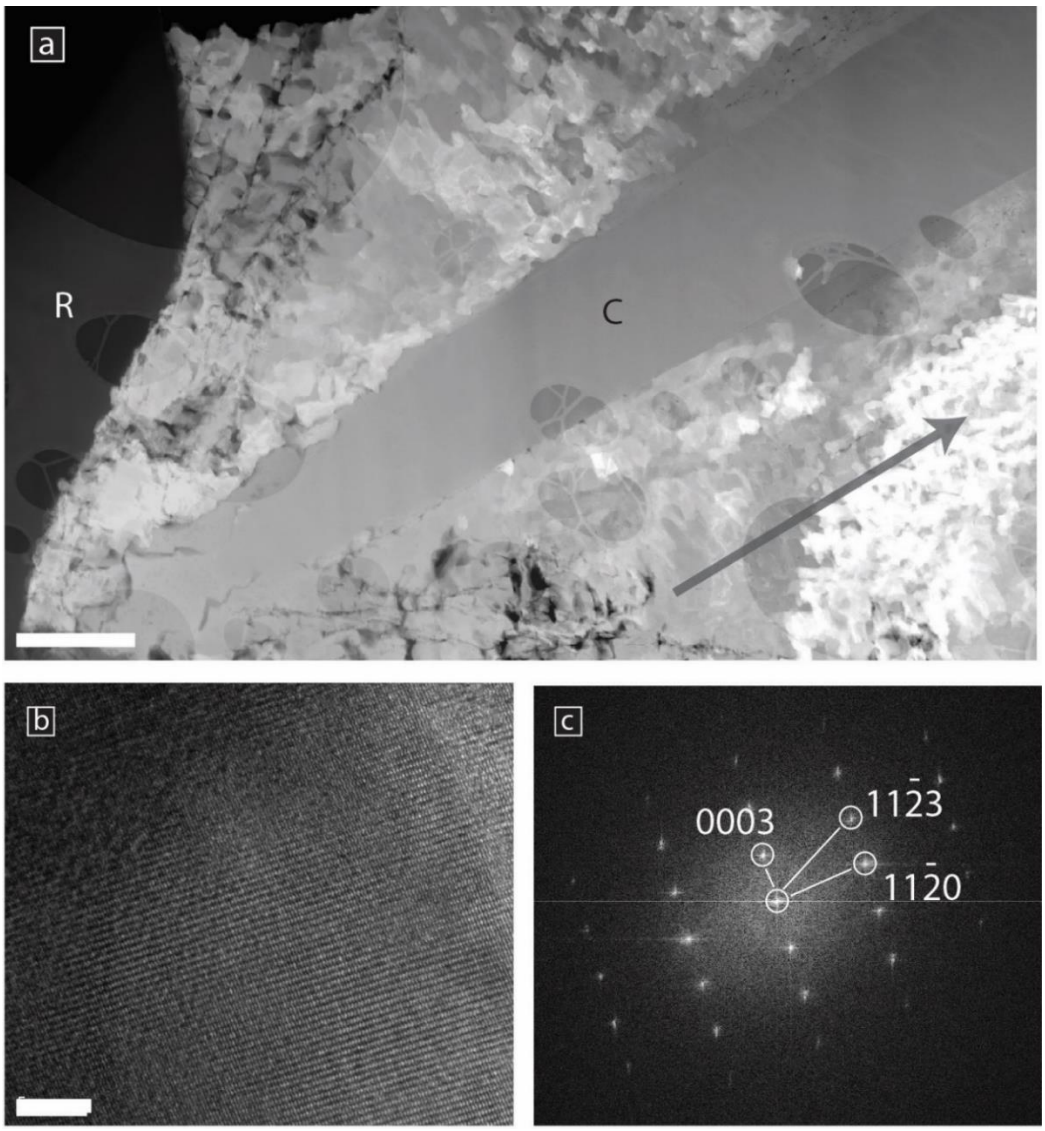

Figure 7.6. Post transformation structure in *N. dutertrei* shells. (a) Foil #4483 cut from a post-transformation shell displays a large calcite single crystal that disrupts the underlying particulate structure (C). High-resolution TEM (b) and indexed Fourier Transform diffraction pattern (c) show the crystal is calcite (see also Supplementary Figure 7.5). Scale bars 1µm (a), 500 nm (b). The dark margin on the left (R) is the sample mounting resin, and the arrow in the lower right points orthogonally towards the inner shell surface. All analyses carried out in analytical session 2.

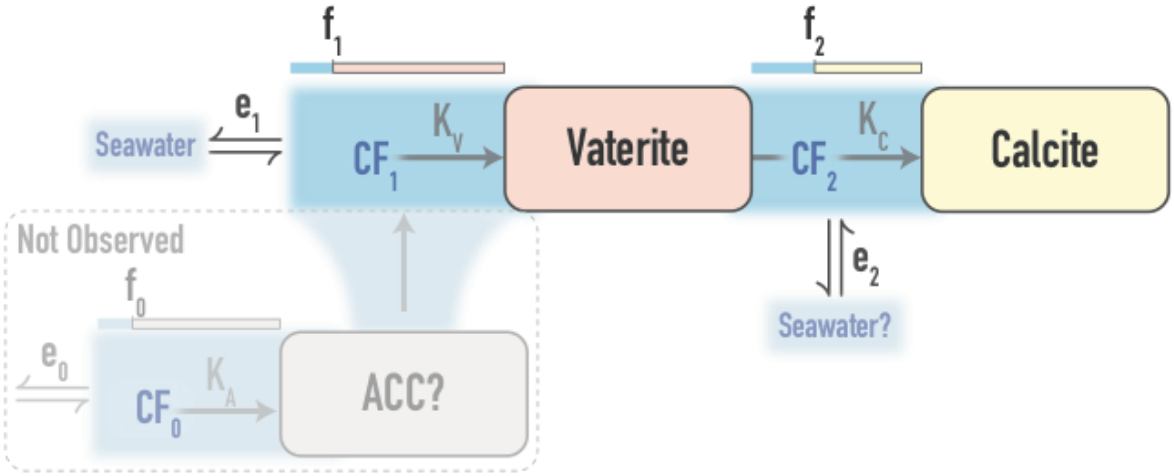

Figure 7.7. The hypothesised double-fractionation mechanism. Initially, vaterite is formed from a calcifying fluid (CF_1), which has a starting composition similar to seawater, and exchanges ions with the external environment (e_1). The trace element composition of vaterite is determined by vaterite-specific partition coefficients (K_V), and the fraction of the available ions precipitated from CF_1 (f_1), which determines the degree of Rayleigh fractionation during precipitation [328]. Next, vaterite transforms into calcite via a localised dissolution-reprecipitation reaction. This creates a second transient calcifying fluid (CF_2) with an initial composition identical to the parent vaterite, which can exchange ions with external fluids (e_2, which interact with seawater, CF_1 or some other localised reservoir). The composition of the resulting calcite is determined by the composition of CF_2, calcite-specific partition coefficients (K_C), the degree of Rayleigh fractionation in CF_2 (f_2) and the degree of ion exchange with external fluids (e_2). Conceptually, the trace element content of the mineral gets more similar to CF as f tends towards 1, while e describes how 'open' or 'closed' the CF is. Note that f and e are incompatible: if e is higher than the rate of ion removal by precipitation the system is relatively 'open' and f will be low, and vice versa. Thus, the dynamics of this space depend on the relative rates of crystal precipitation and ion exchange with the external environment. For a double-fractionation scenario to occur, either e_2 must be significant (relative to precipitation rate) or f_2 must be less than 100%, otherwise the resulting calcite would inherit the same composition as the parent vaterite. It is further possible that vaterite is preceded by an ACC phase, which would introduce a third fractionation step. Testing this model requires knowledge of element-specific and phase-specific partition coefficients ($^{TE}K_X$), which are not currently available in the literature [231].

The presence of vaterite as an intermediate mineral phase in foraminiferal shells may make them more susceptible to dissolution in a future, more acidic ocean, since vaterite is more soluble than calcite [296]. While living foraminifera possess a protective organic layer on the shell surface the degradation of this membrane after death will expose any vaterite present to dissolution as shells sink through the thermocline into the deep ocean. This may explain the large, enigmatic super-lysocline dissolution of planktic foraminifer shells observed across the surface oceans [329]. With increasing ocean acidification, this could reduce the particulate inorganic carbon flux from the surface ocean, with potential significant implications also for any ballasted organic carbon flux to the deep sea and seafloor

[330]. A wider survey of the mineralogy of end-of-life foraminifera could evaluate the potential significance of this to the global carbon cycle.

Acknowledgments: This work is funded by the ARC via a Future Fellowship to D.J and an ARC Discovery Project to D.J., S.M.E. and R.W. The authors are grateful to A. Schreiber for skilful preparation of the FIB foils.

7.5 References

1. Schiebel, R., *Planktic foraminiferal sedimentation and the marine calcite budget.* Global Biogeochemical Cycles, 2002. **16**(4).
2. Berelson, W., et al., *Relating estimates of CaCO3 production, export, and dissolution in the water column to measurements of CaCO3 rain into sediment traps and dissolution on the sea floor: A revised global carbonate budget.* Global Biogeochemical Cycles, 2007. **21**(1).
3. Pawlowski, J., et al., *The evolution of early Foraminifera.* Proceedings of the National Academy of Sciences, 2003. **100**(20): p. 11494-11498.
4. Mucci, A. and J.W. Morse, *The incorporation of Mg2+ and Sr2+ into calcite overgrowths: influences of growth rate and solution composition.* Geochimica et Cosmochimica Acta, 1983. **47**(2): p. 217-233.
5. de Nooijer, L.J., et al., *Biomineralization in perforate foraminifera.* Earth-Science Reviews, 2014. **135**: p. 48-58.
6. Urey, H.C., et al., *Measurement of paleotemperatures and temperatures of the Upper Cretaceous of England, Denmark, and the southeastern United States.* Geological Society of America Bulletin, 1951. **62**(4): p. 399-416.
7. Weiner, S. and P.M. Dove, *An overview of biomineralization processes and the problem of the vital effect.* Reviews in Mineralogy and Geochemistry, 2003. **54**(1): p. 1-29.
8. Erez, J., *The source of ions for biomineralization in foraminifera and their implications for paleoceanographic proxies.* Reviews in Mineralogy and Geochemistry, 2003. **54**(1): p. 115-149.
9. Bentov, S., C. Brownlee, and J. Erez, *The role of seawater endocytosis in the biomineralization process in calcareous foraminifera.* Proceedings of the National Academy of Sciences, 2009. **106**(51): p. 21500-21504.
10. Nehrke, G., et al., *A new model for biomineralization and trace-element signatures of Foraminifera tests.* Biogeosciences, 2013. **10**(10): p. 6759-6767.
11. De Yoreo, J.J., et al., *Crystallization by particle attachment in synthetic, biogenic, and geologic environments.* Science, 2015. **349**(6247): p. aaa6760.
12. Navrotsky, A., *Energetic clues to pathways to biomineralization: Precursors, clusters, and nanoparticles.* Proceedings of the National Academy of Sciences of the United States of America, 2004. **101**(33): p. 12096-12101.
13. Fehrenbacher, J., P.A. Martin, and G. Eshel, *Glacial deep water carbonate chemistry inferred from foraminiferal Mg/Ca: a case study from the western tropical Atlantic.* Geochemistry, Geophysics, Geosystems, 2006. **7**(9).
14. Spero, H.J., et al., *Timing and mechanism for intratest Mg/Ca variability in a living planktic foraminifer.* Earth and Planetary Science Letters, 2015. **409**: p. 32-42.
15. Fehrenbacher, J.S., et al., *Link between light-triggered Mg-banding and chamber formation in the planktic foraminifera Neogloboquadrina dutertrei.* Nature Communications, 2017. **8**.
16. Branson, O., et al., *Nanometer-scale chemistry of a calcite biomineralization template: implications for skeletal composition and nucleation.* Proceedings of the National Academy of Sciences, 2016: p. 201522864.

17. Caron, D.A., et al., *Effects of gametogenesis on test structure and dissolution of some spinose planktonic foraminifera and implications for test preservation.* Marine Micropaleontology, 1990. **16**(1-2): p. 93-116.
18. Blackmon, P.D. and R. Todd, *Mineralogy of some foraminifera as related to their classification and ecology.* Journal of Paleontology, 1959: p. 1-15.
19. Hemleben, C., M. Spindler, and A. R.O., *Modern Planktonic Foraminifera*. 1989, Springer-Verlag New York, NY. p. 363.
20. Spero, H., *Ultrastructural examination of chamber morphogenesis and biomineralization in the planktonic foraminiferOrbulina universa.* Marine Biology, 1988. **99**(1): p. 9-20.
21. Caron, D.A., W.W. Faber, and A.W. Bé, *Growth of the spinose planktonic foraminifer Orbulina universa in laboratory culture and the effect of temperature on life processes.* Journal of the Marine Biological Association of the United Kingdom, 1987. **67**(2): p. 343-358.
22. Makovicky, E., *Vaterite: Interpretation in terms of OD theory and its next of kin.* American Mineralogist, 2016. **101**(7): p. 1636-1641.
23. De La Pierre, M., et al., *Probing the multiple structures of vaterite through combined computational and experimental Raman spectroscopy.* The Journal of Physical Chemistry C, 2014. **118**(47): p. 27493-27501.
24. Lloyd, G.E., *Microstructural evolution in a mylonitic quartz simple shear zone: the significant roles of dauphine twinning and misorientation.* Geological Society, London, Special Publications, 2004. **224**(1): p. 39-61.
25. Jacob, D., et al., *Amorphous calcium carbonate in the shells of adult Unionoida.* Journal of Structural Biology, 2011. **173**(2): p. 241-249.
26. Wirth, R., *Focused Ion Beam (FIB):A novel technology for advanced application of micro- and nanoanalysis in geosciences and applied mineralogy.* European Journal of Mineralogy, 2004. **16**(6): p. 863-876.
27. Branson, O., et al., *The coordination and distribution of B in foraminiferal calcite.* Earth and Planetary Science Letters, 2015. **416**: p. 67-72.
28. Kato, N.I., *Reducing focused ion beam damage to transmission electron microscopy samples.* Journal of Eelectron Microscopy, 2004. **53**(5): p. 451-458.
29. Gower, L.B., *Biomimetic model systems for investigating the amorphous precursor pathway and its role in biomineralization.* Chemical Reviews, 2008. **108**(11): p. 4551-4627.
30. Li, H., et al., *Calcite prisms from mollusk shells (Atrina Rigida): swiss-cheese-like organic–inorganic single-crystal composites.* Advanced Functional Materials, 2011. **21**(11): p. 2028-2034.
31. Demichelis, R., et al., *A new structural model for disorder in vaterite from first-principles calculations.* CrystEngComm, 2012. **14**(1): p. 44-47.
32. Kabalah-Amitai, L., et al., *Vaterite crystals contain two interspersed crystal structures.* Science, 2013. **340**(6131): p. 454-457.
33. Andersen, F.A. and L. Brecevic, *Infrared spectra of amorphous and crystalline calcium carbonate.* Acta Chem. Scand, 1991. **45**(10): p. 1018-1024.
34. Gal, A., et al., *Particle accretion mechanism underlies biological crystal growth from an amorphous precursor phase.* Advanced Functional Materials, 2014. **24**(34): p. 5420-5426.
35. Beniash, E., et al., *Amorphous calcium carbonate transforms into calcite during sea urchin larval spicule growth.* Proceedings of the Royal Society of London B: Biological Sciences, 1997. **264**(1380): p. 461-465.
36. Weiner, S. and L. Addadi, *Crystallization pathways in biomineralization.* Annual Review of Materials Research, 2011. **41**: p. 21-40.
37. Hovden, R., et al., *Nanoscale assembly processes revealed in the nacroprismatic transition zone of Pinna nobilis mollusc shells.* Nature Communications, 2015. **6**.
38. Giuffre, A.J., et al., *Isotopic tracer evidence for the amorphous calcium carbonate to calcite transformation by dissolution–reprecipitation.* Geochimica et Cosmochimica Acta, 2015. **165**: p. 407-417.

39. Wolf, S.E., et al., *Early homogenous amorphous precursor stages of calcium carbonate and subsequent crystal growth in levitated droplets.* Journal of the American Chemical Society, 2008. **130**(37): p. 12342-12347.
40. Blue, C., et al., *Chemical and physical controls on the transformation of amorphous calcium carbonate into crystalline CaCO 3 polymorphs.* Geochimica et Cosmochimica Acta, 2017. **196**: p. 179-196.
41. Politi, Y., et al., *Transformation mechanism of amorphous calcium carbonate into calcite in the sea urchin larval spicule.* Proceedings of the National Academy of Sciences, 2008. **105**(45): p. 17362-17366.
42. Gussone, N., G. Nehrke, and B.M. Teichert, *Calcium isotope fractionation in ikaite and vaterite.* Chemical Geology, 2011. **285**(1): p. 194-202.
43. Marriott, C.S., et al., *Temperature dependence of δ 7 Li, δ 44 Ca and Li/Ca during growth of calcium carbonate.* Earth and Planetary Science Letters, 2004. **222**(2): p. 615-624.
44. Gussone, N., et al., *Model for kinetic effects on calcium isotope fractionation (δ 44 Ca) in inorganic aragonite and cultured planktonic foraminifera.* Geochimica et Cosmochimica Acta, 2003. **67**(7): p. 1375-1382.
45. Lea, D.W., D.K. Pak, and H.J. Spero, *Climate impact of late Quaternary equatorial Pacific sea surface temperature variations.* Science, 2000. **289**(5485): p. 1719-1724.
46. Elderfield, H., C. Bertram, and J. Erez, *A biomineralization model for the incorporation of trace elements into foraminiferal calcium carbonate.* Earth and Planetary Science Letters, 1996. **142**(3-4): p. 409-423.
47. Ishitani, T. and T. Yaguchi, *Cross-sectional sample preparation by focused ion beam: A review of ion-sample interaction.* Microscopy Research and Technique, 1996. **35**(4): p. 320-333.
48. Milliman, J., et al., *Biologically mediated dissolution of calcium carbonate above the chemical lysocline?* Deep Sea Research Part I: Oceanographic Research Papers, 1999. **46**(10): p. 1653-1669.
49. Klaas, C. and D.E. Archer, *Association of sinking organic matter with various types of mineral ballast in the deep sea: Implications for the rain ratio.* Global Biogeochemical Cycles, 2002. **16**(4).

Supplementary Material for Chapter 7

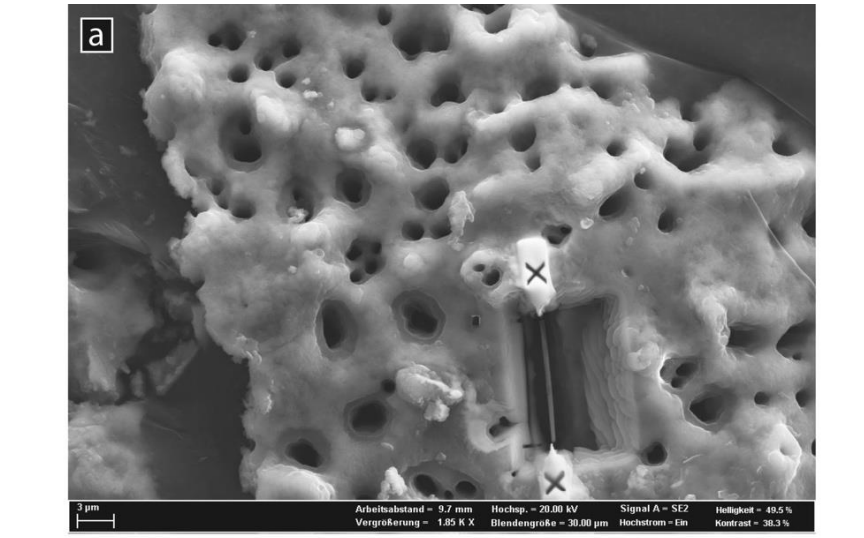

Angle between planes	calculated	observed
01$\bar{1}$8/02$\bar{2}$3	44.5°	42.76°
01$\bar{1}$8/0$\bar{1}$15	64.5°	66.54°
00013/01$\bar{1}$8	26.2°	27.15°
00013/0$\bar{1}$15	37.8°	39.38°
0$\bar{1}$15/0$\bar{2}\bar{2}\bar{3}$	70.4°	70.70°

Supplementary Figure 7.1. Results from *Neogloboquadrina dutertrei*. (a) SEM image of a fragment of the final chamber of a *N. dutertrei* shell with FIB pit of foil #4186. (b) HR-TEM image of area shown after Fourier Transform analysis and indexed as vaterite twin cell A in (c). (d) Schematic indexed crystallographic cell shown in (b, c) with a list of the angles between

crystallographic planes as observed, vs calculated angles using the hexagonal vaterite model proposed by [29].

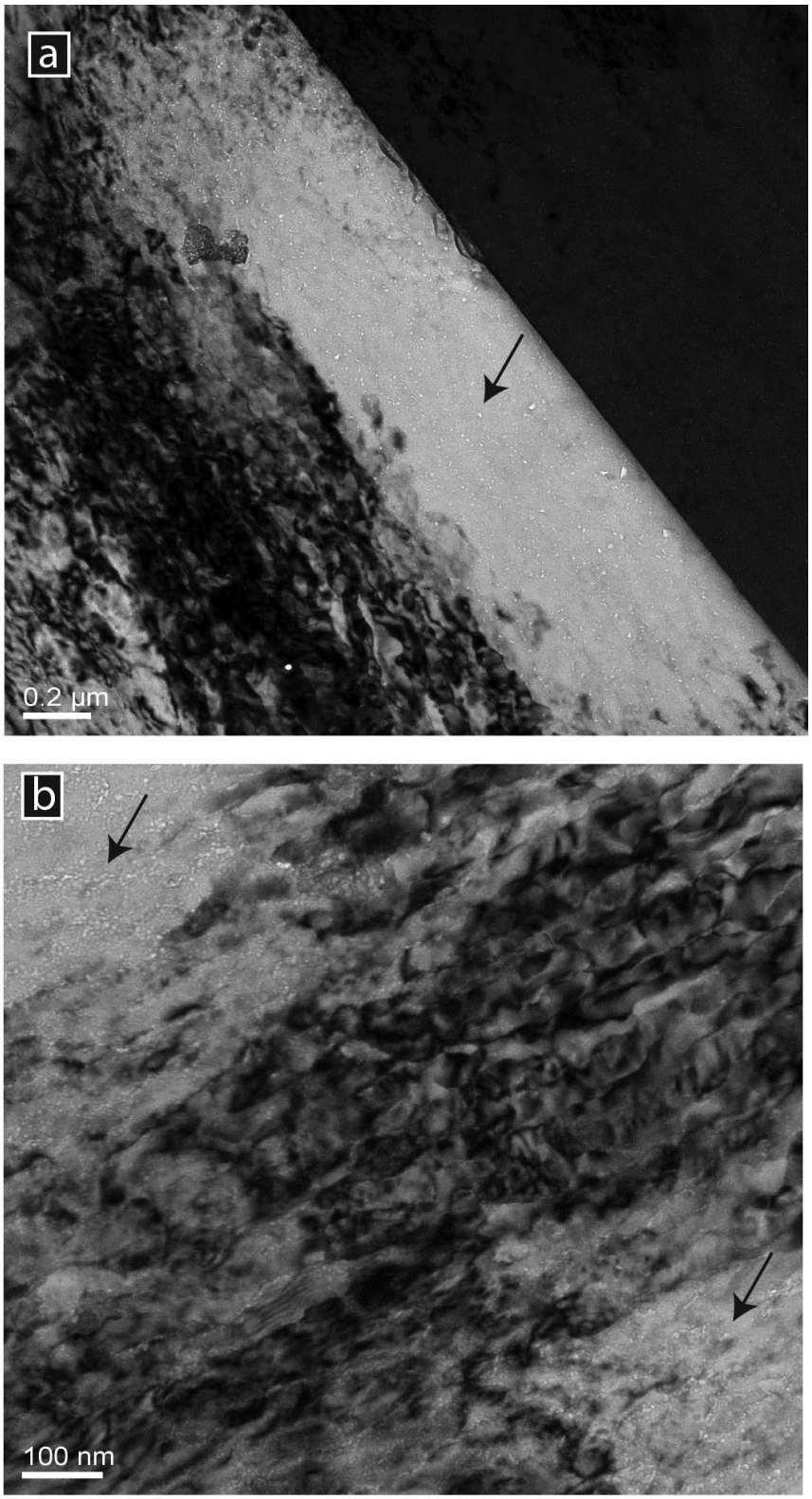

Supplementary Figure 7.2. Nanopores in *O. universa*. (a) Bright-field image showing the speckled contrast due to individual nanocrystals and scattered pores (arrow) in *O. universa* typical of biominerals. (b) typical nanostructure of irregular fibers with 'pores' (arrows).

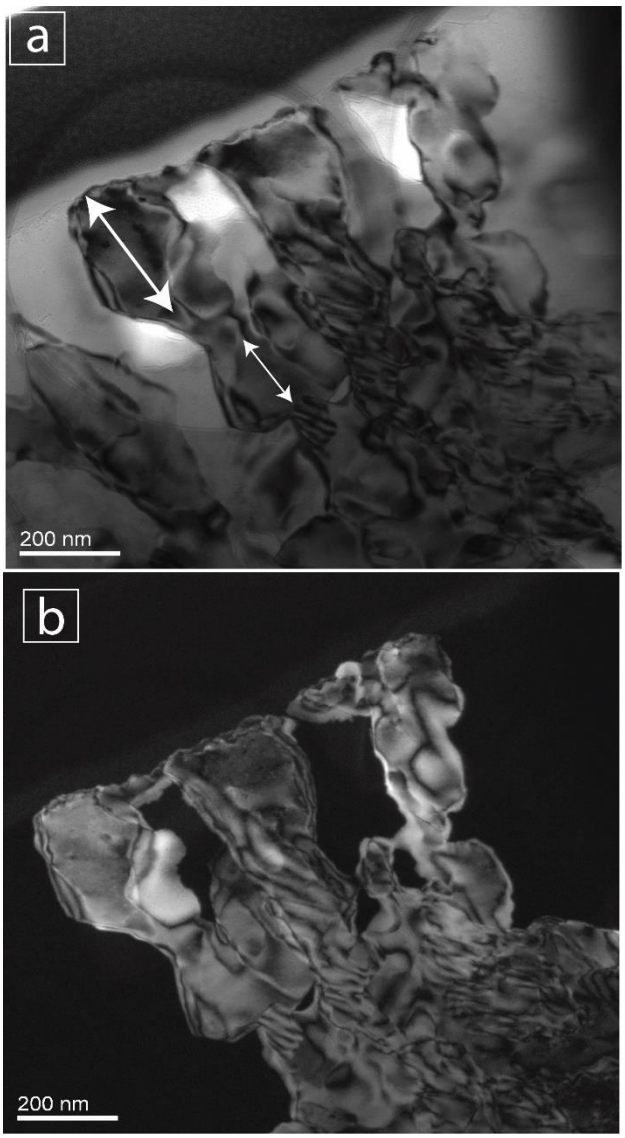

Supplementary Figure 7.3. Grain sizes in *N. dutertrei.* (a) Bright Field image of an area in foil #4186 (first analytical session) consisting of aggregated grains of vaterite. Approximate lengths of two grains are outlines by arrows. Grains are here defined by uniform diffraction contrasts. (b) Corresponding dark field image of the same area.

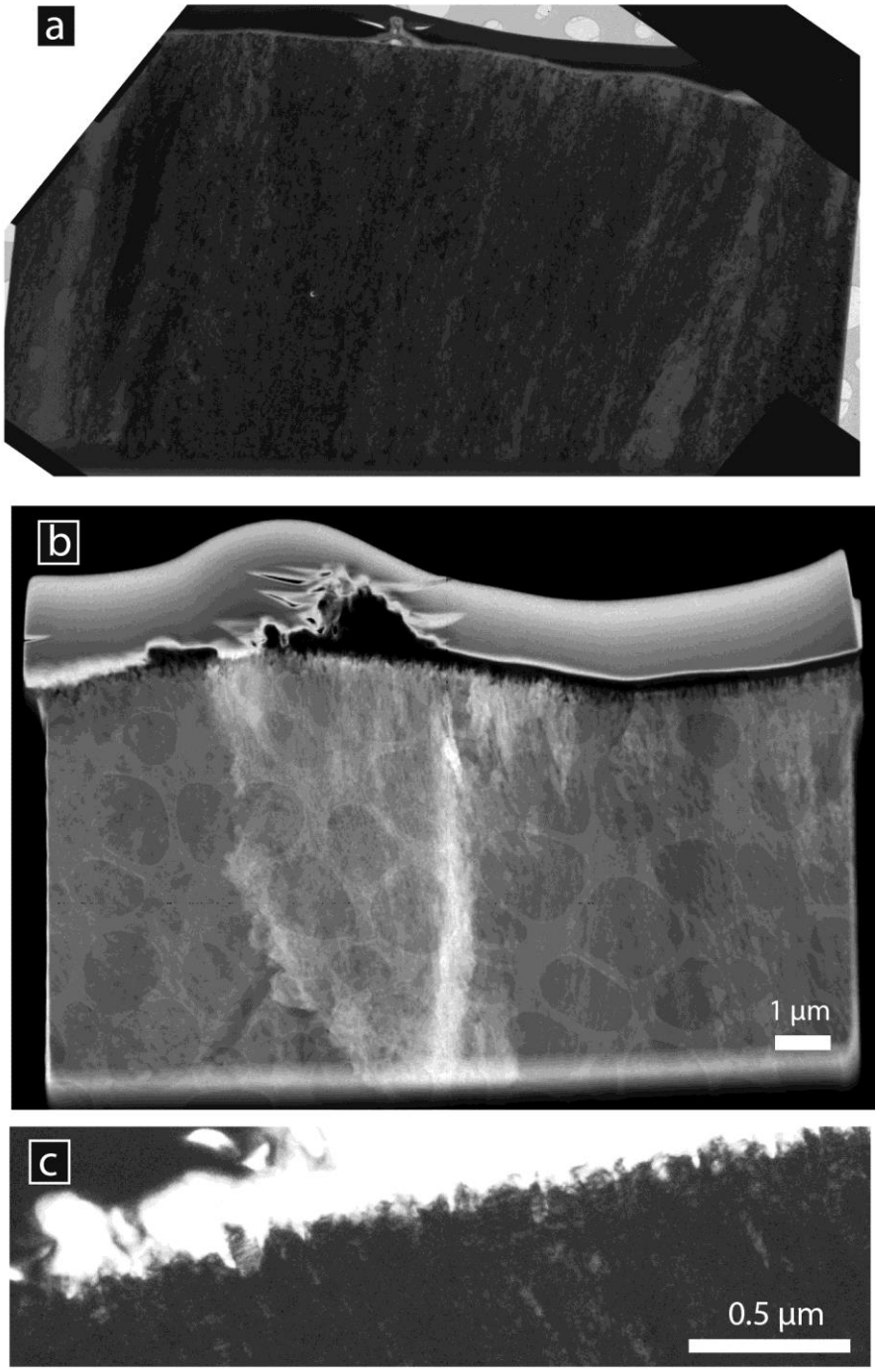

Supplementary Figure 7.4. Microstructure of *O. universa* shells. (a) Integrated image plate image of foil #4199 that shows an almost complete lack of diffraction contrast, indicative of a mesocrystal structure. (b) HAADF image of foil #4187 showing the ragged surface of the shell just below the protective Pt strip. (c) Bright-field image of the ragged surface area showing individual vaterite crystals.

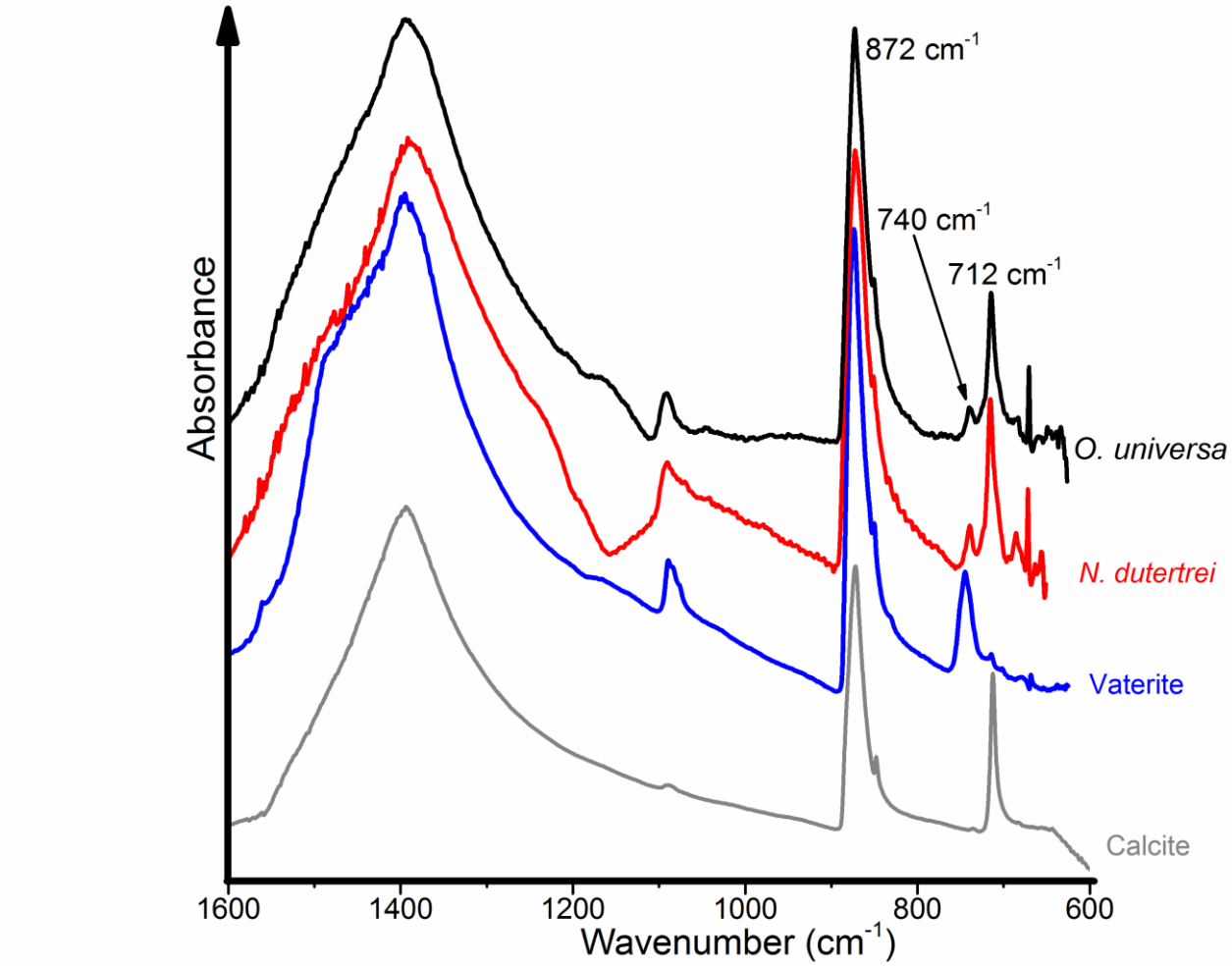

Supplementary Figure 7.5. Complete FTIR spectra (600-1600 cm^{-1}) for foraminifera shells. Spectra collected after dry storage, and compared to biogenic vaterite (*Herdmania momus* spicules) and geological calcite. The shells consist of a mixture of vaterite and calcite. The band at ca. 744 cm^{-1} is indicative for vaterite, while the band at 712 cm^{-1} is calcite [22]. The bands between 740 and 744 cm^{-1} are identical within the resolution of the spectra of 4 cm^{-1}. Bands for vaterite and calcite overlap at 872 cm^{-1} and at ca. 1400 cm^{-1}. Band assignments are given in Supplementary Table 8.2. All spectra are normalized to the band intensity at 872 cm^{-1}.

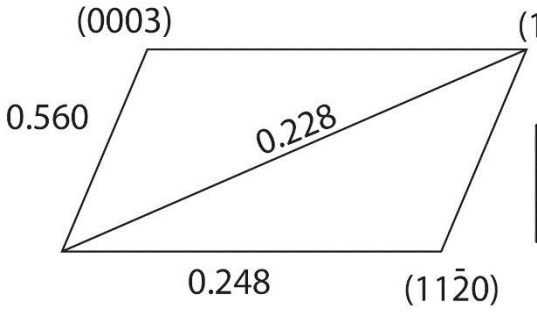

Angle between planes	calculated	observed
11$\bar{2}$3/0003	66.89°	67.00°
11$\bar{2}$3/11$\bar{2}$0	23.11°	22.50°

Supplementary Figure 7.6. Crystallographic analysis of HR-TEM images in Figure 7.6. Lattice distances and measured angles are consistent with calcite and not with vaterite.

Supplementary Table 7.1. Measured d-spacings in *Orbulina universa* and *Neogloboquadrina dutertrei* shells compared with literature data. Several crystals from each foil were indexed by SAED or HRTEM and are compiled in the table.

Observed	**Vaterite ($P3_21$)**		**Calcite (R-3c)**	
d_{hkl} (nm)	***d_{hkl} (nm)***	***hkl***	***d_{hkl} (nm)***	***hkl***
0.841	0.844	0003	-	-
0.563	0.554	01-12	-	-
0.384	0.391	01-15	0.3855	10-12
0.307	0.306	02-23	0.303	01-14
0.280	0.282	01-18	-	-
0.299	0.290	02-23	-	-
0.245	0.248	20-26	0.249	11-20
0.227	0.229	12-32	0.2284	11-23
	0.225	12-33		
0.207	0.206	11-210	0.2094	20-22
0.192	0.1948	00013	0.1927	20-24
	0.190	30-35	0.9124	01-18
0.157	0.158	00016	0.1587	10-110

Supplementary Table 7.2. Band assignment for measured FTIR spectra from *Orbulina universa*, *Neogloboquadrina dutertrei* shells and *Herdmania momus* spicules. Spectral resolution is 4 cm^{-1}.

O. universa **(cm^{-1})**	***N. dutertrei*** **(cm^{-1})**	***H. momus*** **(cm^{-1})**	**Vaterite*** **(cm^{-1})**	**Calcite*** **(cm^{-1})**	**Bond Vibration**
872	872	872	877	876	carbonate ion out-of-plane bending mode (ν2)
740	740	743	744	-	carbonate ion in-plane bending mode (ν4)
712	712	-	-	712	carbonate ion in-plane bending mode (ν4)

*Band assignments for vaterite and calcite from [33].

8.0 General conclusions

The architecture of calcareous biominerals consists two structural elements—inorganic minerals, usually of calcium carbonate, and organic macromolecules (the organic matrix) within and between inorganic minerals. The organic matrix consists a mixture of lipids, glycoproteins, proteins and polysaccharide *β*-chitin. The main structural component of the matrix is thought to be *β*-chitin. Another vital constituent present in some calcareous shells, for instance, nacre, is the silk-like gel. The combination of polysaccharide *β*-chitin and silk-like gel proteins are suggested to be responsible for the formation of the three-dimensional biopolymer in mollusc shells. While the mixture involved multi-hierarchical processing thus influence or modify the mineral phases, macromolecules (proteins) that are rich with acidic sidechains are thought to be involved in controlling crystal morphology and determine the structural pattern of the biominerals. Although polysaccharide *β*-chitin, silk-like gel and the acidic proteins are considered the primary shell constituents macromolecules, many other shell proteins have been sequenced. However, their respective role(s) in the formation of calcareous shells have not been clarified.

In the formation of calcareous biominerals, different morphologies showed topological variability and diversity. By using the principle of molecular universality and bio-diversity herein, this thesis shows that 20 naturally occurring amino acids are the essential ‘toolkit’ for the formation of a three-dimensional assembly of organic matrix in calcareous biominerals. The amino acids represent the largest group of mutually analogous nutrients and are correspondingly broad among metabolites and the matrix macromolecules constituents besides their apparent role in protein synthesis [1, 2].

The composition of shell macromolecules in nacre constitutes the high amount of glycine, alanine and serine (ca 60%), characteristic of silk fibroin-like proteins. Proteins with this amino acid constituents can form a *β*-pleated sheets structure. Whereas non-nacre that is homogeneous (*Arctica islandica*) and crossed lamellar (*Tridacna gigas*, *Fulvia tenuicostata* and *Callista*

disrupta) depicts large proportions of glycine, aspartate and proline (ca 40%), a composition which is more reminiscent of collagen than of silk. However, both, i.e. nacre and non-nacre are nonacidic thus presume that the constituent of Ca-binding proteins may vary predominantly according to shell structure and/or species. This thesis reveals that no hydrophobic and/or acidic proteins appear to be specific to certain calcareous microstructures.

Moreover, by using the theory of universality, identification of chitin-protein-complex from crossed lamellar *Tridacna* shells, *Fulvia tenuicostata* and *Callista* shells representing three molluscan orders and families exhibit that this organic fibre is not only restricted to families with nacroprismatic shells. Though the proportion of chitin (and its derivatives) has/have not been quantifying from crossed lamellar shells, NMR analysis revealed that the amount is smaller and vary. In homogenous shell structure the amount is a ca 1 % and less than 0.5 % in nacre.

The crystallisation particle attachments, of course, include classical ion-by-ion precipitation and ripening during particle motion, collision and aggregation [3]. The universal motif, i.e. a nanogranular biocomposite structure, is shared by most biominerals which rest on a common pathway — a colloid-driven and non-classical crystal growth mechanism [4, 5]. Herein, crossed lamellar *Tridacna* shells, *Fulvia tenuicostata* and *Callista* shells representing three molluscan orders and families composed of a nanogranular composite structure.

A complete picture of shell matrix macromolecules includes 20 naturally occurring amino acids, and these are essential in forming biopolymers. In the biomaterials making up the shells of molluscs, however, biomineralising organisms used bio-diversity pathways/mechanisms to synthesise organics within calcareous shells thus make mollusc shells species-specific at the microstructural level. Silk-based fibre is the primary organic framework in nacre. In homogeneous (and probably in crossed lamellar) microstructures, however, the mesh networks

formed by type IV collagen heparin sulfates and keratanasulfates are the major organic scaffold rather than the more typical fibrillar form.

Significance

Over last few years, our ability to understand the formation of calcareous shells has increased tremendously. Thanks to the advent of high-resolution imaging and modern bioanalytical equipment, the ability to characterise organic macromolecules involved in the mineralisation process and the interactions between them have grown and expanded.

In this work, solid-state NMR, electron microscopy imaging and other bioanalytical techniques have deciphered the actual constituent of biopolymers in calcareous biominerals. The main biopolymer in nacre is silk fibre, whereas network-forming collagen IV gel is the primary bioorganic matrix in homogeneous (and probably in crossed lamellar) structures. As more efforts have recently been directed to replicating key fabrication strategies and structural features into materials design, the finding(s) herein will allow researchers across some fields to design and fabricate a variety of advanced hybrid materials with desired morphologies, compositions, and structures. The present work will guide researchers to use environmentally friendly functional macromolecules and save them from try-and-error analyses that have been practising over several decades.

The key research outcomes achieved through each chapter in this thesis are summarised below.

Chapter 2 shows first analysis of organic macromolecules for *Arctica islandica* shells and distinguish the homogeneous *Arctica islandica* shells from nacroprismatic *H. cumingii*, *P. fucata* and *D. chilensis* shells. Newly adapted fixations and staining protocols reveal many protein bands (e.g. around 20 and 63 kDa) in *H. cumingii* for the first time. The shells with homogeneous and nacroprismatic microstructures have some protein band(s) in common: *A. islandica, P. fucata* and *H. cumingii* exhibit a prominent protein band at 40 kDa. *P. fucata*

demonstrates just one band at 40 kDa, which is a nonacidic-matrix-protein. Moreover, the shell macromolecules of all studied samples are overall non-acidic, containing low amounts of aspartate and glutamate (21% for homogeneous and 16% for nacroprismatic shells).

Chapter 3 utilises solid-state NMR, scanning electron microscope and other spectroscopic techniques to characterise the bioorganic content within the nacreous and homogeneous shells. In nacreous shells polyamino acids – silk fibroins fibres are the primary organic scaffold not chitin and network-forming collagen – type IV collagen is the main organic framework in homogeneous shells (and probably in crossed lamellar). This aspect of the study reveals that the 20 naturally occurring amino acids are the essential 'toolkit' for the formation of a three-dimensional assembly of organic matrix in calcareous biocomposites.

Chapter 4 shows that crossed lamellar *Tridacna derasa* shells are highly mineralised biocomposites consisting of aragonite and a ca 1 wt% organics. In the present work, chitin-protein-complex was evidenced in *Tridacna* shells from Fourier transform infrared and optical activity studies for the first time. The spread of crystal orientation angles due to intense twinning at all hierarchical structures, nano-granularity and random orientation of the aragonitic crystallographic a and b axes, optimise Young's modulus of the shell in all directions and all spatial scales, thus increasing isotropy. This is one of the first comprehensive studies that identify optimization strategies for mechanical properties across all hierarchal structures in the shell.

Chapter 5 presents a detailed biochemical analysis of the organic macromolecules including chitin and its derivatives, shell proteins and saccharidic composition from *Tridacna gigas* and *Fulvia tenuicostata* shells. The quantities of organic matrices are variable, however, newly developed staining methods allowed to detect numerous protein bands in the bivalve shells with crossed lamellar microstructure for the first time. Glycopolymers that transect *T. gigas* and *F.*

tenuicostata shells are visualised using Calcofluor white M2R, chitosan (deacetylated chitin) was demonstrated after staining the SDS-electrophoresis with the Calcofluor white.

Chapter 6 shows in-depth analysis of *Callista* bivalve shells. This shell is composed of an outer composite prismatic, a middle layer with rod-type crossed lamellar and an inner layer that includes both homogeneous and fine complex crossed lamellar structures. The primary amino residues of *Callista* shells including glycine, aspartate and proline are strikingly comparable with the homogeneous *Arctica islandica* shell (39.9% in total vs 39.5%). Exploring glycopolymers in using fluorescence Calcofluor White M2R dye for both *in*-situ and *ex*-situ, the present study revealed chitin containing carbohydrates. However, based on the amount of total organic contents in *Callista* shells (1.7 wt%), the amount of chitin (and its derivatives) could be lower than the one present in the nacroprismatic shells.

Chapter 7 shows that the composition, that is coordination of organic matrix and inorganic mineral extended to the nucleation and growth of the carbonate shells of tiny marine plankton, foraminifera. In living foraminifera the organic layer plays a crucial role; it protects the metastable calcium carbonate – vaterite, degradation of this layer after death will expose any vaterite present to dissolution as shells sink via the thermocline into the deep ocean.

Objectives for future studies and recommendations

This study showed that silk-based fibre is a major organic matrix in nacreous layer of nacroprismatic shells studied (*Hyriopsis cumingii, Cucumerunio novaehollandiae, Alathyria jacksoni, Pinctada maxima*) and network-forming collagen – type IV collagen is a major organic framework in homogeneous *Arctica islandica* (and probably in crossed lamellar) shells. However, several lacunas persist with the multidisciplinary inputs demand to simplify the composition of shell macromolecules and the interfacial carbonates in shells of molluscs. For instance:

1) The detailed proteomics would be necessary to further characterise the constituents of organic framework;
2) As shown by solid state-NMR, nacre consists a measurable amount of phosphorus. The role of phosphorus in shells formation is still vague. However, it has previously been confirmed that a small fraction of either serine or tyrosine residues in *Nephila clavipes* major ampullate gland spider silk is phosphorylated [6]. Accordingly, the phosphorylated glycoprotein is the predominant post-translational modification through which protein function is regulated; it only occurs at the side chains of three amino acids, serine, threonine and tyrosine, in eukaryotic cells. This aspect in the formation of shell has not been probed and thus needs more attention to achieve primary aims of synthesising inorganic (calcium) carbonate materials;
3) Finally, shell decalcification is one of the significant steps to the characterisation of shell macromolecules. The present work revealed that grinding shell into powdered has a lot of effects; it affects nanocrystals that are well-organised within the organic fibres – semi-amorphous region and damaged the extent of fibres in calcareous shells. These are discovered in this thesis, and for sure, other effects will still be discovered in the nearest future.

8.1 References

1. Hoefgen, R., H. Hesse, and G. Galili, *Amino Acids*, in *Handbook of Plant Biotechnology*. 2004, John Wiley & Sons, Ltd.
2. Christensen, H.N., *Role of amino acid transport and countertransport in nutrition and metabolism.* Physiological reviews, 1990. **70**(1): p. 43-77.
3. De Yoreo, J.J., et al., *Crystallization by particle attachment in synthetic, biogenic, and geologic environments.* Science, 2015. **349**(6247): p. aaa6760.
4. Rodríguez-Navarro, C., et al., *Nonclassical crystallization in vivo et in vitro (II): nanogranular features in biomimetic minerals disclose a general colloid-mediated crystal growth mechanism.* Journal of structural biology, 2016. **196**(2): p. 260-287.
5. Wolf, S.E., et al., *Nonclassical crystallization in vivo et in vitro (I): process-structure-property relationships of nanogranular biominerals.* Journal of Structural Biology, 2016. **196**(2): p. 244-259.
6. Hijirida, D.H., et al., *13C NMR of Nephila clavipes major ampullate silk gland.* Biophysical Journal, 1996. **71**(6): p. 3442-3447.

Appendix A: Declaration of authorship contributions

1. Organic macromolecules in shells of *Arctica islandica*: comparison with nacroprismatic bivalve shells

While my supervisor, Dorrit E. Jacob, contributed immensely to the conception and design of the thesis and proofread the manuscripts, **Agbaje, O.B.A.** designed, collected and analysed the thermal gravimetric analysis, Fourier Transform Infrared (FTIR) and SDS-electrophoresis data for this chapter. Amino acid analysis was performed by Denise E. Thomas at Australian Proteome Analysis Facility (APAF), whereas the method for the analysis was designed by me (**Agbaje, O.B.A.**) and I analysed the data.

2. Silk-based Fibres not Chitin: Major Organic Component of Bivalve Shells Revealed by Solid-State NMR

Agbaje, O.B.A. designed this chapter of the thesis and was supervised by Dorrit E. Jacob. I undertook sample preparation and collected scanning electron microscope imaging and Fourier Transform Infrared spectra at Macquarie University. I designed the method used for the analysis of sugar compositions and Fei Chi carried out the analysis at Australian Proteome Analysis Facility (APAF), and I interpreted the data. Ira Ben Shir, David B. Zax and Asher Schmidt contributed as the solid-state NMR experts and adjunct supervisors during my offsite research trip to the Technion-Israel Institute of Technology (TIIT), Technion City, Haifa, Israel.

3. Architecture of crossed-lamellar bivalve shells: The Southern Giant Clam (*Tridacna derasa*, Röding, 1798)

Agbaje, O.B.A. designed and analysed the organic matrix from *Tridacna derasa*, and thus showed that crossed lamellar shells comprising chitin-protein-complex and lipid-lipoproteins. Wirth R. and Jacob D.E. carried out the TEM analyses; Morales L.F.G.

collected and analysed the EBSD data; Shirai K., Kosnik M. and Watanabe T. participated in the design of the study and contributed data.

4. Inorganic-organic relationships in the crossed lamellar shells

Agbaje, O.B.A. designed and analysed the data in this manuscript. The amino acid and monosaccharide compositions were carried out at Australian Proteome Analysis Facility (APAF) by Thomas D.E. and Fei Chi, respectively. Jacob D.E. acted in her capacity as a principal supervisor with insight into the analytical work and was a reviewer of the manuscript. Dominguez J.G. and Kosnik M.A. provided bivalve shells for this chapter of the thesis.

5. Bioorganic-inorganic fibre network in the crossed lamellar bivalve shells: Architecture of shells of *Callista* spp.

Agbaje, O.B.A. designed, collected and analysed the data in this manuscript. Amino acid and saccharide compositions were carried out at Australian Proteome Analysis Facility (APAF). Jacob D.E. is a reviewer of the manuscript. Dominguez J.G. provided *Callista kingii* bivalve shells for this chapter of the thesis.

6. Planktic foraminifera form their shells via metastable carbonate phases

Eggins S.M. and Jacob D.E. designed the experiment, Jacob D.E., **Agbaje O.B.A.**, Wirth R. and Branson O. carried out the measurements and analysed the data.

All knowledge begins as uncommon — unrecognized,

undervalued and sometimes unaccepted.

But with the right perspective,

the uncommon can become the exceptional.

ELSEVIER.COM

…….……everything is possible, a new way of thinking

JESU LOLUWA, AMIN

(JESUS IS LORD, AMEN)